T2R2 東京工業大学リサーチリポジトリ
Tokyo Tech Research Repository

論文 / 著書情報
Article / Book Information

題目(和文)	
Title(English)	Compositional modulation of Zn(S,Se,Te) crystals and their optoelectric properties
著者(和文)	藤原裕之
Author(English)	Fujiwara Hiroyuki
出典(和文)	学位:博士(工学), 学位授与機関:東京工業大学, 報告番号:甲第3272号, 授与年月日:1996年3月26日, 学位の種別:課程博士, 審査員:
Citation(English)	Degree:Doctor (Engineering), Conferring organization: Tokyo Institute of Technology, Report number:甲第3272号, Conferred date:1996/3/26, Degree Type:Course doctor, Examiner:
学位種別(和文)	博士論文
Type(English)	Doctoral Thesis

Powered by T2R2 (Tokyo Institute Research Repository)

Doctor Thesis
January, 1996

Compositional Modulation of Zn(S,Se,Te) Crystals and Their Optoelectric Properties

Hiroyuki FUJIWARA

Department of Electronic Chemistry
The Graduate School at Nagatsuta,
Tokyo Institute of Technology
under the supervision of
Professor Isamu Shimizu

Contents

Chapter 1. Introduction

1.1 Background 1
1.2 Current Problems in II-VI group crystals 11
    1.2.1 Strain Effects 11
    1.2.2 Atomic Fluctuation Effects 13
    1.2.3 Conductivity Control 14
1.3 Objective of this study 17
1.4 Organization of the thesis 20

Chapter 2. Experimental Details

2.1 Growth of Zn(S,Se,Te) crystals by HRCVD 23
    2.1.1 Growth chamber 24
    2.1.2 Hydrogen plasma 27
    2.1.3 Gas supply system 28
    2.1.4 Vacuum system 32
    2.1.5 Surface treatment of substrate 32
    2.1.6 Procedure for crystal growth 36
2.2 In-situ monitoring of reaction process 39
    2.2.1 Quadrupole Mass Spectroscopy 39
    2.2.2 Surface Photo-absorption 42
2.3 Characterization method for semiconductors 49
    2.3.1 Optical characterization techniques 49
    2.3.2 Electronic characterization techniques 57

2.3.3 Structural characterization techniques 60

Chapter 3. Atomic Layer Epitaxy of ZnSe by HRCVD

3.1 Development of ZnSe growth by HRCVD 67
3.2 Decomposition processes of source gases by atomic hydrogen 73
3.2.1 Introduction to metalorganic compound 73
3.2.2 Decomposition process of II-group source 75
3.2.3 Decomposition processes of VI-group sources 80
3.3 Surface reaction process observed by *in-situ* SPA 86
3.3.1 Introduction to *in-situ* monitoring using SPA 86
3.3.2 Flow rate dependence of source gases 92
3.3.3 Growth temperature dependence 99
3.4 Growth mechanism of ZnSe by HRCVD 105
3.4.1 Fundamental characteristics of ZnSe crystal 105
3.4.2 Crystal growth mechanism of ZnSe by HRCVD 107

Chapter 4. Structure and Properties of Zn(S,Se) Ordered Alloys

4.1 Growth of ZnS_xSe_{1-x} alloys by ALE-mode 113
4.1.1 Structure of ZnS_xSe_{1-x} crystals 114
4.1.2 PL properties of ZnS_xSe_{1-x} crystals 116
4.2 Growth of $(ZnS)_n(ZnSe)_m$ ordered alloys 123
4.2.1 Structure and Properties of $(ZnS)_n(ZnSe)_{12n}$ (n=1-4) 123
4.2.2 Structure and Properties of $(ZnS)_3(ZnSe)_m$ (m=12-72) 128
4.3 Exciton dynamics of Zn(S,Se) ordered alloys 135
4.3.1 Exciton under high excitation-states 135
4.3.2 Exciton relaxation process 138
4.3.3 Exciton absorption process 139
4.4 Optical properties of sawtooth superlattices (STS) 145
4.4.1 Introduction to Sawtooth superlattice 147
4.4.2 Structures and PL properties of STS 147
4.5 Crystal structure stability in Zn(S,Se) ordered alloys 155
4.5.1 Photo-induced degradation effect 155
4.5.2 Thermal-induced degradation effect 160

Chapter 5. Carrier Transport Properties of Zn(S,Se) Ordered Alloys

5.1 Growth of n-type Zn(S,Se) crystals using TEGa 165
5.1.1 Growth of n-type ZnSe crystals using TEGa 166
5.1.2 Growth of n-type Zn(S,Se) crystals using TEGa 169
5.2 Growth of n-type Zn(S,Se) crystals using i-BuI 173
5.2.1 Growth of iodine-doped Zn(S,Se) crystals 175
5.2.2 Structure and Optoelectrical properties 178
5.3 Carrier transport properties of Zn(S,Se) crystals 185
5.3.1 Donor activation process 185
5.3.2 Carrier scattering mechanism 190
5.3.3 Effect of 2-dimensional ordered structure 196

Chapter 6. Structure and Properties of Zn(Se,Te) Ordered Alloys

6.1 Introduction to Zn(Se,Te) crystals 205
6.2 Growth of ZnTe crystal 206
6.3 Growth of $(ZnSe)_n(ZnTe)_{11n}$ (n=1-4) on InAs substrate 211
6.3.1 Optimization of growth conditions 211
6.3.2 Structure of $(ZnSe)_n(ZnTe)_{11n}$ (n=1-4) 214
6.3.3 Optical properties of $(ZnSe)_n(ZnTe)_{11n}$ (n=1-4) 216
6.4 Growth of $(ZnSe)_n(ZnTe)_n$ (n=1-4) on InP substrate 225
6.4.1 Structure of $(ZnSe)_n(ZnTe)_n$ (n=1-4) 225
6.4.2 Optical properties of $(ZnSe)_n(ZnTe)_n$ (n=1-4) 230
6.5 Conductivity control of ZnTe crystal 235

Chapter 7. Summery 239

Acknowledgment 243
Research Report 245
Reference 253
Announcement 269
Attendance List 270

Chapter 1

Introduction

During the 1990's incredible breakthroughs have occurred in the area of blue-green light emitters - the realization of ZnSe-based blue-green lasers. Today, blue and green light emitting devices are the hottest topic in compound semiconductors. There is, however, still much fundamental characteristics to be understand in ZnSe-based crystals. The most characteristic feature of II-VI group crystals mainly originate from ionic nature of these crystals. In the first section of this chapter, such basic characteristics of II-VI group crystals are reviewed, together with recent developments of device application. In the following section, strain effects, atomic fluctuation effects and conductivity control are described in detail, which provide the understanding about current problems in II-VI group crystals. A newly developed crystal fabrication technique, "Hydrogen Radical-enhanced CVD", will be also introduced in this chapter. The objective of this study as well as the organization of this thesis will be described at the end of this chapter.

1.1 Background

II-VI group compounds such as ZnS and CdS are originally used as a material for a fluorescence light and a photoconductor. The fabrication of II-VI semiconductor crystals have been the object of intense research for many years. The motivation of these researches are the expectation that the wide bandgap II-VI compound semiconductors can be used for a variety of optical devices which cover the entire range of the visible spectrum from infrared to ultraviolet. Despite the fact that the direct bandgap II-VI semiconductor crystals offer the most promising materials for realizing diode

lasers and light-emitting diode (LED) displays over the green-blue region of the visible spectrum, the growth of high-quality II-VI group crystals was not established by the late 1970s. In the early 1980s, a number of research efforts began by applying the modern nonequilibrium epitaxial growth methods, such as molecular beam epitaxy (MBE) and metalorganic vapor phase epitaxy (MOVPE), to the growth of the wide bandgap II-VI semiconductors. The application of the new growth techniques resulted in substantial progress in the research on II-VI group crystals. At the same time, structure controls of these crystals such as quantum wells and superlattices became possible by these crystal growth techniques. During 1991, a group of 3M Corporate Research Laboratories finally announced the first demonstration of ZnSe-based diode lasers operated under the pulsed excitation at low temperature, which created a new phase of developments.

1.1.1 Basic characteristics

II-VI group compound semiconductors can be categorized in two major part depending on their bandgaps; narrow-bandgap and wide-bandgap materials. Bandgaps of mercury-based compounds, such as HgTe and HgSe, are 0 eV due to degeneration between the conduction band and the valence band, and show specific behavior in absorption spectra and dielectric functions.[1] By forming alloy of HgTe with CdTe, the bandgap of HgCdTe alloys can be changed from 0~1.44 eV, and infrared detector made of HgCdTe has been commercialized using this character. In contrast to HgTe compounds, all Zn-based crystals used in this study, such as ZnS, ZnSe and ZnTe, have wide-bandgaps, which cover the range of visible spectrum from green to ultraviolet. Figure 1-1 shows the lattice parameter of various semiconductor crystals plotted as a function of their bandgap energy. As shown in this figure, wide-gap II-VI crystals have the higher bandgaps and lattice parameters compared with other IV or III-V group crystals. Figure 1-2 shows the band structure of ZnSe.[2] All the II-VI crystals have direct transitions; the lowest position of the conduction band agrees with the highest position of the valence band at Γ point, as indicated in Figure. 1-2. Accordingly, II-VI semiconductors are promising materials for various optoelectric devices, since the direct transition of these crystals provides the high-efficiency light absorption or emission probabilities.

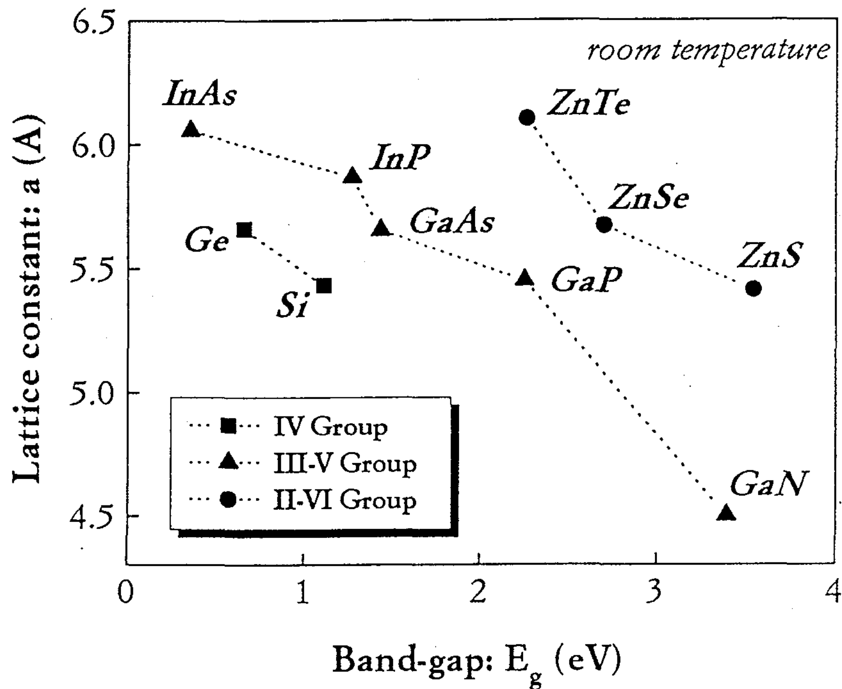

Figure 1-1 Lattice parameter of various semiconductors including II-VI group crystals used in this study plotted as a function of bandgaps of the crystals at room temperature.

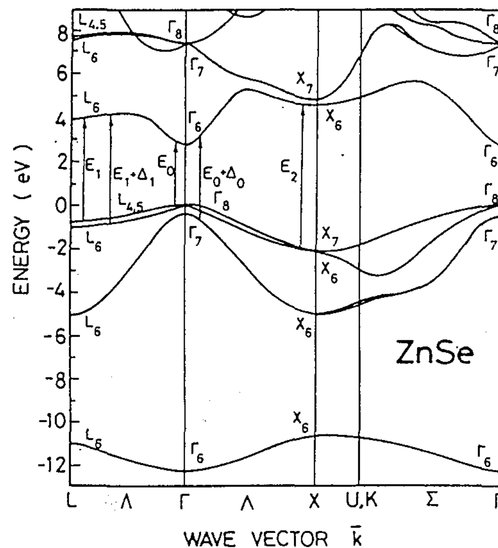

Figure 1-2 The calculated band structure of ZnSe near bandgap region.[2)]

All the II-VI crystals have crystal structures of wurtzite and zinc blende, since the energy difference in these two type of crystal structure is very small in II-VI crystals. ZnSe and ZnTe, however, show dominant zinc blende

structure, while the dominant crystal structure in ZnS, CdSe and CdS crystals are wurtzite.

1.1.2 Crystal growth method

The most characteristic feature of II-VI semiconductors is the high ionicity of the crystals. Because of this nature, unfavorable formation of native defects such as vacancy generation is a inevitable problem in II-VI crystals. In order to prevent the formation of these native defects, the low-temperature growth techniques such as MOVPE or MBE have been employed for the growth of ZnSe-based crystals.[3-15]

Figure 1-3 shows a schematic diagram of a crystal growth by MOVPE. In this method, metalorganic compounds including crystal constituent atoms are simply decomposed at a thermally heated susceptor, which results in the crystal growth on a substrate placed on the susceptor. These metalorganic molecules are supplied into a growth chamber by a vapor phase using hydrogen gas as a carrier gas. The reaction chamber walls are typically made of quartz and the susceptor is heated by radio-frequency induction. MOVPE is used in manufacturing environments for the production of optoelectronic devices. Multiwafer systems are frequently used in such manufacturing systems.

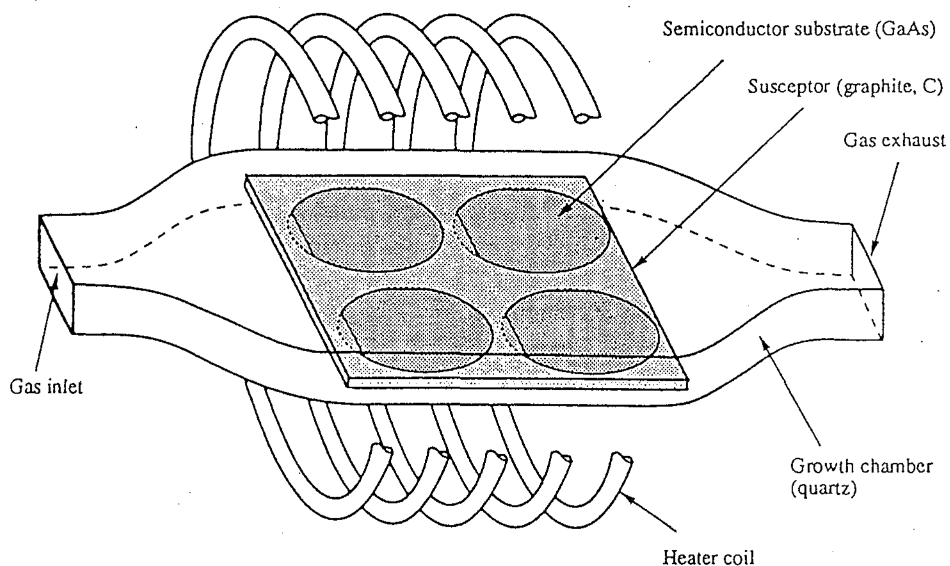

Figure 1-3 Schematic illustration of the growth chamber of MOVPE system.

Accordingly, MOVPE is a promising candidate for the high-throughput epitaxial growth systems. Typical growth temperature of II and VI group source molecules used in MOVPE are summarized in Table 1-1.

Table 1-1 Typical growth temperature of ZnSe for source molecules

VI group	II-group	Growth temperature	Ref.
H_2Se	DMZn	250 °C	[3-6]
DESe	DMZn	450~550 °C	[7]
MASe	DMZn	520 °C	[8,9]
DiPSe	DEZn	~480 °C	[10,11]
DtBSe	DEZn	~310 °C	[11]

MASe: methylallyselenide, DiPSe: diisopropylselenide,
DtBSe: ditertiarybutylselenide

In the early years of ZnSe or ZnS growth by MOVPE, various hydrides (H_2Se or H_2S) were mainly employed as sources for VI group atoms.[3-6] These hydrides are, however, so unstable and lead to homogeneous nucleation of dust and wall deposition even at room temperature when they are mixed with II group alkyls. To solve these problems, simple Se and S alkyls, such as dimethylselenide (DMSe) or diethylselenide (DESe), was used during 1980s.[7] The higher stability of these alkyls, on the contrary, requires increased growth temperatures around 400°C, which gives rise to the formation of native defects in ZnSe crystals. Most recently, t-buthyl alkyl sources of S and Se have been utilized to lower the growth temperature of ZnSe crystals to around 300°C.[10,11] Generally, the growth temperature of ZnSe crystals are higher in MOVPE than that in MBE, because the growth temperatures of MOVPE are originally determined by the decomposition temperature of the stable metalorganic sources. Accordingly, further reduction of the growth temperature is required for the growth of high-quality crystals.

MBE systems have been also utilized for the growth of ZnSe crystals. In addition, most of the optical devices including LD have been fabricated using this technique.[12-15] Figure 1-4 illustrates the typical schematic growth chamber of MBE system. In this method, the constituents of the crystals are evaporated from Knudsen cells which are equipped with mechanical shutters.

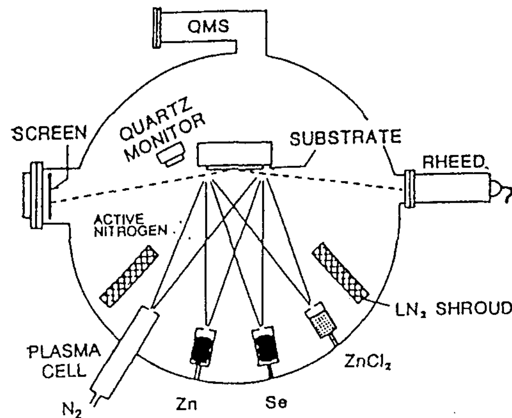

Figure 1-4 A schematic diagram of MBE growth chamber used for the growth of ZnSe crystals.

These effusion cells are placed in ultra-high vacuum (UHV) to form stable "molecular beams" which are supplied to a rotating substrate. A cryoshroud filled with liquid nitrogen (LN_2) encircles the growth area to maintain the UHV in the growth chamber. The UHV in MBE system enables in-situ analysis by reflection high-energy electron diffraction (RHEED) or quadrupole mass spectrometer (QMS).

The crystal growth by MBE offers the relatively low temperature growth compared with MOVPE, since the elemental atoms can be directly supplied from the effusion cells in MBE. As a result, the low temperature growth of ZnSe crystals at around 250~300°C has been established in MBE.[11-15] One of the disadvantages of MBE is a low-throughput of the epitaxial growth and the requirement of the UHV system. Consequently, a mass production of the semiconductor devices are limited in MBE. In addition, there is a difficulty for controlling beam flux of atoms with high vapor pressure such as S atoms.

1.1.3 Atomic layer epitaxy

Recent developments of crystal growth techniques such as MOVPE or MBE create a new field - realization of "atomic control technology". The structure control of a crystal on an atomic scale has been achieved by the technique called "Atomic Layer Epitaxy (ALE)". ALE was first proposed

in 1980 by Suntola et al. for ZnO. More recently, it has been applied in various compound semiconductors such as II-VI and III-V crystals. [16-21) Basically, ALE is a surface controlled process for the crystal growth. Figure 1-5 shows a schematic diagram of ALE process for compound A and B. In ALE, each of the source gases A and B are supplied alternately to form one atomic layer on the crystal growing surface, as shown in Fig. 1-5. Saturation effects of each surface reaction is the characteristic feature of ALE, and this mechanism will be discussed in chapter 3. This self-limiting reaction on the crystal surface in ALE provides several advantages over the crystal growth as follows:

1) accurate thickness control defined by the number of reaction cycles,
2) precise heterointerface control which is needed for the fabrication of superlattice structures,
3) film thickness uniformity over larger areas,
4) reduction in a gas phase reaction between source molecules

So far, the ALE of ZnS, ZnSe and ZnTe crystals has been reported for MBE and MOVPE processes and the saturation effects of the growth rate at the monolayer have been observed.[17-21) The saturation mechanism of ALE, however, still remains to be clarified in II-VI crystals.

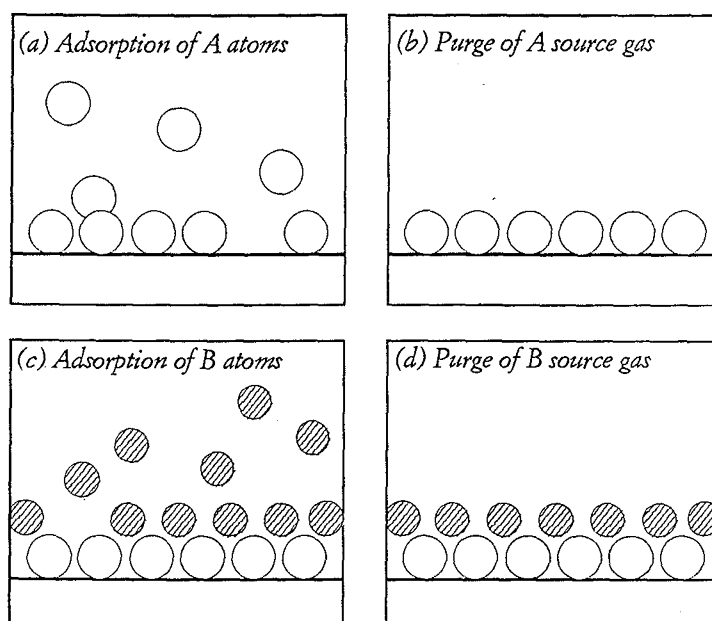

Figure 1-5 A schematic diagram of ALE process for compound A and B. The source gases of A and B are alternately supplied to the reactor with the purge time.

1.1.4 Device applications

So far, ZnSe-based crystals have been employed for various optical devices such as light-emitting diodes (LEDs)[14] and diode lasers (LDs) [11-15] as well as non-linear optical devices.[22,23] Optical data storage is cited as the key application for such wide-bandgap semiconductor lasers, which provide a 5 times increase in storage capacity as compared to current optical technology. Most recently, great progress was made in the fabrication of optoelectronic devices using (Zn,Cd)Se/ZnSe heterostructure, which led to the successful preparation of blue-green LEDs and LDs.[11-15] The first room-temperature continuous-wave (cw) operation of LD were demonstrated at Laboratories of SONY in 1994.[15] Figure 1-6 illustrates a famous structure of the ZnCdSe/ZnSe/ZnMgSSe SCH laser. This blue-green LD is grown on n-type GaAs substrate using MBE. The structures consist of various alloys of ZnSe in which an attempt has been made to preserve lattice matching to GaAs to reduce generation of defects. The LD structure employs ZnMgSSe quaternary optical cladding layers with ZnSSe waveguiding regions and typically use one ZnCdSe quantum well to provide optical gain. In order to form ohmic contact with p-type ZnSe crystals, a graded Zn(Se,Te) structure was adapted in this LD. A room temperature operation of this blue laser diode with a wavelength of 491 nm has been successfully demonstrated by this laser structure, as shown in Fig. 1-7.

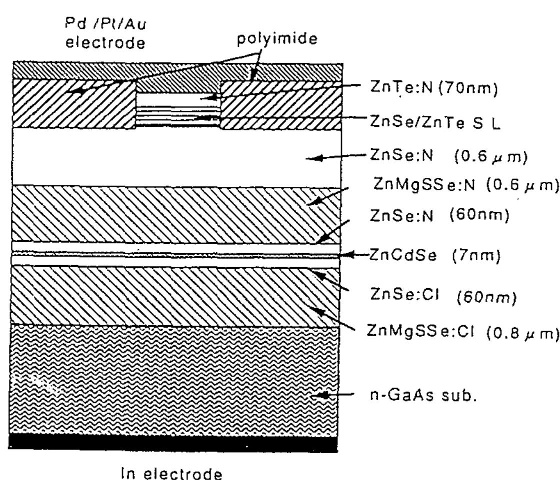

Figure 1-6 A famous structure of the ZnCdSe/ZnSe/ZnMgSSe SCH laser.[15]

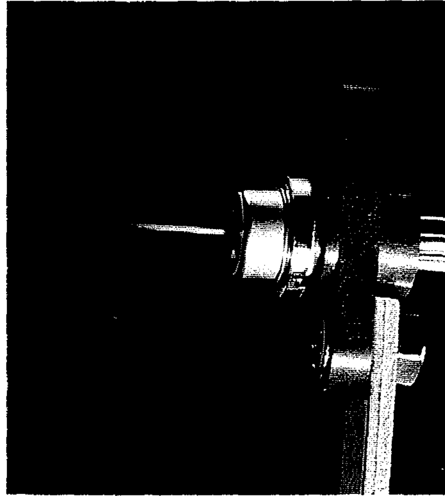

Figure 1-7 A photograph of a ZnSe-based laser diode operating at room temperature with its wavelength of 491nm.[24)]

Most recently, on the other hand, a application of II-VI crystals to non-linear optical devices also began in order to realize an effective optical information processing.[22,23)] ZnSe crystals is one of the candidate for such non-linear optical devices due to its large third order optical polarizability $\chi^{(3)}$ and short switching time τ. Figure 1-8 shows $\chi^{(3)}/\alpha$ plotted as a function of $1/\tau$, where α is the absorption coefficient[25)] The empirical law of $\chi^{(3)}/\alpha$=const is drawn by the gray line in the figure.

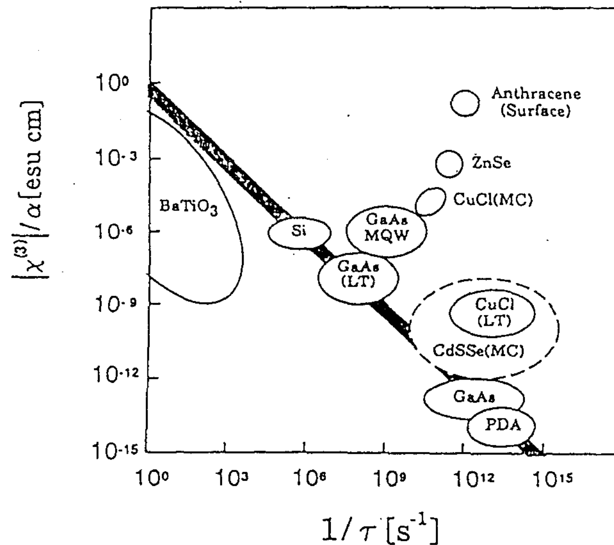

Figure 1-8 $\chi^{(3)}/\alpha$ plotted as a function of $1/\tau$. The empirical law of $\chi^{(3)}/\alpha$=const is drawn by the line in this figure.[25)]

Due to the high ionicity of ZnSe crystals, the stable "Exciton" formation occurs in ZnSe crystals. It has been proposed that such exciton formation enhances $\chi^{(3)}$ and $1/\tau$ due to a increased oscillator strength in crystals.[26,27] Consequently, ZnSe has the higher $\chi^{(3)}/\alpha$ and $1/\tau$ under resonant optical pumping, which is not defined by the empirical law in Fig. 1-8. A huge non-linear of 10^{-2} esu with a response time about 20 psec has been reported in ZnSe grown on GaAs substrate.[23]

1.2 Current problems in II-VI group crystals

There are still many problems for realizing new optical devices using ZnSe-based crystals, although the recent developments in the crystal fabrication techniques enable the growth of high-quality crystals. In general, formation of dislocations as well as stacking faults due to strains existing in II-VI crystals causes serious problems in II-VI crystals. In addition, there are some difficulties for compositional modulations of II-VI crystals due to their large lattice mismatches between II-VI crystals, which lead to larger atomic fluctuation effects in II-VI alloy semiconductors. Among the traditional problems, one of the most troubling is the inability to control the electrical properties of II-VI crystals. This problem is a fundamental one in wide bandgap compound semiconductors, which tend to be "semi-insulators" because of the large polarization by the ionic bonding between II and VI group atoms. These traditional problems, which are directly reflected to the objective of this study, are reviewed in this section.

1.2.1 Strain effects

ZnSe-based crystals are typically grown on GaAs substrates, since the high-quality ZnSe substrates are not commonly available at present. GaAs substrates have a close lattice parameter with ZnSe crystal, as shown in Fig. 1-1, and the lattice mismatch between them is only 0.27%. This small lattice mismatch, however, gives rise to various defect formations including dislocations and stacking faults in the grown ZnSe crystals.

When the thickness of ZnSe crystals grown on GaAs substrate is small, the coherent growth of ZnSe crystal occurs by adjusting the lattice parameter of ZnSe layer to that of the substrate.[28,29] If the thickness of the grown layers exceeds "Critical thickness", the misfit dislocation are then generated in the grown layers to relax the strain induced by the difference in their lattice parameters. The critical thickness of ZnSe crystals grown on GaAs substrates has been estimated to be around 1500Å from X-ray diffraction (XRD) and transmission electron microscopy (TEM).[28-32] Figure 1-9 shows the TEM images of the lattice relaxed ZnSe crystal (2700Å) grown on GaAs substrate.[31,32] As shown in this figure, many misfit dislocations along $\langle 110 \rangle$ directions can be seen in the lattice relaxed ZnSe crystal.

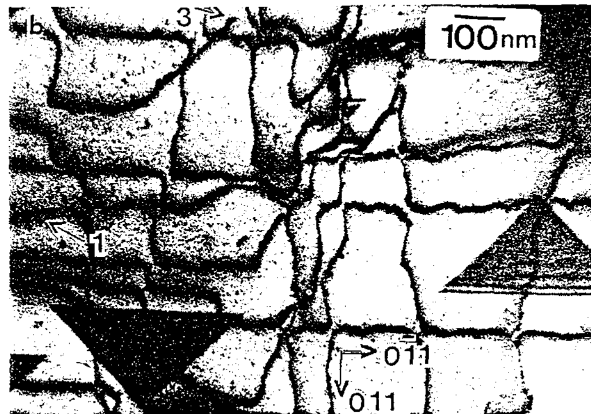

Figure 1-9 Bright field TEM images of ZnSe crystals (2700Å) grown on GaAs substrate.[31]

ZnSe-based crystals generally exhibit the triangular-shaped stacking fault, which are generated at the GaAs interface, as shown in Fig. 1-9. The density of the stacking fault is typically in a range of 10^5-10^8cm^{-2}, and is greatly influenced by the crystal structure or the growth conditions.[30-33] It is reported that these dislocation networks are nucleated at threading dislocations which originate from these V-shaped stacking faults.[33,35] These dislocations multiply during the crystal growth and result in the degradation of crystal properties such as lower light-emission efficiency or increased film resistivity.

Another important problem is the large lattice mismatches among II-VI crystals. The lattice mismatch between ZnS and ZnSe crystals, for example, is almost 4%, and the critical thickness of ZnS on ZnSe crystals is estimated to be only few monolayers.[36] As a result, the compositional modulation of these crystals for "band-engineering" can not be made easily, since larger composition modifications of the crystal lead to the generation of the misfit dislocations to relieve such large strain.

It should be emphasized that even if the ZnSe-base crystals are grown perfectly lattice matched to GaAs, and exhibit very low defects, when the samples are cooled after growth, the ZnSe layers will experience a tensile strain due to differences in the thermal expansion coefficients between GaAs substrate and ZnSe layers.[29,30,37] These values for II-VI and III-V semiconductors are summarized in Table 1-2. This difference in the thermal expansion coefficients also induce the generation of misfit

dislocations. Accordingly, there is still strong requirements for a *"extremely low-temperature growth technique"*.

Table 1-2 Thermal expansion coefficient (α) of II-VI/ III-V crystals

III-V[a]	α ($x10^{-6}$ K^{-1})	II-VI[b]	α ($x10^{-6}$ K^{-1})
GaAs	5.7	ZnS	6.7
InAs	5.1	ZnSe	7.5
		ZnTe	8.2

a) Reference 38
b) Reference 39

1.2.2 Atomic fluctuation effects

Generally, ternary or quaternary alloys of II-VI crystals have been widely used for the band structure modulation in order to realize various optical devices. In these alloys, however, it is known that there exist the statistical fluctuation of constituent atoms, which induces the degradation of crystal properties. Alloy broadening is one of the characteristic feature of these semiconductor alloy, which is induced by the statistical fluctuations of component atoms; the microscopic fluctuations in alloys lead to the anomalous of broadening of excitonic emission lines of both free and bound excitons.[40-43] These potential fluctuations due to the local compositional change greatly degrades the optical properties. Figure 1-10 shows the concentration dependence of the photoluminescence (PL) spectrum of $ZnSe_xTe_{1-x}$ alloys.[43] It is evident that the sharp free exciton emissions gradually broaden with increasing Se contents. The alloy broadening effects have been observed in all the II-VI semiconductor alloys such as ZnS_xSe_{1-x},[40] $ZnSe_xTe_{1-x}$[42,43] and CdS_xSe_{1-x}.[41,44]

A mobility reduction in semiconductor alloys is another serious effects induced by the local atomic fluctuation. Typically, semiconductor alloys show smaller mobilities compared with their host crystals due to "disorder scattering", where the electron is scattered by the random potential fluctuations.[45,46] In fact, Hall mobility of 100 cm^2/Vs obtained for the n-type doped ZnS_xSe_{1-x} (x=0.07)[47] is clearly lower compared with that of 460 cm2/Vs obtained for ZnSe films.[48]

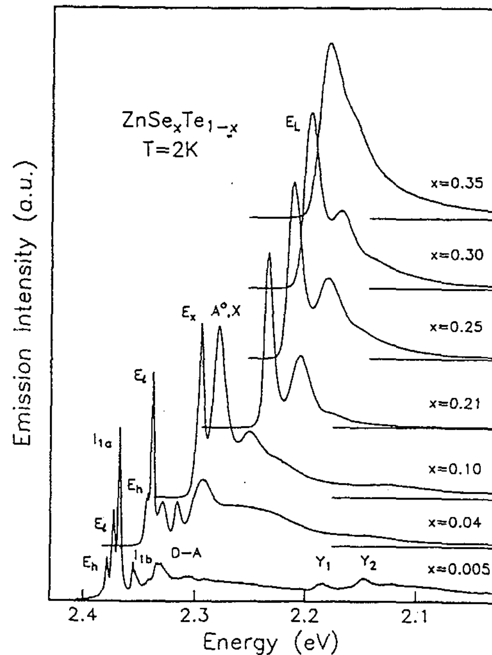

Figure 1-10 The concentration dependence of $ZnSe_xTe_{1-x}$ crystals for the PL spectra measured at 2K.[43]

The formation of the local atomic fluctuation is a substantial problem for the device applications. Basically, the local compositional fluctuation in semiconductor alloys originate from the large lattice mismatch between the constituent atoms. It is known that the large lattice mismatch produces the large positive enthalpy of mixing.[49,50] If this positive enthalpy of mixing overwhelm the negative *entropy* of mixing, a random alloy will decompose into a mixture of two phases, creating a large compositional fluctuation in a crystal. In other word, the growth of lattice mismatch alloys prefers the cluster formation on the surface to reduce the surface chemical potential induced by the strain energy. In order to realize a "band engineering" of various crystals, the suppression of the atomic fluctuation effects is required.

1.2.3 Conductivity control

During the 1980's, ZnSe-based crystals suffered from the big problem - inability to make p-type crystals. Yasuda et al. at Tokyo Institute of Technology first reported the successful fabrication of p-type ZnSe crystals

using Li as a dopant by MOVPE.[51] Then in 1990, Ohkawa et al. at Matsushita Central Research Laboratory developed a MBE technique using nitrogen radicals to produce p-type doping crystal up to $1x10^{18}cm^{-3}$ in ZnSe crystal.[52] This breakthrough directly led to the operation of ZnSe-based laser fabrication.

The difficulty of p-type doping in wide-bandgap II-VI crystals has been explained by the number of theories. It should be emphasized that ZnTe crystal has the opposite behavior with ZnSe, in which p-type doping can be easily achieved while n-type doping is extremely difficult.[53,54] Tokumitu explained this specific doping behavior by Fermi level stabilization energies.[55] Theoretically, this Fermi level stabilization energy (E_{FS}) is defined by the average energy between bonding and anti-bonding states.[56,57] Figure 1-11 shows maximum carrier concentrations for n-type and p-type materials as a function of the energy separation $|E_F-E_{FS}|$.[55] A good liner relations can be seen between the maximum carrier concentration and the energy separation. ZnSe has a large energy separation of 1.7 eV which makes it difficult to be doped p-type, whereas ZnTe has a smaller energy separation of 0.84 eV for $|E_{FS}-E_V|$. Accordingly, the contrast between ZnSe and ZnTe can be interpreted in terms of the position of the Fermi level stabilization in these materials.

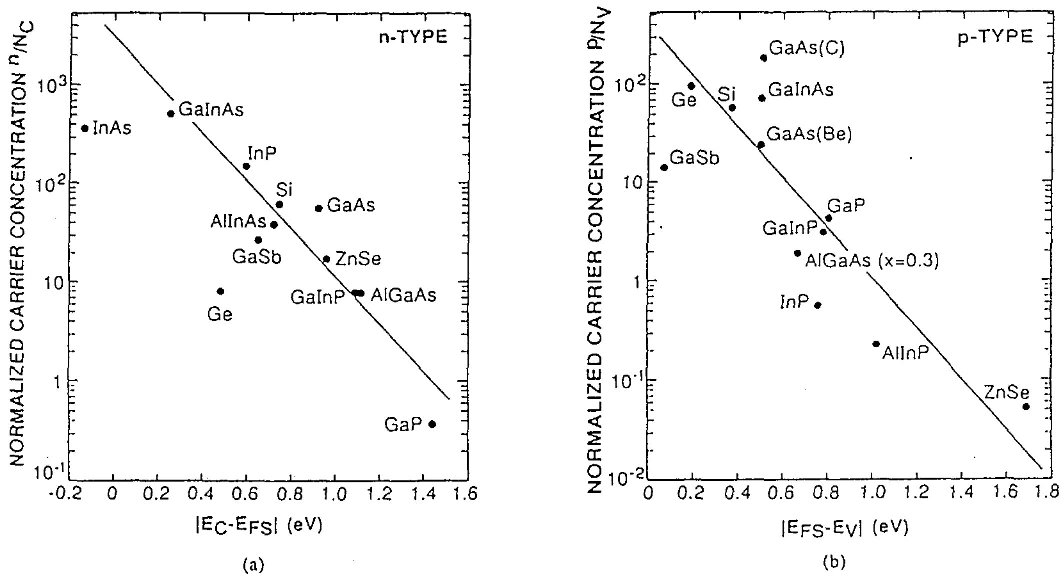

Figure 1-11 Maximum carrier concentrations for n-type and p-type materials as a function of the energy separation $|E_F-E_{FS}|$.[55]

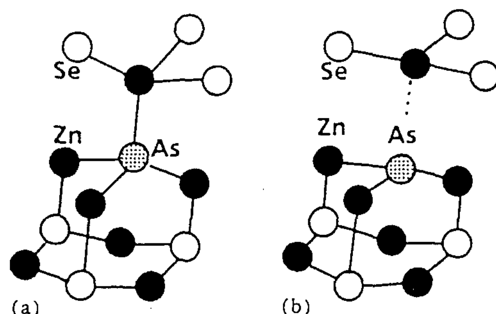

Figure 1-12 The normal substitutional state of acceptor impurity (As) in ZnSe is shown in (a). The localized deep acceptor state *AX* is shown in (b).

Chadi also explained the difficulties of doping in II-VI semiconductors using pseudopotential calculation.[58-60] He suggests that neutral acceptors in ZnSe crystals create specific localized states what is called "AX center". This AX center is proposed to result from the following reaction:

$$2a^0 \rightarrow a^- + AX^+ , \qquad (1\text{-}1)$$

where a^0 and a^- represent neutral and negatively charged state of the acceptor and AX^+ denotes the positively charged state having a large lattice relaxation. The reaction of (1-1) is schematically shown in Fig. 1-12.[60] From the results of the calculation, he suggested nitrogen impurities are the most suitable acceptor for the fabrication of p-type ZnSe.

Current obstacle of p-type doping in ZnSe is a "passivation effect" of acceptors by hydrogen atoms in MOVPE, where the hydrogen typically used as a carrier gas passivate the acceptor sites.[61,62] It has been confirmed that this passivation effect by hydrogen greatly reduce the carrier concentration in ZnSe crystals. Yanashima et al., however, reported the reactivation of these passivated acceptors in ZnSe by the thermal annealing after the crystal growth, which show the hole concentration up to 5×10^{17} cm^{-3}.[62] Another important problem is the significant decrease in acceptor concentration in the crystal having higher bandgaps than ZnSe crystal, such as ZnMgSe and ZnMgSSe.[63-66] This effect has been also explained in terms of the Fermi level stabilization energy[63,64] or other mechanisms.[59,66] To overcome these problems, a progress of a novel doping technique is necessary especially for the growth system where a mass production of devices is possible.

1.3 Objective of this study

As described above, there are still many difficulties for realizing various optical devices using II-VI crystals. In order to solve these problems, we propose a crystal structure called "Ordered Alloy" in this study. A novel crystal growth technique, "Hydrogen Radical-enhanced Chemical Vapor Deposition (HRCVD)" which was originally developed in this laboratory, is adapted for the fabrication of these ordered alloys. In this section, the concept of the ordered alloys as well as HRCVD is presented as a objective of this study.

Figure 1-13 shows a schematic of Zn(S,Se) crystals with ordered and disordered structures. In the disordered alloys typically used for band profiling, each group VI layers have random configuration of S and Se atoms. In contrast to the disordered alloys, the ordered alloys have a two-dimensional layered structures of ZnS and ZnSe. Accordingly, several advantages are expected in this crystal with ordered structures. First, the atomic fluctuation effects induced by the local compositional changes can be suppressed in the ordered alloys since the layer-by-layer structure of the ordered alloys provides the uniform distribution of constituent atoms. A higher mobility as well as a narrow optical emission line is, therefore, expected in the ordered alloys.

Moreover, in the ordered alloys, the suppression of the dislocation generation due to lattice mismatches is also expected by taking advantage of

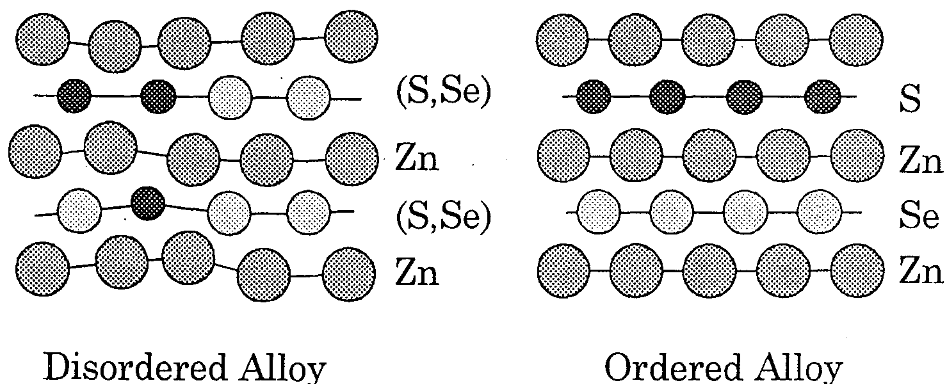

Figure 1-13 A schematic diagram of Zn(S,Se) crystals with disordered and ordered structure.

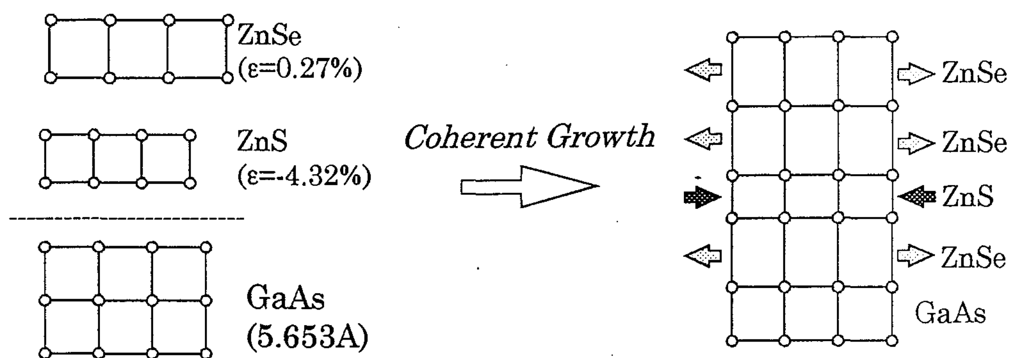

Figure 1-14 A schematic diagram of crystal structure in ZnS-ZnSe ordered alloys. Lattice mismatch strains in ZnS and ZnSe layers are denoted as ε.

the opposite strain effects of each layers. Figure 1-14 shows a schematic diagram of crystal structure in ZnS-ZnSe ordered alloys. When ZnS and ZnSe crystals are grown on GaAs substrates, for example, ZnSe layers receive a compressive strain since ZnSe layer have the larger lattice parameter than the GaAs substrate, while tensile strains are applied to ZnS layer having smaller lattice constant compared with the substrate. As a result, the defects formation caused by the large lattice mismatch could be reduced by this opposite strains in the ordered alloys, if the thickness of each layer is only few monolayers. The problem in conductivity control of the II-VI crystals can be also solved by this ordered structures. By combining ZnTe layers with ZnSe crystals, the realization of p-type conductivity becomes possible by the selective doping to ZnTe layers, where the p-type conductivity is easily obtained as discussed above.

Consequently, there are the expectations that the crystal structure of the ordered alloys provides a larger compositional modulation of II-VI crystals, while suppressing the defect formation caused by the large lattice mismatch and the property degradation induced by the local compositional fluctuations. Accordingly, the ordered alloys create a new possibility that we can freely change the band structure of the II-VI crystals to realize new functional optical devices.

For the fabrication of the high-quality crystals with ordered structures, a low temperature growth is essential to reduce the interdiffusion as well as the native defect or dislocation generations. A novel technique called HRCVD provides a low temperature growth, which can not be attained by other crystal growth techniques such as MBE or MOVPE.

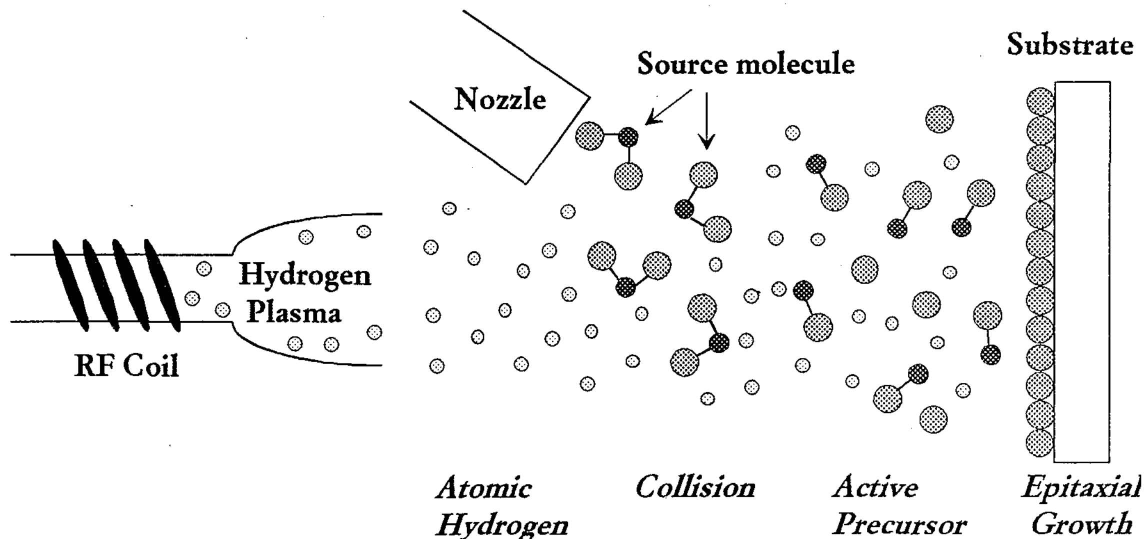

Figure 1-15 A schematic mechanism of the crystal growth in HRCVD.

A schematic growth mechanism in HRCVD is illustrated in Figure 1-15. In this method, the formation of precursors are enhanced by a chemical reaction between metalorganic source molecules and atomic hydrogen generated by remote hydrogen plasma. These reactive precursors enable the low temperature growth of ZnSe crystals at the temperature of 200°C. The crystal structure modulations on the atomic scale is also needed for the fabrication of the ordered alloys. Atomic layer epitaxy is adapted in this study for the fabrication of such ordered structures.

In this study, we made several types of Zn(S,Se,Te) crystals with ordered structures by ALE using HRCVD method. The fundamental characteristics of the ordered crystal on the atomic scale are described in detail from the results mainly obtained from the PL and XRD measurements. Especially, the superior properties of the ordered alloys over the disordered alloys will be emphasized in this thesis.

1.4 Organization of the thesis

The content of this thesis can be categorized by three major parts; experimental section (chapter 2), result & discussion (chapter 3~6) and conclusion (chapter 7). The content as well as the objective of each chapters are briefly summarized in this section as follows:

Chapter 2

The equipment and the design of HRCVD are mainly described in this chapter. In addition, *in-situ* monitoring systems of quadrupole mass spectroscopy (QMS) and surface photo-absorption (SPA) are shown. Details of various characterization techniques are also presented.

Chapter 3

Decomposition processes of metalorganic compounds by atomic hydrogen are determined from the QMS analysis. In the following section, the growth of ZnSe crystals by ALE-mode are shown. Crystal growth mechanisms of ZnSe in HRCVD are discussed by the *in-situ* monitoring of surface reactions using SPA .

Chapter 4

The various structures of Zn(S,Se) ordered alloys are fabricated by HRCVD using ALE-mode to clarify the fundamental characteristics. In addition, graded potential formation by sawtooth superlattices (STS) is discussed as a potential application for optical modulators. In the following section, the optical and thermal stability of the ordered alloys are shown.

Chapter 5

In order to determine the "disorder scattering effect" in the disordered alloys, the carrier transport properties of Zn(S,Se) ordered alloys are investigated. The fabrication of n-type Zn(S,Se) is made using Ga and I as a dopant. From the temperature dependence of Hall measurement, the carrier scattering mechanisms for ordered and disordered structures are determined.

Chapter 6

Zn(Se,Te) crystals are fabricated on InAs and InP substrates by HRCVD to realize p-type conductivity. The specific optical behaviors of Zn(Se,Te) crystals are shown by the various optical measurement such as time-resolved PL and PL excitation spectra. Especially, the contrast between Zn(S,Se) and Zn(Se,Te) crystals is discussed in detail.

Chapter 7

Summery of the compositional modulation by the ordered structure in Zn(S,Se,Te) crystals together with the future prospects of the research is described.

Chapter 2

Experimental Details

Hydrogen radical-enhanced chemical vapor deposition (HRCVD) can be used to control Zn(S,Se,Te) crystal composition with atomic scale precision. The newly developed HRCVD design and apparatus are described in details. The substrate preparation is also discussed in section 2.1. In Section 2.2, experimental setups for in-situ crystal growth monitoring using surface photo-absorption (SPA) and a quadrupole mass spectroscopy (QMS) of source gases are shown. In the last part of this chapter, material characterization methods for grown crystals will be summarized. In particular, optical characterization techniques and a electrical measurement using Hall effect are emphasized.

2.1 Growth of Zn(S,Se,Te) crystals by HRCVD

A schematic diagram of HRCVD chamber is shown in Fig. 2-1. During crystal growth by HRCVD, source gases (metalorganic compounds) are introduced through a nozzle where they collide with atomic hydrogen creating the active chemical precursors. These active precursors impinge on a thermally heated substrate. Atomic hydrogen is generated by a radio-frequency hydrogen plasma in a quartz tube, which is located in front of the substrate. The process is carried out at low pressure (140 mTorr). The vacuum system is fitted with a turbo molecular pump (TMP), a mechanical booster pump (MBP) and rotary pumps (RP). During the thermal substrate treatment in vacuum, the TMP is used, while the MBP is used during crystal deposition. Whenever samples are transferred into main chamber, a

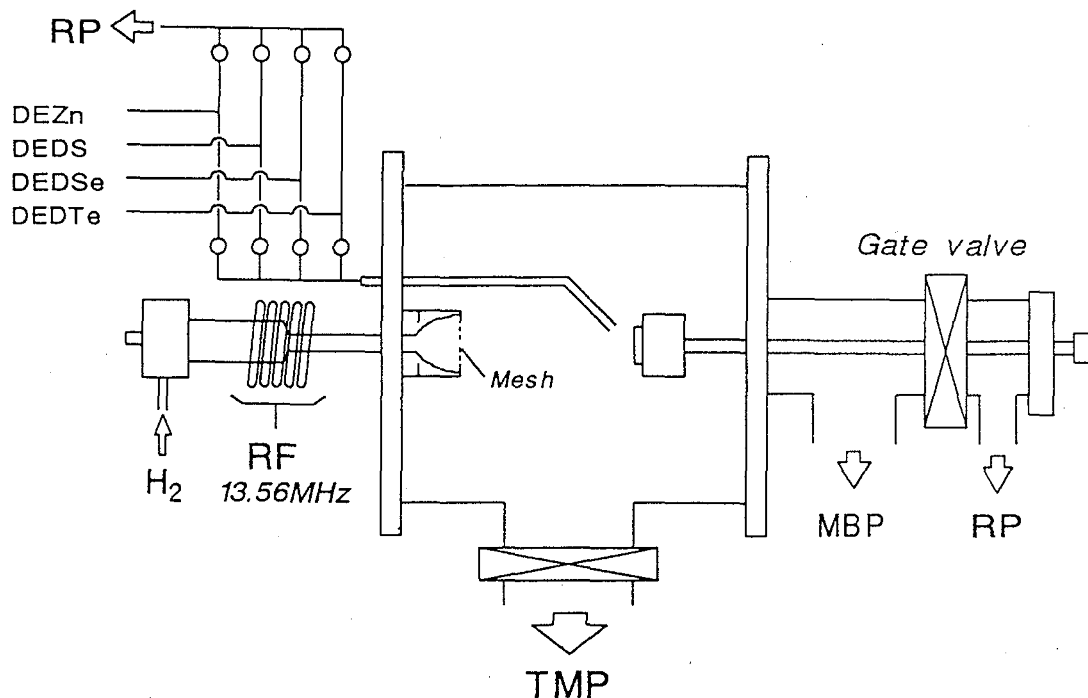

Figure 2-1. The schematic diagram of HRCVD chamber. RF: radio-frequency, TMP: turbo molecular pump, MBP: mechanical booster pump, RP: rotary pump.

gate valve is closed and preliminary evacuation is carried out by the RP. In the following section, details about the growth chamber, the hydrogen plasma and the gas supply (exhaust) system are mentioned, respectively.

2.1.1 Growth chamber

The growth chamber is made of stainless steel except for the quartz windows, as shown in Fig. 2-2. Growth chamber pressure is monitored by a nude-ion gauge (WIT type: ULVAC) when at low pressures, while a baratron gauge (Diaphragm type: MKS) is used during growth. Typical base pressures are $\sim 5 \times 10^{-6}$ Torr. The susceptor in the chamber is heated by an electric heater, and the susceptor temperature is monitored by a CA thermocouple. A load-lock is fitted to the system for sample exchange. The source molecules are introduced through a nozzle located at the mid-way between the plasma cell and the susceptor. The distance between the nozzle and the susceptor can be varied from 1 ~ 2 cm, and this distance has a

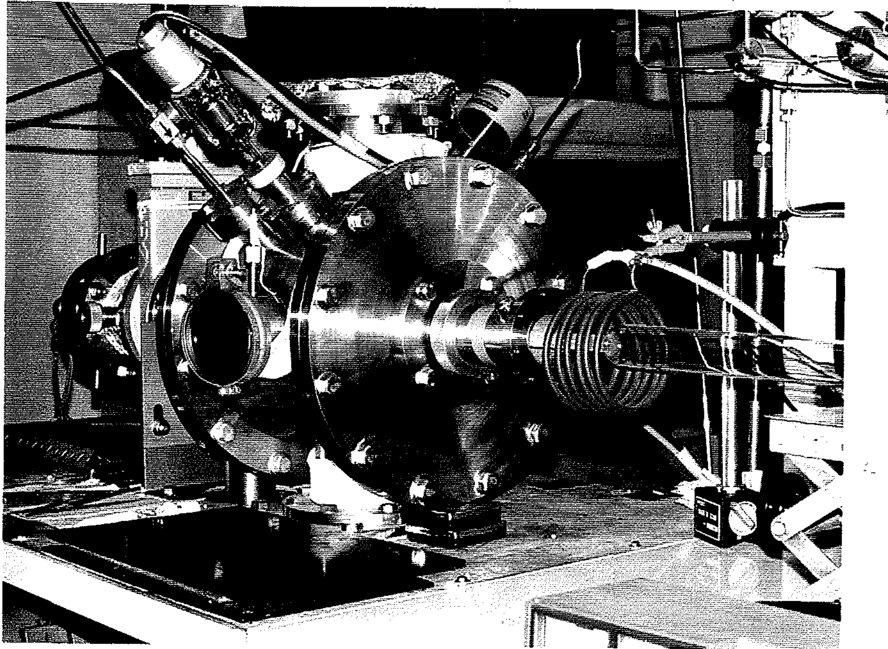

Figure 2-2. The photograph of HRCVD growth chamber.

large effect on the crystal growth condition.

It is essential in HRCVD to control the flux of atomic hydrogen while simultaneously suppressing the ion species in order to obtain high quality crystals. Previously, it was shown that the ionic hydrogen generated by the hydrogen plasma seriously degrades the crystal quality, as will be discussed in chapter 3.[1,2] In order to reduce the number of ionic species impinging on the growth surface, two methods have been employed,

1) introduction of stainless mesh,
2) electrically floating substrate.

As shown in Fig. 2-3, a stainless mesh is positioned at the exit of the plasma effusion cell to contain the plasma and prevent it from reaching the substrate. Secondly, the susceptor is electrically floating by inserting teflon at the contact between the susceptor and the main chamber, as shown in Fig. 2-4. As a result, an ion sheath is formed at the surface of the substrate, which reduces the number of ion species impinging on the substrate by a retarding field.

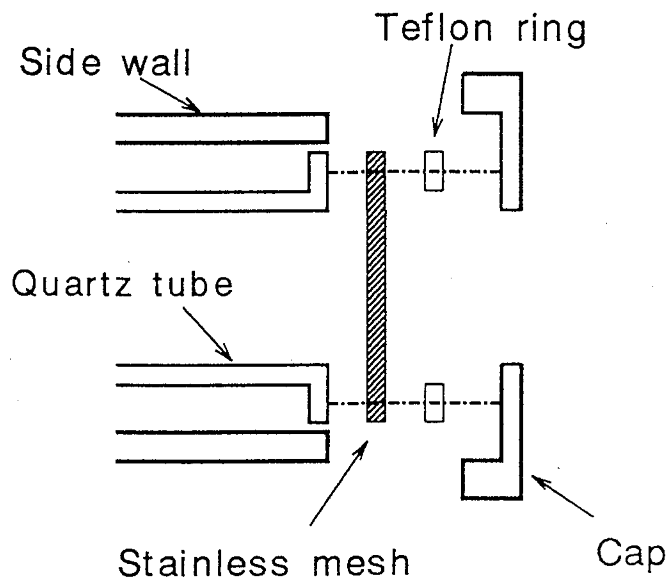

Figure 2-3. The introduction of the stainless mesh at the exit of the plasma effusion cell.

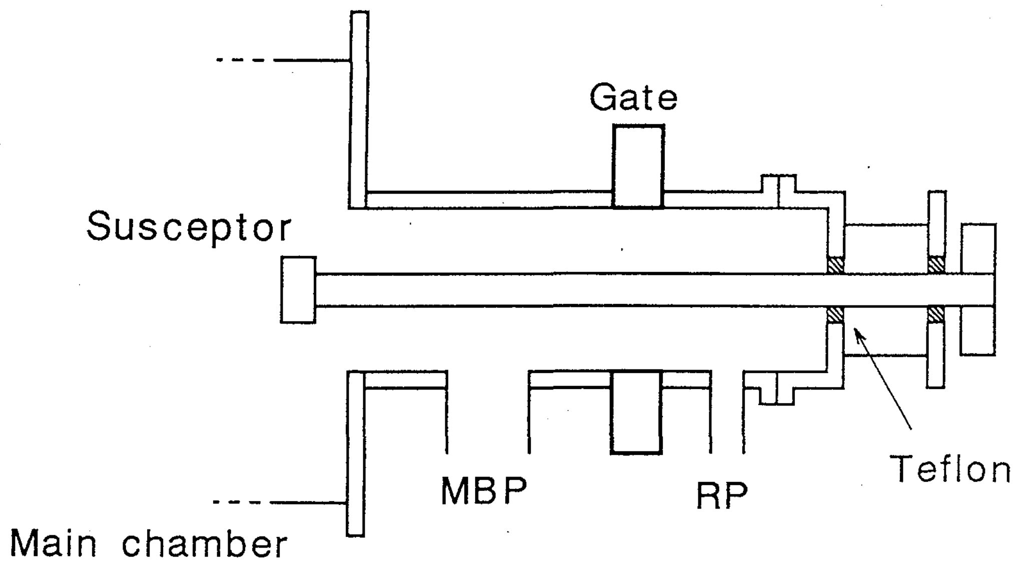

Figure 2-4. The electrically floated susceptor by the insertion of the Teflon between the contact.

2.1.2 Hydrogen plasma

Previously, a 2.45 Ghz microwave plasma (MW) was used for atomic hydrogen generation. However, the MW plasma damages the apparatus as both the stainless and quartz tubes are etched by the energetic hydrogen species. In addition, the crystal quality is also degraded when the MW was used, as will be mentioned in chapter 3.[2] In this study, a radio-frequency (RF, 13.56 MHz) was used to reduce the apparatus damage and the possibility of impurity contamination. Inductively coupling was provided by external RF coil. Since this type of plasma requires no plasma electrodes, effects of metal electrodes can be reduced. To enhance the hydrogen plasma density, the quartz tube has the two different diameters. The external RF coil is located at the mid-point of this quartz tube, as shown in Fig. 2-1. The emission of the RF hydrogen plasma is shown in Fig. 2-5. A impedance matching between the generator and the RF coil was made by a π-type matching circuit, as illustrated in Fig. 2-6. The RF power in the plasma was determined from the incident and reflected powers which were measured.

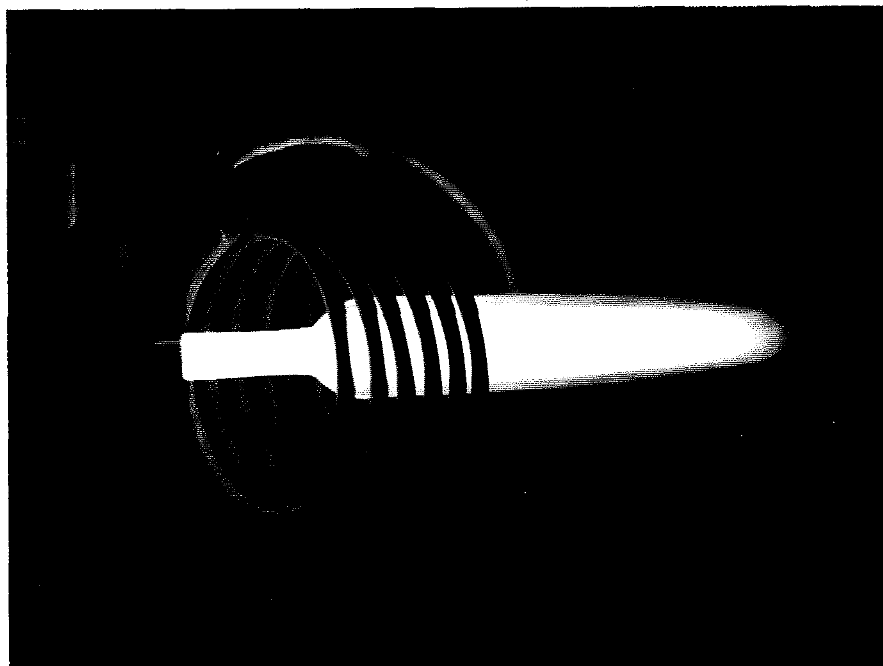

Figure 2-5. The photograph of the typical hydrogen plasma emission.

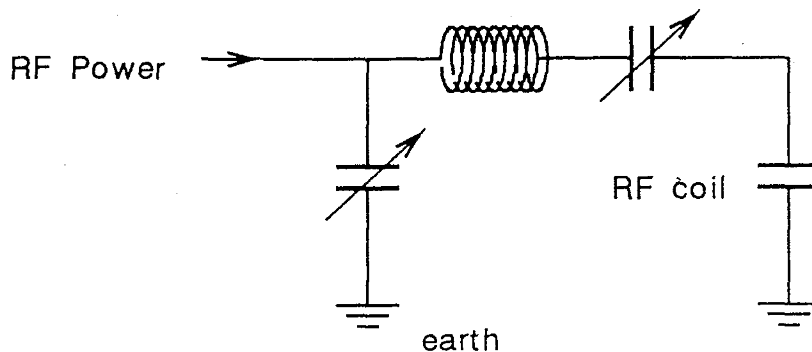

Figure 2-6. π-type matching circuit for the impedance matching between the generator and the plasma.

2.1.3 Gas supply system

The gas supply system plays the important part in HRCVD, because the compositional modulations used in this study were made by switching the source gases for each atomic layers. Figure 2-7 shows the schematic diagram of the source gas supply system for the metalorganic compounds. The total number of supply lines is seven, six lines for metalorganic compound supply and one for hydrogen gas as a plasma source. All the gas lines are 1/4 inch stainless tubes. Each of the source gas supply lines was fitted with a mass flow controller (MFC) to regulate the flow rates of the hydrogen.

To precisely control atomic-scale crystal structures precisely, high-speed switching of source gases is required for gas supply system. Metal diaphragm valves (LD4VO: Hitachi metals) are adapted to this gas supply system to reduce the residence time by reducing the dead space between the valve and MFC. In addition, there is a manifold at the end of the line (indicated by the dotted line in Fig. 2-7) to decrease the distance between valves for the various source gases and the system. The manifold diaphragm valves are connected near each other with a distance between the valves of less than 5 cm. Un-used source gas lines are constantly evacuated by the RP to stabilize the flow rate, as shown in Fig. 2-7. All valves are air-operated and controlled by a computer.

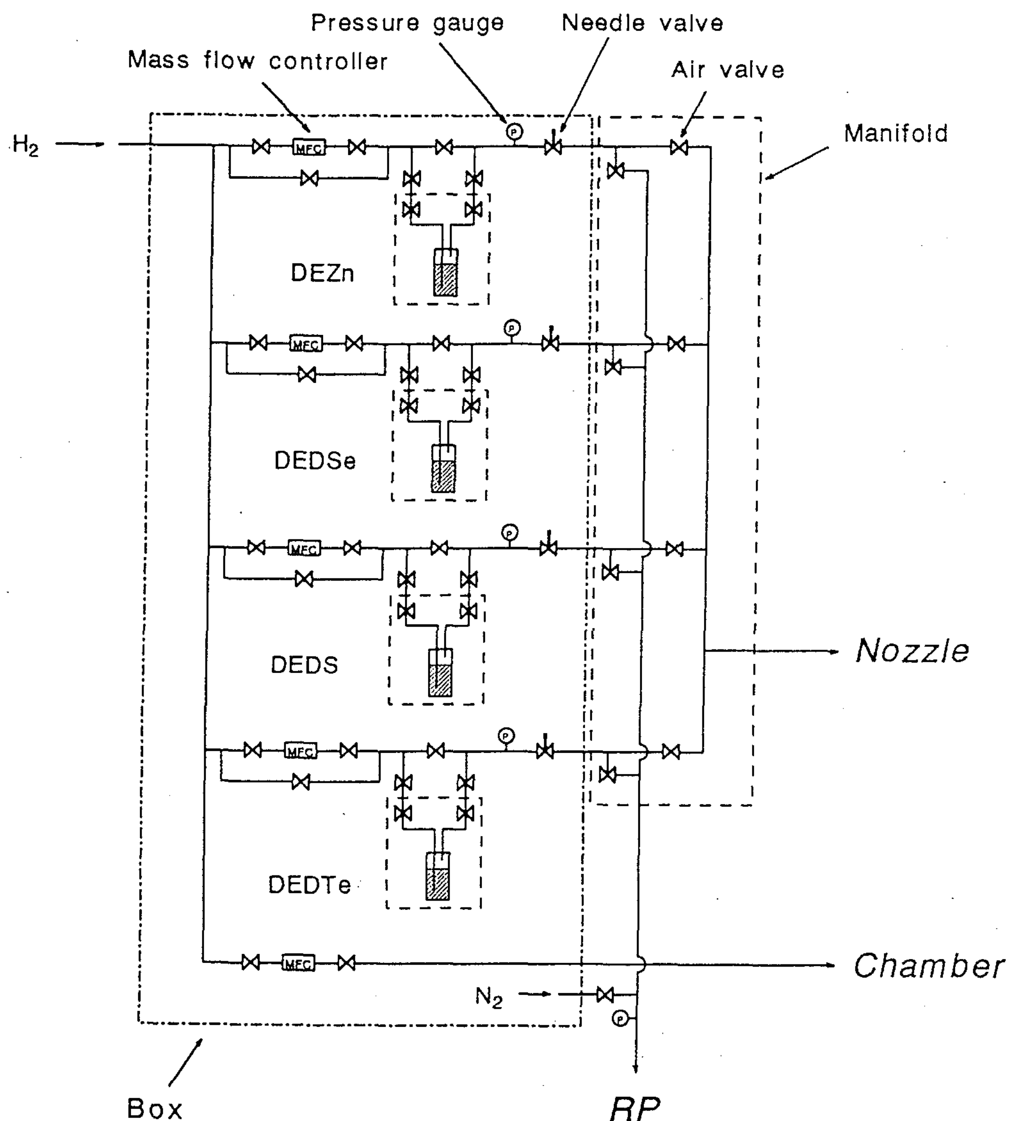

Figure 2-7. The schematic diagram of the source gas supply system used in HRCVD system. The valves circled by the dotted line indicate the manifold.

For the growth of Zn(S,Se,Te) ordered alloys, diethylzinc (DEZn), diethyldisulfide (DEDS), diethyldiselenide (DEDSe) and diethylditellurium (DEDTe) metalorganic source compounds were used. To obtain a sufficient vapor pressure, these metalorganic compounds are maintained in heated bubblers where the vapor pressures are precisely controlled by thermoelectric isothermal baths (DW 610: Komatsu electronics). The temperature of the isothermal bath could be varied between -20 to 60 °C. The pressure of the gas supply lines between MFC and needle valves was monitored by vacuum gauges, and generally maintained at about 760 Torr by adjusting the needle valve. In this case, the flow rate of the source gas is:

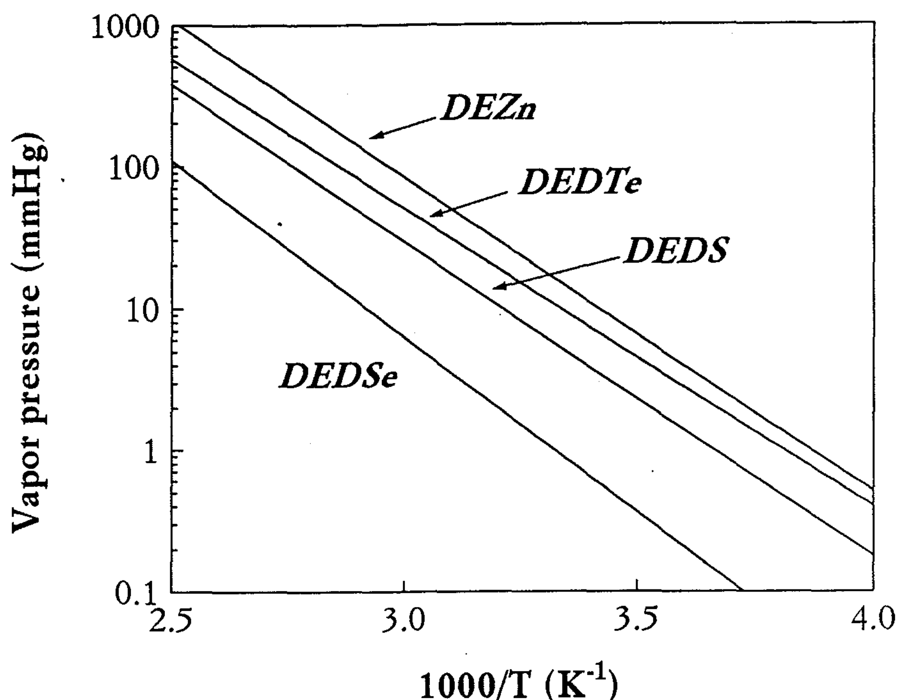

Figure 2-8. The vapor pressure of the metalorganic compounds (DEZn, DEDS, DEDSe, DEDTe) as a function of the reciprocal temperature.

$$n = \frac{P(T_c)V}{RT}, \qquad (2\text{-}1)$$

where n is the flow rate of source molecule (mol/min). V, R and T indicate the flow rate of hydrogen (sccm), gas constant (R= 82.05 [cc•atm/deg•mol]) and the temperature of gas (usually taken as T=300K), respectively. $P(T_c)$ denotes the vapor pressure of the metalorganic compound (atm) and this pressure can be controlled by the temperature of the bubbler (T_c). The flow rates can be controlled by either $P(T_c)$ or V. The vapor pressures of the metalorganic compounds used in this study are plotted as a function of the temperature in Fig. 2-8. The vapor pressures of these source molecules follow the Clausius-Clapeyron's equation

$$\log P(T_C) = a - \frac{b}{T_C}, \qquad (2\text{-}2)$$

where a and b are the constant which depend on the source molecules. The

values of *a* and *b* as well as boiling points for the metalorganic compounds in this study are also listed in Table 2-1.

Table 2-1 Properties of II and VI-group metalorganic compounds

Precursor	Boiling point, °C	a	b, K
DEZn	123	8.936	2295
DEDS	153	8.194	2246
DEDSe	186	9.244	2804
DEDTe		8.019	2209

During deposition these source gas flow is varied in order to modulate the crystal compositions and structure of Zn(S,Se,Te). A typical gas supply sequence used in this study is illustrated in Fig. 2-9. The source materials are supplied alternately through the nozzle at intervals, T_{int} (Zn and Se or S), while the hydrogen supply and plasma are not interrupted. When ZnSe layers are grown by this sequence, one cycle of gas sequence consists of the supply of Se source (T_{Se}), the interval time ($T_{Se,int}$), the supply of Zn source (T_{Zn}) and the interval time ($T_{Zn,int}$). To simplify the description, the gas

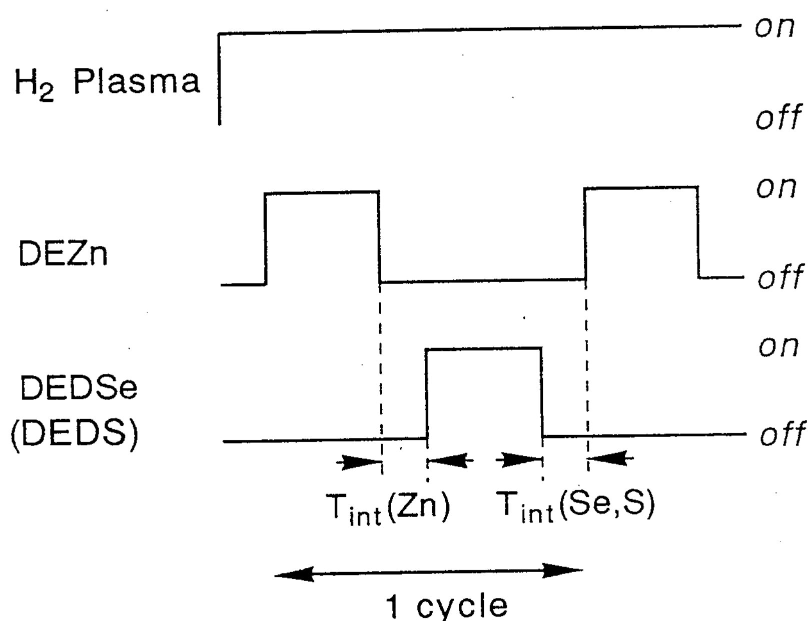

Figure 2-9. A schematic diagram of the gas supply sequence used in HRCVD. T_{int} (Zn, Se, S) indicates the interval time between the source gas supplies.

supply sequences will be described in form of T_{VI}-$T_{VI,int}$-T_{II}-$T_{II,int}$ in this study. For example, the sequence of 4-0-4-3 indicates the supply of VI-group sources for 4 sec with no interval time followed by the supply of II-group source for 4 sec with the interval of 3 sec.

2.1.4 Vacuum system

Vacuum system in HRCVD utilized a TMP (TMP-280: Shimazu) and MBP (PMB001C: ULVAC), and each pumps is evacuated by the RP. During substrate thermal etching or when the system was not used, the TMP was utilized to maintain system cleanness, while the MBP is employed only during the actual crystal growth. The MBP pumping speed can be controlled by the frequency of its power supply (FREQROL-Z120: Mitsubishi). All of the exhaust gases pass through the adsorption column (Silica ace: Tomoe) to remove dangerous and toxic species before releasing to the atmosphere.

In this system, the mean free path of hydrogen operated at 140 mTorr is determined to be around 0.7 mm. The MBP pumping speed can be estimated from the relationship between the chamber pressure and the hydrogen flow rate introduced into the chamber. Pumping speed S (l/sec) can be expressed in form of $S=F/P$, where F and P indicate the flow rate (Torr•l/sec) and the reactor pressure (Torr), respectively. The pumping speed during crystal growth was determined to be 23.9 l/sec when the frequency of MBP was maintained at 50 Hz. Residence time of a gas τ (sec) in a reactor is given by the pumping speed S and the volume of the reactor V (l) and can be written $\tau=V/S$. The reactor volume of HRCVD is 13.6 l; thus, the residence time is τ=0.65 sec.

2.1.5 Surface treatment of substrate

A substrate surface treatment is one of the important parameters influencing crystal-quality. Typically, ZnSe crystals are grown on a GaAs substrate. The lattice parameter of GaAs substrate is close to that of ZnSe. The surface of untreated substrates is usually covered by native oxide with its thickness of about 10Å.[3,4] It is widely known that this native oxide remaining on the substrate surface hinders crystal growth and nucleation and

leads to the degradation of the crystal quality. Therefore, a thermal etching of the GaAs substrates is conventionally employed to remove the surface oxide at a temperature above 600°C.[5] This process, however, results in a rough substrate surface because the selective vaporization of As atoms begins at about 450°C. In this case, a three-dimensional ZnSe crystal growth is enhanced at the substrate surface, which degrades the quality.[6]

Recently, there have been a number of reports on the GaAs surface treatment by ammonium sulfide solution $(NH_4)_2S_x$ to remove the native oxide while keeping a flat surface.[7-13] By this treatment, the various surface states at the substrate surface are passivated by sulfur atoms. Compared with the conventional thermal etching process, the advantages of $(NH_4)_2S_x$ treatment process are summarized as follows:

1) two-dimensional growth from an earlier stage of the growth,[7]
2) better optical properties of pseudomorphic ZnSe epilayers,[8]
3) lower state of densities at the heterointerfaces with the substrate,[9,10]
4) lower interdiffusions of constituent elements at ZnSe/GaAs interface.[11]

Nannich et al. explained the passivation effects by $(NH_4)_2S_x$ solution as shown in Fig. 2-10.[12] First, the oxide film on the surface is removed by $(NH_4)_2S_x$ solution (Fig. 2-10 (A)). This fresh surface is instantly covered with sulfur, and further precipitation of sulfur form an amorphous layer as shown in Fig. 2-10 (B). When this substrate is placed in vacuum, this amorphous sulfur layer is easily sublimated away, leaving monolayer of sulfur atoms (Fig. 2-10 (C)). This sulfur monolayer is stable at low temperature. Figure 2-11 shows the temperature dependence of the sulfur atomic coverage ratio on the GaAs substrate surface.[13] Sulfur atoms begin to desorb at temepratures above 500°C, and complete desorption at ~600 °C. In this study, therefore, the thermal etching of the GaAs substrates was done at 400°C to suppress the surface desorption of the sulfur atoms.

This $(NH_4)_2S_x$ substrate treatment is also effective for other III-V group crystal substrates, such as InAs,[14] InP[14-16] and GaP.[17] Thermal stability of the sulfur monolayer, however, depends on the substrate used, as shown in Fig 2-12.[14] The desorption temperature of sulfur atoms on InAs can be as low as 400°C, due to the weak back-bonding of the sulfur atoms to the In

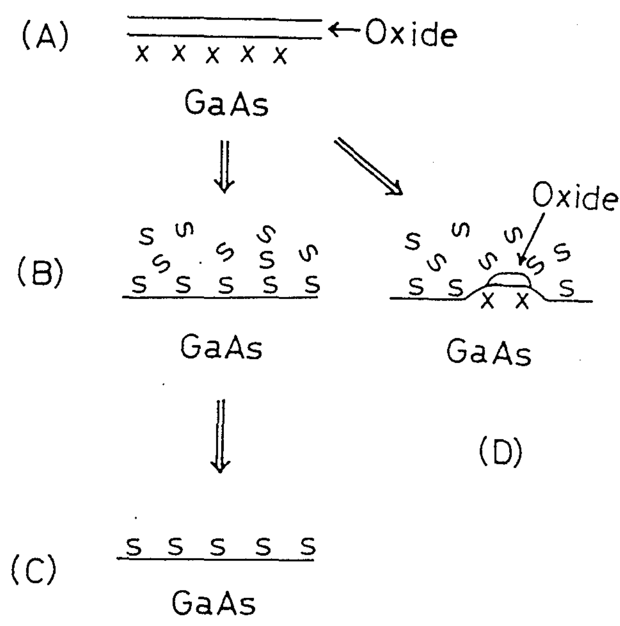

Figure 2-10. The model of GaAs surface treated by $(NH_4)_2S_x$ solution.[12] (A) GaAs surface is covered with native oxide. (B) After treatment with $(NH_4)_2S_x$ solution. (C) The amorphous layer disappears in vacuum by sublimation. (D) Insufficient amount of reactive sulfur results in incomplete etching and covering.

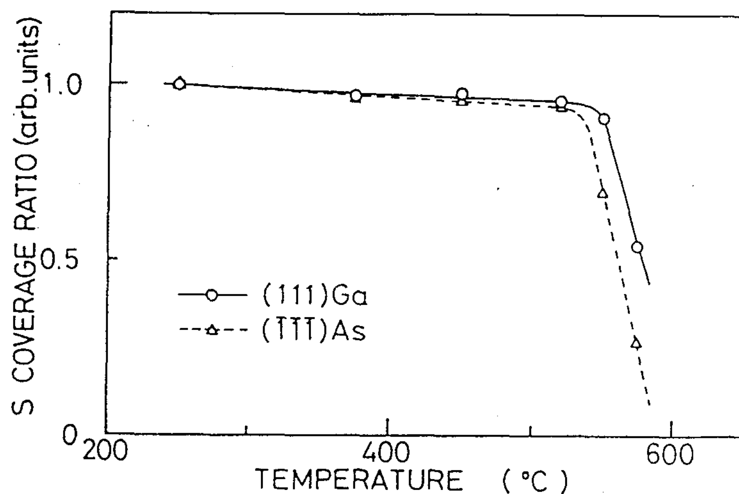

Figure 2-11. The changes of the coverage ratio of sulfur on the (111) Ga and ($\bar{1}\,\bar{1}\,\bar{1}$) As surfaces at heat treatments in vacuum. The coverage ratio of sulfur is normalized by the value at 250 °C.[13]

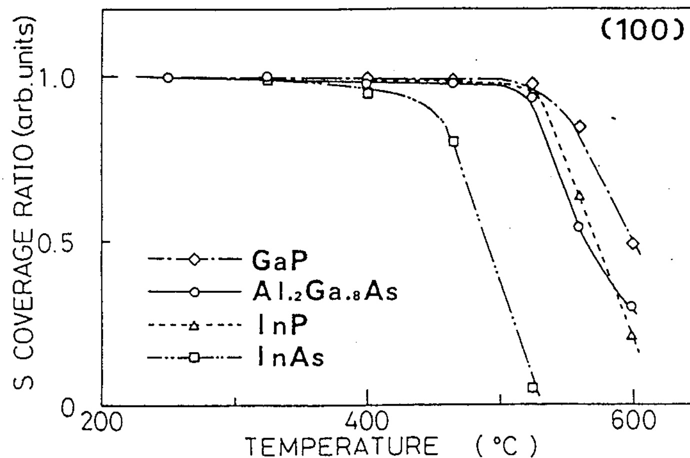

Figure 2-12. Thermal stability of sulfur on the $(NH_4)_2S_x$ -treated surfaces in various III-V compounds. the coverage ratio of sulfur is normalized by the Auger peak-to-peak height of sulfur at 250°C.[14)]

atoms. Consequently, thermal etching of the InAs substrates is performed at only 300°C.

In this study, Zn(S,Se,Te) ordered alloys were grown on GaAs, InAs or InP substrates. All the substrates were pretreated by the $(NH_4)_2S_x$ solution in all the case. The substrates were immersed in the $(NH_4)_2S_x$ solution for 3 min and did not show any time dependence as reported by others.[13)] The substrates preparation technique used in this work is as follows:

1) cleaning by organic solvent (ethanol ⇨ acetone ⇨ trichloroethylene ⇨ acetone ⇨ ethanol, each for 20 min using ultrasonic cleaning)
2) substrate treatment (wet etching of substrates ⇨ sulfur passivation by $(NH_4)_2S_x$)
3) thermal etching in the growth chamber

Details of the wet-etching processes of these substrates, such as etchant, etching time and temperature, are also summarized in Table 2-2.

Various semi-insulating substrates can be used for the fabrication of the ordered alloys to avoid a carrier conduction through the substrates. A GaAs: Cr,O semi-insulating substrate was used when an insulating substrate was

Table 2-2 Wet-etching processes for III-V group crystal substrates

Substrates	Etchant	Etching time	Etching temperature
GaAs	$NH_4OH:H_2O_2:H_2O$ (1:1:10)	1 min	room temperature
InAs	$H_2SO_4:H_2O_2:H_2O$ (3:1:1)	1 min	50 °C
InP	$H_2SO_4:H_2O_2:H_2O$ (5:1:1)	1 min	60 °C

required. The carrier conduction through this substrate is negligible because of the high resistivity greater than 10^7 Ωcm. A slightly n-type InAs substrate was used for the growth of Zn(Se,Te) ordered alloys, since there is no semi-insulating substrates due to the small band-gap of this crystal (Eg=0.35eV at room temperature). The basic characteristics of the III-V group crystal substrates employed in this study are listed in Table 2-3.

Table 2-3 Properties of III-V group crystal substrates

	GaAs	InAs	InP
Growth method	HB[a)]	LEC[b)]	LEC
Conductivity type	SI[c)]	n-type	SI
Dopant	Cr, O	non-dope	Fe
Resistivity (Ωcm)	$>10^7$	$\sim 10^{-2}$	$\sim 10^8$
EPD (cm^{-2})[d)]	$<5x10^3$	$<5x10^4$	$<5x10^4$
Orientation	(100) ±0.5°	(100) ±0.5°	(100) ±0.1°
Thickness (μm)	300	350	350

a) Horizontal Bridgman method
b) Liquid Encapusulated Czochralski method
c) semi-insulating substrate
d) etch-pit densities

2.1.6 Procedure for crystal growth

A general procedure for the growth in HRCVD consists of sample loading, thermal etching, growth and after crystal growth process. Each of these procedures for the growth are reviewed:

1) Sample loading

After the substrate is prepared by the wet etching process followed by

$(NH_4)_2S_x$ treatment, the substrate is placed on the susceptor. The load-lock chamber is evacuated by RP before the susceptor is introduced through the gate valve.

2) Thermal etching

The substrate temperature is raised to the thermal etching temperature, and the TMP is used to maintain a low pressure during this procedure. After thermal etching, hydrogen gas is introduced into the chamber to help decrease the susceptor temperature, and the MBP is employed to pump the hydrogen gas.

3) Growth of crystal

Before the growth of crystals, the supply of the metalorganic source gases are stabilized for 20 min using the bypass lines. The hydrogen plasma is then generated and maintained for 5 min for stabilization. After this process, the source gases are supplied through the nozzle and crystal grown is initiated. During the growth, the output power of the RF is maintained at a constant level.

4) After crystal growth

After the crystal growth is finished, the generation of the hydrogen plasma is stopped and the source gases turned off, while the hydrogen gas for the plasma is maintained to help lower the substrate temperature. When the substrate temperature is less than 120°C, the sample is removed through the load lock.

In process (4), when the sample was removed from the growth chamber at 200°C (immediately after the growth), degradation of crystal properties was observed. Perhaps this degradation was due to defect formation caused by

Table 2-4 Typical growth conditions in HRCVD

Growth temperature	200 °C
Flow rate (H_2 plasma)	200 sccm
RF power	38 W
Chamber pressure	140 mTorr
Frequency of MBP	50 Hz

the difference in the thermal expansion coefficients of the substrate and the grown layers.[18,19]

Typical growth conditions used in this study are summarized in Table 2-4. The flow rate of hydrogen for the hydrogen plasma was kept at 200 sccm and the conventional reactor pressure is about 140 mTorr . The RF power was also maintained to 35~40 W throughout the deposition. The flow rates of the source gases is frequently changed, and its effects will be discussed in chapter 3.

Chapter 2.2 *In-situ* monitoring of reaction process

In HRCVD, the crystal growth process can be divided into two major parts, i.e., source molecule decomposition by atomic hydrogen and surface reaction. To determine the growth mechanism atomic layer epitaxy (ALE) in HRCVD, these two processes are measured using *in-situ* monitoring. The source gas decomposition process was studied by quadrupole mass spectroscopy (QMS), while the surface reaction kinetics were observed by a surface photo-absorption (SPA) method. In the following section, details about the experiments are given.

2.2.1 Quadrupole mass spectroscopy

The QMS is a powerful tool for the gas analysis, since the source gas species are directly detected in this method. In addition, commercial quadrupoles are small (~ 30 cm) and can be easily connected to a vacuum system, because they do not require magnets. So far, *in-situ* crystal growth monitoring by QMS in ALE have been reported, and the resulting surface reactions, decompositions[20,21] or desorptions[22-24], have been determined.

Figure 2-13 shows the principle of ion separation used by a quadrupole mass filter, where *S* and *C* indicate the ion beam source and the ion collector

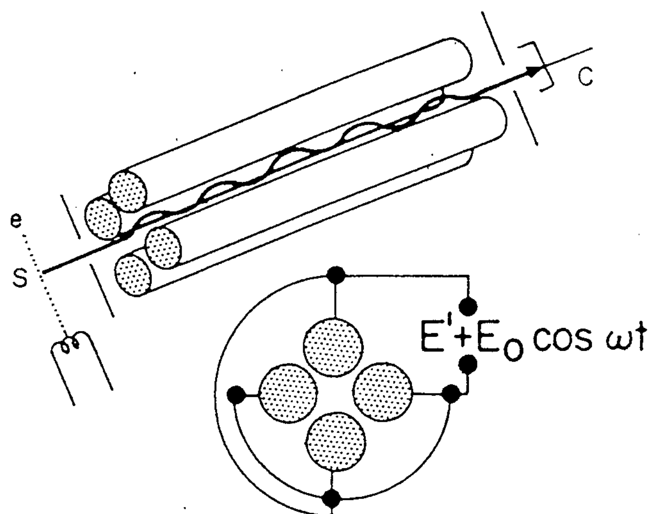

Figure 2-13. Principles of ion separation in the quadrupole mass filter. *S* :source of ion beam, *C* : ion collector, *E* : DC field, $E_0 cos\omega t$: RF field.

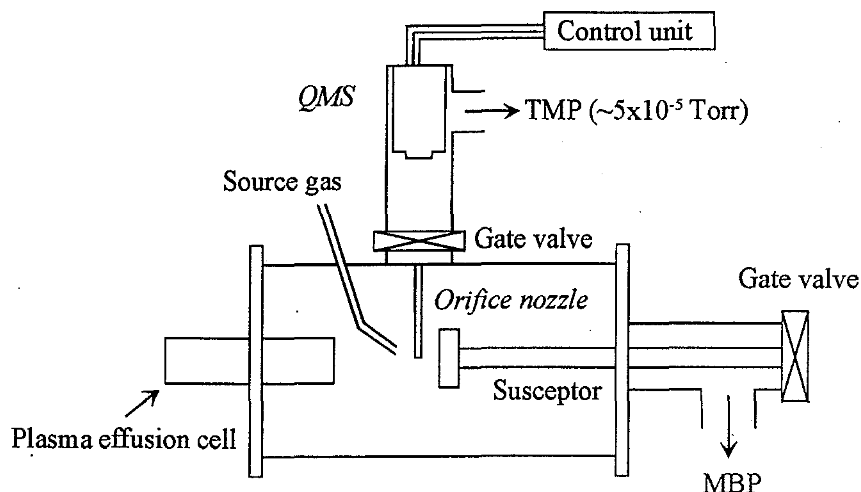

Figure 2-14. Configuration diagram for QMS system used in HRCVD. MBP: mechanical booster pump, TMP: turbo molecular pump.

, respectively. In this method, pairs of opposing rods are connected to DC and RF voltage supplies, and the ions are accelerated along the axis between the rods. The DC and RF voltages are chosen to allow ions of only one mass to oscillate in stable orbits and reach the collector at the end of the tube, as shown in Fig. 2-13. The trajectories of all other ions are spiral outward and terminate at the rod surfaces. Ion separation and mass scanning are attained by varying the frequency of the RF voltage, while the ratio of DC to RF voltages are altered to gain sensitivity.

Figure 2-14 shows the configuration diagram for QMS (MSQ-200: ULVAC) used in our HRCVD apparatus. The photograph of the QMS system is also shown in Figure 2-15. The QMS system consists of an analyzing units, a control unit and a pump unit, and is positioned on the growth chamber. The QMS system can be isolated from HRCVD by a gate valve. To collect the decomposed gas species as directly as possible, a stainless tube was fitted to pick up vapor samples, which is 5 mm away from the susceptor. In addition, there is a orifice (~200 μm) at the head of this collecting tube to reduce the pressure of the QMS unit. Typical pressures in the QMS were about $5x10^{-5}$ Torr. At this pressure, the mean free pass of hydrogen molecules in the QMS unit are calculated to be ~ 180 cm, and is long enough considering the distance from the orifice to the analyzer ~50 cm. Consequently, it is reasonable to expect that the collected gas samples have no collisions before reaching the quadrupole analyzer. In the QMS, these introduced molecules are ionized by the electron source in front of the

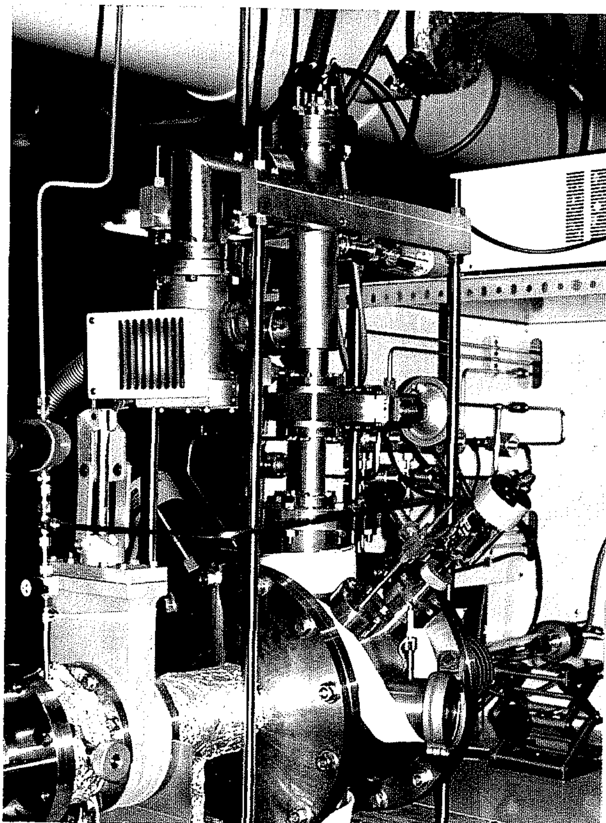

Figure 2-15. The photograph of the QMS-HRCVD system. The QMS units is placed on the top of the growth chamber.

quadrupole, since the QMS can measure only the ionized species. The acceleration voltage of electrons in the filament was typically 3.5 eV. The ion species selected by the quadrupole filter were detected by a secondary electron multiplier (Cu-Be type). This QMS system can measure mass numbers ranging from 1 to 200 (m/e=1~200) and the detection limit is $\sim 10^{-13}$ Torr.

The experimental conditions for the source gas decomposition analysis are summarized in Table 2-5. The hydrogen flow rate for the plasma was reduced to 100 sccm, since the chamber pressure is too high to maintain a QMS pressure low enough when the conventional hydrogen flow rate (200 sccm) was used. In addition, all the source gas flow rates were increased to

increase the sensitivity. Especially, the flow rate of DEDSe is increased because of the low sensitivity of the source molecules.

Table 2-5 Typical conditions for QMS

H_2 for the plasma (sccm)			100
RF power (W)			40
Source gas	DEZn	DEDS	DEDSe
H_2 carrier gas (sccm)	30	30	50
Vapor pressure (mmHg)	45	63	60
Flow rate (μmol/min)	72.2	101.0	160.3

2.2.2 Surface photo-absorption (SPA) method

So far, various methods have been developed to monitor surface reactions; for example, reflection high energy electron diffraction (RHEED)[25,26], low energy electron diffraction (LEED)[27], X-ray photo-electron spectroscopy (XPS)[28] and X-ray scattering.[29,30] Among these, RHEED has been widely employed as a in-situ monitoring method in molecular beam epitaxy (MBE), since the atomic surface coverage as well as the surface roughness can be determined from the resulting diffraction patterns. In a chemical vapor deposition (CVD), however, all of these methods including RHEED can not be used because of the high reactor pressure during the growth.

Aspnes et al. first developed a in-situ monitoring method, called reflectance-difference spectroscopy (RDS), which can be used even in the CVD systems.[31,32] Figure 2-16 shows the configuration of optical apparatus used in the RDS system. In this method, the difference between normal incidence reflectances R_{110} and $R_{\bar{1}10}$ for light polarized along the (110) and ($\bar{1}$10) principal axis about the (001) surface of semiconductor crystals are measured. By taking the reflectance difference between these two axis, the effect of the isotropic substrate can be excluded. Consequently, RDS can be employed as a CVD monitoring system, since this method utilizes optical probes which are not largely affected by vapor species. Using this technique, they observed a reflectance anisotropy in the Ga-stabilized GaAs surface due to light absorption associated with the Ga-

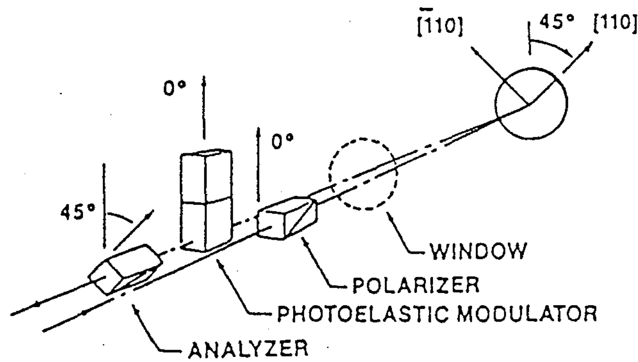

Figure 2-16. The configuration of optical apparatus used in the reflectance-difference spectroscopy (RDS).[31)]

Ga surface dimer bonds.[31)] In this method, however, only the anisotropic signals such as dimer formations are detected and the isotropic surface reaction are not observable.

SPA method which is first established by Kobayashi et al., is characterized by its simplicity and high sensitivity compared with RDS system.[33-37)] The SPA method also uses laser or monochromatic light as optical proves, and can be applied to the CVD systems. To reduce the reflection effect from the crystal substrates, this technique utilizes a p-polarized light at a Brewster angle. When light is reflected by a surface of films, the light polarization yields different reflection intensities. The polarization of light is defined by its p- or s-polarized component, where the oscillation of lights is parallel (p-polarization) or perpendicular (s-polarization) to the incident plane, as shown in Fig. 2-17. The reflection intensities for these light components at the film surface are given by Fresnel's equation,

$$R_p = \left| \frac{n_0 \cos\phi_1 - n_1 \cos\phi_0}{n_0 \cos\phi_1 + n_1 \cos\phi_0} \right|^2 , \qquad (2\text{-}5)$$

$$R_s = \left| \frac{n_0 \cos\phi_0 - n_1 \cos\phi_1}{n_0 \cos\phi_0 + n_1 \cos\phi_1} \right|^2 , \qquad (2\text{-}6)$$

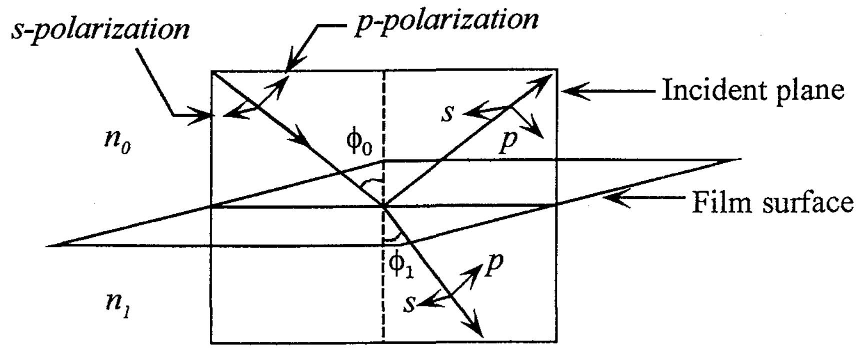

Figure 2-17. The schematic sketch of the p- and s-polarized lights reflected at the film surface. ϕ_0: incident angle, ϕ_1: angle of transmitted light into film.

where R_p and R_s indicate the reflection intensities for the p- and s-polarized lights. The refractive index of the film and the air are denoted as n_1 and n_0, respectively. The angle of light in the film at an incident angle of ϕ_0 is obtained from Snell's law,

$$n_0 \sin\phi_0 = n_1 \sin\phi_1 \ . \tag{2-7}$$

Figure 2-18 shows the calculated incident angle dependence on the reflectivity for both p- and s-polarized lights at the GaAs substrate (n =4, k =2). In the p-polarized light, the reflection from the substrate is effectively reduced at the Brewster angle which is expressed by

$$\phi_{Brew} = \tan^{-1}\left(\frac{n_1}{n_0}\right). \tag{2-8}$$

In the SPA method, by using the p-polarized light at Brewster angle, the surface reaction process can be observed as a reflectivity oscillation due to the difference of the reflectivity of growing material.[33,34] Obviously, this SPA method can be applied to either the isotropic or the anisotropic surfaces of the growing crystals. Moreover, since the p-polarized lights have the perpendicular oscillation to the growing surface, the surface structure and the adsorbed molecular species having perpendicular electron transitions to the surface are also detected.[33,37] The reflectivity change of the growth surface

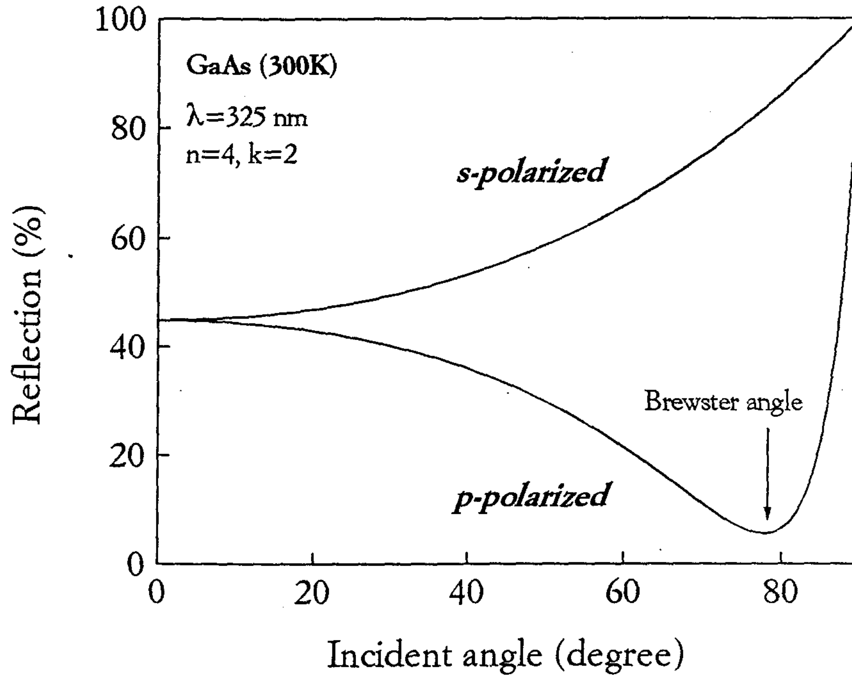

Figure 2-18. The calculated angle dependence on the reflectivity for p- and s-polarized lights at the GaAs substrate. The wavelength of light is 325 nm and the refractive index is $\hat{n}$=4+2i at this wavelength.

can be expressed by[34)]

$$\frac{\Delta R}{R} = \frac{R_A - R_B}{R_B}, \tag{2-9}$$

where R_A and R_B represent the reflectivity of the substrate before and after the thin film deposition with thickness d. Then the reflectivity change for p- and s-polarized light can be expressed by[38)]

$$\left(\frac{\Delta R}{R}\right)_s = \frac{8\pi d\cos\phi_0}{\lambda}\mathrm{Im}\left(\frac{\hat{\varepsilon} - \hat{\varepsilon}_{sub}}{1 - \hat{\varepsilon}_{sub}}\right), \tag{2-10}$$

$$\left(\frac{\Delta R}{R}\right)_p = \frac{8\pi d\cos\phi_0}{\lambda}\mathrm{Im}\left\{\left(\frac{\hat{\varepsilon} - \hat{\varepsilon}_{sub}}{1 - \hat{\varepsilon}_{sub}}\right)\left(\frac{1-(1/\hat{\varepsilon}\hat{\varepsilon}_{sub})(\hat{\varepsilon} + \hat{\varepsilon}_{sub})\sin^2\phi_0}{1-(1/\hat{\varepsilon}_{sub})(1+\hat{\varepsilon}_{sub})\sin^2\phi_0}\right)\right\}, \tag{2-11}$$

where $\hat{\varepsilon}$ and $\hat{\varepsilon}_{sub}$ indicate the dielectric constant of the deposited film and the

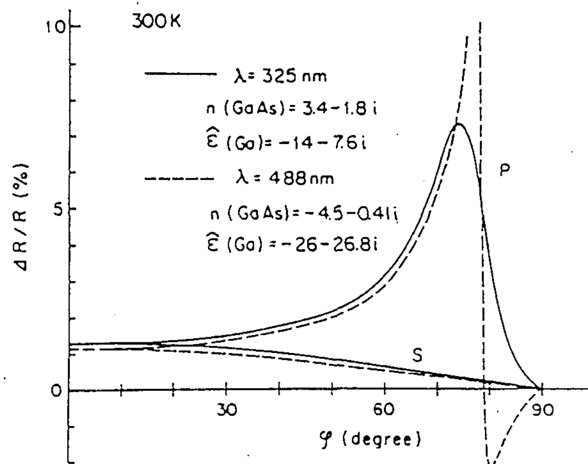

Figure 2-19. Reflectivity change on the GaAs (100) substrate covered with 1 atomic Ga layer as a function of the incident angle. The optical constants of GaAs and Ga used in the calculation are shown in the inset.[34)]

substrate, respectively. The calculated reflectivity change using Eqs. (2-10) and (2-11) for a (100) GaAs substrate with one atomic Ga layer on top is shown in Fig. 2-19.[34)] This calculated results indicate that the detection of ultra thin film can be accomplished by the p-polarized light at the Brewster angle.

So far, the *in-situ* monitoring of ALE of GaAs has been observed using SPA method. Figure 2-20 shows the SPA signals dependence on the pulse duration of TMGa in the ALE growth.[36)]

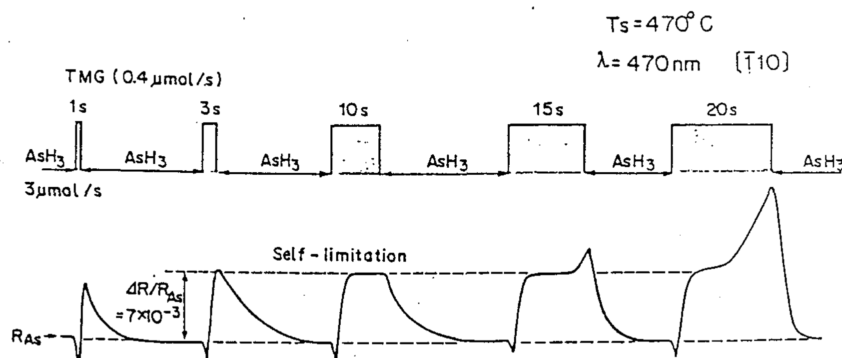

Figure 2-20. TMGa flow duration dependence of SPA reflectivity at T_s=470°C with a constant TMGa flow rate of 0.4 μmol/sec.[36)]

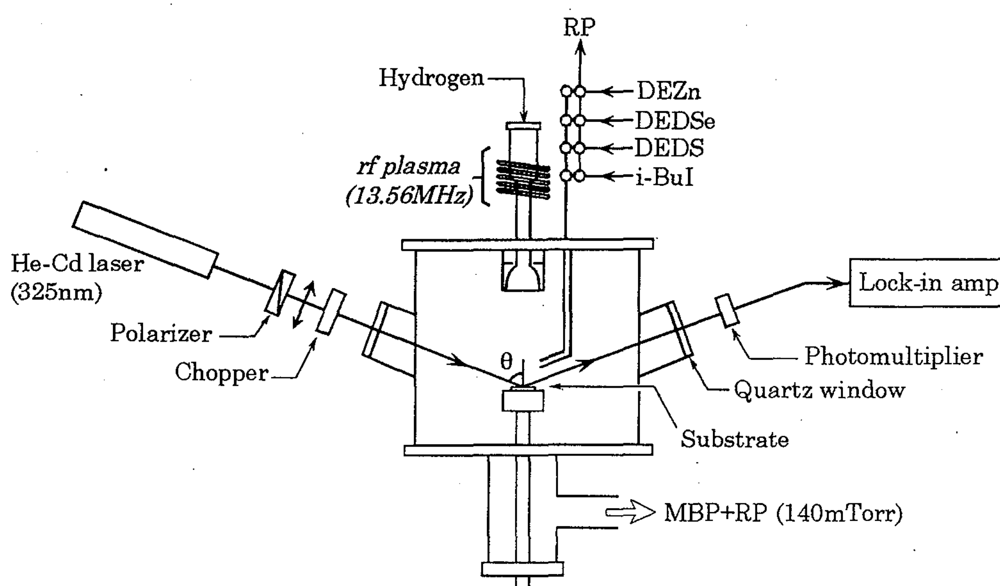

Figure 2-21. The schematic diagram for the surface photo-absorption (SPA) measurement in HRCVD. He-Cd laser is used as a light source.

The saturation of the SPA signals are clearly seen in the duration between 3~10 sec. From this result, it can be understand that the surface coverage of the constituent atoms on the growing surface is simply estimated from the intensity of the SPA signals. The desorption of the CH_3 molecules from the Ga-stabilized surface was also reported.[37] Therefore, the SPA technique is quite useful for not only the estimation of the surface atomic coverage but also the surface reaction process. This technique, however, can be used only for the observation of the compound semiconductors which consist of more than two atomic species, since this technique observes the reflectivity difference in these different atomic surfaces.

Figure 2-21 shows the schematic diagram for the SPA measurement in HRCVD. A He-Cd laser (325 nm, 4230B:Liconix) light source were used. The light was p-polarized using a Glan thompson polarizer (GTPC-10-AN, Shiguma). The substrate (or the growing crystal) is irradiated by these linearly polarized lights though a quartz window at the angle close to the Brewster angle. The resulting reflected light intensities are monitored by a conventional lock-in amplifier technique (SR530: Stanford) fitted with a chopper. The time-intervals for the measurement were typically 0.3 sec, which were determined by a computer system (RS232C). Silicon

photodiode deterctor (S1226-8BQ: Hamamatsu) was first used, but later changed to a photomultiplier (H5773: Hamamatsu) because of the low sensitivity of the photodiode at the short-wavelength region (~325 nm). The incident angle of the laser light (θ) was ~ 70°, which is the Brewster angle of ZnSe (~71°) calculated from Eq. (2-8). The growth conditions in HRCVD were maintained at the same during SPA mesurement.

2.3 Characterization method for semiconductors

The sample characterization techniques included (i) optical, (ii) electronic, and (iii) chemical or structural determination. In this section, various characterization techniques used in this study are described. In particular optical characterization techniques are emphasized as these are most closely related to the potential device applications of these materials.

2.3.1 Optical characterization techniques

Optical characterization in semiconductors includes photoluminescence spectroscopy, photocurrent spectroscopy, excitation spectroscopy and reflectivity spectroscopy. These optical measurements can be divided into two parts depending on the character of the optical transition, i.e., absorption and recombination processes. In semiconductors, luminescence spectroscopy observes a recombination process involving excitons or free carriers, while photocurrent, photoluminescence excitation and reflectivity spectroscopies measure optical absorption processes. In the following section, experimental set up and fundamental principles of the measurements used are reviewed.

• Photoluminescence

When semiconductors absorb photons having energy greater than the band-gaps, electron-hole pairs are created. Some of these photo generated electron-hole pairs recombine, in such a way as to emit a photon. This photoluminescence (PL) provides informations about energy states in the crystal, including the band-gap as well as impurity and deep-level states. In addition, the quality of materials can also be determined from the radiative efficiency or the deep-level emission intensity of the PL.

In the PL measurements at a low temperature, the excitonic emissions are mainly observed in semiconductors having direct optical transitions. When a free hole and a free electron are generated by a optical transition in a crystal, a pair of opposite charges induces a coulomb attraction. The coulombic binding energy of this pair reduces the energy of this electron and hole pair.

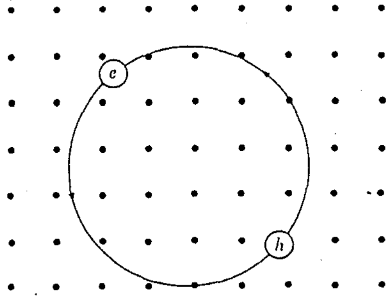

Figure 2-22. A Mott-Wannier exciton in a real space. Electron and hole is bound together.

Consequently, when this pair recombine, the photon energy is slightly less than that of the bandgap. This electron-hole pair is called a "free exciton", and is free to move as a bound electron-hole pair, as schematically shown in Fig. 2-22. The exciton shown is a Mott-Wannier exciton, which has a larger delocalization of wavefunction compared with a lattice constant. The ionization energy of a exciton are given by

$$E_n = -13.56\frac{m^*}{m_0}\left(\frac{\varepsilon_0}{\varepsilon}\right)\frac{1}{n^2} \quad [\mathrm{eV}], \qquad (2\text{-}12)$$

where n is an integer larger than 1 indicating the various exciton states and m^* is the reduced mass expressed by

$$\frac{1}{m^*} = \frac{1}{m_e^*} + \frac{1}{m_h^*}, \qquad (2\text{-}13)$$

where m_e^* and m_h^* indicate the electron and hole effective masses, respectively. In this case, a Bohr radius of the exciton is calculated from

$$a_B = \frac{\varepsilon\hbar^2}{me^2} = 0.053\frac{m_0}{m^*}\frac{\varepsilon}{\varepsilon_0} \quad [\mathrm{nm}]. \qquad (2\text{-}14)$$

In ZnSe crystal, the calculated binding energy of the exciton from Eqs. (2-12) and (2-13) is 24 meV and is about 5-times larger than that of GaAs, due to the ionic nature of II-VI group semiconductors. The exciton binding energies of II-VI group semiconductors are summarized in Table 2-6.

Table 2-6. The properties of free excitons in II-VI group crystals

	m_e^*	m_h^*	ε	$E_{n=1}$ (meV)	a_B (Å)
ZnS[a)]	0.27	0.49	8.32	34.2	25.3
ZnSe[b)]	0.17	0.60	8.66	24.0	34.6
ZnTe[c)]	0.12	0.70	9.67	14.9	50.0

a) Reference 39
b) Reference 40
c) Reference 41

In this study, the three types of PL measurements were carried out as follows:

a) PL measurement using conventional laser light (λ=325 nm),
b) PL measurement using YAG laser (λ=355 nm),
c) time-resolved PL measurement.

The measurement (a) is done as a basic characterization method for the grown crystals. The method (b) is mainly carried out to learn about exciton dynamics at high density states. The photo-degradation effects in Zn(S,Se) ordered alloys are also measured by the measurement (b), as will be shown in chapter 4. The measurement (c) gives the information about the stability of excitons, which directly reflect the carrier relaxation process in crystals.[42,43]

a) PL using conventional laser light

Figure 2-23 shows the schematic diagram of a typical PL measurements carried out in this work. Typically, low temperatures were used. A He-Cd laser (325 nm) was used as a excitation light source. The sample was placed in a cryostat for temperature control. The temperature of the cryostat was typically fixed at 25K. The PL from the samples is introduced into the monochromater through a color filter and is detected by a photomultiplier (R-374: Hamamatsu). Conventional lock-in amplifier techniques were used to reduce noise. The accelerating voltage of the photomultiplier was usually kept at 1 kV.

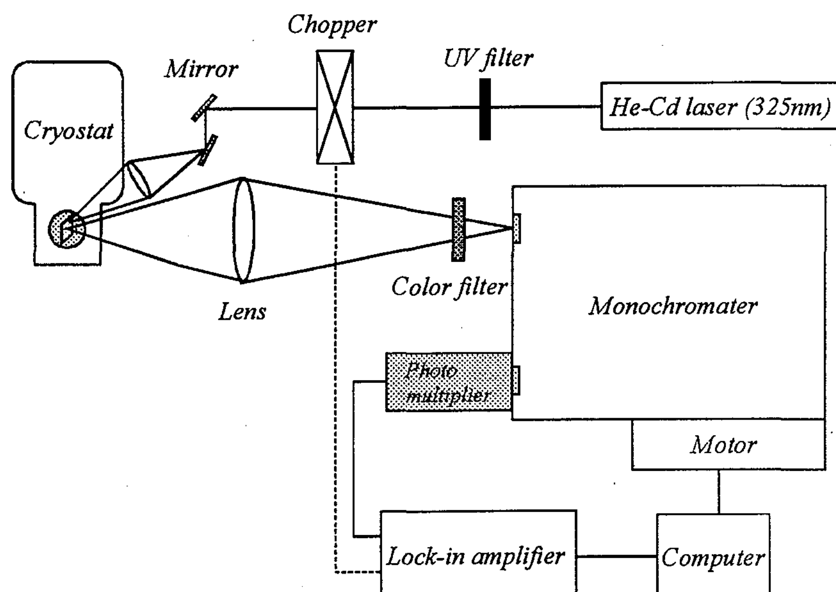

Figure 2-23. The schematic diagram for the photoluminescence (PL) measurement at a low temperature.

b) PL using YAG laser

The schematic diagram for the YAG laser PL measurements is shown in Fig. 2-24. The basic configuration of this measurement is same with that of (a), except for the detection system of luminescence and the excitation light source. As shown in Fig. 2-24, a SMA (spectroscopic multichannel analyzer) detector was used, instead of the photomultiplier. The SMA uses a photodiode array consisting of 1024 ch and the different wavelengths of the luminescence (in a region about 600Å from a center wavelength) can be measured at the same time. One scan takes only 30 msec, and the signal are electrically integrated. This SMA system and the YAG laser system are powered by a pulse generator, and a high voltage gate trigger is sent from the pulse generator to the SMA to control the photodiode array shutter. The SMA has a resolution of 2~2.4Å with an equivalent grating number of 1200 G/mm. Typically, Nd:YAG laser was used in this study. The third harmonic generation (THG) with its operating wavelength of 355nm was provided by a commercial generator fitted to the system (Spectron laser systems). To generate the THG, a potassium dideuterium phosphate (KDP) crystal is adapted in this system. The power intensities of THG-YAG laser were changed by the insertion of neutral density filters. The conditions for

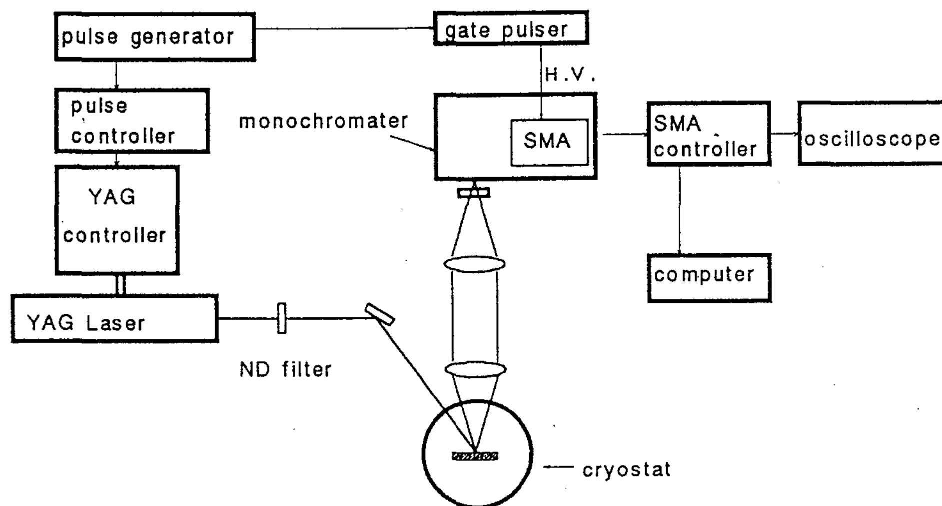

Figure 2-24. The PL measurement under the high-power excitation using short-pulse operated YAG laser. SMA: spectroscopic multichannel analyzer.

the short-pulse laser operation are listed in Table 2-7.

Table 2-7. The operating conditions for THG-YAG laser.

Laser	Nd:YAG laser
Wavelength	1064 nm
	532 nm (SHG[a]: KDP)
	355 nm (THG: KDP+1064nm)
Frequency (Hz)	10
Half width (nsec)	10~20
Power density (mJ)	100 (at 10 Hz operation)

a) second harmonic generation

c) time-resolved PL measurement

Figure 2-25 shows the schematic diagram for the picosecond time-resolved PL measurement. This measurement employed a mode-locked titanium-sapphire (Ti:S) laser excited by a argon laser (Ar^+). The wavelength of Ti:S laser (780 nm) is further converted to 390 nm by a second harmonic generation (SHG) of a LBO crystal. The average output

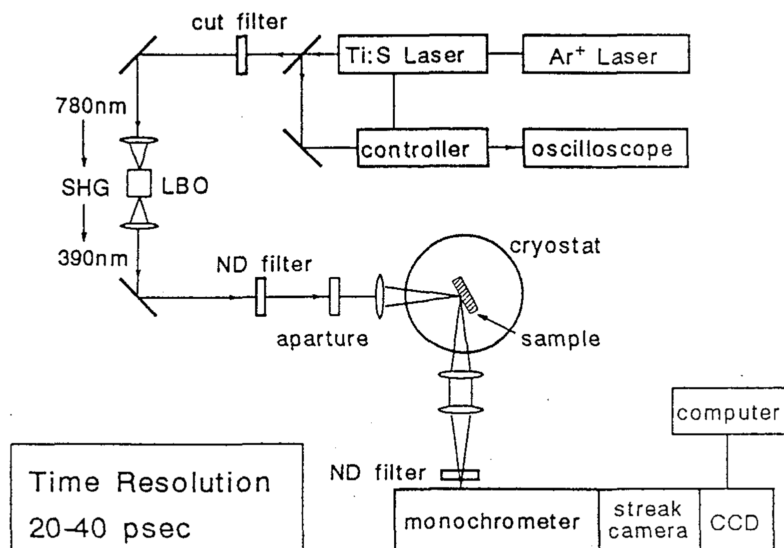

Figure 2-25. The schematic diagram for the picosecond time-resolved PL measurement.

was typically 5 to 15 mW at about 82 MHz repetition rate, and the full width at half maximum of the laser pulse is 1.2 psec. To further increase the time-resolution of the system, a synchroscan streak camera which was used with a CCD (charge coupled device) detector. The time resolution of the experiments was approximately 20~40 psec. The samples were typically cooled in a cryostat to 2K.

• Photocurrent spectroscopy

Usually, optical absorption spectroscopy is directly measured. The Zn(S,Se,Te) crystals in this study, however, are grown on the III-V group semiconductor substrates which have the lower band-gaps than the grown layer. As a result, the substrates absorption makes the film absorption measurement extremely difficult. So far, a few attempts have been reported on the absorption spectrum made by etching the substrate away chemically.[44,45] A complicated processes are required in this case, since the thickness of the grown films is typically ~1 μm.

The photocurrent (PC) is a simple alternative to optical absorption spectroscopy, which can be applied to the thin film measurement. In PC spectroscopy, absorption processes can be detected by measuring the

conducting free carriers in the valence or conduction bands. From the PC spectra, the density of state such as quantum levels or tail states as well as the direct absorption processes, can be determined.[46,47] The comparison of the PC spectra with that of the PL spectra provide the information about the carrier relaxation process in crystals and the band-structure fluctuations can be estimated from the difference between these two spectra.[48] The PC at a constant carrier generation rate F is given by

$$J_{ph} = eGF = \frac{e\mu\tau VF}{L^2}, \tag{2-15}$$

where μ and τ are the mobility and life time of the photo carriers, respectively. L is the distance between the electrodes, and G is the gain of the photocurrent, which is given by

$$G = \frac{\tau}{t_T} = \frac{\mu\tau V}{L^2}, \tag{2-16}$$

where t_T indicates the transit time defined by the transport time between the electrodes. Accordingly, J_{ph} is proportional to V or F, and inversely proportional to L. In a ideal crystal, the carrier generation rate F by the

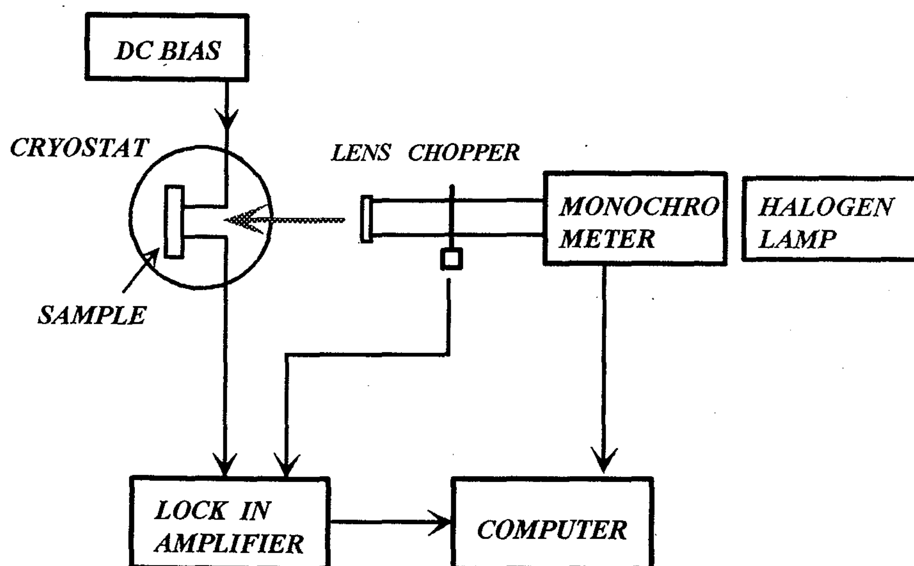

Figure 2-26. The experimental setup for the photocurrent (PC) spectroscopy.

constant light irradiation is proportional to the absorption coefficient (α).

Figure 2-26 shows the experimental setup for PC spectra measurement. In the PC measurement, a halogen lamp (100 W) is monochromed with a monochrometer. The resulting photo carrier current is measured by a conventional lock-in amplifier. On the samples, two electrodes were used. DC bias was applied to these electrode to measure the photocurrent. The distance between the two electrodes was 200μm. Au-Ge (Ge: 12 wt%) was used as electrodes for the ZnSe crystals. The low temperature measurement was performed in a cryostat at ~ 30 K.

• Photoluminescence excitation spectroscopy

The absorption processes are also measured by the photoluminescence excitation (PLE) spectroscopy. Figure 2-27 shows the experimental PLE setup. In this method, the experimental setup is very similar to that of the PL measurement. The excitation light source was a monochromated xenon lamp. Standard lock-in amplifier techniques with a light chopper were used. The resulting luminescence was detected by a photomultiplier. In this case, the PL can be obtained as a function of not only the excitation wavelength but also the emission wavelength. If the wavelength of the excitation

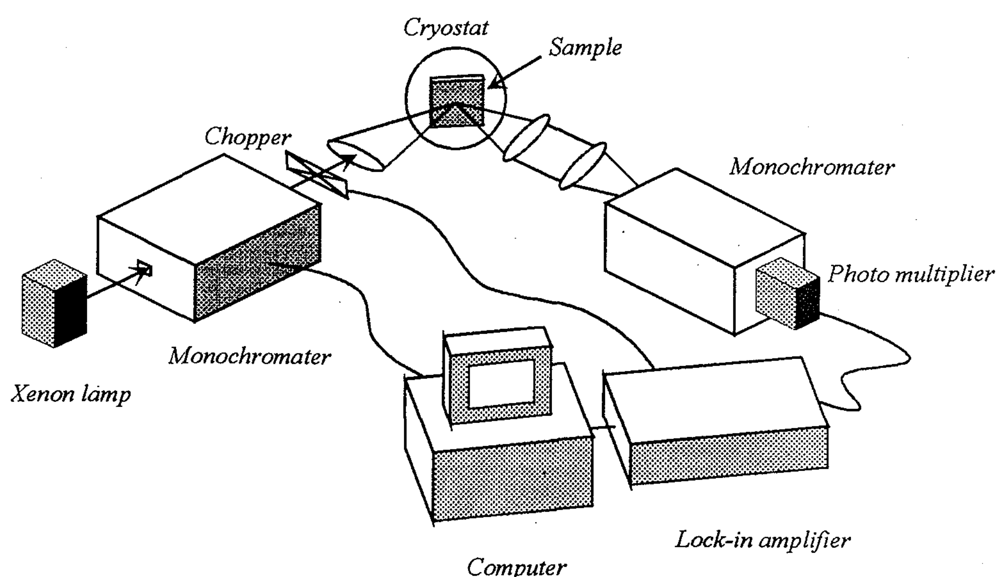

Figure 2-27. The schematic diagram for the photoluminescence excitation (PLE) spectroscopy.

source is fixed by the monochromater (A), the conventional PL can be measured. Alternatively, when the wavelength of the emission is fixed by the monochromater (B), the origin of the emission at the fixed wavelength can be obtained as a function of the excitation wavelength. In the PLE spectra, therefore, the absorption process concerning the monitored wavelength is obtained. From the PLE spectra, the absorption processes in complicated quantum-well structures have been determined.[49] Nevertheless, to measure the PLE spectra, high-sensitivity optical detectors are needed, since the PL emission intensity is very low due to the low excitation power of the incoherent xenon light.

• Reflectivity spectroscopy

The reflectivity spectra can be used to help establish the free exciton peaks in the PL spectra. In the reflectivity spectra, the free-exciton resonance absorption can be observed at a photon energy close to the band-gap. Since the reflectivity peaks are not perturbed by impurities in crystals, the position of the free exciton peaks can be accurately determined from the reflectivity spectra. A halogen lamp was used, and the reflected halogen light is directly introduced into the monochromater (detector). The experimental condition is almost the same of that of the PL measurement (a). The acceleration voltage of the photomultiplier was decreased to 250~500 V for the reflectivity measurement to reduce the background signal resulting from the halogen lamp.

2.3.2 Electronic characterization technique

The electrical properties of crystals can be characterized by electrical measurement. There exist many electrical characterization techniques, such as Hall effect, resistivity, capacitance-voltage (C-V) and current-voltage (I-V) measurement. Among these, Hall effect measurement gives direct evidences on carrier transport characteristics, because three important parameters which determine the electrical properties, i.e., mobility, carrier concentration and resistivity, are obtained from this measurement. In this section, the details about the Hall effect measurement are shown.

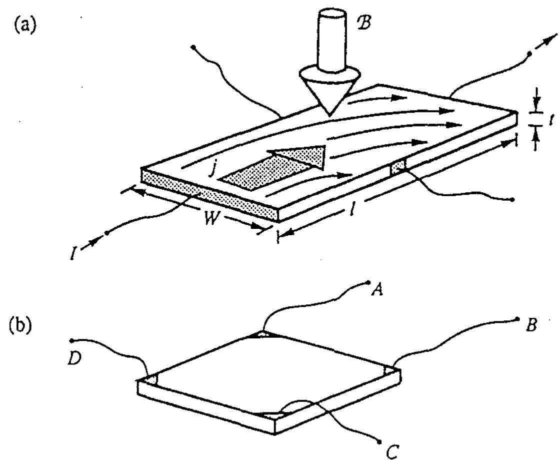

Figure 2-28. (a) Hall measurement geometry and (b) van der Pauw geometry of a semiconductor for Hall effect measurement.

Hall effect measurements allow one to determine the carrier concentration in unipolar semiconductors in which the minority carrier concentration can be neglected. A simple Hall measurement geometry is shown in Fig. 2-28 (a). When a magnetic field B is applied perpendicular to the sample surface, charge carriers flowing through the sample *(I)* experience the Lorentz force

$$F_L = -ev \times B \ , \tag{2-17}$$

where $-e$ is the charge of electrons and v is the carrier velocity. Carriers are deflected by the Lorentz force from their flow pattern without a magnetic field, as shown in Fig. 2-28 (a). As a result, an electric field is induced due to the displacement of electron changes. Carriers experience a force in the electric field, given by:

$$F_H = -eE \ , \tag{2-18}$$

In steady-state, the Lorentz force is balanced by the electric field. Equating Eqs. (2-17) and (2-18), the Hall carrier concentration n_H is given by

$$n_H = \frac{IBt}{eV_H} \ , \tag{2-19}$$

where V_H is the Hall voltage (V_H=EW) and t is the thickness of the sample. In this case, the Hall coefficient R_H is expressed by

$$R_H = \frac{1}{en}. \quad (2\text{-}20)$$

The Hall effect measurement and a conductivity measurement allows one to determine the mobility of carriers. The conductivity of an n-type semiconductor is given by σ=$en\mu$, where μ is the drift mobility. The Hall mobility is then given by

$$\mu_H = \frac{\sigma}{en} = \frac{1}{en\rho}, \quad (2\text{-}21)$$

where ρ is the resistivity of the sample.

A sample with van der Pauw-type geometry is shown in Fig. 2-28 (b). In this method, the sample is square-shaped and has four ohmic contacts at the corners. A current source is applied to two of the four contact, A and B, for example. The voltage between the contacts C and D is then measured. In this case, the resistance is expressed by $R_{AB,CD}$=V_{CD}/I_{AB}. The Hall coefficient in van der Pauw geometry is given by

$$R_H = \frac{t}{B}\Delta R_{AB,CD}, \quad (2\text{-}22)$$

where $\Delta R_{AB,CD}$ indicates the difference between the forward and reverse polarization of the magnet. The resistivity of the samples in van der Pauw geometry is obtained from

$$\rho = \frac{\pi d}{\ln 2}\frac{(R_{AB,CD}+R_{BC,DA})}{2} f\left(\frac{R_{AB,CD}}{R_{BC,DA}}\right), \quad (2\text{-}23)$$

where f is the correlation function for the asymmetric electrodes.

The Hall effect measurements were performed in Zn(S,Se) ordered alloys to determine the carrier transport properties in these crystals, as will be discussed in chapter 5. In this case, In-Ga electrodes were used, and were annealed at 200°C for 5 min in a N_2 atmosphere to form ohmic contacts to

the films. The Hall coefficients were then determined using the van der Pauw method. In the Hall effect measurement, the cleaved-square sample with contacts in the corners, which is about 5x5 mm^2 square in area, was used. The Hall measurements were performed at a magnetic field of 5 kG. The temperature of these measurement ranged from 77 to 300 K.

2.3.3 Structural and compositional characterization techniques

In this section, characterization of crystal structure and composition are discussed. The X-ray diffraction method (XRD) is an important characterization technique, since the local lattice distortion as well as 2-dimensional crystal structures can be attained. For surface structure observations or film thickness evaluations, scanning electron microscope (SEM) was employed, while larger surface structures were observed by Nomarski interference microscope. Conventional atomic composition in a alloy semiconductor was measured by electron probe micro analysis (EPMA), and secondary ion mass spectra (SIMS) provides further microscopic composition with a sensitivity in the ppb range.

• X-ray diffraction

Figure 2-29 shows the schematic diagram of the double-crystal X-ray diffraction (XRD) spectrometer. In addition to a sample crystal, a spectroscopic crystal (GaAs) is introduced at the exit of the x-ray source, as shown in Fig. 2-29. The primary purpose of the spectroscopic crystal is to provide a monochromatic and parallel beam so that the line width observed is dependent on the sample and not on the spectrometer. In this method, the diffracted beam from first crystal provided the x-ray source for measurement. Although the spectroscopic crystal is not perfect, the obtained X-ray beam is far more parallel than that provided by slits alone. In this way, only $K\alpha 1$ x-ray generating from Cu target (λ=1.5405Å) are used as the X-ray source for XRD spectra. The x-ray diffraction condition is given by Bragg's law

$$2d\sin\theta = n\lambda \ , \qquad (2\text{-}24)$$

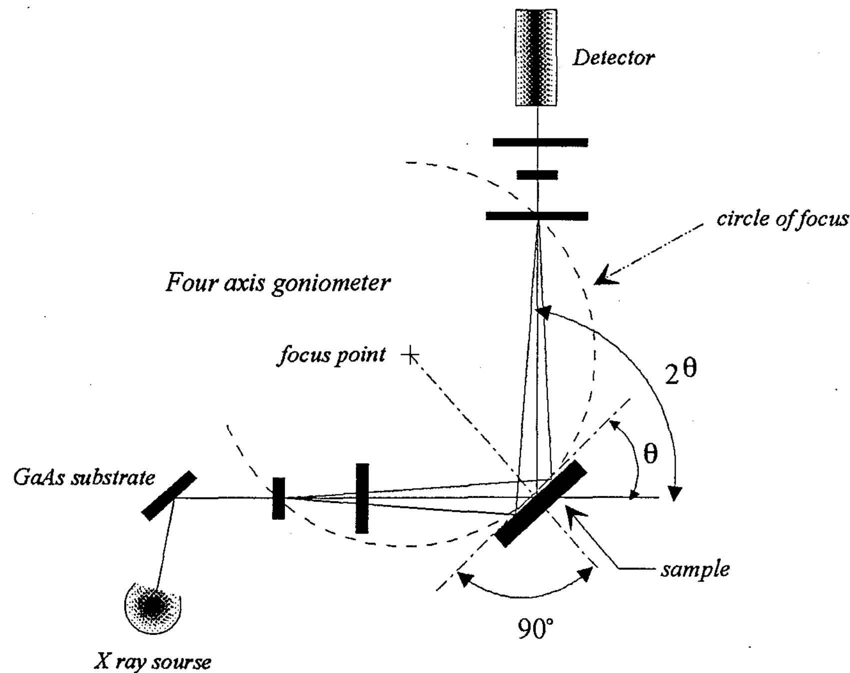

Figure 2-29. The schematic diagram of the double-crystal XRD spectrometer. The GaAs substrate is used as a first crystal.

where n is an integer, λ is the x-ray wavelength, and d is the spacing between two consecutive scattering planes. Lattice parameters of the crystals are then given by

$$a = d\sqrt{h^2 + k^2 + l^2} \ , \qquad (2\text{-}25)$$

where h, k, l are Miller indices (hkl). In experiments, XRD spectra were measured by θ/2θ mode using (400) diffraction planes of the grown samples to determine lattice constants of crystals. XRD rocking curve was obtained from ω-mode, and full width of half maximum (FWHM) of the diffraction peak was evaluated from this spectrum.

Another important feature of XRD measurements is the estimation of 2-dimensional layered structure of crystals from "satellite peaks". So far, various superlattice structures have been determined from peak angles of the satellite peaks,[50)] and very short-period crystal structure such as that of $(GaAs)_1(AlAs)_1$ has been confirmed from the analysis of satellite peaks.[51)] Satellite peak positions around (N00) plane in $(ZnS)_n(ZnSe)_m$ are given by

$$L = \left(N \pm \frac{1}{(m+n)/2}, 0, 0 \right), \tag{2-26}$$

where m and n are the number of each layers. L can be obtained from the position of the satellite peaks (θ_σ) by Bragg's law, assuming average lattice constants in superlattices to be a_m:

$$L = \frac{2a_m \sin\theta_s}{n\lambda}. \tag{2-27}$$

Therefore, from Eqs. (2-26) and (2-27), the number of layers in layer-by-layer structures (m+n) can be calculated from θ_s. In addition, average compositions in ternary alloys are obtained from peak positions of (400) diffractions (0-order peak) using Vegard's law. Consequently, the number of each layers (n and m) can be determined from the 0-order peaks and the satellite peaks. In strained layer superlattices, however, lattice distortions by strain make the estimation of the average compositions difficult, since the lattice parameters in such crystals depend on film thickness and/or growth conditions.[52]

The satellite peak intensities of $[(ZnS)_n(ZnSe)_m]_p$ were calculated as a function of diffraction angles using the following equation;[51]

$$\sum_{h=1}^{p}\sum_{k=1}^{m}\sum_{l=1}^{n} I(\theta) = \frac{1+\cos^2(\theta)}{2}\left\{ F_n \sum_{l=1}^{n} \exp[2\pi i K d_n] \times F_m \sum_{k=1}^{m} \exp[2\pi i K d_m] \right\}$$

$$\times \sum_{h=1}^{p} \exp[2\pi i K (m+n) p] \tag{2-28}$$

where F_n and F_m are atomic scattering factors of ZnS *(n)* and ZnSe *(m)* layers, which are proportional to number of electrons in atomic orbitals. Lattice spacing of n and m layers are expressed in d_n and d_m, respectively. The calculated satellite peaks from Eq. (2-28) will be shown in chapter 4-6.

- Scanning electron microscope

Microscopic surface structures and film thickness of the grown samples

were examined by scanning electron microscope (SEM: JSM-T200, JEOL). For these SEM observations, the electron accelerating voltages were chosen to be 10~20 kV, since higher accelerating voltages could lead to "charge-build up" on the sample resulting in dark images as the samples studied here were relatively resistive. The film thicknesses are directly determined by observing the cleaved samples in the [110] direction. The error in the thickness evaluation was typically ~100Å.

• Nomarski microscope

Normarski microscope has been widely accepted as a surface structure observation technique of semiconductors.[53,54] In Nomarski microscope, surface structures are observed as color differences which are produced by interference effects at surface. Figure 2-30 shows the configuration diagram for Normarski microscope. In this method, the light is resolved into two perpendicular components which emerge from the biprism with slight path deviations. The biprism is oriented at a 45° angle with the polarizer. The analyzer and polarizer have the crossed configuration. Therefore, any phase difference due to a path difference of the two lights can be detected as a polarization color. The surface observation by Nomarski microscope are made for all the samples grown.

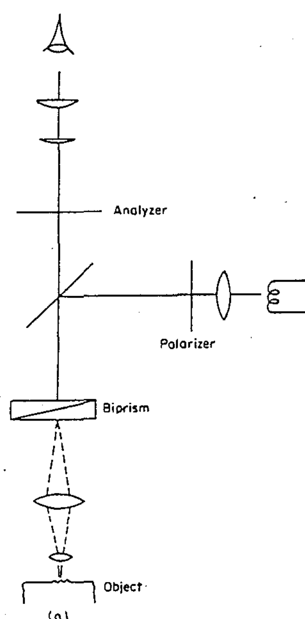

Figure 2-30. The optical configuration diagram for Nomarski microscope.

• Electron probe micro analysis

Figure 2-31 shows the schematic diagram of electron probe micro analysis (EPMA). By irradiating a material with a high-energy beam of electrons, the crystal can be induced to re-emits x-rays just as same with the x-ray source of XRD system. These x-rays have the characteristic nature of sample elements; therefore these x-ray can be used for compositional analysis. Various alloy compositions in the ordered alloys are determined from EPMA. A SEM is combined with EPMA system, since a controlled electron beam is an important part of this equipment. A crystal detector (LIF or PET crystals) combined with a monochromater are used for the purpose of x-ray detection. Accelerating voltage for electron beam was typically 20 keV.

• Secondary ion mass spectrometry

Secondary ion mass spectrometry (SIMS) is one of the most versatile chemical characterization techniques. A film is sputtered away using accelerated primary ions. The ions originated from the film can be collected and analyzed to establish the composition. Analysis of the secondary ions by SIMS provides compositional depth profiles of crystals. In this study, SIMS was used to reveal the doping depth profiles of the Zn(S,Se) ordered alloys. During the SIMS measurement, a primary ion beam is used to sputter the sample, as shown in Fig. 2-32. Secondary ions

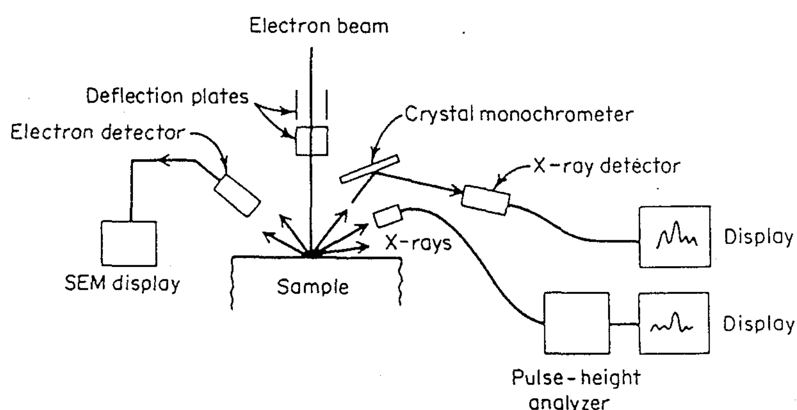

Figure 2-31. The schematic diagram of electron probe micro analysis (EPMA).

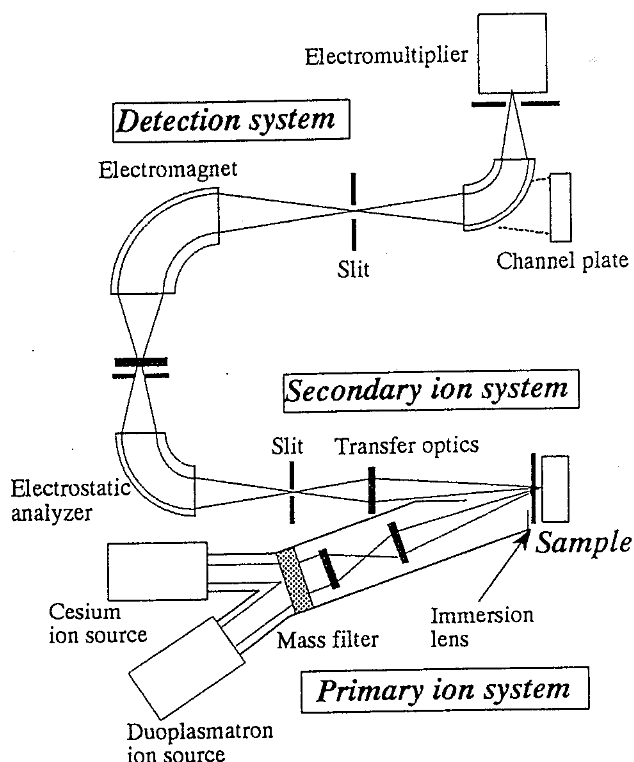

Figure 2-32. The schematic diagram of secondary ion mass spectrometry (SIMS). Primary ion system and secondary ion detection system are shown.

are released from the specimen as a result of the sputter process. These secondary ions are then measured by a mass spectrometer. The primary ion beams have an off-normal incidence about 60° with respect to the sample surface. As a primary ion beam, Cs^+ was used since the use of Cs^+ enhances the yields of both negative and positive secondary ions. The accelerating voltages of the primary ion is 10 keV using a raster size of 250 μm^2 and a detected region of 150 μm^2.

Chapter 3

Atomic Layer Epitaxy of ZnSe by HRCVD

Controlling decomposition of source gases and reactions at the growth surface are key features in HRCVD. In addition, a technique called atomic layer epitaxy allows one to control the precise atomic scale structure and composition. In this chapter, the decomposition analysis of metalorganic source compounds and the surface reaction process for ZnSe growth by HRCVD are described in detail. The relationship between reaction parameters such as time interval, susceptor distance and film properties are also discussed. In particular, in-situ optical growth monitoring method by surface photo-absorption provides important feedback of ZnSe growth in ALE by HRCVD. Crystal growth mechanisms in ALE-mode will be discussed from these results.

3.1 Development of ZnSe growth by HRCVD

So far, several types of HRCVD have been used to deposit ZnSe-based crystal films and can be categorized into three generations up to now. Figure 3-1 shows the schematic diagrams of three types of HRCVD in order of development. First type of the system (a) developed by Oda et al. used a quartz tube.[1] Diethylzinc (DEZn) and diethylselenide (DESe), which are the typical sources for the growth of ZnSe crystal in MOVPE,[2-5] are adapted as source gases and supplied to susceptor through this quartz tube. To reduce the premature reaction between DEZn and DESe in the gas phase, these source gases are supplied separately; DEZn are introduced through a stainless inner tube, while DESe are supplied through the quartz tube, as

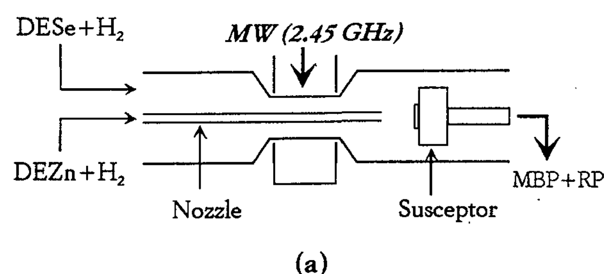

(a)

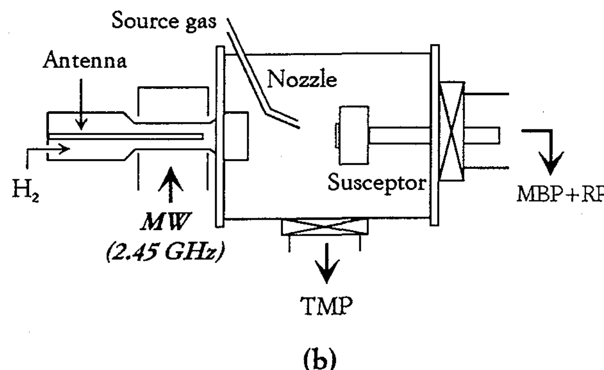

(b)

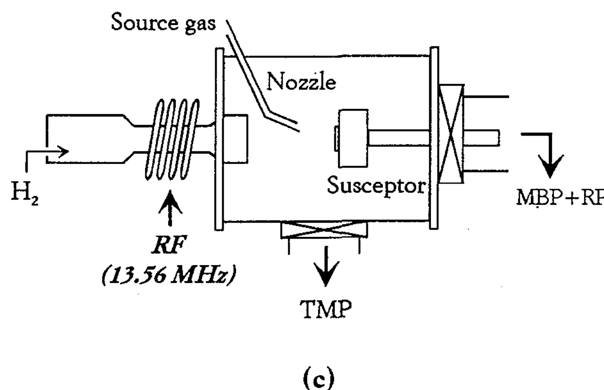

(c)

Figure 3-1 Schematic diagram of three types of HRCVD systems in order of development. MW (microwave) was used in (a) and (b), while RF (radio-frequency) was employed in (c).

shown in Fig. 3-1 (a). Atomic hydrogen was generated by a microwave plasma (MW: 2.45 GHz) at the middle of the reactor. Single crystal epitaxial growth of ZnSe on GaAs substrates was confirmed at temperature of 230°C by this HRCVD.[6,7] In this system, however, direct decompositions of source molecules by MW plasma lead to film deposition on the quartz wall, which seriously affects the crystal growth conditions. As a result, poor reproducibility and low crystallinities in the crystals were found.

In the second HRCVD system developed by Gotoh et al. (b), the

generation of the hydrogen plasma was separated from the source gas supply nozzle to reduce chamber wall film depositions.[8,9] In addition, a stainless chamber and a load-lock system were utilized in order to reduce contamination. Instead of DESe, diethyldiselenide (DEDSe) was used as a source molecule because of the low decomposition rate of DESe by the remote hydrogen plasma (see section 3.2). The XRD spectra of ZnSe and ZnS_xSe_{1-x} crystal grown by this technique showed epitaxial films, with its reduced full width at half maximum (FWHM) of about ~300 arcsec. Nevertheless, dominant deep-level emissions were found in the photoluminescence (PL) spectra, indicating high defect densities in the crystal.[8] The growth conditions of the reported ZnSe growth conditions are summarized in Table 3-1.

Table 3-1 Typical growth conditions

Flow rate	
DEZn	1.8 μmol/min
DEDSe	14.0μmol/min
H_2	200 sccm
Pressure	140 mTorr
MW power	380 W
Growth temperature	200 °C

Remarkable improvements were achieved in the quality of ZnSe grown on GaAs by adopting both the alternate gas supply and the electrically floating susceptor.[8,10] The formation of unfavorable adduct was prevented efficiently by supplying the sources alternately to the reactor. In addition, the ion-bombardment was dramatically reduced by floating the susceptor electrically from the chamber wall. Figure 3-2 shows the PL spectra of ZnSe grown under the similar conditions, except for various combinations of gas supply and connection of susceptor as follows: [8,10]

a) simultaneous supply of both DEZn and DEDSe and grounded susceptor,
b) simultaneous gas supply and floating susceptor,
c) alternate supply of sources and grounded susceptor, and
d) alternate supply and floating susceptor.

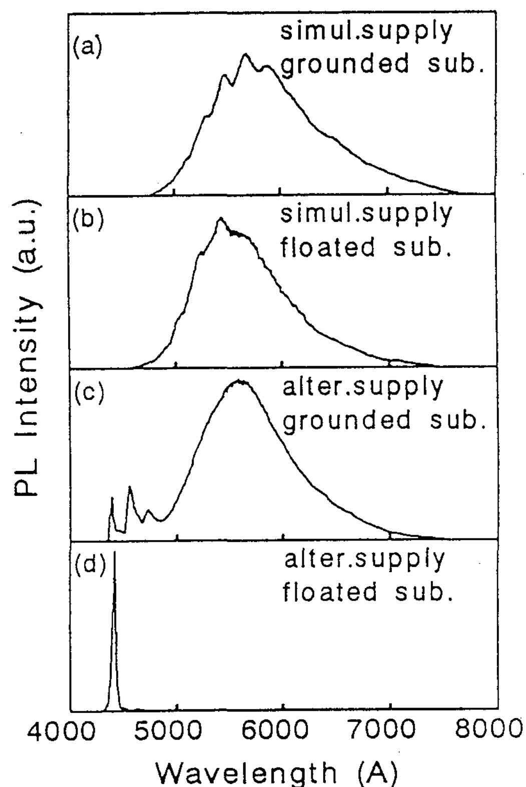

Figure 3-2 PL spectra at 35 K of ZnSe grown at 230 °C by each of both gas supply method and electric condition of substrate.

As is shown in the spectra (a) and (b) of Fig. 3-2, the PL emissions attributed to the deep levels are dominant as far as the crystals were made by the simultaneous gas supply regardless of the electric connection. Deep level emissions are markedly reduced by adopting the alternate gas supply as show in the spectrum (c). The PL spectra (d) shows sharp peaks consistent with free exciton emission lines at the band edge. In addition, a sharp XRD peak of 90 arcsec in FWHM for (400) diffractions was obtained in the ZnSe fabricated under the condition shown in (d). The effect of ion-bombardment was also studied by applying a DC bias to the susceptor. The ratio of the emission lines from the deep states to those from exciton depended greatly on the current passing through the susceptor, and the minimum value was obtained when the current was zero.[8] Therefore, the generation of defects is efficiently reduced by avoiding ion-bombardment.

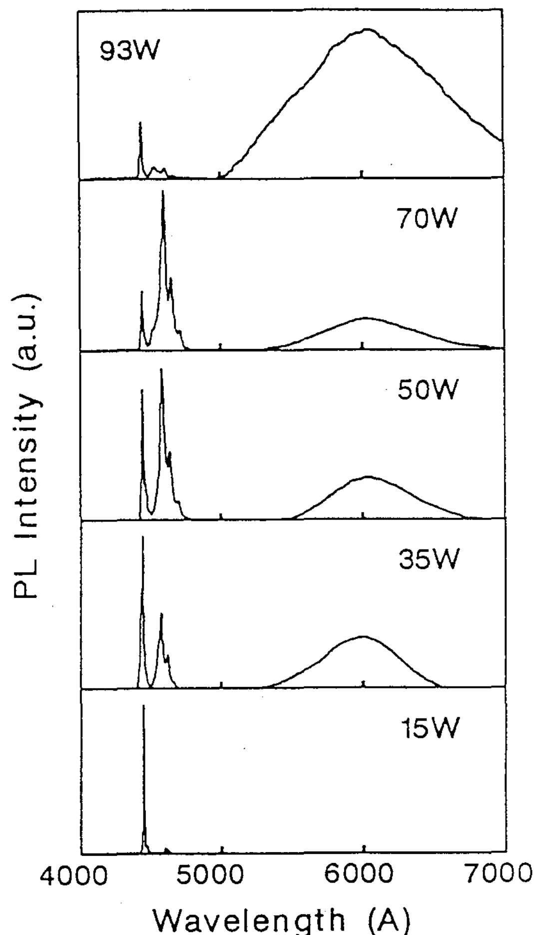

Figure 3-3 The PL spectra of ZnSe at 35 K on various MW power from 15 to 93 W.

Moreover, ion-bombardment can be reduced by fitting a metallic mesh at the end of the tube, as shown in Fig. 2-3.

There is, however, room for improvement in the second HRCVD system, although the fabrication of high-quality ZnSe crystals have been established. In Fig. 3-3, the PL spectra of ZnSe grown by varying the microwave power from 15 to 93 W are illustrated.[10] As shown in Fig. 3-3, the emissions related to the donor to acceptor pairs (DAP) and the deep levels increase with an increase in MW power. Simultaneously, the growth rate was lowered at powers greater than 50 W due to the atomic hydrogen etching. Therefore, high crystal quality requires low plasma energy. Moreover, the stainless antenna within the quartz tube also affects crystal quality. After a long time generation of the hydrogen plasma (a few months), dark metallic

films are deposited inside the quartz tube probably due to a sputtering effect of the stainless tube by MW hydrogen plasma. As a result of these deposits, the emission intensity of the hydrogen plasmas became weaker, since the metallic films around the wall absorb MW energy; thus reducing the MW power coupled into the plasma.

In the last HRCVD system, the generation of the hydrogen plasma was made by the RF coil, which require no electrodes inside the quartz tube, as shown in Fig. 3-1 (c). In addition, a low frequency of RF at 13.56 MHz provides lower ionization states of the hydrogen plasma compared with the MW, which is preferable for the crystal growth since the ion-bombardment effect can be further reduced. In fact, the electric potential at the susceptor is less than 0.3 V when a remote RF hydrogen plasma was employed, which is far small compared with ~2 V of the MW plasma. Using RF plasma, the quartz tube have not showed any color change in almost 4 years and quite stable since the generator was changed from MW to RF. Also, the metalorganic compound gas supply system has been changed in this HRCVD system as described in section 2.1.3.

In summery, the three different types of HRCVD systems have been developed since 1986. Improvements of HRCVD systems have been made to avoid the gas phase reactions between the source molecules, while decomposing the sources efficiently. Improvements include alternate supply of the source gases and separation of atomic hydrogen from the source gas supply nozzle. Another key factor in HRCVD is the generation of atomic hydrogen. It was found that the ion-bombardment largely degrades the crystal's optical properties. By adapting RF hydrogen plasma, the formation of the stable hydrogen plasma with reduced ion-bombardment was realized. Consequently, the growth of high quality Zn(S,Se,Te) crystals at low temperature (~ 200°C) have been realized.

3.2 Decomposition Processes by Atomic Hydrogen

Gas phase chemical reactions have a large influence on film properties in HRCVD. So far, the fabrication of high-quality ZnSe crystals at the low temperature of 200°C has been established by decomposing source molecules by atomic hydrogen. Previously, however, the in-situ observations of decomposition processes were not carried out to this work. In this section, direct observation of metalorganic compound decomposition (DEZn and DEDS and DEDSe) are made by quadruple mass spectrometer (QMS).

3.2.1 Introduction to metalorganic compounds

The epitaxial growth of compound semiconductors using metalorganic compounds has dramatically advanced since the first experiments by Manasevit et al. about 30 years ago.[11,12] These precursors have been used for the crystal growth in metalorganic vapor phase epitaxy (MOVPE). So far, MOVPE has been widely employed to prepare GaAs and InP crystals. The purity of these crystals exceeds all other techniques including molecular beam epitaxy (MBE) and liquid-phase epitaxy (LPE). In the following section, the fundamental characteristics of the metalorganic compounds are reviewed.

The bonding configurations of the metalorganic compounds are extremely important to understand the kinetic aspects of the pyrolysis reactions. These metalorganic compounds are usually written as MR_n, where M and R indicate the metal and the alkyl (hydrocarbon) with the number bonded with the metal *n*. The II group metalorganic compounds, such as DEZn used in this study, can be described as MR_2.

The group II elements have two *s* electrons in the outer shell. To form two covalent bonds a hybridization occurs. The hybridization results in two *sp* orbitals which bond the ligands. The schematic configuration of dimethylzinc (DMZn), typical source for ZnSe growth by MOVPE,[13,14] is shown in Fig. 3-4 (a). The *sp* hybridized orbitals are linear, where the two ligands are separated at an angle of 180°. The group VI sources, also expressed in form of MR_2, have two *s* electrons and four *p* electrons in the outer shell. In this case, two lone pairs occupy the other two tetrahedral positions, and the two covalent sp^3 bonds are separated by the tetrahedral

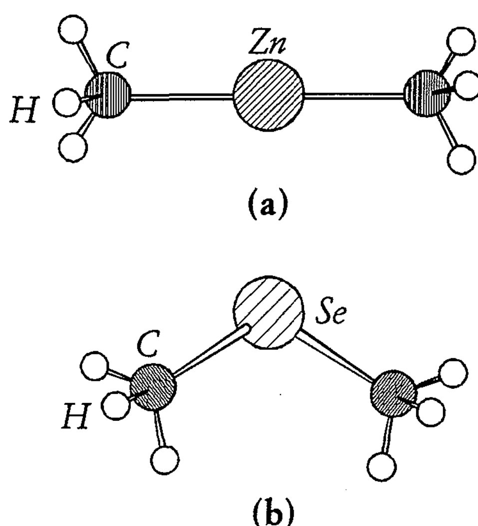

Figure 3-4 Schematic diagrams of metalorganic molecules typically used for MOVPE growth: (a) DMZn and (b) DMSe.

angle. Figure 3-4 (b), for example, shows the configuration of atoms in dimethylselenide (DMSe). The metal-carbon bond energy is another factor which determines the dissociation energy of the molecule. In general, the metal-carbon bond strength depends on the nature of the metal, including its the electron-negativity, and the size and configuration of the molecule. Figure 3-5 shows the average metal-carbon bond strength plotted as a function of atomic number for the common group II and VI atoms.[15) It is evident that the bond strength in both the group II and VI molecules decreases as the electron-negativity of atom decreases. Obviously, the group VI metalorganic molecules have the higher stability than the group II molecules, which agree well with the experimental results observed. In addition, the metal-carbon bond strength is decreased as the number of carbons bonded to the central carbon is increased. This effect is attributed to the delocalization of the free-radical electronic charge. Consequently, higher decomposition rates is expected in the molecule with the alkyls having larger number of carbons bonded to the central carbon, such as tertiarybuthyl (t-butyl) or isobutyl (i-butyl). In HRCVD method, these metalorganic compounds are decomposed by the chemical reaction with atomic hydrogen. The reactions of metalorganic compound with atomic hydrogen are also subject to the rules which are described above. The decomposition or reaction mechanism by atomic hydrogen will be discussed in the following section of 3.2.2 and 3.2.3.

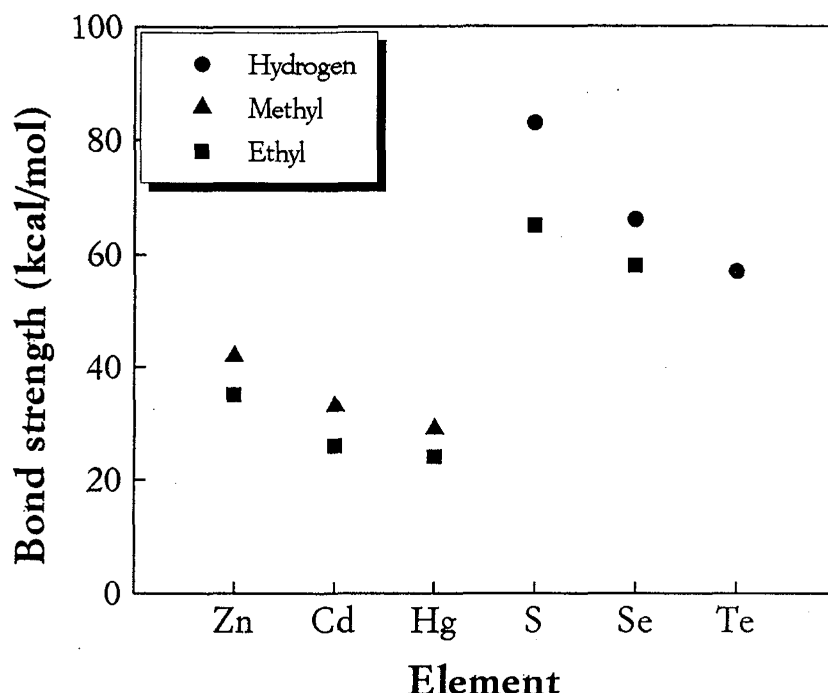

Figure 3-5 Metal-ligand bond strengths (average) of group II and VI metalorganic compounds for various alkyls

3.2.2 Decomposition process of group II source

Diethylzinc (DEZn) have been used as a source molecule for the group II elements in HRCVD. There are several reasons that this molecule was chosen. First, this species has a favorable vapor pressure (~10mmHg at room temperature) as shown in Fig. 2-8. Second, carbon incorporation into crystals can be reduced by the ethyl alkyls. It has been reported that the GaAs and AlAs grown by trimethyl-sources (such as trimethylgallium (TMGa) or trimethylaluminum (TMAl)) leads to a large carbon incorporation (~10^{19} cm^{-3}) which seriously degrades crystal properties.[16-18] Accordingly, a reduction in the carbon concentration is expected by using DEZn. In fact, the large carbon incorporation was reported in MOVPE when DMZn and methylallylselenide (MASe) were used.[19] Furthermore the large quantity of atomic hydrogen used by HRCVD is expected to further inhibit carbon incorporation since it promotes the formation of stable carbon species.

Generally, the decomposition of source molecules by the QMS ionizer complicate the analysis of QMS spectra. To avoid this process, a neutral

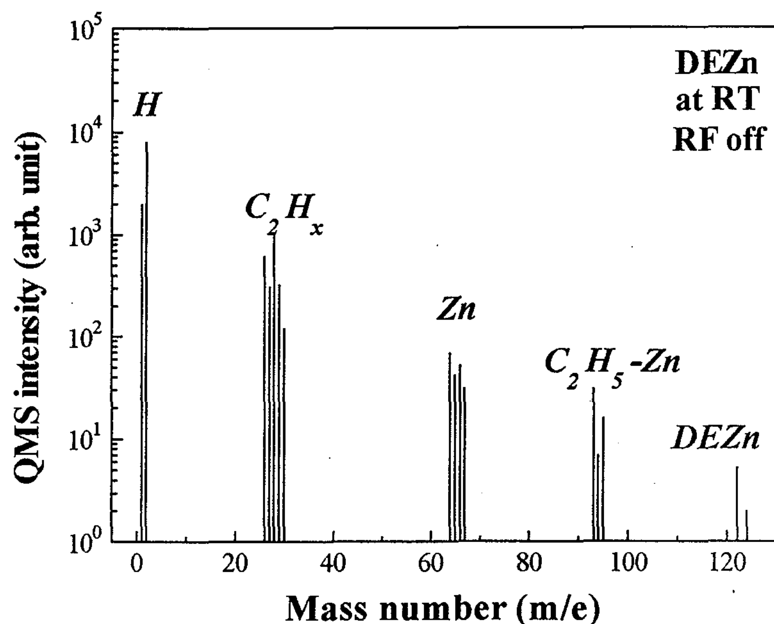

Figure 3-6 The QMS spectrum of DEZn at room temperature without plasma generation

radical detection by apearance mass spectrometry has been developed.[20)] In any case, the ionizer voltage can not be changed in this QMS system and was maintained at 3.5 eV. In this study, therefore, the decomposition processes are determined from the relative intensities of the QMS spectra. In order to determine the thermal decomposition temperature of DEZn, the temperature dependence of the QMS was measured.

First of all, the thermal decomposition of DEZn was analyzed to characterize the decomposition process. Figure 3-6 shows the QMS spectrum at room temperature when no hydrogen plasma or hydrogen radicals were present. As shown in the spectra, various fragment peaks of DEZn, such as C_2H_5Zn (m/e=79) and C_2H_x (m/e=24-30), were observed due to decomposition by the ionizer of QMS. The peak splitting of Zn (m/e=64) is caused by the isomer formation and agreed well with the abundance ratio. Figure 3-7 shows the QMS relative intensities for the various fragments plotted as a function of the substrate temperature. In this figure, the relative intensities of the QMS peaks from the value at substrate temperature of 100°C are shown. Hydrogen gas for the hydrogen plasma at the flow rate of 100 sccm were also introduced into the chamber without

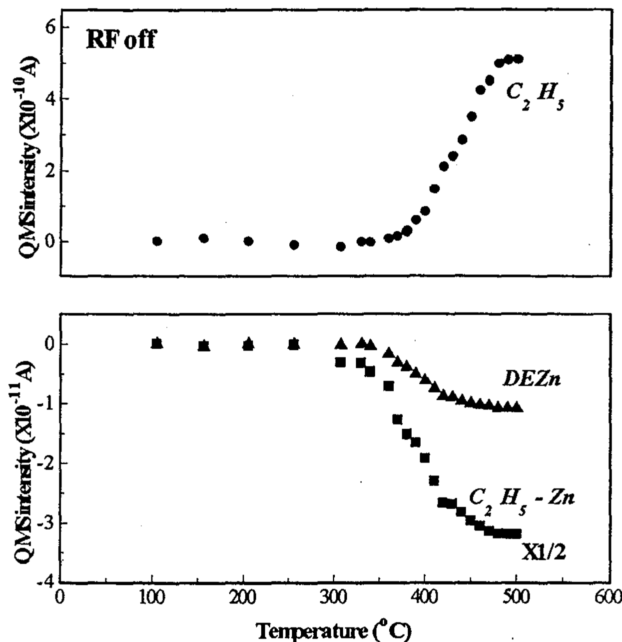

Figure 3-7 The temperature dependence of the relative QMS intensities for the various fragment peaks.

generating hydrogen plasma to maintained the measurement condition same. As shown in Fig. 3-7, at temperatures above 350°C, the C_2H_5 concentration increases. This temperature corresponds to the temperature where the reduction in DEZn and C_2H_5Zn concentration begins. The changes of these concentration ceases at a substrate temperature of ~500°C. It should be mentioned that the C_2H_5Zn QMS peak intensity is considered to originate from the decomposition by the QMS ionizer, since the same behavior with DEZn was observed in this peak. From these results, the decomposition temperature of DEZn are estimated to be 350°C or higher. Note that the substrate temperature can not be below 350°C to fabricate high quality ZnSe crystals by MOVPE, in which the thermal decomposition of sources is used. This measured decomposition temperature is, however, dependent on the time allowed for decomposition (or residence time) and other experimental conditions such as the surface area and wall condition.[21)]

Now the case in the hydrogen radical decomposition is considered. Figure 3-8 shows the relative concentration for the various fragment peaks plotted as a function of the hydrogen plasma RF power. In this figure, the

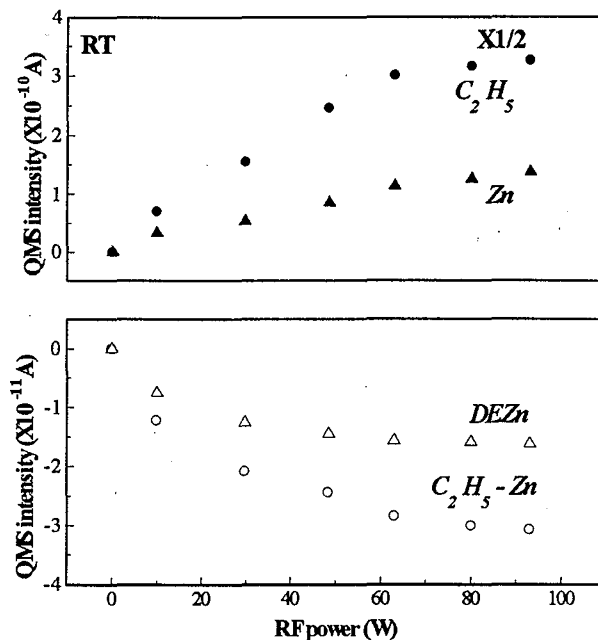

Figure 3-8 The relative QMS intensities for fragments of DEZn plotted as a function of the RF power for the hydrogen plasma in HRCVD. Measurement was made at room temperature.

changes from the value at RF=0 are plotted to avoid the influence of decomposition resulting from the QMS filament. In addition, these measurement were carried out at room temperature, where thermal decomposition of DEZn is negligible. As shown in Fig. 3-8, the C_2H_X and Zn concentrations increase with increasing the RF power. The peak intensities of source molecules correspondingly decrease. This indicates that DEZn can be decomposed through chemical reactions with atomic hydrogen even at room temperature. Similar results are obtained at the substrate temperature of 200°C (typical growth temperature in HRCVD).

In Fig. 3-9, the QMS intensities of atomic hydrogen (m/e=1) as a function of the RF power at room temperature is shown. The QMS intensity is normalized by the no RF power value. An increase in atomic hydrogen intensity with the RF power clearly indicates the generation of atomic hydrogen by the hydrogen plasma. In order to confirm the chemical reaction of DEZn with atomic hydrogen, the QMS intensities of DEZn are further normalized by that of atomic hydrogen, and the result is shown in Fig. 3-10. All the QMS intensities of the fragment peaks show the constant

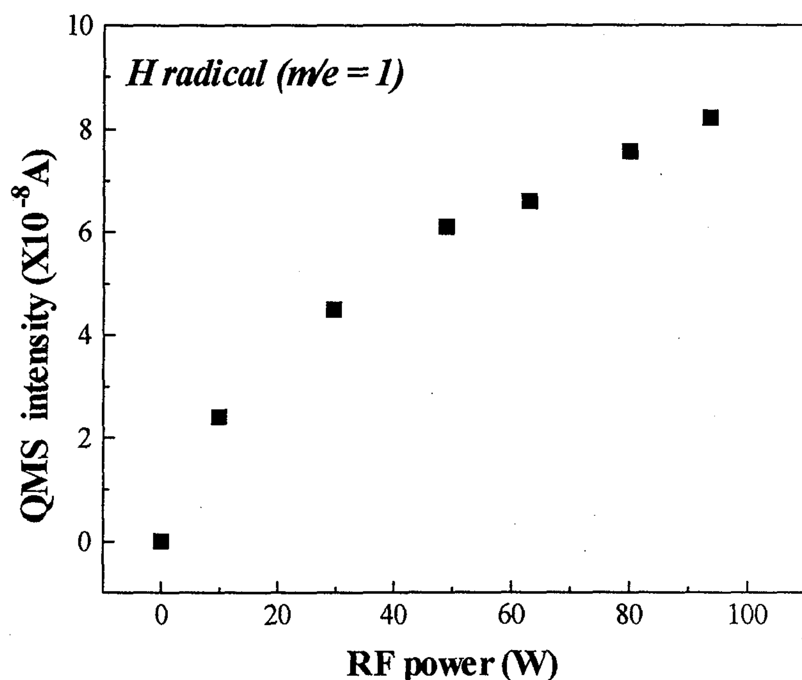

Figure 3-9 The relative intensity of atomic hydrogen plotted as a function of the RF power of hydrogen plasma measured at room temperature.

values over the changes of the RF power. This result clearly indicates that the decomposition of DEZn is proportional to the concentration of atomic hydrogen. From the results mentioned above, the chemical reaction of DEZn with atomic hydrogen suggests that a first order reaction is involved;

$$(C_2H_5)_2Zn + H\bullet \longrightarrow C_2H_5\text{-}Zn\bullet + C_2H_6 \qquad (4\text{-}1)$$

Consequently, the Zn precursor in HRCVD is considered to be C_2H_5-Zn radicals.

On the other hand, Ozeki et al. calculated the radical dissociation energy of DMZn by ab initio method. The dissociation energy of first methyl, expressed in reaction (4-2), is calculated to be 301.6 kJ/mol, while the second methyl are decompose by the lower energy of 92.5 kJ/mol (reaction (4-3)), suggesting that the methylzinc radical is an unstable presursor.[22)]

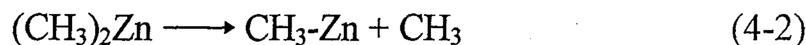

$$(CH_3)_2Zn \longrightarrow CH_3\text{-}Zn + CH_3 \qquad (4\text{-}2)$$

$$CH_3Zn \longrightarrow Zn + CH_3 \qquad (4\text{-}3)$$

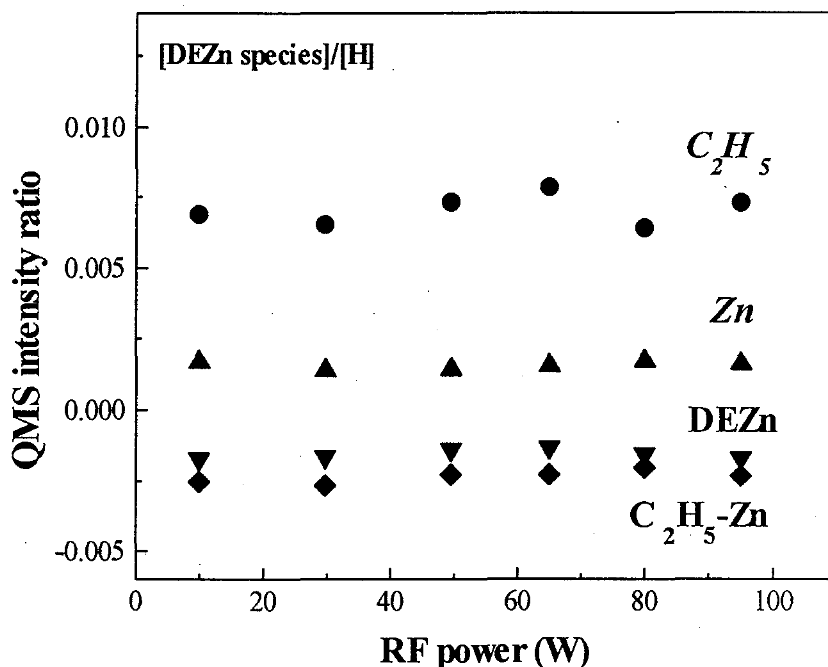

Figure 3-10 The normalized QMS peak intensities for DEZn fragments by that of atomic hydrogen plotted as a function of the RF power for the hydrogen plasma

As a result, there is a possibility that the primary reaction of (4-1) induces the further decomposition of ethylzinc radical. This process, however, was not observed in this experiment due to the background decomposition products resulting from the QMS filament.

3.2.3 Decomposition processes of group VI sources

In HRCVD, we employed special group VI molecules such as DEDS, DEDSe and DEDTe. Figure 3-11 shows the schematic diagram of DEDS calculated from the molecular mechanics. Similar configurations are also predicted for DEDSe and DEDTe. These molecules have intermoleculer bonding among each of group VI atoms, as shown in Fig. 3-11. The chemical reaction of atomic hydrogen at the central atom of this molecule is expected. In fact, the growth of high-quality ZnSe crystals has been achieved by using these sources. It should be emphasized that there is no atomic hydrogen chemical reaction when diethylselenide (DESe) was used,

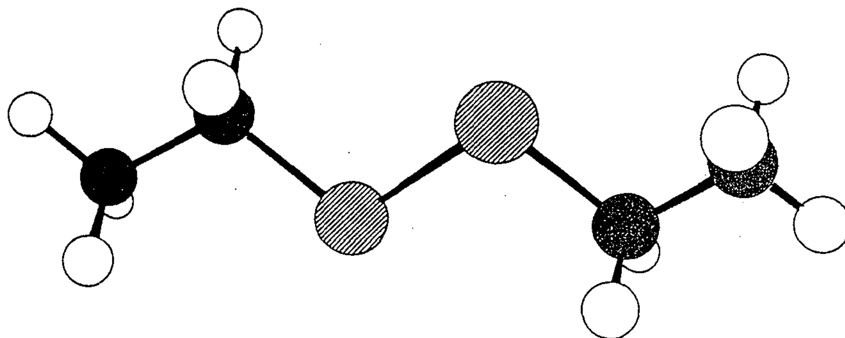

Figure 3-11 The schematic diagram of diethyldisulfide (DEDS) calculated from the molecular mechanics. The shading of two atoms in the middle of the molecule illustrates the sulfur atoms.

since group VI metalorganic compounds have a higher stability than the group II sources, as shown in Fig. 3-5.

Figure 3-12 shows the typical QMS spectrum for the DEDS with no RF power. The substrate temperature is room temperature, and other measurement conditions are almost same with that of DEZn except for the flow rate of the source gas. As seen in Fig. 3-12, various fragment peaks are observed. Stable neutral hydrogenated sulfides such as H_2S (m/e=34) and C_2H_5SH (m/e=65) are also observed in this spectrum. These peaks have higher measurement sensitivity than their radical counter parts probably due to their high vapor pressure of these molecules. To increase the signal to noise ratio, these peaks of hydrogenated molecules were used for the analysis. Consequently, the same procedure with that of DEZn was carried out to analyze the decomposition process. The QMS spectrum for DEDSe is also shown in Fig. 3-13. The experimental conditions were maintained same with that of DEDS. The similar characteristics with that of DEDS are seen in the spectrum; the similar trend of fragment peaks and also the higher sensitivities for hydrogenated molecules. Nevertheless, the presence of source molecule (DEDSe) is not observable since it has a larger mass number (m/e=218) than the QMS measurement limit of this system (m/e=200).

No thermal decomposition of DEDS and DEDSe molecules was observed up to the substrate temperature of 500°C. Therefore, it can be concluded that the thermal decomposition temperature of these molecules is over 500°C.

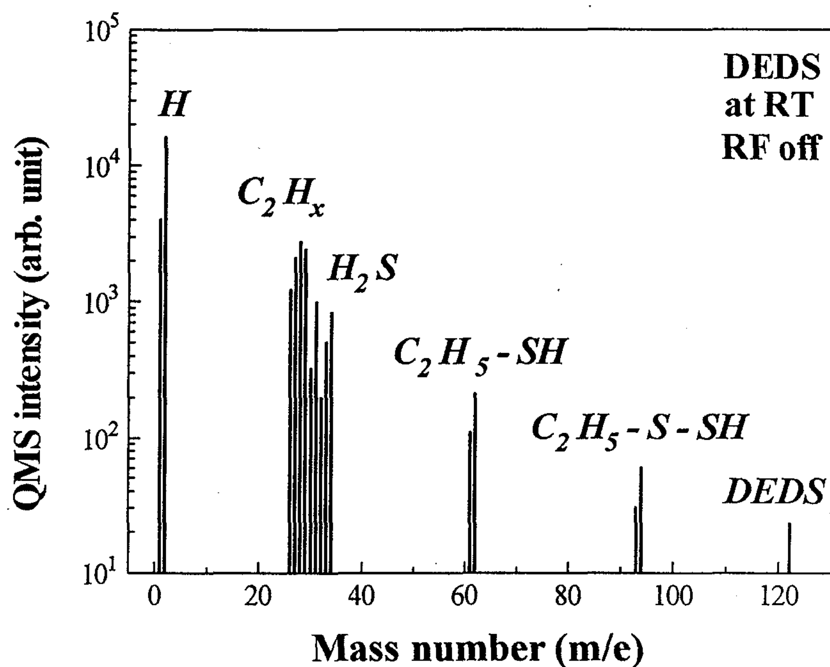

Figure 3-12 The typical QMS spectrum for DEDS without plasma generation measured at room temperature.

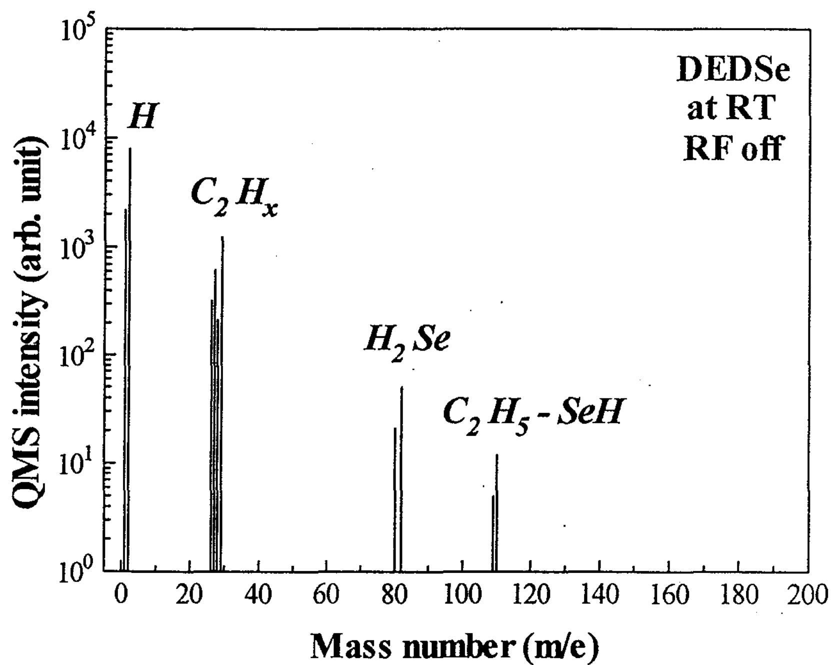

Figure 3-13 The typical QMS spectrum for DEDSe without plasma generation measured at room temperature.

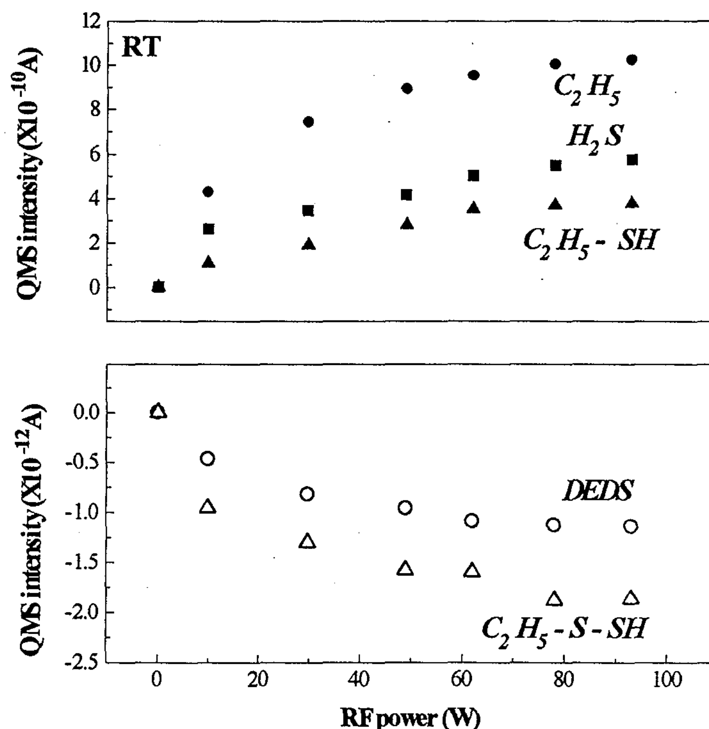

Figure 3-14 The relative QMS intensities for fragments of DEDS plotted as a function of the RF power for the hydrogen plasma.

The thermal decomposition temperature of DESe and DMSe are also reported to be over 500°C,[23)] indicating that the group VI metalorganic compounds have higher stability than that of the group II counter parts.

The decomposition of these metalorganic sources was also determined as a function of the RF power. Figure 3-14 shows the concentration of the fragment peaks plotted as a function of the RF power. The increase (or decrease) in the concentration is normalized to the zero RF power case. The spectra were measured at room temperature, where the thermal decomposition of these molecules is negligible. As shown in the spectrum, the QMS intensities of DEDS and C_2H_5-S-SH gradually decrease with increasing RF power, while the concentration of the fragment such as C_2H_5, H_2S and C_2H_5-SH increase. The same constant ratio of C_2H_5-S-SH to DEDS concentration indicates that the formation of C_2H_5-S-SH is caused by the filament, not hydrogen induced dissociation. Similar decomposition patterns were also observed in DEDSe, as seen in Fig. 3-15. In this case, however, only the small mass fragment peaks could be observed due to the

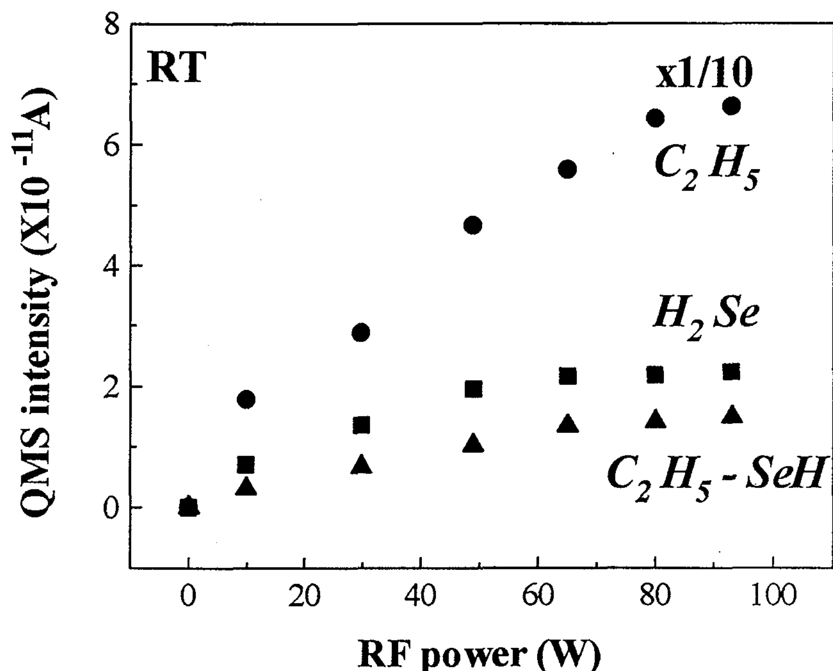

Figure 3-15 The relative QMS intensities for fragments of DEDSe plotted as a function of the RF power for the hydrogen plasma.

limit of the system. The experimental condition is almost same with that of DEDS. As shown in the spectrum, the decomposition of source takes place at the center of this molecule, which generates the fragment peak of C_2H_5-SeH. When the QMS intensities of DEDS are normalized by the QMS intensity of atomic hydrogen, these intensities show constant values which suggests that the reaction between DEDS and atomic hydrogen is a primary reaction. The fragment peaks of DEDSe also shows similar constant values when the normalization was performed.

From these results, the chemical reaction of DEDS and DEDSe with atomic hydrogen in HRCVD can be given as follows:

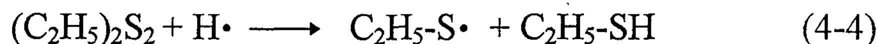

$$(C_2H_5)_2S_2 + H\cdot \longrightarrow C_2H_5\text{-}S\cdot + C_2H_5\text{-}SH \qquad (4\text{-}4)$$

$$(C_2H_5)_2Se_2 + H\cdot \longrightarrow C_2H_5\text{-}Se\cdot + C_2H_5\text{-}SeH \qquad (4\text{-}5)$$

The formation of C_2H_5-S-S or C_2H_5-Se-Se radicals is considered to be small, since the QMS peak intensities of these peaks decrease with increasing RF power. Consequently, it is concluded that the decomposition process of DEDS and DEDSe occurs at the S-S or Se-Se bond in the middle of the

molecule, and the resulting precursors are assumed to be C_2H_5-S and C_2H_5-Se radicals, respectively.

In summery of this section, the decomposition of DEZn, DEDS and DEDSe by the chemical reaction with atomic hydrogen was observed from the QMS spectra. In addition, these molecules can be decomposed by hydrogen radicals even at the room temperature, where the thermal decomposition processes are negligible. The group II reaction precursor is considered to be the H_5C_2-Zn radical. On the other hands, the group VI precursors are found to be H_5C_2-Se and H_5C_2-S radicals, respectively. It was confirmed that the low temperature growth at 200°C in HRCVD is proceeded by the formation of these chemically active precursors.

3.3 Surface reaction process observed by *in-situ* SPA

In the previous section, the creation of the chemically active precursors by atomic hydrogen were probed by the QMS. In this section, the surface reaction processes are discussed. For the observation of the crystal growth, an in-situ surface photo-absorption (SPA) method was adapted. The SPA measurements provide information about kinetic factors of the crystal growth. The crystal growth mechanism of ZnSe in ALE mode will be discussed. The relationship between material and deposition parameters will also be considered.

3.3.1 Introduction to *in-situ* monitoring using SPA

As described in chapter 2, the SPA method is a powerful tool for crystal growth observation. Until now, this method has not been applied to ZnSe-based crystals, while this method has been widely employed in the III-V group semiconductor field.[24-28] Yoshikawa et al. developed the surface photo-interference (SPI) method for the observation of ZnSe growth.[29,30] In this method, a laser light having lower energy than the band-gap of crystal was used so as to avoid a photo-induced crystal growth.[31-33] Nevertheless, the interference effects between grown layers and GaAs substrate tended to complicate the spectra analysis in SPI method.

In this study, we adapted the SPA method which use a laser light having higher energy than the band-gap of crystal. Accordingly, the photo-assisted growth of ZnSe crystal is expected in SPA method. In this section, the results of fundamental characteristics of SPA measurement along with the photo-induced crystal growth effect will be discussed.

Figure 3-16 shows the typical SPA signal of ZnSe growth in ALE mode. The inset show the gas supply sequences for DEZn and DEDSe, respectively. In Fig. 3-16, the SPA signal intensity is shown in form of $(R_{Se}-R_{Zn})/R_{Zn}$ (%), which indicates the difference in the reflectivity between Se and Zn surfaces normalized to the reflectivity of the Zn surface. The growth conditions of ZnSe are summarized in Table 3-2.

The SPA signal increases when DEDSe is supplied to the growing surface, while the supply of DEZn leads to the SPA signal reduction, as shown in Fig. 3-16. These oscillations correspond to the surface coverage ratio of each

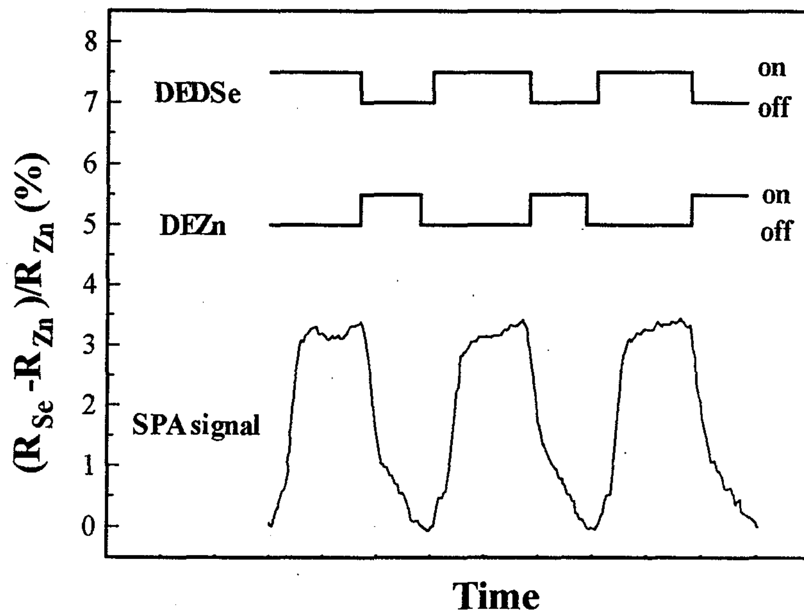

Figure 3-16 The typical SPA signal of ZnSe in ALE mode during crystal growth. The inset illustrates the gas supply sequences of DEZn and DEDSe, respectively.

Table 3-2 Typical growth condition for ZnSe

Flow rate	
DEZn	7.53 μmol/min
DEDSe	0.96 μmol/min
Sequence (sec)	4-0-4-1
RF	40 W
Growth temperature	200°C

atom type, therefore, the crystal growth can be monitored by this behaviors. Similar oscillations have been observed in the crystal growth of GaAs.[24-26] In addition, these oscillation continued during the whole crystal growth, suggesting that the layer-by-layer growth were maintained within the crystal thickness grown.

When the *in-situ* observation was made by SPA, however, the place on the surface where He-Cd laser was irradiated showed increased film thickness. This effect is caused by the photo-assisted growth of ZnSe. In order to suppress this effect, the light intensity of He-Cd laser was lowered with neutral density filters. Figure 3-17 shows the growth rate of ZnSe

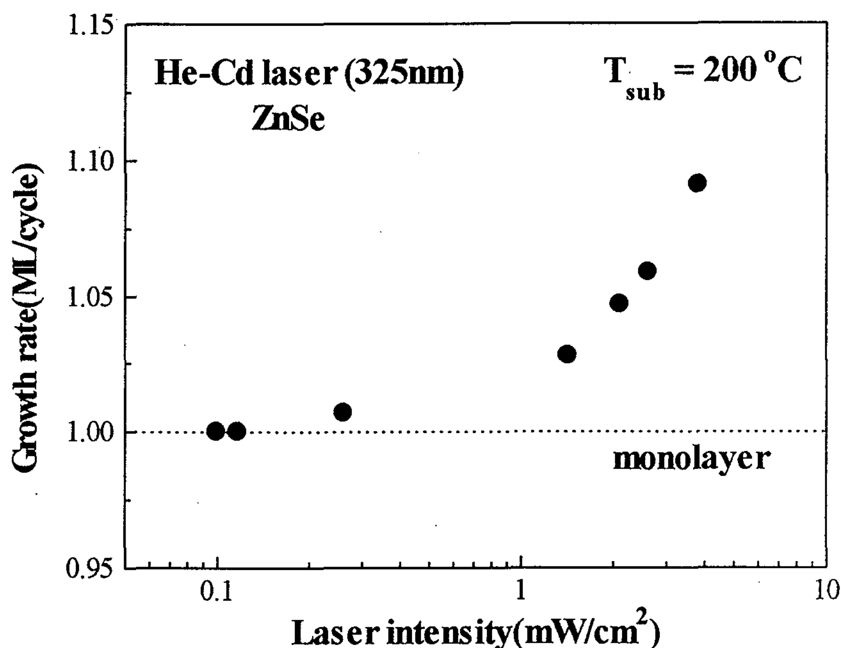

Figure 3-17 The growth rate of ZnSe crystal plotted as a function of the light intensity of He-Cd laser (325 nm).

crystal plotted as a function of the laser intensity of He-Cd laser (325 nm). When the laser was not irradiated to the sample surface, the growth rate of ZnSe is one monolayer per one cycle. The growth rate of ZnSe gradually increase with increasing the light intensities, as shown in Fig. 3-17. In the PL spectra of these samples, the sample irradiated by the laser showed the almost same spectra as a the sample without laser irradiation. Consequently, the laser irradiation effect on the crystal quality was negligible in this case. When the laser intensity was less than 0.2 mW/cm^2, there was no increase in film thickness, and the SPA signals can be observed at this condition. As a result, the suppression of the photo-assisted growth was accomplished by reducing the laser intensity with the neutral density filters. In this study, therefore, the laser intensity for the SPA measurement was maintained at 0.1 mW/cm^2; where the photo-assisted growth is insignificant.

Figure 3-18 shows the SPA signal intensity as a function of the He-Cd laser incident angle. The highest SPA signal (~4 %) was observed at an incident angle of 75°. A rapid decrease in the SPA signal is seen as the incident angle increases or decreases from this value. The calculated

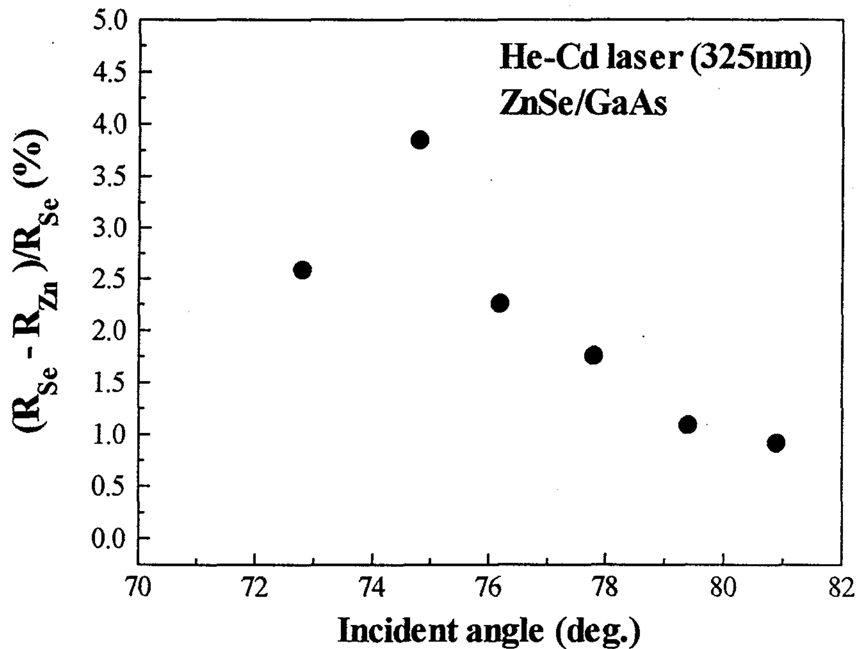

Figure 3-18 The SPA signal intensity of ZnSe crystal plotted as a function of the incident angle of He-Cd laser light (325 nm)

reflectivity of ZnSe crystal for s- and p-polarized light from Eqs. (2-5)~(2-7) is shown in Fig. 3-19. The refractive index of ZnSe is assumed to be *2.94-0.61i* in this calculation.[34)] The light reflection from the thick ZnSe crystal can be suppressed by using p-polarized light at Brewster angle. Brewster angle of ZnSe crystal is calculated to be 71° from Eq. (2-8) and is slightly different from the observed angle. This discrepancy might be caused by the error in the estimation of the incident angle. The substrate temperature of 200°C is another factor of this difference, since the calculation is made by the refractive index at room temperature.

As described before, ZnSe crystals made in this study are grown on GaAs substrates which have a different refractive index than that of ZnSe. At the wavelength of He-Cd laser (325 nm), the penetration depth of laser light in ZnSe crystal is about 500 Å. As a result, an interference fringes are evident in the SPA signal intensity when the film thickness is less than the penetration depth. Figure 3-20 shows the typical reflectivity spectrum observed in the SPA signal during growth. When this reflectivity signals are magnified, the oscillations of the Zn and Se covered surfaces can be

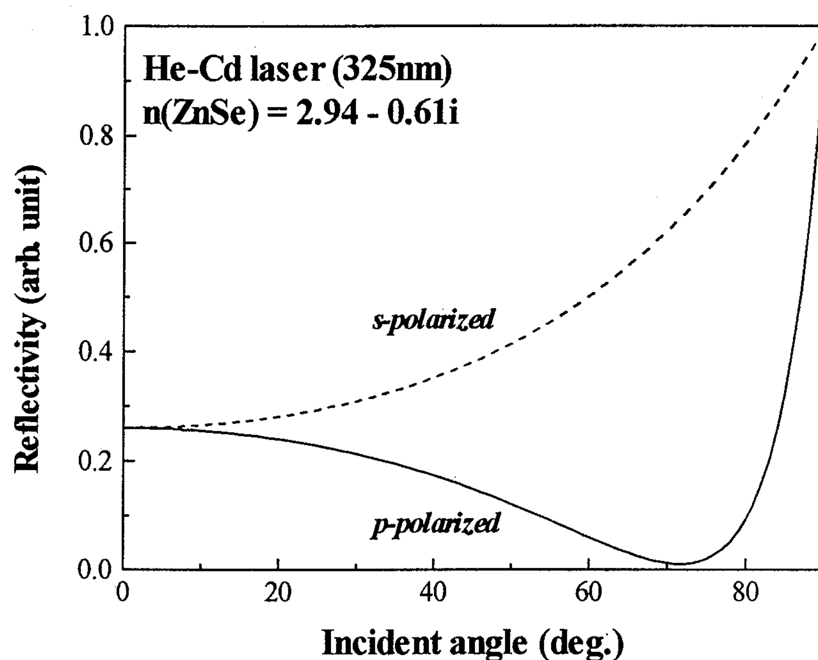

Figure. 3-19 The calculated reflectivity of ZnSe crystal for s- and p-polarized light from Eqs. (2-5)~(2-7). The refractive index of ZnSe is *n=2.94-0.61i*.

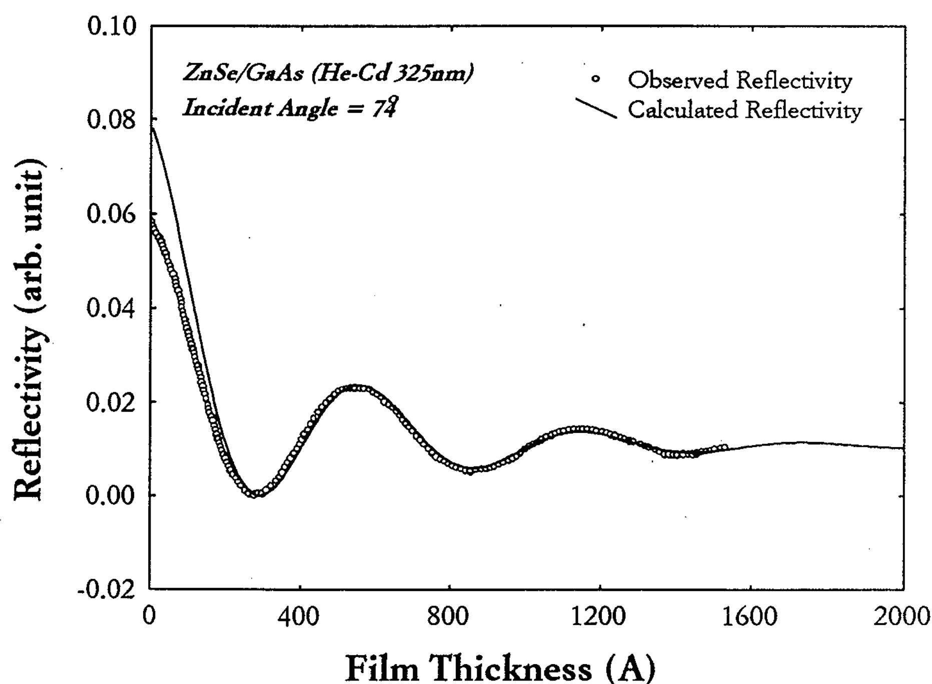

Figure 3-20 Typical reflectivity spectrum observed in the SPA measurement during ZnSe growth.

observed. The reflectivity from heteroepitaxial layers can be calculated in the following way. The difference in the light path of multiple internal reflections is given by

$$2\Delta_{11} = \frac{4\pi d n \cos\theta_1}{\lambda}, \tag{3-1}$$

$$2\Delta_{12} = \frac{4\pi d \kappa \cos\theta_1}{\lambda}, \tag{3-2}$$

where d, n, κ and λ indicate the film thickness, refractive index, extinction coefficient and the wavelength of light, respectively. The incident angle of θ_1 indicates the light angle in ZnSe layers, and can be obtained from the Snell's law of Eq. (2-7). The oscillator strength of the multiple internal reflection is expressed by

$$r = \frac{r_{01} + r_{12}\exp(-2\Delta i)}{1 + r_{01} r_{12}\exp(-2\Delta i)}, \tag{3-3}$$

where r_{01} indicates the reflection at the interface between vacuum and ZnSe, and r_{12} indicates the reflection at heterointerface of ZnSe/GaAs. The values of r_{01} and r_{12} are given by Fresnel' law. The resulting reflectivity is given by

$$R = rr^* = \frac{R_{01}e^{2\Delta 12} + R_{12}e^{-2\Delta 12} + 2\sqrt{R_{01}R_{12}}\cos(2\Delta_{11})}{1 + R_{01}R_{12}e^{-2\Delta 12} + 2\sqrt{R_{01}R_{12}}\cos(2\Delta_{11})}, \tag{3-4}$$

where $R_{01}=r_{01}r_{01}^*$ and $R_{12}=r_{12}r_{12}^*$. The result calculated from Eq. (3-4) is also shown in Fig. 3-20. The refractive index for GaAs substrate is taken as 3.4-$1.8i$ for this calculation.[25] The good agreement is seen between the observed and calculated reflectivity, as shown in Fig. 3-20. The observed reflectivity, however, shows the reduction at the initial stage of the crystal growth. This effect could be induced by a contamination or a rough GaAs surface. In a region where a fringe is dominated, a phase shift causes the change in the SPA signal intensity. In order to suppress the phase effect, the SPA signal was mainly determined from the value when the thickness of the ZnSe films exceeds 160 nm. The conditions used here are summarized

in Table 3-3.

Table 3-3 The experimental conditions for the SPA

Laser	He-Cd laser (325 nm)
Laser power	0.1 mW/cm^2
Incident angle	74°
Film thickness	over 160 nm

3.3.2 Flow rate dependence of source gases

In order to determine the HRCVD growth mechanism of ZnSe crystal, the SPA signals were measured as a function of growth parameters, including pulse durations and flow rates. First of all, we observed the changes of the SPA signals over the pulse duration for each of the II and VI group surfaces.

Figure 3-21 shows the SPA signal intensities for different pulse durations (T_{Se}=1~7 sec) after DEDSe are supplied. The gas flow sequences are also shown in this figure, together with the flow rate of the source gases. As shown in the figure, after the supply of DEDSe source, a rapid increase in the SPA signal intensity can be seen in all cases. In addition, the SPA signals show a saturation between 2~7 sec. At this growth condition, the growth rate of ZnSe also shows a saturation corresponding to a monolayer per cycle, as shown in Fig. 3-22. In this figure, the growth rate of ZnSe crystals was obtained by SEM examination of a cleaved sample. From these results, it was evident that the self-limiting growth was achieved. Also the observation of the growth can be made by the SPA. Moreover, when DEDSe is supplied for the much longer time after the end of crystal growth, the saturation of the SPA signal on Se covered surface was maintained for over 30 sec. Accordingly, the self-limiting reaction of Se atoms on the growing surface is considered to be very stable. In the PL spectra of these crystals grown under the various pulse durations, all the crystals show the prominent band- edge emission with suppressed deep level emission and also no remarkable differences in the PL spectra. Above evidences imply the extremely high selectivity of chemical reaction of Se atoms on Zn covered surface, which provides the growth of high-quality crystals.

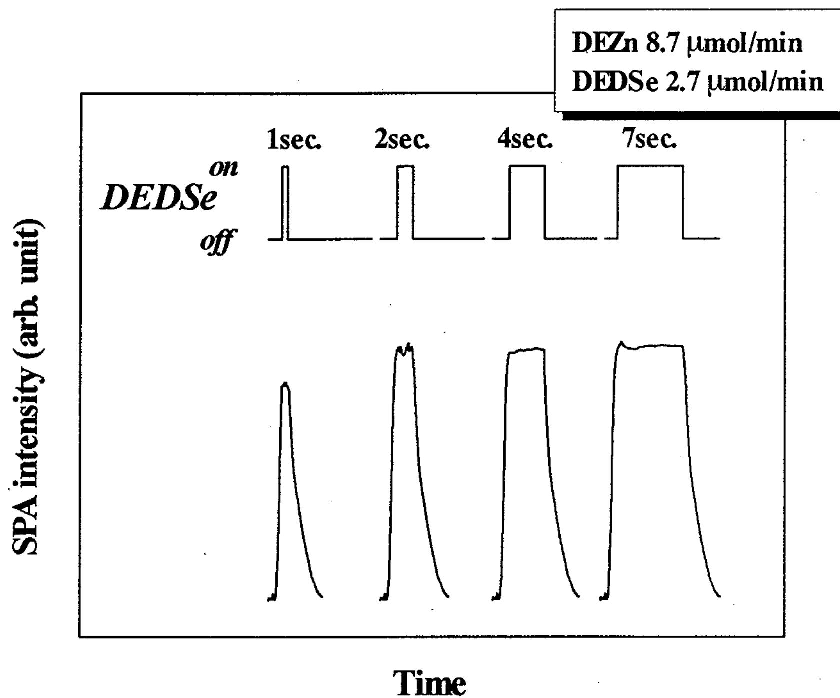

Figure 3-21 The SPA signal intensities for the different pulse durations (T_{Se}=1~7 sec) after DEDSe is supplied. The gas flow sequences are also shown in this figure, together with the flow rate of the source gases.

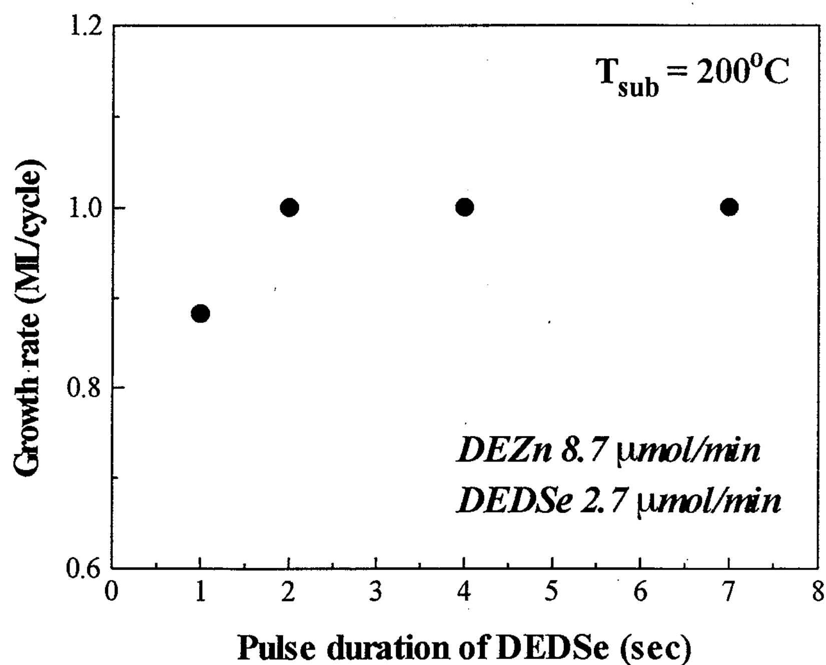

Figure 3-22 The growth rate of ZnSe plotted as a function of the pulse duration of DEDSe. The flow rates of the source gases are also indicated.

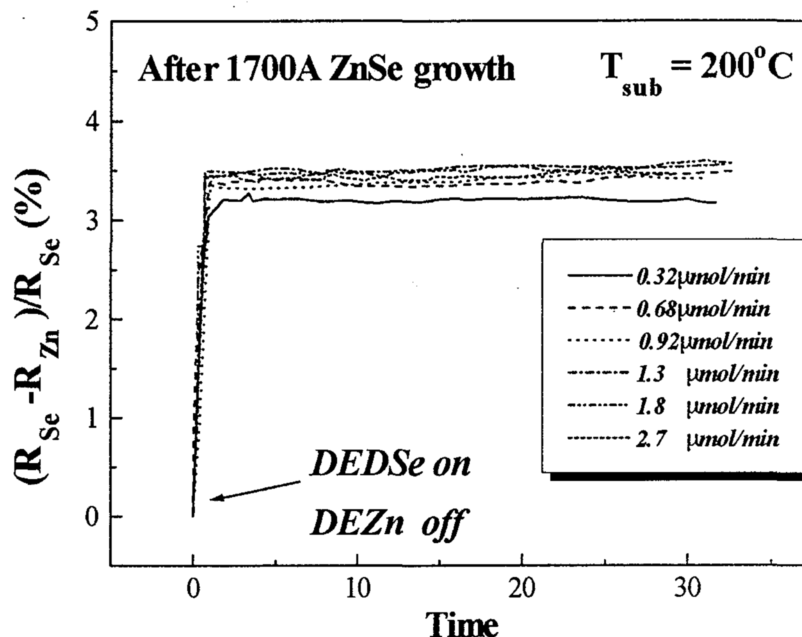

Figure 3-23 The SPA signal intensities of ZnSe crystals for the different flow rate of DEDS. These signals were measured after the growth of conventional ZnSe crystals.

Figure 3-23 shows the SPA intensities of ZnSe growth as a function of time for the various DEDSe flow rates (0.32~2.7 μmol/min). In order to determine the long pulse duration effects, these SPA signals were measured after the growth of ZnSe (~1700Å) by the conventional growth conditions. In this case, the flow rate of DEDSe was maintained at 2.7 μmol/min. As shown in Fig. 3-23, the saturation of the SPA signals is also seen under all the flow conditions except for the lowest flow rate of 0.32 μmol. All Se stabilized surfaces are maintained for over 30 sec, suggesting the ideal self-limiting growth of Se layers.

Figure 3-24 shows the growth rate of ZnSe crystals for the different flow rates of DEDSe when the pulse duration was kept at 4-0-4-1 sec (T_{Se}-$T_{Se,int}$-T_{Zn}-$T_{Zn,int}$; see p.31). As mentioned above, the effect of the pulse duration is negligible in this case. A clear saturation of the growth rate of ZnSe can be observed over a wide range of the DEDSe flow rate. From this results, the minimum flow rate for Se monolayer coverage is estimated to be 0.32 μmol/min, and the growth rate does not depend on the flow rate at values greater than this. A good correlation between the SPA signals and the

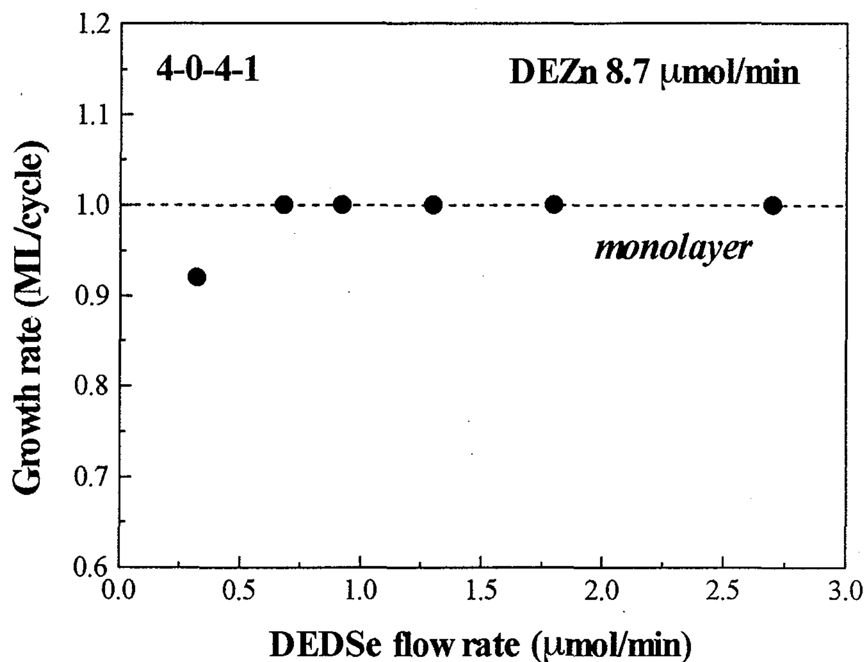

Figure 3-24 The growth rate of ZnSe crystals for the different flow rates of DEDSe when the pulse duration was kept at 4-0-4-1 sec.

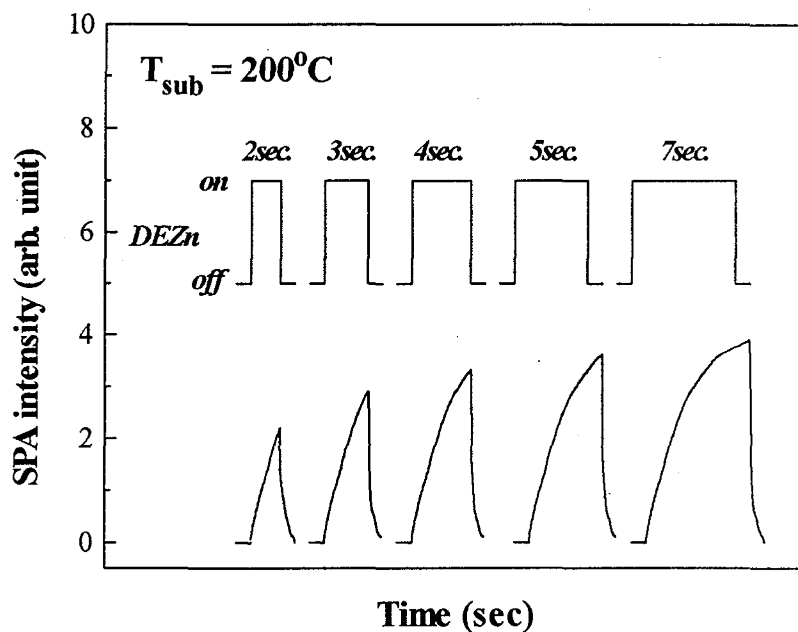

Figure 3-25 The SPA signal intensities plotted as a function of the pulse duration of DEZn (T_{Zn}=2~7 sec). The gas flow sequences are also illustrated in the figure.

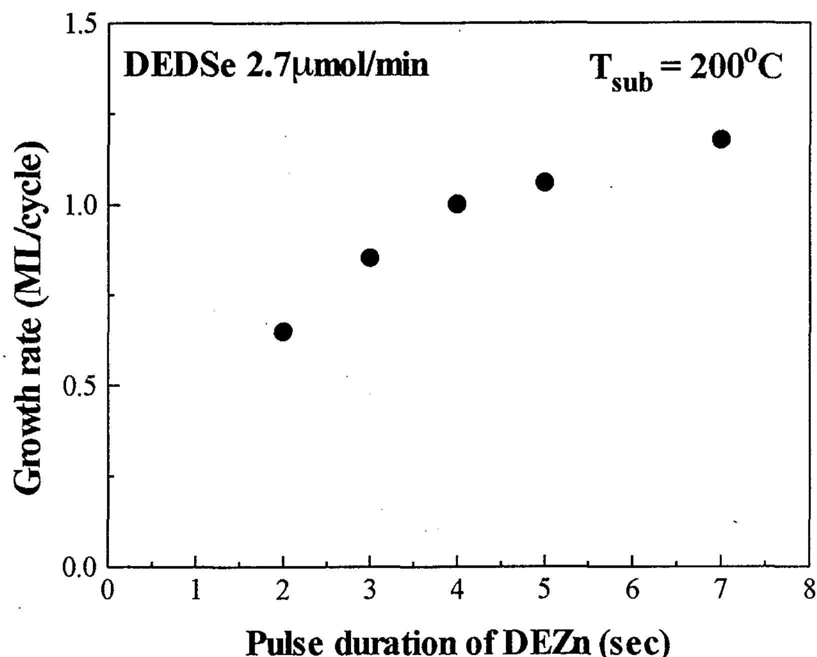

Figure 3-26 The growth rate of ZnSe crystals plotted as a function of the pulse duration of DEZn (T_{Zn}=2~7 sec).

growth rates indicates one of the usefulness of the SPA measurement. The growth reaction of Zn covered surfaces could also be determined from the SPA signal dependence on the DEZn flow rate. Figure 3-25 shows the SPA signal intensities plotted as a function of the DEZn pulse duration (T_{Zn}=2~7 sec). The gas flow sequences are also illustrated in the figure. In this measurement, the DEDSe pulse duration was held constant (T_{Se}=4 sec) with a flow rate of 2.7 μmol/min. In this figure, the SPA signals were reversed corresponding to that of Fig. 3-21 are shown, since the decrease in the SPA signal intensities indicates the increasing Zn covered surface. As shown in Fig. 3-25, compared with the DEDSe SPA signal, a large difference can be seen in behavior of the SPA signal intensities for DEZn. The SPA signal intensities increase with increasing pulse duration of DEZn, and the self-limiting growth was not observed in Zn covered surfaces. In addition, the layer formation of Zn precursors is obviously slow compared with that of Se precursors.

Figure 3-26 shows the growth rate of ZnSe crystals plotted as a function of the DEZn pulse duration. The growth rate of ZnSe gradually increased as the DEZn pulse duration increased, which agreed well with the observed

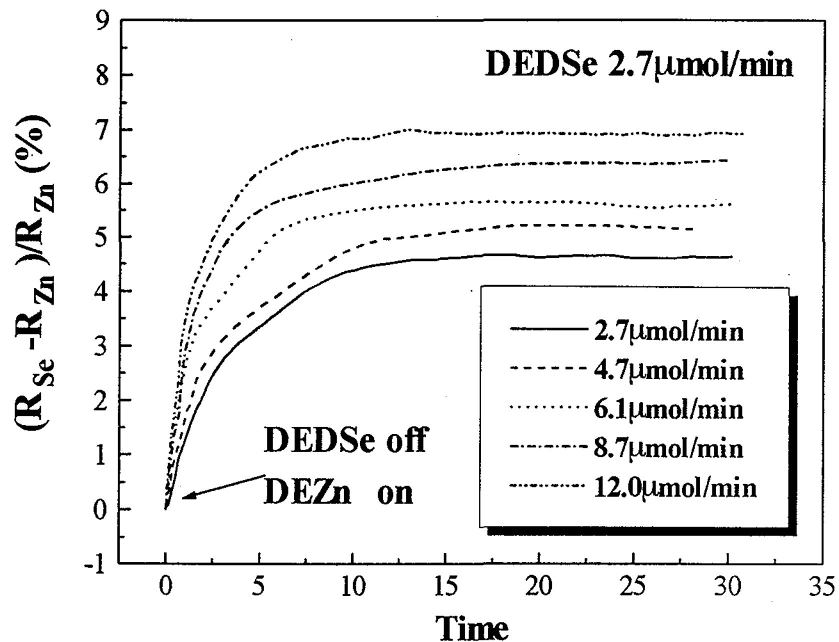

Figure 3-27 The SPA signal intensities for the different flow rate of DEZn (2.7~12 mmol/min). The reversed SPA signal intensities are shown in this figure. These SPA signals were measured after ZnSe growth.

behavior in the SPA signal intensities. As a result, the growth rate of Zn surface can be also observed by the SPA measurement. In contrast to Se covered surfaces, self-limiting action was not observed in this case. The change of the growth rate, however, slightly reduces after the growth rate of ZnSe exceeds monolayer. Accordingly, the layer formation of Zn precursors could be reduced after the surface is completely covered with Zn atoms.

Figure 3-27 shows the SPA signal intensity as a function of the DEZn flow rate (2.7~12 μmol/min). This figure also shows the results which were measured after ZnSe crystal growth by the conventional conditions. As shown in this figure, the saturation of the SPA signal intensity occurs at pulse durations ~15 sec, and does not have a flow rate dependence. The saturated level of the signal increases as the flow rate of DEZn increases, indicating the flow rate limited growth of Zn covered surface. The growth rate as a function of the DEZn flow rate is shown in Fig. 3-28. In this case, the sequence for the growth was kept at 4-0-15-0 sec, in order to compare the measured and SPA growth rates. The observed growth rate shows the

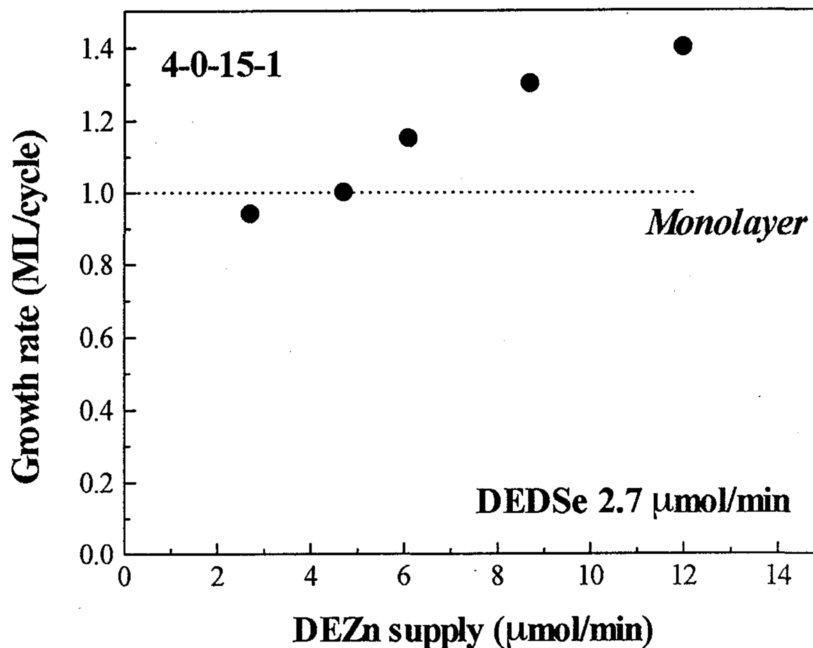

Figure 3-28 The growth rate of ZnSe crystals plotted as a function of the flow rate of DEZn. The pulse duration was kept at 4-0-15-1.

good agreement with the relative SPA. Therefore, the SPA signal changes are proportional to the thickness of the surface layers, as expressed by Eq. (2-11). The growth rate, however, indicates the saturation at about 1.4 ML/cycle, which is not understand well at the present stage. Nevertheless, the monolayer growth of ZnSe was achieved when the flow rate of DEZn was maintained to 4.7 μmol/min. At this flow rate, the constant growth rate can be obtained for the DEZn pulse duration for over 15 sec.

As mentioned above, the self-limiting growth of Zn covered surface was not observed in the SPA measurement for the flow rate dependences, although the self-limiting reactions of Zn surface are reported in MOVPE using DMZn or DEZn.[35,36)] Previously, we observed the self-limiting growth of Zn covered surface when the pulse duration was changed.[37)] Figure 3-29 shows the growth rate of ZnSe crystals plotted as a function of the pulse duration of DEZn. In this figure, the results obtained from the different interval after Zn source supply (T_{int}(Zn)) are also shown. On Se covered surface, the clear self-limiting growth is seen in Fig. 3-29. In addition, this growth rate does not show any difference when the time interval after Se source supply was changed. In contrast to Se surface, a

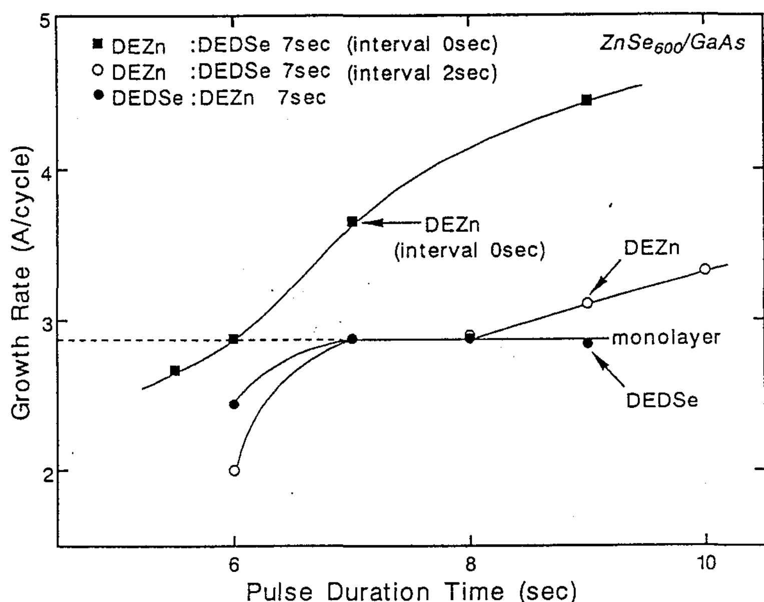

Figure 3-29 The growth rate of ZnSe crystals plotted as a function of the pulse duration of DEZn and DEDSe. The results obtained from the different interval after Zn source supply are also shown in the figure.

large difference can be seen in the growth rate of ZnSe as T_{int}(Zn) is increased from 0 to 2 second. As shown in this figure, the constant growth rate was observed between 7 and 8 sec when T_{int}(Zn) is 2 sec. The growth rate, however, increases gradually beyond 8 sec. Obviously, there is no self-limiting growth of ZnSe when the interval was not provided. This discrepancy can be explained by the etching effect of atomic hydrogen at the growing surface. The mixing of the source gases in the supply system must be the another reason for this. Accordingly, it is expected that the self-limiting growth can be also achieved on the Zn covered surface by adjusting the interval time. Nevertheless, when the time interval after DEZn supply was varied in the SPA measurement, the self-limiting of Zn surface was not observed. The change of the plasma condition could be the reason that the self-limiting growth has not been observed in this experiment.

3.3.3 Growth temperature dependence

The growth rate dependence on crystal growth temperature provides the important knowledge about an adsorption-desorption process of the

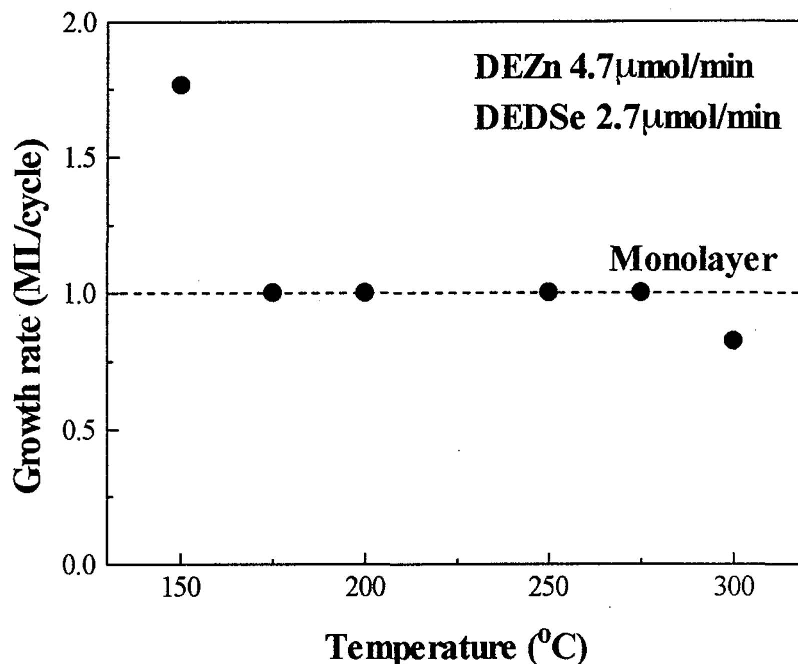

Figure 3-30 The growth rate of ZnSe crystals plotted as a function of the growth temperature.

precursors on the growing surface. In this section, the ZnSe SPA signals for various growth temperatures is investigated. The pulse duration and the DEZn flow rate are kept at 4-0-15-0 and 4.7 μmol/min, at which a constant growth rate of 1 ML/cycle can be maintained.

Figure 3-30 shows the growth rate of ZnSe crystal grown at various growth temperatures (T_{sub}=150~300°C). A clear indication of the self-limiting growth at a monolayer can be seen in the substrate temperature range from 175 to 275°C. In the high temperature region (T_{sub}>275°C), however, the reduction in the growth rate was observed, while increased growth rates was found at lower temperature (<150°C). Usually, the crystal growth rate is expected to increase with increasing substrate temperature, if the metalorganic decomposition is the rate-limiting process. On the other hands, HRCVD uses chemically active precursors to deposit and etch the film forming species. Instead of the decomposition process, therefore, the adsorption (or desorption) process becomes the rate-determing step in HRCVD. Consequently, it can be understood that the increased growth rate at low temperature is caused by the low desorption rate of precursors from the crystal surface, while high-temperatures growth enables much

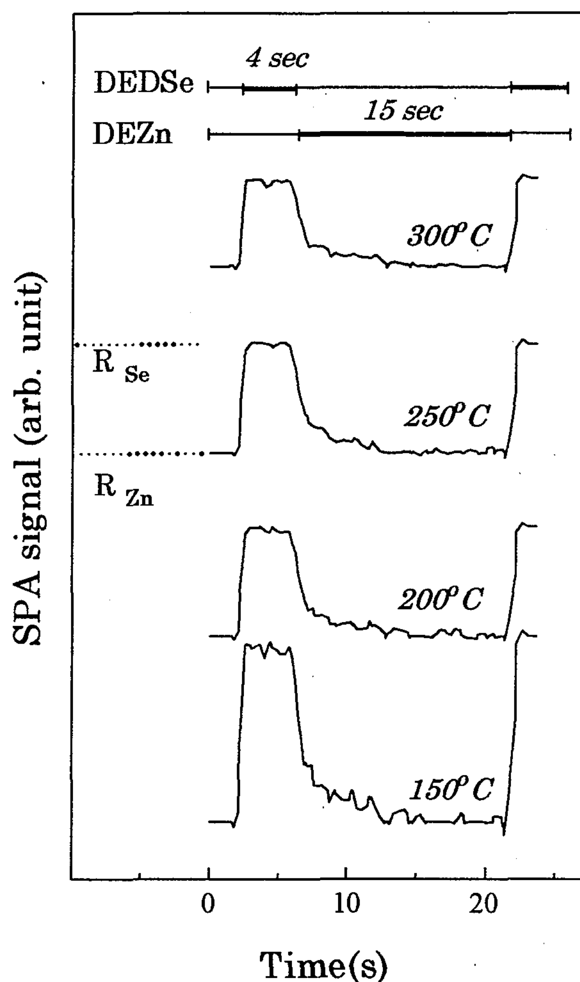

Figure 3-31 The SPA signal intensities dependence on the growth temperature of ZnSe crystals. The gas supply sequences of DEZn and DEDSe are also illustrated in the figure.

easier desorption of precursors from the surface, which leads to growth rate reductions. Se-precursors could be responsible for the growth rate reduction at higher temperatures, since Se atoms have the higher vapor pressure than Zn atoms.

Figure 3-31 shows the SPA signal intensities versus time for several growth temperatures. The gas supply sequences of DEZn and DEDSe are also indicated in the figure. In this SPA measurement, the substrate temperature was changed after ZnSe crystals were grown at a temperature of 200°C. As shown in Fig. 3-31, the same SPA signal intensities are seen at substrate temperatures between 200~250°C, where the self-limiting growth can be observed. At a substrate temperature of 300°C, the reflectivity difference (R_{Se}-R_{Zn}) becomes small, corresponding to the growth rate

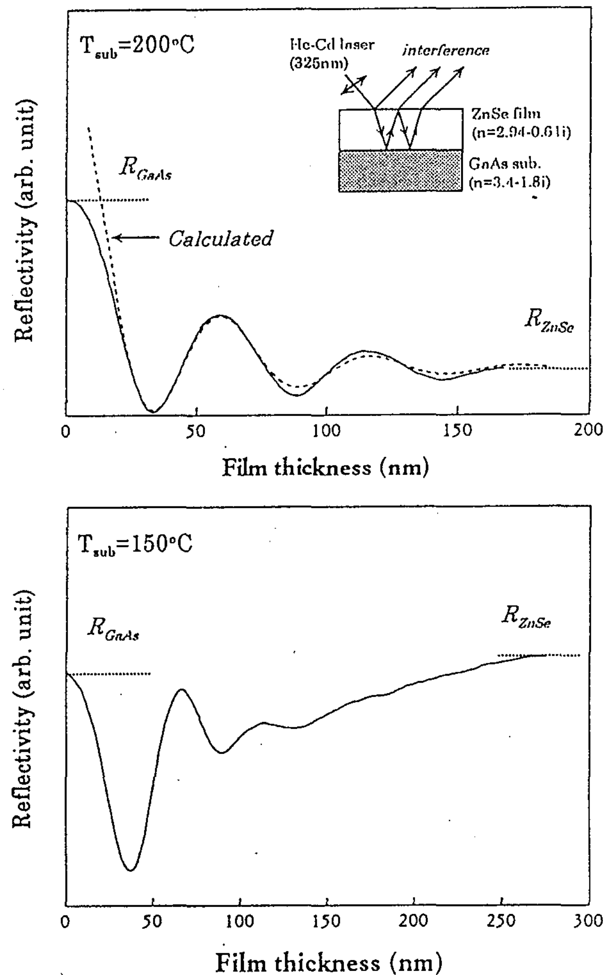

Figure 3-32 The reflectivity of ZnSe crystals at 150 and 200°C potted as a function of the film thickness. The calculated reflectivity is also indicated in the crystal grown at 200°C.

reduction. However at low growth temperature (150°C), the SPA signal intensity indicated increased film thickness per cycle. The SPA signals again showed good agreement with the actual growth rate for the temperature change. Nevertheless, the changes of desorption (or adsorption) processes over the growth temperature were not observed by SPA measurement probably due to the narrow temperature range of this experiment.

When the growth temperature of ZnSe crystal was kept constant, the SPA signals show the specific behavior at low temperatures. The reflectivities of ZnSe crystals grown at 150 and 200°C are plotted as a function of the film thickness in Fig. 3-32. The reflectivity of ZnSe agreed well with the calculated reflectivity at 200°C, as shown in Fig. 3-32. At 150°C, however,

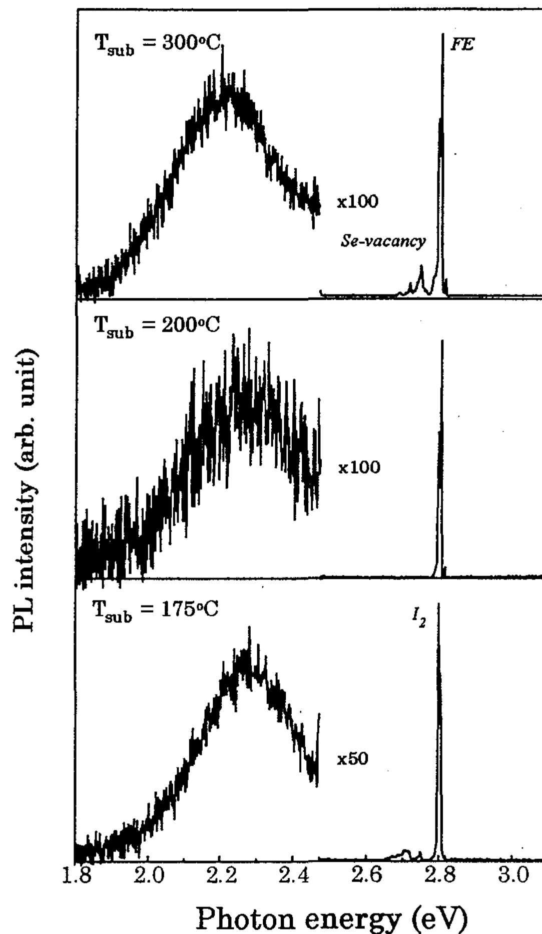

Figure 3-33 The PL spectra of ZnSe crystals grown at the differentsubstrate temperature. The temperature of the PL measurement was kept at 25K.

the large difference can be seen in reflectivity of ZnSe crystals; this ZnSe reflectivity increases with film thickness. In addition, the SPA signal intensity decreases and does not correspond to the growth rate of the crystal at the low substrate temperature. The SEM scans indicated the rough surface in these cases with surface roughness of ~1000Å. This may be explained by the suppressed surface migration or increased sticking coefficient of the precursors at the low substrate temperature. It is suggested that increased film reflectivity at low temperature is caused by anomalous light scattering of the rough surface. As a result, it is evident that the SPA is sensitive to surface morphology.

Figure 3-33 shows the PL spectra of ZnSe crystals grown at the different substrate temperatures. All the samples show the predominant free exciton emissions, indicating high crystal quality. These assignments of free

exciton emissions are made from the reflectivity spectra. In addition, the emission intensities of the deep level are quite low compared to the band-edge emission intensity.

The sample grown at the low temperature (T_{sub}=170°C), however, shows the increased donor bound exciton emission, perhaps due to incomplete desorption of impurity atoms. The slightly increased deep-level emission could also be observed in this sample. In contrast to this, a new emission peak at 2.75 eV was seen in the sample grown at 300°C. The second emission from this peak is LO-phonon replica of this new peak. This emission has been assigned to the Se-vacancy.[35)] Consequently, it can be understood that the high substrate temperature enhance the desorption of Se atoms from the crystal growing surface. At high substrate temperatures (300°C), the FWHM of the x-ray rocking curve shows a broadened diffraction peak (~200 arcsec) compared with the sample grown at 200°C (~100 arcsec), due to the thermoelastic strain effects.[36-38)] The crystals grown at low temperature (T_{sub}<200°C) also indicate the degraded crystal quality, which is induced by the rough surface morphology of the crystal, since the rough surface morphology induces the inhomogenuous strain fields. As a result, the growth temperature of 200°C is considered to be the ideal substrate temperature for the growth of high-quality ZnSe crystals.

3.4 Growth mechanism of ZnSe by HRCVD

As have been discussed in previous sections, HRCVD growth process can be divided into two categories; source gas decomposition and surface reaction kinetics. Some fundamental characteristics of ZnSe crystals grown by this technique such as the structure and optical properties as determined by XRD and PL will be considered in this section. In the following section, the overall growth mechanism of ZnSe in ALE by HRCVD for each of group II or VI surfaces is summarized. In particular, the roles of atomic hydrogen on the ZnSe crystal growth are emphasized.

3.4.1 Fundamental characteristics of ZnSe grown by HRCVD

To examine the crystal structure, XRD techniques were used. A typical XRD spectrum of ZnSe crystal grown on GaAs by ALE is shown in Fig. 3-34. The growth conditions for this ZnSe crystal film are listed in Table 3-2 (substrate temperature: 200°C). As seen in this figure, there is a sharp (400) diffraction peak associated with ZnSe, and also seen is the (400) diffraction peak of GaAs substrate. The FWHM of ZnSe diffraction peak determined from the X-ray rocking curve is 101 arcsec, indicating that the ZnSe crystal is highly oriented.

Note that the ZnSe crystal and the GaAs substrate have the different lattice parameters. As a result, the lattice parameter of ZnSe crystal is influenced by the substrate strain. Critical thickness of the film is defined as the thickness at which dislocations are generated in the film due to strain produced by the lattice mismatch with substrates. The film thickness of this crystal was 1700Å, which corresponds to the critical thickness of ZnSe on GaAs.[36] Consequently, the coherent growth of ZnSe crystal is expected at film thickness less than this thickness. The lattice parameter perpendicular to the surface of crystals grown on lattice mismatch substrates is calculated by the following equation assuming biaxial strain,[36]

$$a^* = a_0 + \frac{c_{11} + 2c_{12}}{c_{11}}(a - a_0), \qquad (3\text{-}5)$$

where a_0 and a are lattice constants of substrate and bulk ZnSe, respectively,

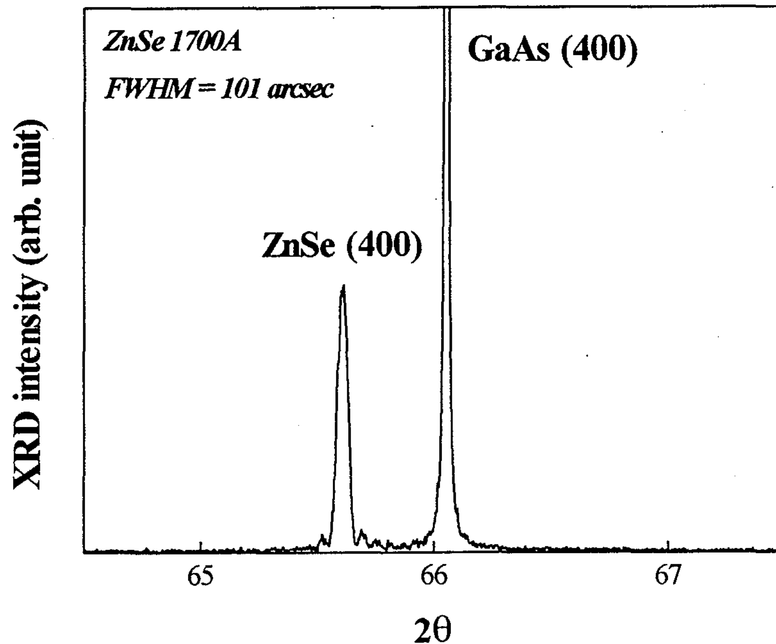

Figure 3-34 Typical XRD spectrum of ZnSe crystal grown by HRCVD using ALE.

and c_{11} and c_{12} are the elastic stiffness constants of ZnSe. The values of the elastic stiffness constants of ZnSe are taken as c_{11}=8.10x10^{11} dyn/cm^2 and c_{12}=4.88x10^{11} dyn/cm^2.[39] The calculated lattice parameter of ZnSe crystals using Eq. (3-5) is 5.687Å, which agrees well with the observed value of 5.685Å.

Figure 3-35 shows typical PL spectrum of ZnSe crystal grown using the same growth conditions. The fine structure of the emission lines, attributed to the exciton, is illustrated in the inset together with the optical reflectivity spectrum in the near band-gap region. As shown in the spectrum, the band edge emission is dominant and the emission from deep levels is suppressed. The deep level emission intensity at 2.3 eV, which we have tentatively attributed to the Zn vacancies[40], is more than a hundred times weaker than the intensity of the band edge emission. The pair of emission lines at the higher energies are assigned to the free excitons, FE(lh) (light holes) and FE(hh) (heavy holes), respectively, and corresponding reflectivity peaks are clearly observed. This assignment has also been confirmed by the temperature dependence of the PL spectra. The compressive strain in the grown layer due to the lattice mismatch with GaAs substrate is responsible

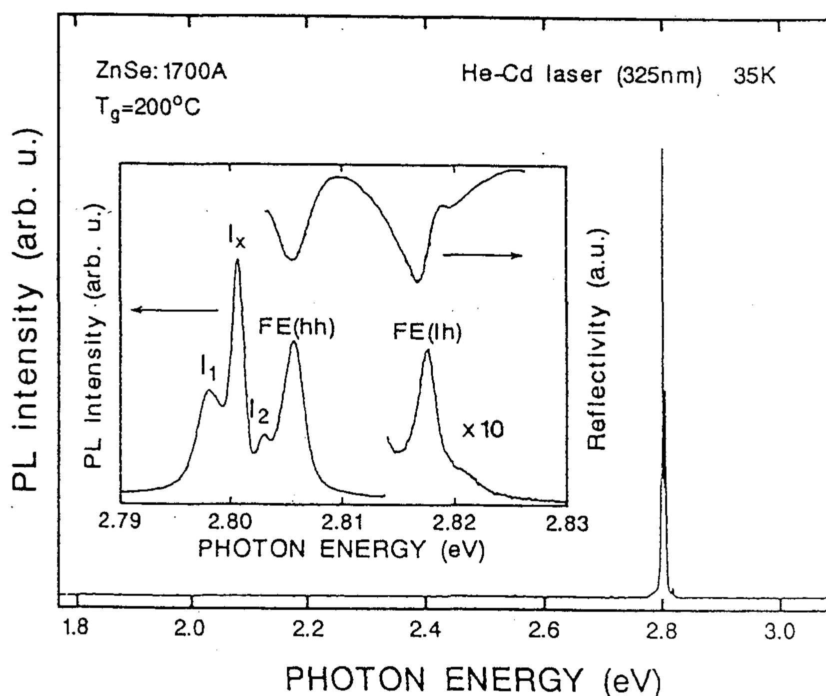

Figure 3-35 Typical PL spectrum of ZnSe crystal grown at 200°C and measured at 25K. The inset shows the enlarged PL and reflectivity spectrum near the band-gap region.

for splitting the FE peaks[41], as will be discussed in detail in chapter 4.

The widths (FWHM) of FE(lh) and FE(hh) peaks are very narrow (2.0 and 1.9 meV, respectively). This is a clear evidence that ZnSe crystal has high quality, compared with the crystals obtained by other growth methods.

These XRD and PL results indicate that highly ordered crystals with low defect densities can be prepared by HRCVD. The low temperature growth (200°C) used for HRCVD growth is one reason for such high crystallinity, since low temperature growth reduces the thermoelastic strains at heterointerfaces due to thermal expansion mismatch between the film and substrate.[37]

3.4.2 Crystal growth mechanism of ZnSe by HRCVD

In this section, crystal growth mechanisms are discussed from the results obtained by QMS and SPA measurements depending on Se- or Zn-covered surfaces, respectively. Figure 3-36 shows a growth model for ZnSe on Se-covered surface. As confirmed by QMS, the reactive Se-precursor is determined to be Se-C_2H_5 radical, which is created by chemical reactions

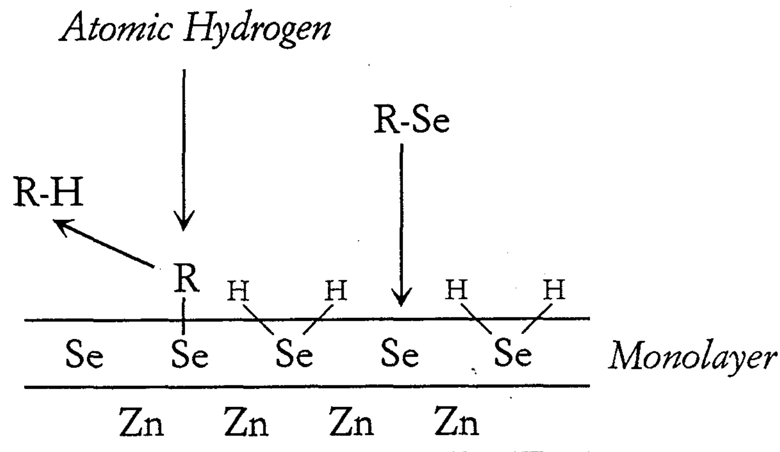

Figure 3-36 A growth model of ZnSe crystal on Se-covered surface

with atomic hydrogen. The thermal DEDSe decomposition on the growth surface is negligible, since this thermal decomposition requires much higher substrate temperature (T_{sub}>500°C). SPA analysis is consistent with this precursor having higher sticking coefficient on the Zn-covered surface, and the monolayer formation of Se atoms is completed within 2 sec under typical growth conditions. The surface reaction of Se atoms on the growing surface automatically stop after a monolayer is deposited, and adsorption of additional Se atoms on this *Se-covered surface* does not occur under the condition investigated here. In other words, this Se-covered surface is stable with respect to the desorption or adsorption process. These facts could be explained in terms of the existence of hydrogen atoms bonding with Se atoms on the surface (as shown in Fig. 3-36). Therefore, surface hydrogen atom prevent the adsorption of excess Se atoms. Such hydrogen atom termination of surfaces was previously reported in ZnSe crystal growth using MOMBE system.[42)] Moreover, the termination of dangling bonds by hydrogen atoms have been confirmed on GaAs and Si surfaces using RHEED.[43,44)] These results support this speculation that the self-limiting growth can be achieved through the hydrogen termination on the surface.

Figure 3-37 shows a growth model of ZnSe crystal on Zn-covered surface. The precursor for the formation of Zn surface is considered to be Zn-C_2H_5 radicals, as shown in chapter 3.2.2. Similar to DEDSe, the thermal decomposition of DEZn on the crystal surface is negligible at the growth temperatures used in this work (~200°C). In contrast to Se-precursors, the sticking coefficient of Zn-precursors is quite low, and the growth rate

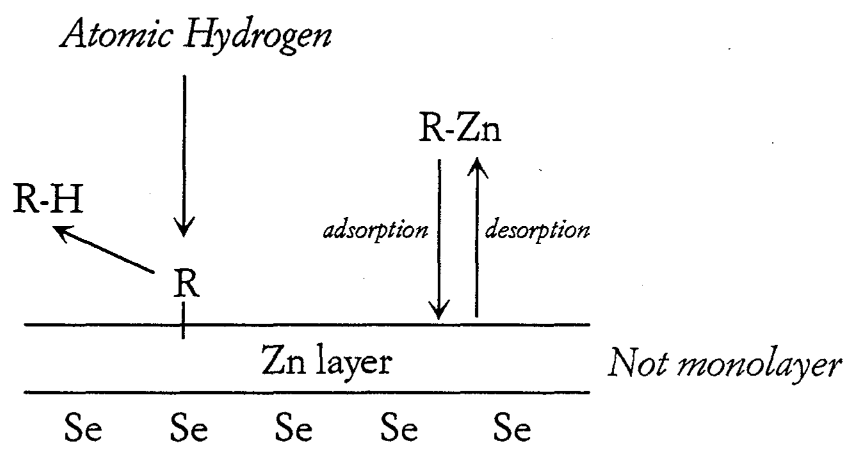

Figure 3-37 A growth model of ZnSe for Zn-covered surface

saturation of the Zn-covered surface can be seen to increase over the pulse duration (15 sec). Low chemical reactivity of Zn-precursors or the hydrogen atom termination on Se-covered surface might be responsible for such a slow adsorption rate of Zn-precursors. In addition, only the weak self-limiting reaction has been observed in Zn-covered surfaces. This effect could be caused by the weak interaction between Zn and hydrogen atoms since Zn atom does not have enough orbitals to form stable bond with atomic hydrogen on the surface. As a result, the growth rate of Zn surface depends on the flux rate of the source molecules. The growth rate of Zn-covered surface is, therefore, determined from the adsorption-desorption equilibrium.

From secondary ion mass spectroscopy (SIMS) measurements, it was found that a hydrocarbon incorporation into ZnSe crystal is under the detection limit of SIMS measurement ($<10^{16}$ cm^{-3}). Therefore, the ethyl radicals of DEZn and DEDSe must be efficiently removed by chemical reactions with atomic hydrogen, as illustrated in Figs. 3-36 and 3-37. At this stage, however, it is unclear that these ethyl radicals are removed by gas phase or surfaces.

As mentioned above, the hydrogen radical plays many important roles in HRCVD growth. Figure 3-38 illustrates a possible model for these atomic hydrogen roles. Needless to say, the decomposition of the source molecules by atomic hydrogen is an essential part of HRCVD growth. In addition to this, it was suggested that the hydrogen termination on Se-covered surface enhances the self-limiting reaction in ALE. In fact, enhanced 2-dimensional growth may be induced by atomic hydrogen

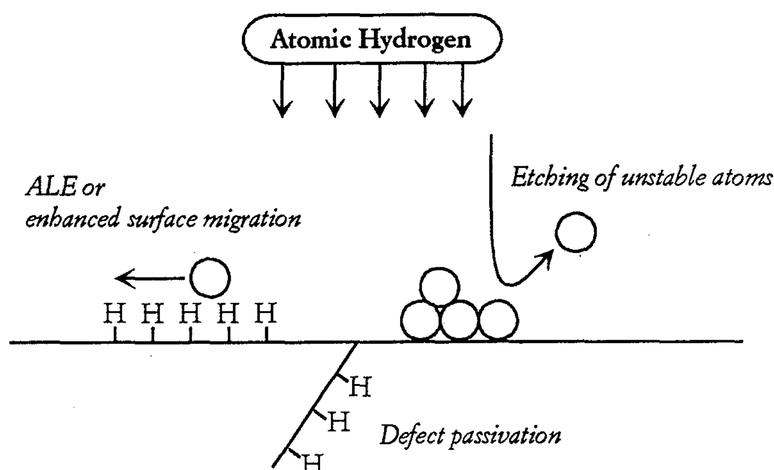

Figure 3-38 A possible roles of hydrogen radical on a crystal surface in HRCVD.

passivation as has been reported in the ZnSe and GaAs cases.[45,46] Especially, the growth of lattice mismatch crystals tends to form clusters on the surface to reduce the chemical potential of the surface areas. When the dangling bonds are passivated by the hydrogen atoms, the chemical potential of the surface can be reduced; thus enhancing the migration of precursors on the crystal surface while suppressing the droplets formation. Similar mechanism can be also applied to ALE growth on a Se-covered surface.

Moreover, III-V semiconductor defect passivation by atomic hydrogen has been reported.[47,48] In II-VI crystals, the passivation of acceptor dopants by atomic hydrogen induced a serious problem in p-type ZnSe crystals.[49] Therefore, it is possible that atomic hydrogen passivates defects in the ZnSe crystals grown by this work. Extremely small defect densities in ZnSe crystal confirmed by the PL analysis also support this idea. Another important role of atomic hydrogen is etching effect. When ZnSe crystals are exposed to the flow of atomic hydrogen, ZnSe crystals can be easily etched away by atomic hydrogen. This indicates that smooth surfaces can be achieved by hydrogen radical etching in HRCVD, as illustrated in Fig. 3-38.

In summery, the hydrogen radical in HRCVD acts many important parts for the preparation of high-quality ZnSe crystals. These effects are summarized as follows:

1) decomposition of metalorganic source molecules, which leads to the

low temperature growth as low as 200°C,

2) self-limiting growth of ZnSe in ALE mode and also the 2-dimensional growth enhancement by hydrogen termination of surface dangling bonds,
3) defect passivation effects by atomic hydrogen.

As a result, HRCVD is a powerful new technique for the fabrication of II-VI crystals with low defect densities.

Chapter 4

Structure and Properties of Zn(S,Se) Ordered Alloys

Fundamental characteristics of a new artificial layered structures, "Ordered Alloys", are investigated in this chapter. The Zn(S,Se) ordered alloys have a structure in which thin ZnS layers are alternated with ZnSe layers. As a result, dislocation-free epitaxial crystal layers with suppressed compositional fluctuations can be prepared on various substrates by taking advantage of the asymmetric strain effect of ZnS and ZnSe layers. In order to confirm these advantages, we fabricated $(ZnS)_n(ZnSe)_m$ (n=1~4) ordered alloys on GaAs substrate by HRCVD using ALE (section 4-1~4-2). In addition, specific optical properties are expected in the ordered alloys having short-period 2-dimensional structures. In section 4.3, "exciton dynamics" of the ordered alloys is characterized by a systematic study including steady- and transient-state PL and photocurrent measurement. The structure of the ordered alloys are further applied to fabricate "Sawtooth" superlattices (section 4-3). In this structure, larger scale variations in band-gap are introduced by systematically varying the ratio of ZnS and ZnSe thickness. Finally, the photo- and thermal-stability of ionic Zn(S,Se) crystals are investigated in the last part of this chapter.

4.1 Growth of ZnS_xSe_{1-x} alloys by ALE-mode

Before the fabrication of Zn(S,Se) ordered alloys, we first tried to make ZnS_xSe_{1-x} crystals on GaAs (100) substrate in a wide compositional range by inserting single ZnS monolayer between large numbers of ZnSe layers. In this section, structures and properties of these ZnS_xSe_{1-x} crystal layer are considered. These crystals were grown at a temperature as low as 200°C

by HRCVD in ALE-mode using the alternate supply of S and Se source gases. Typical growth conditions for ZnS_xSe_{1-x} are shown in Table 4-1. ZnS_xSe_{1-x} alloys were grown directly on GaAs (100) substrate in ALE-mode. The DEDS and DEDSe pulse ratio required to produce the multilayer crystal ranged from 1:12 to 1:2. The total film thickness was kept constant at 1700Å.

Table 4-1 Typical growth conditions

Flow rate	
DEZn	2.6 μmol/min
DEDS	2.7 μmol/min
DEDSe	1.9 μmol/min
H_2 (plasma)	200 sccm
Pulse Duration (sec)	
ZnSe	7-0-6-2
ZnS	7-0-6-1

4.1.1 Structure of ZnS_xSe_{1-x} crystals

Figure 4-1 shows the lattice parameters (perpendicular to the substrate) plotted as a function of the layer ratio (1/1+m) calculated from the gas pulse ratio, where *m* denotes the number of ZnSe layers. The dotted line indicates the Vegard's law estimated lattice parameter (Eq. (3-5)), assuming that the crystal layers grow coherently. The elastic stiffness constants of II-VI crystals used in the calculation are summarized in Table 4-2.[1-3] As shown in Fig. 4-1, there is a marked discrepancy in the behavior of the lattice parameters between the observed and calculated values. In order to better understand this difference, the sulfur contents of these samples were measured by ICP (induced coupled plasma atomic absorption) analysis. The alloy corresponding to n=8 was found to contain 7 at% (x=0.07). This composition (x=0.07) is in good agreement with the composition calculated from the Vegard's law lattice parameter. Consequently, the practical sulfur content of these alloys is smaller than the value estimated from the pulse ratio. This disagreement between pulse ratio and composition may originate from imperfect ZnS monolayer. For simplicity, the sulfur content used in this section are determined from the Vegard's law lattice parameters,

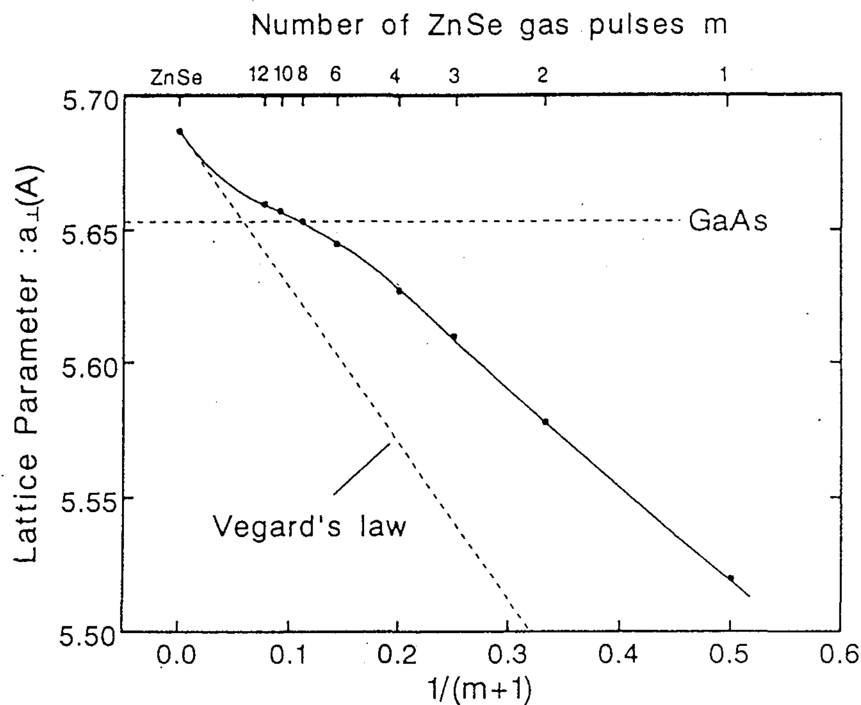

Figure 4-1 The lattice parameter perpendicular to the substrate plotted as a function of 1/(1+m), where *m* indicate the number of gas pulses for the ZnSe growth.

Table 4-2 Elastic stiffness constants and lattice parameter of II-VI crystals

	a (Å)	c_{11}	c_{12} ($\times 10^{11}$ dyn/cm^2)
ZnS	5.4093	10.04	6.50
ZnSe	5.6686	8.11	4.88
ZnTe	6.1037	7.11	4.07

as illustrated by the dotted line in Fig. 4-1. It should be emphasized that the growth condition used to deposit the ZnS monolayers was same as those used to deposit pure ZnS crystal films. Therefore, the thickness difference of ZnS layer in ZnS_xSe_{1-x} implies that the ZnS sticking coefficient is relatively smaller on a ZnSe covered surface compared to a ZnS surface.

Figure 4-2 shows the full width at half maximum (FWHM) of the (400) diffraction peaks obtained from the x-ray rocking curves plotted as a function of the sulfur composition. When the sulfur composition is small ($x<0.15$),

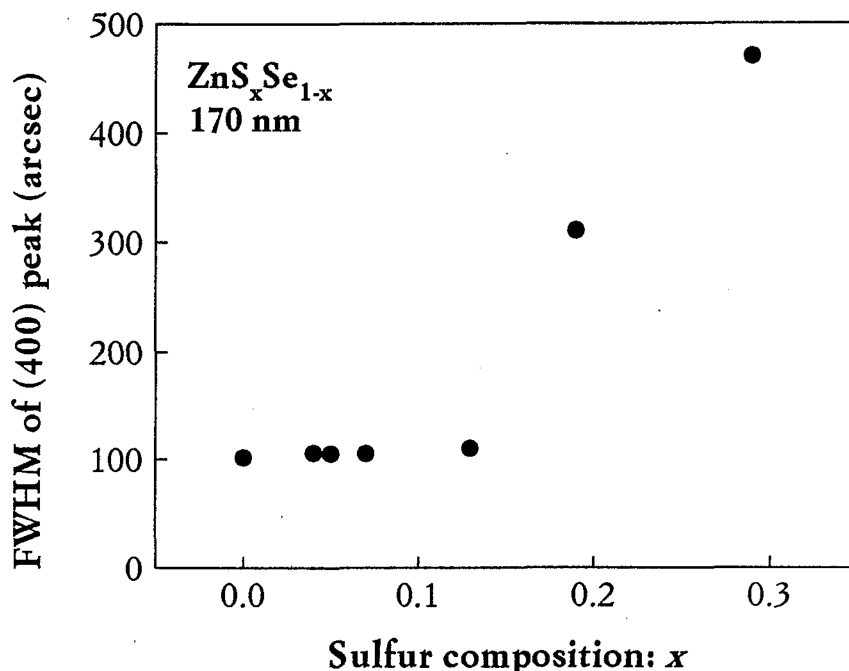

Figure 4-2 The FWHM of the (400) diffraction peaks plotted as a function of the sulfur composition of ZnS_xSe_{1-x} crystals.

sharp diffraction peaks can be seen, indicating the high crystallinity of the grown crystals. It is obvious that the lattice mismatch strain is negligible at this sulfur content because of the thin film thickness (~1700Å). For the x=0.19 and x=0.29 alloys, however, the peak widths became wider; 300 and 500 arcsec, respectively. The lattice matching sulfur composition of ZnS_xSe_{1-x} crystal grown on GaAs is 6 at%. Therefore, the broadening effect in the x=0.19 and 0.29 alloys may be caused by the large lattice mismatch with the substrate (ε=-4.32%). So far, similar XRD peak broadening effects have been observed in ZnS_xSe_{1-x} disordered alloys[4--7]

4.1.2 PL properties of ZnS_xSe_{1-x} crystals

Figure 4-3 shows the PL spectra of the different alloys (x=0.05~0.29) near the band-edge region measured at low temperature. Free exciton emission is seen as sharp emission lines near the band-edges. Note that deep level emission is negligible for all crystals made in this study. These facts imply

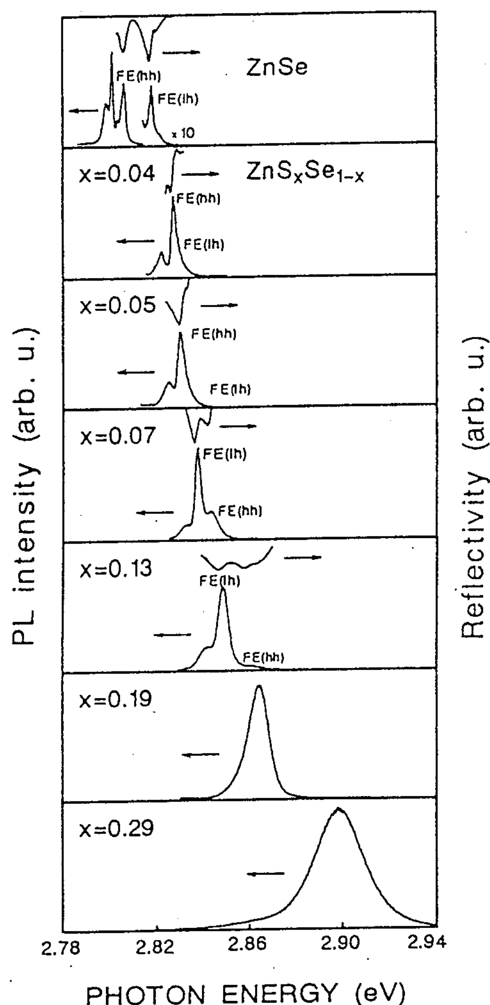

Figure 4-3 The free exciton emission in the PL spectra of the different alloys (x=0.05~0.29) near the band-edge.

that the defect concentrations are low in the alloys fabricated by this technique despite the wide range of compositions. As shown in Fig. 4-3, the energies of the strong PL peaks shift monotonously to higher energies for the alloys with the increasing sulfur content. This indicates that the band-gap is widens smoothly with the increasing sulfur content. In the low S content crystals (x<0.19), the FWHM of free exciton emission lines are as narrow as 2~5 meV. For the higher S content alloys (x=0.19 and x=0.29), however, only the single broad emission line (FWHM=12, 21 meV, respectively) are obtained. The PL results are consistent with the XRD spectra (Fig. 4-2), where the structural deformations result in broad peaks. It should be noted that there is no marked increase in the deep level defect density despite the large mismatch of the lattice parameters between these

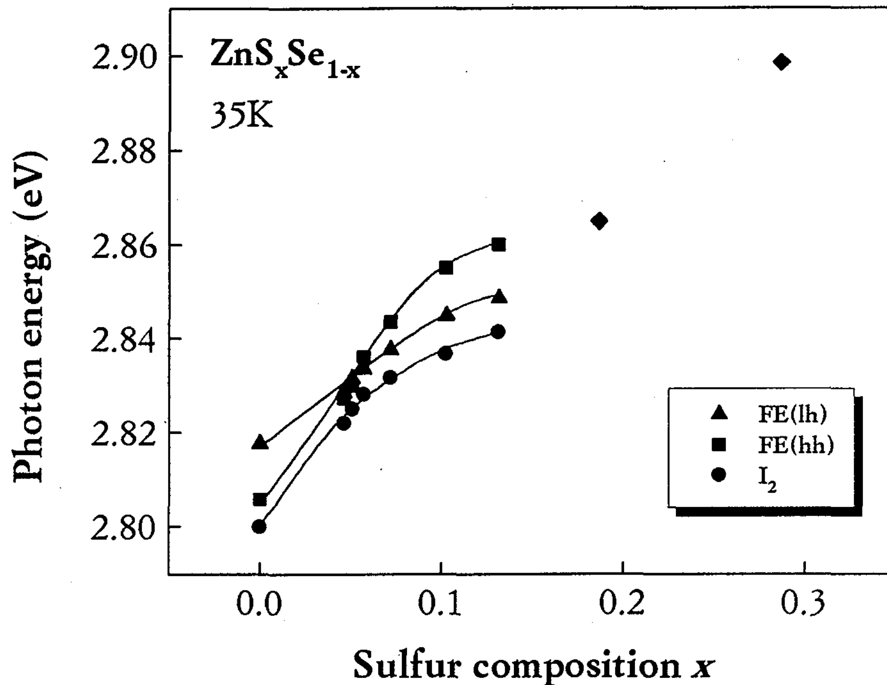

Figure 4-4 The peak energies of the free excitonic emission lines of the different alloys as a function of the sulfur composition.

alloys and the substrate. Consequently, structural deformations must release the strain in these crystals, instead of the formation of defects at the heterointerface.

The FWHM of the PL emission line for ZnS_xSe_{1-x} mixed crystal (x=0.1, 1700Å), fabricated by the simple mixing of the S and Se sources, is 18.6 meV which is six times broader than that of the alloys made by the ALE mode. In addition, we have observed a distinctive increase in the PL intensities of the alloys grown by ALE-mode. These results indicate that the structural fluctuations in these crystal are minimized by the layer-by-layer epitaxy of ZnS-ZnSe layers.

In Fig. 4-4, the peak energies of the PL peaks obtained from the deconvolution assuming Gaussian distribution are plotted as a function of the sulfur content x. The two emission lines at higher energy side are assigned to light-hole free exciton peak (FE(lh)) and heavy-hole peak (FE(hh)) from corresponding reflectivity peaks, as shown in Fig. 4-3. This assignments are also confirmed from the temperature dependence of the PL measurement. The peak position of the donor-bound excitons is also shown as I_2 in Fig. 4-4.

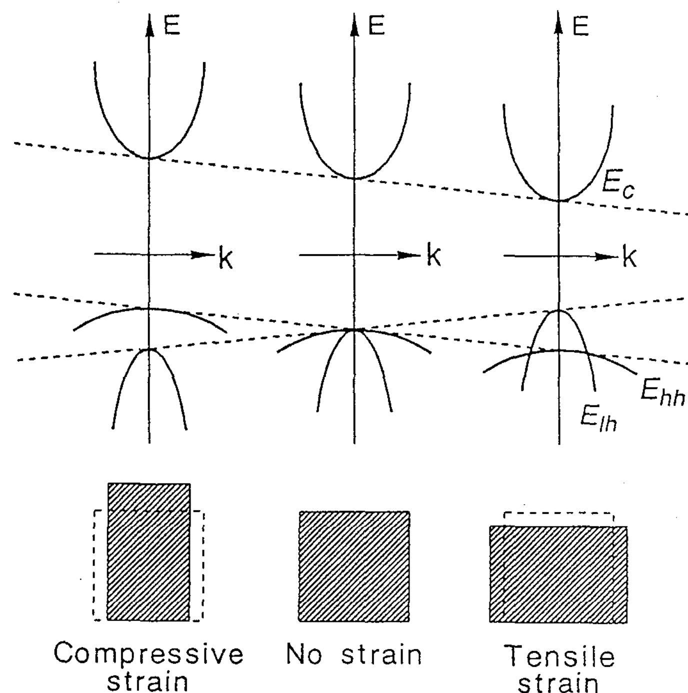

Figure 4-5 A schematic band diagram of the valence bands and the lowest conduction band under the different strain conditions.

As shown in Fig. 4-4, the peak energies of the excitonic lines are smoothly shifted to higher energies with increasing S content because ZnS crystal have a higher band-gap than the ZnSe crystal. There are, however, some discontinuities at the x=0.15 sulfur content, indicating a abrupt change in the band structure. Within the compositional range ($0 \leq x \leq 0.15$), the FE emission lines are clearly separated into FE(hh) and FE(lh) and their peak energies shift linearly with the sulfur content, as shown in curves (a) and (b). This energy splitting of FE(lh) and FE(hh) are caused by the strain effect due to the lattice mismatch between the substrate and the grown layer.[8-11]

It is well known that the biaxial strains applied to zinc-blende crystals induce the band splitting of light-hole and heavy-hole due to the change in the T_d to D_{2d} crystal symmetry.[8-11] This lattice strain effects on band structure are schematically shown in Fig. 4-5. When there is no strain in the crystal, the heavy-hole band (J=3/2, $m_j=\pm3/2$) and light-hole band (J=3/2, $m_j=\pm1/2$) are degenerated at k=0. In the crystal under the biaxial strain, the degenerated valence bands are split at k=0 by the uniaxial component of the strain, as shown in Fig. 4-5. The relative position between light-hole and heavy-hole are also shifted by the strain; under tensile stress the light-hole

band has a lower band-gap than the heavy-hole band, while under compressive stress the heavy-hole band is the lower one. In addition, the stress hydrostatic component shifts the center of gravity (average) of these two bands, which also induces a band-gap change. By considering these two strain effects, the shift of band-gaps under strain parallel to (100) direction is:

$$\Delta E_{hh} = \left(-2a\frac{c_{11} - c_{12}}{c_{11}} + b\frac{c_{11} + 2c_{12}}{c_{11}} \right)\varepsilon \ , \qquad (4\text{-}1)$$

$$\Delta E_{lh} = \left(-2a\frac{c_{11} - c_{12}}{c_{11}} - b\frac{c_{11} + 2c_{12}}{c_{11}} \right)\varepsilon \ , \qquad (4\text{-}2)$$

where a and b are the hydrostatic and shear deformation potentials, respectively. The value of ε indicates stress in the crystal along the (100) plane:

$$\varepsilon = \frac{a_{sub} - a_{epi}}{a_{epi}} \ , \qquad (4\text{-}3)$$

where a_{sub} and a_{epi} indicate the lattice parameter of the substrate and epitaxial layers, respectively. Therefore, the energy difference between the heavy-hole and light-hole bands are calculated using Eqs. (4-1)~(4-3) as follows:

$$\Delta E_{lh} - \Delta E_{hh} = -2b\frac{c_{11} + 2c_{12}}{c_{11}}\varepsilon \ . \qquad (4\text{-}4)$$

From Eq. (4-4), it is evident that the energy separation between these two bands is proportional to the strain applied to the crystals. In Fig. 4-6, the energy split of the free exciton emissions of ZnS_xSe_{1-x} are plotted as a function of the sulfur composition. The calculated value using Eqs. (4-3) and (4-4) is also indicated in the figure. It is important to note that energy separation obtained from the PL spectra is measured at low temperature (35 K), where the grown layer has an additional strain caused by the thermal expansion coefficient mismatch between the substrate and the grown

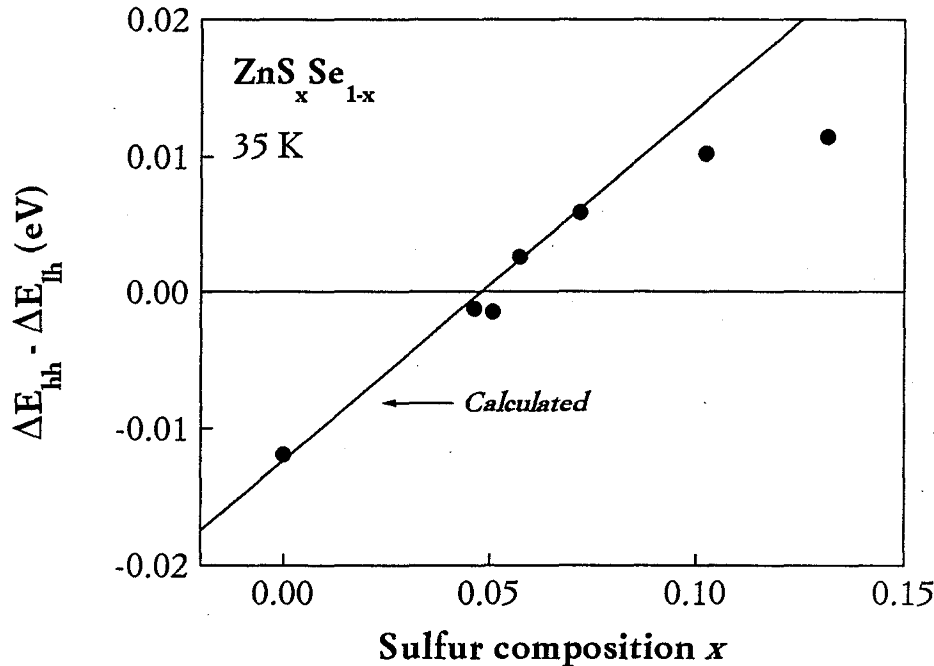

Figure 4-6 The energy separation between FE(lh) and FE(hh) in the PL spectra plotted as a function of the sulfur composition of ZnS_xSe_{1-x} crystals.

crystal.[12,13] We calculated the energy separations in Fig. 4-6 by taking into account the lattice parameter change. The lattice parameter at low temperatures is given by

$$a_T = a_{rt} - (\alpha_{rt} - \alpha_T)(T_{rt} - T_T)a_{rt} \,. \qquad (4\text{-}5)$$

where α_{rt} and α_T are the thermal expansion coefficient at room and low temperature, respectively, and T and a_{rt} indicate the temperature and the lattice parameter at room temperature. Thermal expansion coefficients as well as the lattice parameter at 35K are listed in Table 4-3.[14] As a result, the lattice parameters at 35 K are obtained from Vegard's law assuming the coherent crystal growth. The deformation potentials of ZnSe crystals are estimated to be -1.8 eV from the sample of ZnSe. Similar hydrostatic deformation potential of -1.2 eV has been reported for ZnSe crystal.[15] The reported value of -1.25 eV was adapted for the calculation of ZnS crystal.[11] As shown in Fig. 4-6, the calculated energy difference between heavy-hole and light-hole bands agrees well with the observed PL peak splitting of FE(lh) and FE(hh). In ZnS_xSe_{1-x} with large sulfur composition (x>0.1),

Table 4-3 Thermal expansion coefficients and lattice parameters

	α_{rt}	α_{35K}	a_{rt}	a_{35K}
	($\times10^6$ K^{-1})		(Å)	
ZnS	6.7	-0.7	5.4093	5.4000
ZnSe	7.5	-1.0	5.6686	5.6571
GaAs	5.7	-0.1	5.6533	5.6455

however, energy split deviates from the calculated values. This result indicates that the lattice mismatch strain in the crystal layer exceeds its elastic limit due to the increased sulfur content.

In the samples having sulfur composition more than x=0.19 (indicated by diamond in Fig. 4-4), on the other hand, the excitonic fine structure of the PL peaks disappear, and large shifts of the broad PL peaks can be seen. As mentioned above, these effects are obviously result from the excess strain applied to the grown layers. In addition, these sample show the tail state in their PL emission peaks as shown in Fig. 4-3. From these results, it is suggested that the potential fluctuations are formed in the crystals due to the large lattice deformation. Local compositional fluctuations originate from the imperfection of ZnS layer could be the another reason of these effects. Similar effects have been also reported in ZnS_xSe_{1-x} mixed crystals.[9,16) Nevertheless, it should be emphasized that deep level emissions are extremely small even at this high sulfur content. In other words, this excess amount of strain does not create dislocations to release their strains in ZnS_xSe_{1-x} crystals, indicating the feasibility of this crystal fabrication technique.

In summary, the high-quality ZnS_xSe_{1-x} alloys in a wide compositional range were grown coherently on GaAs (100) substrate by HRCVD using ALE-mode. These alloys were fabricated by introducing ZnS monolayer to ZnSe crystals. The sharp free excitonic emissions are observed in the PL spectra, and the peak energies shift smoothly from 2.8 to 2.9 eV by varying the gas pulse supply ratio, while suppressing the deep level emission caused by the dislocation formation.

4.2 Growth of $(ZnS)_n(ZnSe)_m$ (n=1~4) ordered alloys

In the previous section, we discussed about the basic properties of ZnS_xSe_{1-x} alloys prepared by HRCVD in ALE-mode. The structures of that crystals are, however, ambiguous due to the imperfect surface coverage of ZnS layer. In this section, we attempted to fabricate the crystal having precise 2-dimensional structures of ZnS and ZnSe layers. Two types of ordered alloys, $(ZnS)_n(ZnSe)_{12n}$ (n=1~4) and $(ZnS)_3(ZnSe)_m$ (m=12~72), were grown on GaAs substrates at low temperature of 200°C by ALE. In the case of $(ZnS)_n(ZnSe)_{12n}$, the number of ZnS layers "n" was varied from 1 to 4 (n=1~4) while keeping the average composition same, and the structural differences associated with the repeat spacing were investigated. In $(ZnS)_3(ZnSe)_m$ (m=12~72), on the other hand, the sulfur composition was systematically increased from 4 to 20 at% by decreasing the number of ZnSe layers from 72 to 12 to clarify the strain effect due to the GaAs substrate. These ordered alloys were grown directly on the GaAs substrate without any buffer layers. The thickness of the ordered alloys was 5000Å and 4000Å for $(ZnS)_n(ZnSe)_{12n}$ and $(ZnS)_3(ZnSe)_m$, respectively. The growth condition of these crystals is the same as those listed in Table 4-1.

4.2.1 Structure and properties of $(ZnS)_n(ZnSe)_{12n}$

The $(ZnS)_n(ZnSe)_{12n}$ ordered alloys (n=1~4) was chosen so as to provide good lattice matching with the GaAs substrate. The average sulfur composition in this structure is 7 at%. Since the ZnS layer has a large lattice mismatch with the GaAs substrate (ε =-4.32), the number of ZnS layers was held four or less to avoid lattice relaxation. In addition, the critical thickness of the ZnS layer grown directly on GaAs substrate was also calculated to be around 4 layers,[16,17] although these calculation methods is not reliable under the excess strain condition. The stain in the ZnSe layers are considered to be small in this ordered structures since ZnSe layers have the larger critical thickness of 1500Å (or 500 layers) on the substrate.

Figure 4-7 shows XRD spectra of $(ZnS)_n(ZnSe)_{12n}$ ordered alloys where the value of n was varied between 1 and 4. Satellite peaks corresponding to the layer-by-layer structure of the ordered alloys are seen in all cases except n=1. The satellite peaks broadened when the ZnS thickness was reduced to

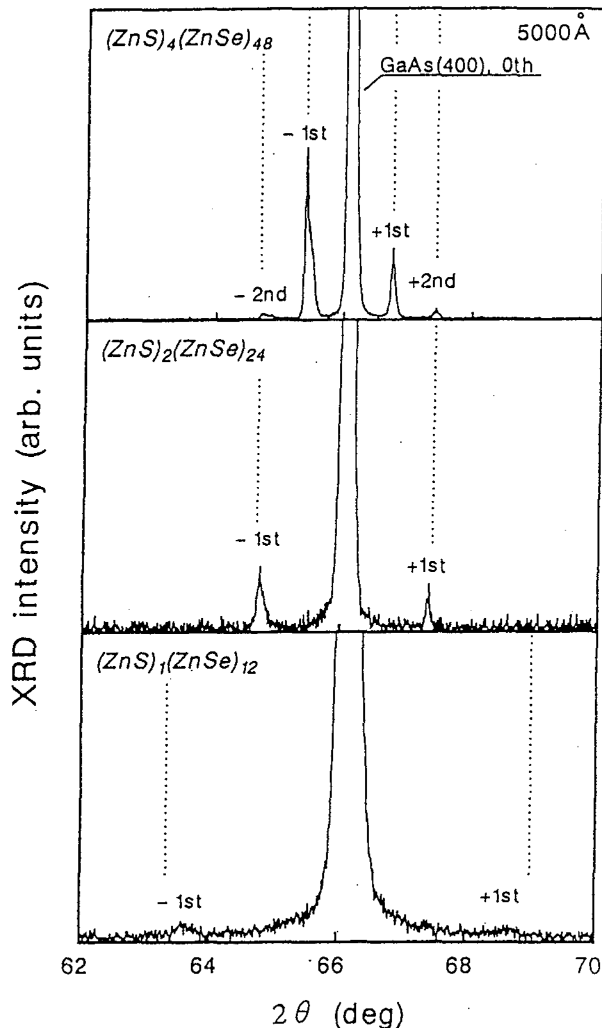

Figure 4-7 X-ray diffraction patterns of $(ZnS)_n(ZnSe)_{12n}$ ordered alloys (n=1~4). Theoretical angles of satellite peaks assuming coherent growth are also indicated by the dotted lines.

about one monolayer, perhaps indicating that the monolayer is not continuous or that its thickness varied spatially. Theoretical angles for the satellite peaks, calculated from Eq. (2-27) assuming that the crystal films grow coherently (indicated by the dotted lines), show good agreement with those observed. Figure 4-8 also shows the XRD spectra of $(ZnS)_4(ZnSe)_{48}$ ordered alloys (a), and the calculated XRD intensity using Eq. (2-28) (b). It is shown that the each calculated intensities of the satellite peaks agree quite well with the observed XRD spectra. In the observed higher-order satellite peaks (±2nd and ±3rd), however, the diffraction angles slightly different

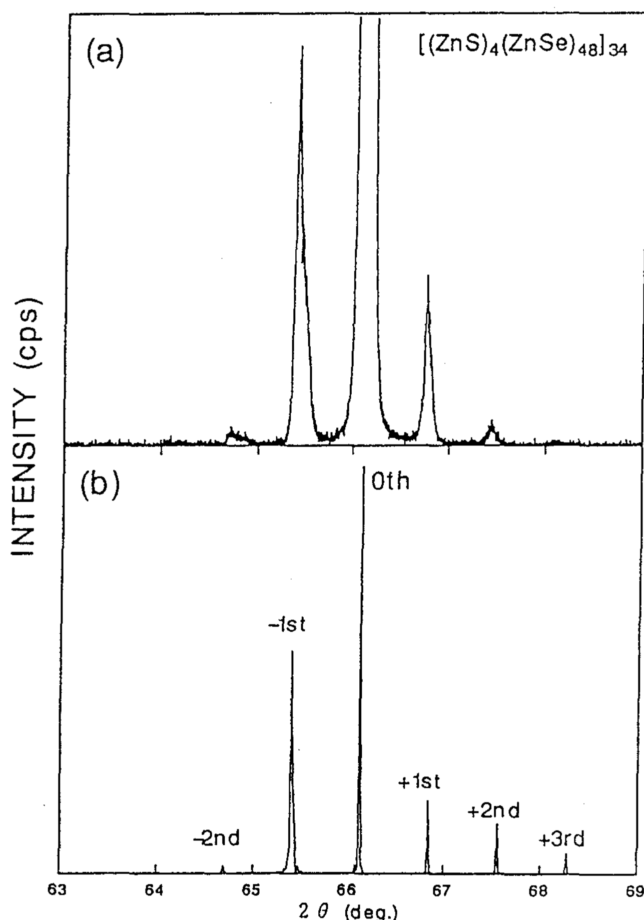

Figure 4-8 The observed XRD spectra of $(ZnS)_4(ZnSe)_{48}$ ordered alloys (a), and the calculated XRD intensity using Eq. (2-28) (b).

from the calculated angles due to the long-range compositional fluctuation of the ordered structures. The thickness of a single $(ZnS)_n(ZnSe)_{12n}$ unit cell estimated from the angles of satellite peaks, were 0~10% more than the calculated values for n=2~4, and 15% more than that for n=1. The lattice parameter perpendicular to the surface obtained from the zero-order peaks was ~5.650Å, in good agreement with values predicated by Vegard's law with coherent structure. The FWHM of zero-order peaks obtained from x-ray rocking curves was ~150 arcsec for all cases. The above results indicate that the ordered alloys grown by this work have the expected ordered structure with little monolayer structural fluctuation.

Figure 4-9 shows a typical PL spectrum of the n=2 ordered alloy at 35 K. The emission line fine structure is also shown in the inset. As seen in the

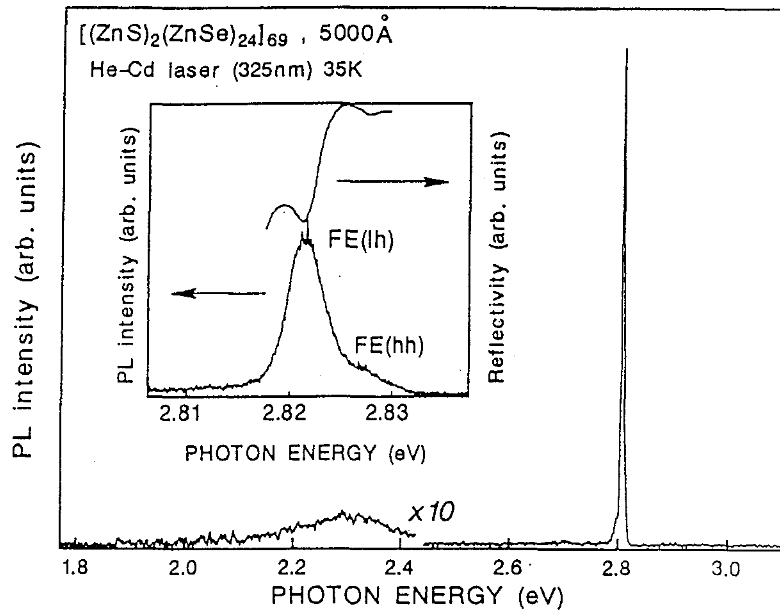

Figure 4-9 Photoluminescence spectra of $(ZnS)_2(ZnSe)_{24}$ ordered alloy measured at 35 K. The inset shows enlarged PL spectrum near band-edge.

PL spectrum, the band-edge emission was dominant while deep level emission is not obvious. The emission lines with near the band-edge are attributed to the free-exciton because the reflectivity spectrum also shows these peaks (as seen in the inset). A pair of emission lines at higher energies is attributed to FE(lh) and FE(hh), respectively. This assignment of the free exciton peaks is consistent with the strain applied to the grown layers, as mentioned before. It is noteworthy that the PL emission intensity of the bound exciton is negligible in the ordered alloy, although the emission of the donor-bound exciton (I_2) has been observed in ZnSe crystals under the similar growth conditions. The FWHM of the FE(lh) peaks show a small value (4 meV) in the $n \geq 2$ case, while a rather broad emission peak (6 meV) is observed in the n=1case.

The presence of exciton emission peaks supports the conclusion that these ordered alloys behave as coherent materials and have low defect densities. The low deposition temperature of ALE growth in this study results in low defect densities, because defect formation induced by the thermal expansion mismatch between the grown layer and GaAs is small.

The peak energies of FE(lh) and FE(hh) as a function of the number of ZnSe layers are shown in Fig. 4-10. The peak energies of ZnS_xSe_{1-x} (x=0.06) which have the same sulfur content as the ordered structure as well

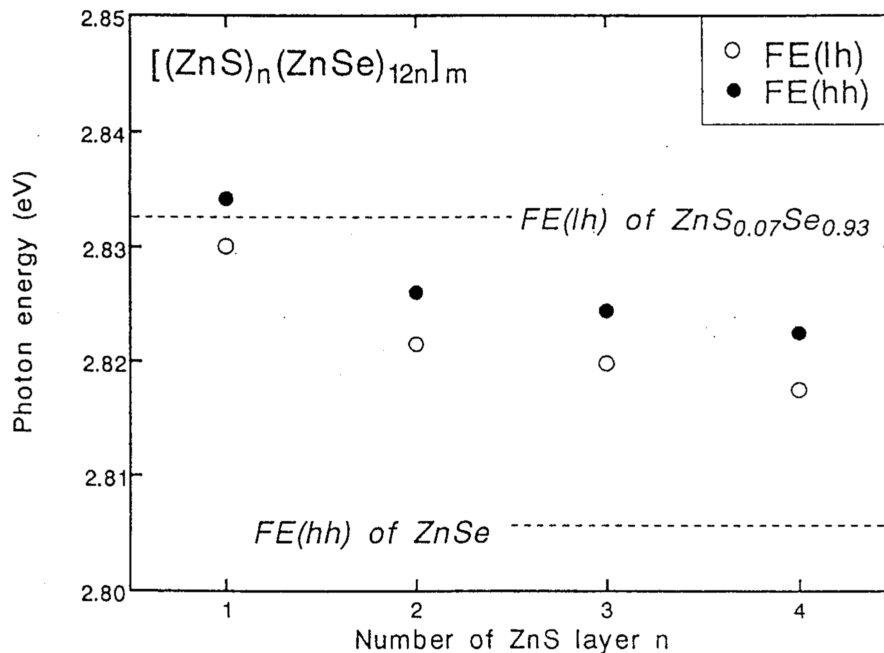

Figure 4-10 Peak energies of $(ZnS)_n(ZnSe)_{12n}$ (n=1~4) ordered alloys as a function of the number of ZnS layers. Peak energy of $ZnS_{0.07}Se_{0.93}$ (4000Å) and ZnSe (1500Å) are also shown.

as ZnSe crystals with coherent growth (1500Å) are also shown in the figure. In the ZnS_xSe_{1-x} disordered alloys, the band-gaps are completely determined by the sulfur composition. In $(ZnS)_n(ZnSe)_{12n}$ ordered alloys, on the other hand, the excitonic PL peaks shift to lower energies with increasing "*n*", even though the macroscopic chemical composition is unchanged. Therefore, this PL peak shifts could be a "quantum-size effect" originating from the extremely thin 2-dimensional structure of these ordered alloys. It is observed that the peak energies of the ordered alloys gradually shift to those of ZnS_xSe_{1-x} disordered alloys with decreasing *n*. In addition, PL peaks energy of the ordered alloy at *n*=1 is the same as that of the disordered alloys with the same composition. This suggests that the band structure in this ordered alloy is similar to that of the disordered alloys having the same composition. A similar result was also predicted for $(ZnS)_n(ZnSe)_n$ by theoretical calculations using the tight-binding theory.[18] This band structure of $(ZnS)_n(ZnSe)_{12n}$ will be discussed further by comparing with that of $(ZnSe)_n(ZnTe)_{11n}$ ordered alloys in chapter 6.

It was found that FE(lh) and FE(hh) energy separation is almost same

(4.6±0.4 meV; n=1~4). Energy separation caused by the strain distribution at 35 K is calculated to be ~5 meV from Eq. (4-5), and is in a good agreement with the observation. This result indicates that the strain is independent of the number of ZnS layers n. Consequently, the extremely thin ZnS layers provide the homogeneous distribution of the lattice mismatch strain. This result is quite hopeful for "strain engineering" using the structure of the ordered alloys.

4.2.2 Structure and properties of $(ZnS)_3(ZnSe)_m$ (m=12~72)

In this type of the ordered alloys, the sulfur contents were changed from 4 to 20 at% by changing the number of ZnSe layers from m=12 to m=72, in order to clarify the strain effects induced by the GaAs substrate.

Figure 4-11 shows XRD spectra of $(ZnS)_3(ZnSe)_m$ ordered alloys and ZnSe crystals grown by HRCVD using ALE. Satellite peaks were observed in all the samples in this study. It was also observed that differences in diffraction angles of satellite peaks between the -1 and +1 peaks increase with a decrease in layer thickness of 1 period of $(ZnS)_3(ZnSe)_m$. The layer thicknesses determined by satellite angle and by calculation agreed within 7%. The zero-order peaks shift to higher diffraction angles with increasing sulfur content, or decreasing number of ZnSe layers, implying that the average lattice parameter gradually decreased with increasing sulfur content. These results indicate that ordered alloys have the layer-by-layer structure with the intended number of each layers. The FWHM of the zero-order peaks obtained from the x-ray rocking curve are ~100 arcsec when the lattice mismatch with GaAs is small (m=18~72). The zero-order peaks broaden rapidly due to the lattice mismatch in the ZnSe or the m=12 ordered alloy, and the FWHM of these crystals were 300 and 400 arcsec, respectively.

In Fig. 4-12, the lattice parameters perpendicular to the surface are plotted as a function of sulfur content of the ordered alloys. The sulfur content of the ordered alloys were determined by x-ray photoelectron spectroscopy (XPS). It has been confirmed that the sulfur contents of the ordered alloys determined by XPS agrees well with that determined by XRD analysis. The lattice parameters obtained according to Vegard's law are also shown in this figure for the various conditions (bulk and coherent). It was observed

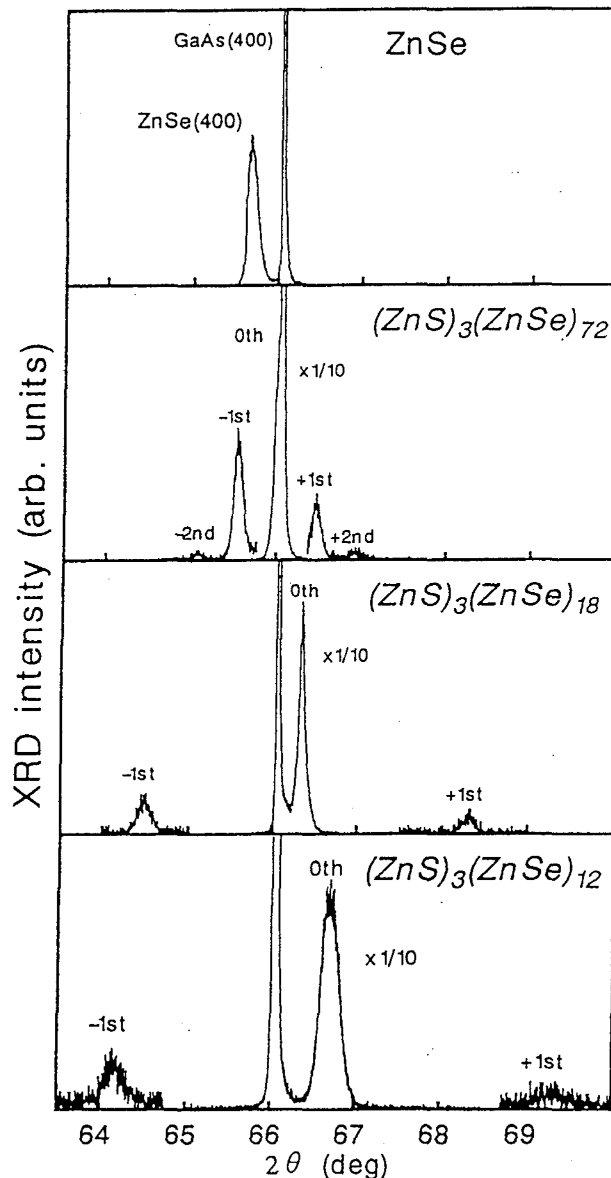

Figure 4-11 XRD spectra of $(ZnS)_3(ZnSe)_m$ ordered alloys (m=12~72) and ZnSe crystal.

that lattice parameters of the ordered alloys agree well with the coherent state when the lattice mismatch is small (S=4~8 at%), and the lattice parameters gradually approach the bulk value when the lattice mismatch is large (S>8%). The critical layer thickness for ZnSe is generally considered to be 1500Å [4)] and 1000Å for the ordered alloy with sulfur content of 20 at%.[16,19)] Obviously, the thicknesses of the grown ordered alloy and ZnSe in this work (~4000Å) are thicker than these critical thicknesses.

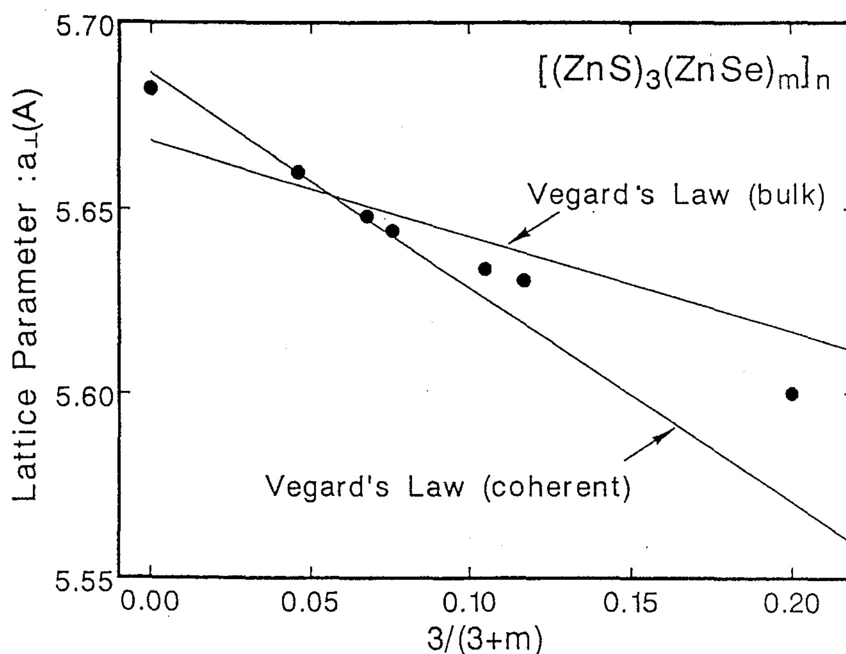

Figure 4-12 Lattice parameter perpendicular to the surface as a function of the sulfur content of $(ZnS)_3(ZnSe)_m$ ordered alloys. Lattice parameters for various conditions of crystal (coherent and bulk states) obtained from Vegard's law are also indicated by the solid lines.

Accordingly,the lattice of the ZnSe and ordered alloys with the high sulfur content deform from a coherent state to a bulk like state so as to release the large lattice mismatch strains within the crystal.

Figure 4-13 shows the typical PL spectra of $(ZnS)_3(ZnSe)_{18}$ ordered alloy and ZnSe at 35 K. The PL spectrum of $(ZnS)_3(ZnSe)_{18}$ shows that free exciton emission at near band-edge are dominant while deep level emission (~2.3 eV) is negligible. Similar PL spectra were obtained from the other ordered alloys examined in this work. On the contrary, bound-exciton emission was dominant in ZnSe crystal film grown under similar condition with the ordered alloy. In addition, the deep level and donor-to-acceptor pair (DAP) emissions can be also seen in ZnSe crystal. The PL intensity of $(ZnS)_3(ZnSe)_{18}$ was two orders of magnitude greater than that of ZnSe, indicating the existence of many non-radiative centers in ZnSe. These defect-oriented PL peaks induced by the lattice relaxation have been widely observed in ZnSe crystal.[20,21]

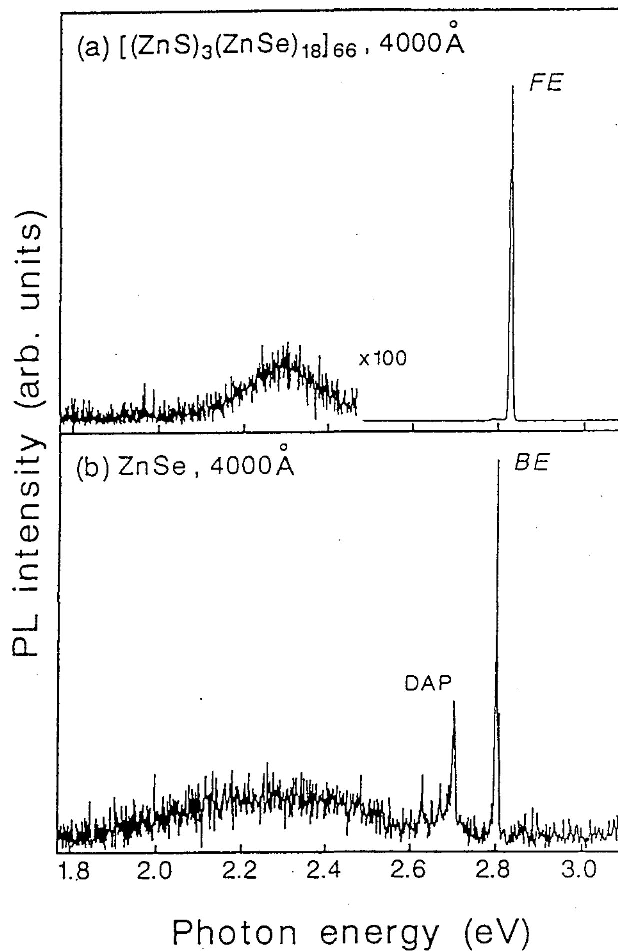

Figure 4-13 PL spectra of $(ZnS)_3(ZnSe)_{18}$ (a) and ZnSe (b) measured at 35 K.

In Fig. 4-14, the ratio of PL deep level emission intensity at 2.3 eV to free exciton (I_{deep}/I_{FE}) is plotted as a function of sulfur content for the ordered alloys. As shown in Fig. 4-13 (b), the I_{deep}/I_{FE} ratio is high for the ZnSe crystal. On the contrary, the I_{deep}/I_{FE} ratio for the ordered alloys is quite low and independent of the sulfur content. These results strongly support the idea that defect generation due to lattice mismatch can be suppressed by the layer-by-layer structure of these ordered alloys.

The reductions of dislocation densities using multilayer structures were also reported in III-V[22-24] and IV group[25,26] semiconductors. This effect has been explained by two strain relaxation mechanisms: formation of edge-dislocation at heterointerfaces[24,25] or paired loop dislocations.[26] These two strain relaxation mechanisms are schematically shown in Fig. 4-15.

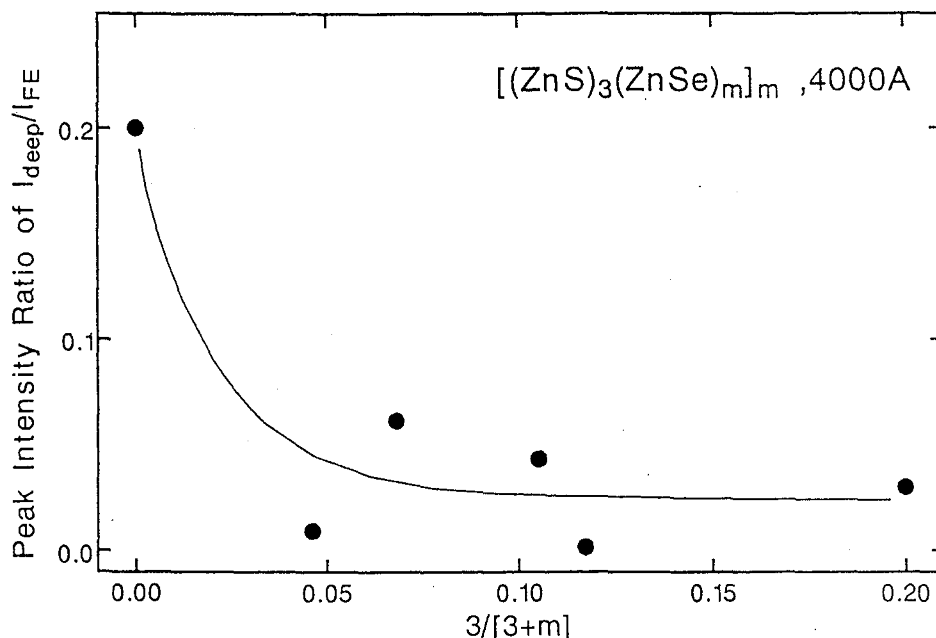

Figure 4-14 Peak intensity ratio of the deep level at 2.3 eV to the free exciton near the band-edge (I_{deep}/I_{FE}) as a function of the sulfur content of the ordered alloys.

Generally, misfit dislocations are introduced at the interfaces between the substrate and the grown layers in order to relief the existing mismatch strain in the crystals, and stacking faults at the ZnSe/GaAs interfaces was reported to be the source for the misfit dislocations.[27,28] On the other hands, in the crystals having layer-by-layer structures, high strain-fields at the individual heterointerface prevent the propagation of the dislocation segment to upward direction, as shown in Fig. 4-15. As a result, dislocation networks in the multilayer structures form a "closed loop", which effectively reduces the dislocation density in the crystal.[26] Recently, it was also confirmed from TEM observation that strain relaxation process of $(InAs)_1(GaAs)_m$ (m=1~11) occurs by the generation of misfit dislocations propagating parallel to the heterointerface without generation of threading dislocations.[24] Accordingly, similar strain relaxation mechanism is expected for $(ZnS)_n(ZnSe)_m$ ordered alloys. Moreover, because of the localized ionic bonding of II-VI crystals, the deformation of local atomic bond may also contribute to the strain relaxation.[29,30] As a result, the lattice deformation as well as the diffraction peak broadening observed in the XRD spectra can be explained in terms of these lattice relaxation effects near the substrate

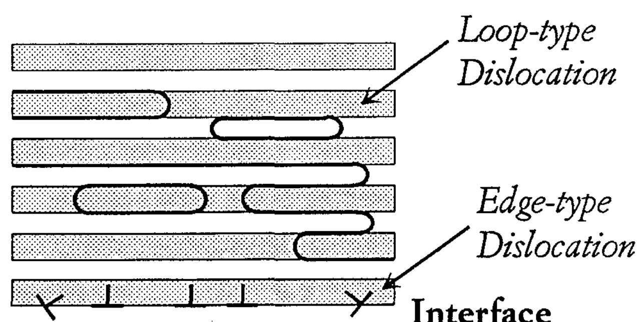

Figure 4-15 Schematic illustration of two possible strain relaxation mechanisms: edge-type dislocation generation at the interface with the substrate, and closed loop formation of dislocations by the strain field at the heterointerface.

interface region. It should be emphasized that the detected region in the PL measurement is only ~1000A from the sample surface, and is far enough from the interface region where the dislocation networks might be generated. Strong PL emissions in the ordered alloys also support this speculation that the dislocation propagation toward the surface can be efficiently prevented by the 2-dimensional structure of the ordered alloys. In addition, it is expected that the generation of the misfit dislocations is suppressed by the 2-dimensional growth by ALE, as observed by other works.[31,32] The low temperature growth by HRCVD also contribute to the suppression of the dislocation generation since the low temperature growth simply reduce the thermoelastic strains.

Figure 4-16 shows the peak energies of FE(lh) and FE(hh) as a function of the sulfur content of the ordered alloys. The PL peaks near band-edge are also shown in this figure. It was observed that FE peaks shifted to higher energies monotonously with increasing sulfur content. The peak broadened significantly (13 meV) in $(ZnS)_3(ZnSe)_{12}$, while fine structure of FE(lh) and FE(hh) can be seen when the sulfur content is less than 12 at%. It is evident that the large lattice strain in the ordered alloy with high sulfur composition leads to this broadening effect. The above results strongly suggest the ability of the ordered alloys to independently control the band-gap of the crystals while maintaining low densities of misfit dislocations.

In summary of this section, two types of ordered alloys, $(ZnS)_n(ZnSe)_{12n}$ (n=1~4) and $(ZnS)_3(ZnSe)_m$ (m=12~72), were grown at 200°C by HRCVD using ALE. Satellite peaks corresponding to the two-dimensional

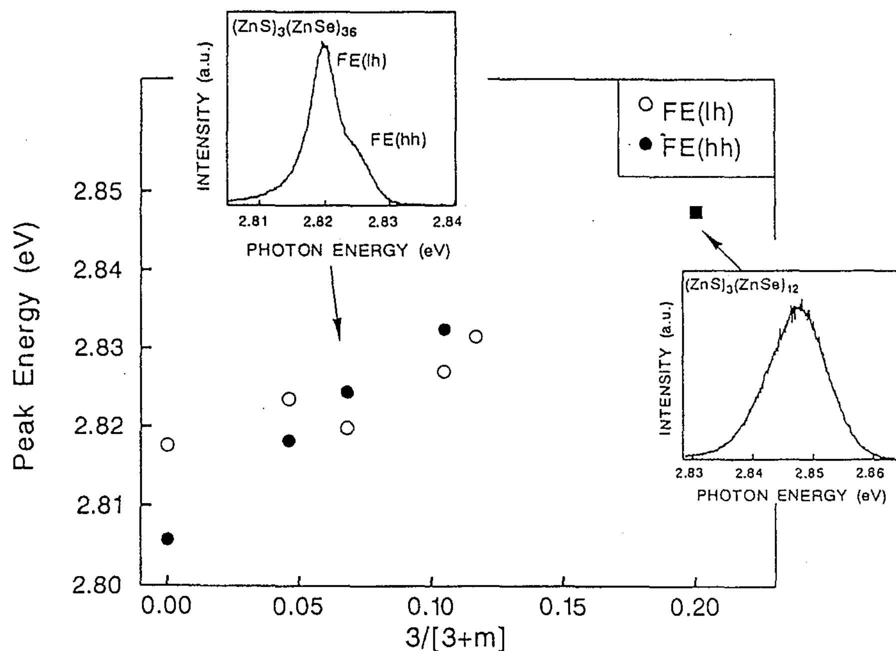

Figure 4-16 Peak energies of FE(lh) and FE(hh) as a function of the sulfur composition of $(ZnS)_3(ZnSe)_m$. PL spectra of $(ZnS)_3(ZnSe)_{36}$ (a) and $(ZnS)_3(ZnSe)_{12}$ (b) are also shown.

structures were observed in all the samples. As a result, it was confirmed that the these ordered alloys grow coherently on the substrate. In $(ZnS)_3(ZnSe)_m$ ordered alloys, deep level emissions were well suppressed compared with ZnSe crystal despite the large lattice distortion caused by the strain. The peak energies of the ordered alloys moved systematically with the changes in the number of ZnSe layers. Therefore, the band-gap can be changed without the formation of the dislocations by variation of the ordered alloys.

4.3 Exciton dynamics of Zn(S,Se) ordered alloys

In the ordered alloys having short-periods 2-dimensional structures, specific behaviors of the "exciton" are expected. In this section, therefore, exciton dynamics of the ordered alloys are characterized by transient-state and time-resolved PL spectra. In addition, the exciton relaxation process will be further discussed by the exciton absorption process measured by the photocurrent (PC) spectra.

4.3.1 Exciton under high excitation-states

The exciton dynamics of $(ZnS)_n(ZnSe)_{12n}$ (n=1~4) under the high excitation-state were studied by measuring PL spectra with a pulsed high intensity YAG laser. The detail of the experimental conditions is described in section 2.3.1. Figure 4-17 shows the emission intensities of $(ZnS)_1(ZnSe)_{12}$ ordered and $ZnS_{0.07}Se_{0.93}$ disordered alloys plotted as a function of the YAG laser intensity. The measurement was carried out at the low temperature of 10 K, and the emission intensities were normalized by that of 250 mW. A distinctive difference in the behavior of the PL emission intensities can be seen in these crystals; the PL emission intensity rapidly increases with increasing excitation power in the ordered alloy while the saturation is observed in the disordered alloy. Obviously, this effect originates from the difference in the electronic states of these crystals.

Figure 4-18 shows FE(lh) peak energies of $(ZnS)_n(ZnSe)_{12n}$ ordered alloy (n=1~4) and $ZnS_{0.07}Se_{0.93}$ plotted as a function of increasing light intensity. The peak energies obtained from a He-Cd laser is also shown in this figure at a laser intensity of 0 mW. The red shift of FE(lh) peaks along with the laser power increase can be seen in all the ordered alloys, while no distinct peak shifts was observed in $ZnS_{0.07}Se_{0.93}$. There are three possible excitonic processes that shift the free exciton peaks to lower energy side as follows:

1) exciton molecule recombination,[33]
2) exciton-exciton scattering,[34]
3) formation of electron-hole plasma (EHP).[35-37]

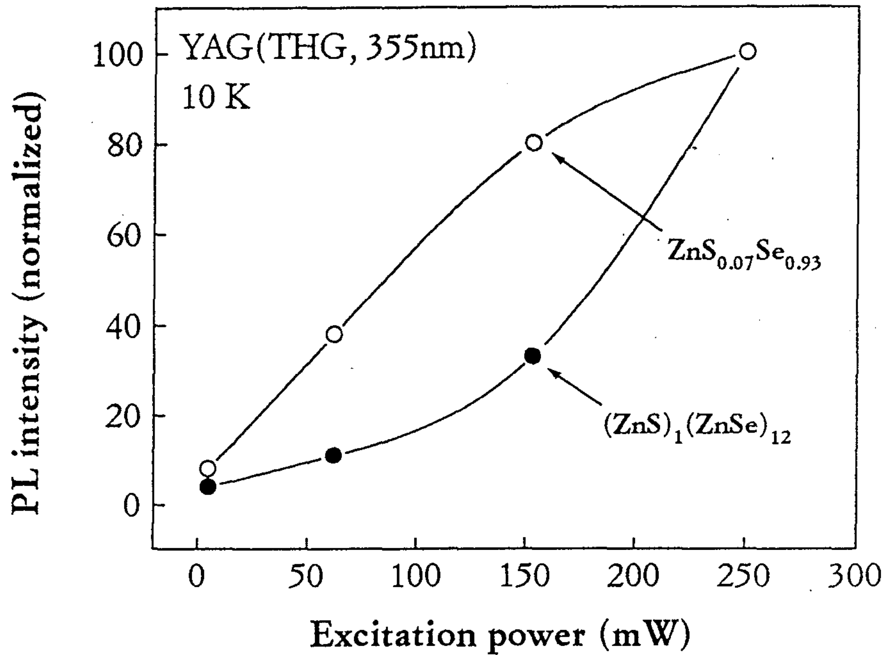

Figure 4-17 The PL intensities of $(ZnS)_1(ZnSe)_{12}$ ordered and $ZnS_{0.07}Se_{0.93}$ disordered alloys plotted as a function of the excitation power of YAG laser (355 nm) at 10 K.

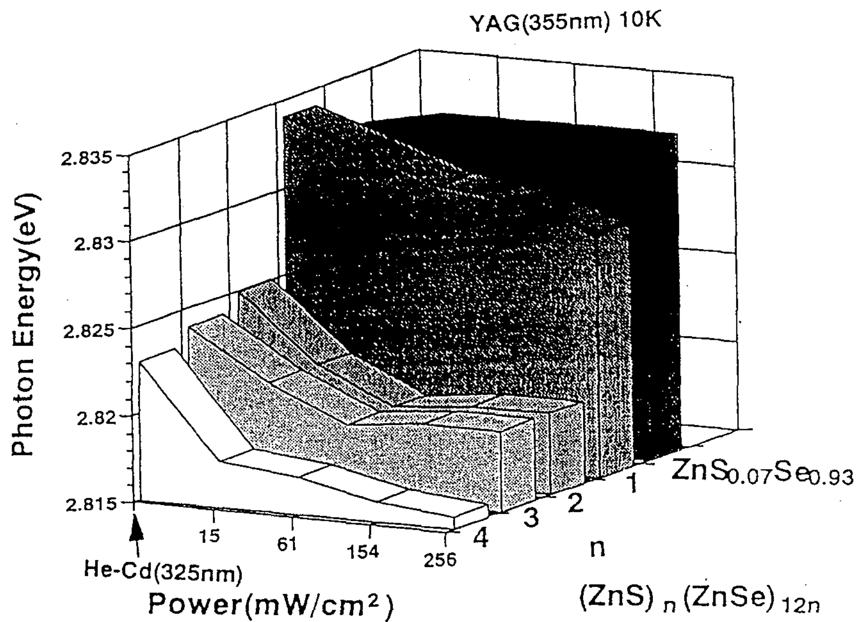

Figure 4-18 The FE(lh) peak energies of $(ZnS)_n(ZnSe)_{12n}$ ordered alloy (n=1~4) and $ZnS_{0.07}Se_{0.93}$ plotted as a function of increasing light intensity. The peak energies obtained from a He-Cd laser is also shown in this figure at a laser intensity of 0 mW.

Exciton molecule recombination process (1) can be written by

$$h\nu_M = E_g - E_x - E_M \, , \tag{4-6}$$

where E_g is the band gap, E_x is the exciton binding energy and E_M is the exciton molecule binding energy. When the excitons recombine through this process, the emission energy is reduced by E_M, which causes the red shift of the PL peaks. E_M for ZnSe is, however, predicted to be small (<1 meV).[38] In addition, we did not observed any PL peaks which can be assigned to the exciton molecule recombination. Accordingly, this process can be excluded in this case. Another possible mechanism is the exciton-exciton scattering process (2), in which one exciton is dissociated by the scattering while the other is converted into a photon-like state. In this process, one exciton loses the energy corresponding to a binding energy by a collision with another exciton as follows:[34]

$$h\nu_S = E_g - 2E_x - \delta E_{kin} \, , \tag{4-7}$$

In Eq. (4-7), δE_{kin} is the resulting electron and hole kinetic energies, which is considered to be small. In the process (3), which is not the exciton process, the electrons and holes excited by a strong light condense into electron-hole drops, called electron-hole plasma (EHP). The peak energy of EHP also move to lower energy side due to the band-gap renormalization (band-gap shrinkage).[35-37] In general, the formation of EHP occurs when the carrier (or exciton) density exceeds Mott critical density, which is defined by[39]

$$n_{Mott} = \left(\frac{0.24}{a_B} \right)^3 = 3 \times 10^{17} cm^{-3} \, , \tag{4-8}$$

where a_B indicates the Bohr radius of exciton which is calculated by Eq. (2-14). This critical exciton concentration is larger than that estimated from the excitation power in this study (~10^{16} cm^{-3}). Accordingly, this process (3) is not probable for the PL peak shift. In addition, the narrowness of the free-exciton line (10 meV) indicates that EHP is not involved which would otherwise show much broader lines, up to 50 meV. Sample heating by the

laser radiation is also considered as a reason for peak shifts to lower energy side, which is unlikely in this case because PL emission intensity increases with increasing excitation intensity.

These results suggest that the exciton-related interaction takes place in the ordered alloys because of its specific electronic state. As shown in Fig. 4-10, the ordered alloys have the weak quantum-size effect due to the layer-by-layer structure. Consequently, it is possible that the confinement of excitons at the valence band of the ordered alloys increases exciton scattering, which result in the red shift of the PL peak. This suggestion is consistent with the fact that the peak shift can not be observed in ZnS_xSe_{1-x} disordered alloys.

4.3.2 Exciton relaxation process

In order to investigate the exciton relaxation process in the ordered alloys, we attempted to measure the time-resolved PL measurement. Figure 4-19 shows typical time-resolved PL spectrum from FE(lh) peak of the $(ZnS)_2(ZnSe)_{24}$ at 10 K. The luminescence from the ordered alloy shows an immediate response to the laser radiation at t=0. In the decay of the PL emission, the PL intensity falls exponentially with time. The rise (τ_r) and decay (τ_d) times were obtained by fitting the data to the theoretical curve which is expressed by[40,41]

$$I(t) = \exp\left(-\frac{t}{\tau_d}\right) - \exp\left(\frac{t}{\tau_r}\right). \qquad (4\text{-}9)$$

The rise time of 10 psec and the decal time (life time) of 83 psec were obtained from Fig. 4-19. The PL intensity decay, however, slightly deviates from the single exponential line probably due to the effect of the surface recombination. Life times of the ordered alloys (n=1~4) are plotted as a function of the number of ZnS layers in Fig. 4-20. The life time of $ZnS_{0.07}Se_{0.93}$ is also indicated as the dotted line in the figure. It was found that the rise times of all the ordered alloys are in a range of 5-10 psec, indicating the low trapping density in the crystals. The exciton life time in superlattice structures is reported to be proportional to exciton volume,[40,42]

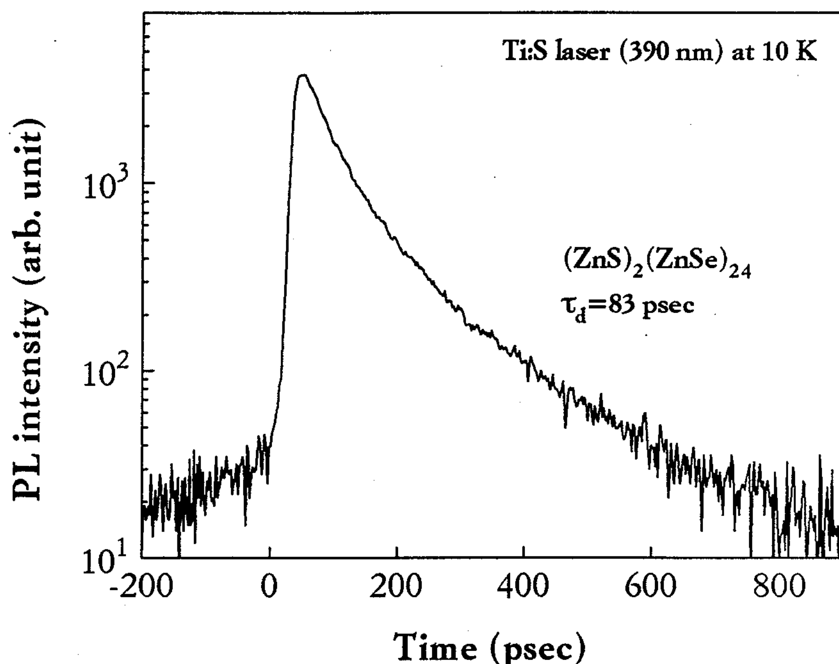

Figure 4-19 The time resolved PL spectrum of $(ZnS)_2(ZnSe)_{24}$ at 10 K.

$$\tau_d = a_{2D}^2(L_z) \times L_z \,, \qquad (4\text{-}10)$$

where a_{2D} is the Bohr radius of exciton under the confinement state, and L_z is the well width. Accordingly, similar effect is also expected in the ordered alloys. In the ordered alloys, however, no structural differences can be seen depending on the layered structure. Exciton life times of the ordered alloys are about 50~100 psec, and these values are almost same with that of the disordered alloys, as shown in Fig. 4-20. These short life times of excitons are considered to be the favorable feature for high-speed optical switching devices.

4.3.3 Exciton absorption process

In this section, the absorption process of exciton will be probed by the photocurrent (PC) measurement in order to clarify the density of states of the Zn(S,Se) ordered crystals. Figure 4-21 shows the PC and PL spectra of

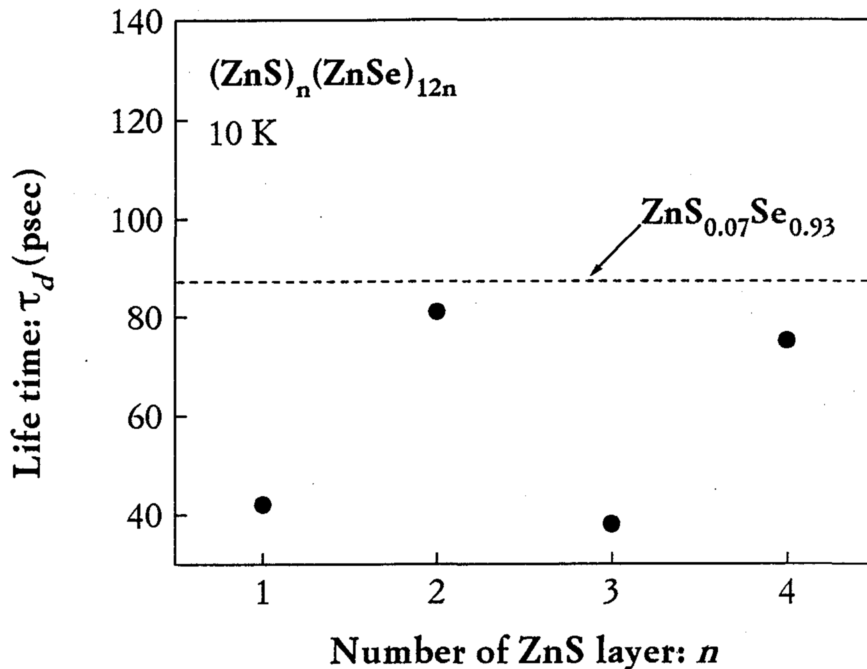

Figure 4-20 The life time of $(ZnS)_n(ZnSe)_{12n}$ ordered alloys (n=1~4) plotted as a function of the number of ZnS layers. The life time of $ZnS_{0.07}Se_{0.93}$ is also indicated as a dotted line in the figure.

$(ZnS)_1(ZnSe)_4$ measured at 35 K. The PLE spectrum of the same sample at 2 K is also shown in this figure. The measurements were made at an electric field of 25V/cm. The sample thickness is only 1000Å. The PC was linear in electric field, indicating that the contacts were ohmic. The PC response was also linear in light intensity. From these results, the ideal PC measurement conditions were confirmed.

The exciton absorption can be seen in the PC spectra at around 2.9 eV, as shown in Fig. 4-21. In addition, similar spectrum was obtained from the corresponding PLE spectrum, which indicates the reliability of the PC measurement. The absorption peak, however, shows a some stokes shift of about 50 meV with the PL peaks in both case. It has been reported that potential fluctuations provides the peak energy difference between the absorption and recombination process. A high sulfur content (20 at%) in this ordered alloy might be the reason for this peak shift since the lattice mismatch strain prefers the formation of tail states (or potential fluctuation) to remove the strain in the crystal. The PC spectrum of $(ZnS)_3(ZnSe)_{42}$ ordered alloy is also shown in Fig. 4-22. In this PC spectrum, the relatively

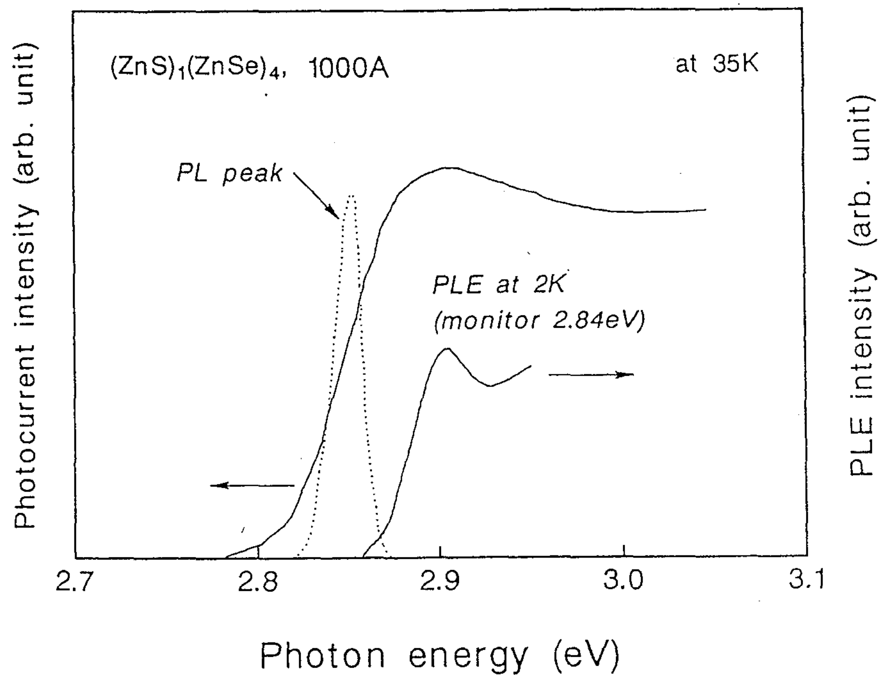

Figure 4-21 The PC and PLE spectra of $(ZnS)_1(ZnSe)_4$ ordered alloys measured at 35 K. The corresponding PL peak is also shown.

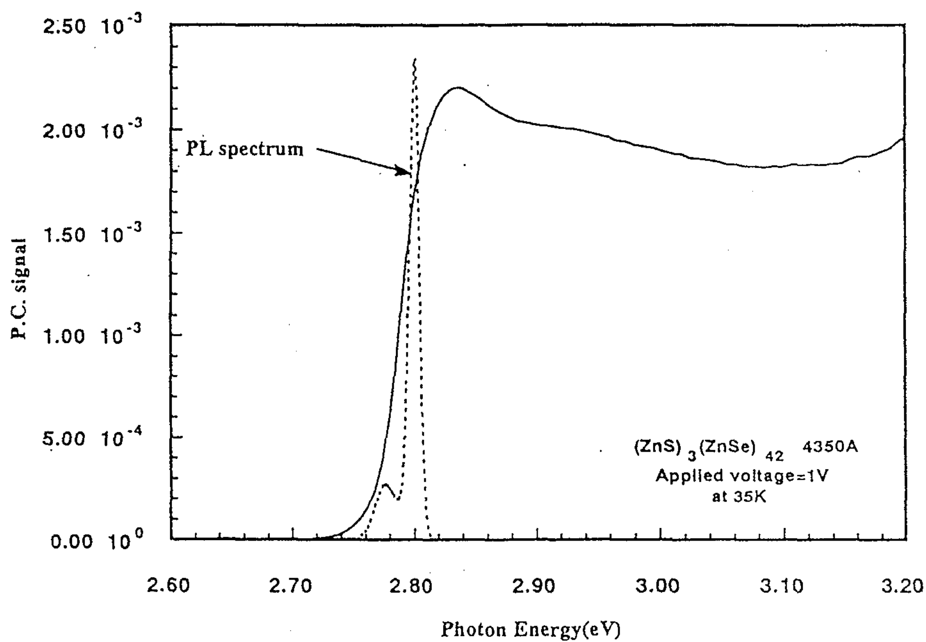

Figure 4-22 The PC spectrum of $(ZnS)_3(ZnSe)_{42}$ ordered alloys measured at 35 K. The PL peaks at the same temperature is also shown.

sharp exciton absorption peak can be seen compared with that of $(ZnS)_1(ZnSe)_4$. Moreover, the PL energy separation with the PC absorption peaks becomes smaller (~25 meV) in $(ZnS)_3(ZnSe)_{42}$ since the lattice parameter of this ordered alloy is perfectly matched to the substrate using the average sulfur composition of 7 at%. Accordingly, it is proved that the potential fluctuation effects in the crystals can be obtained from the PC measurements.

The slope of the absorption edge, on the other hand, also gives the important information concerning the tail states, and this slope is often called "Urback edge". The absorption coefficient in the Urback regime can be expressed by[43,44)]

$$\alpha = \alpha_0 \exp\left(\frac{E - E_f}{E_0(T,X)}\right), \qquad (4\text{-}11)$$

where E_f is the Urback focus and $E_0(T,X)$ is a function of temperature (T) as well as static disorder (X). In addition, it is known that these two contributions of thermal and static disorder to E_0 can be separeted,[43)]

$$E_0(T,X) = E_0(T) + E_0(X)\ . \qquad (4\text{-}12)$$

From the Einstein single oscillator model, $E_0\,(T)$ is calculated by

$$E_0(T) = A\left(\frac{1}{\exp(\theta / T) - 1}\right), \qquad (4\text{-}13)$$

where θ is Debye temperature of the crystal. As a result, from the temperature dependence of the Urback parameters, $E_0(T,X)$, the statistical disorder in the crystals, $E_0(X)$, can be estimated using Eqs. (4-11)~(4-13).

Figure 4-23 shows the temperature dependence of the PC spectra for $(ZnS)_3(ZnSe)_{42}$ ordered alloy measured from 40 to 290 K. In this ordered alloy which is lattice matched to the substrate, two clear Urback focus can be seen depending on the two temperature region. At the low temperature region denoted as E_{F2} (40~160 K), the Urback parameter of the PC spectra shows excitonic absorption process, and does not reflect the statistical potential disorder in the crystal. At the higher temperature region (200~290

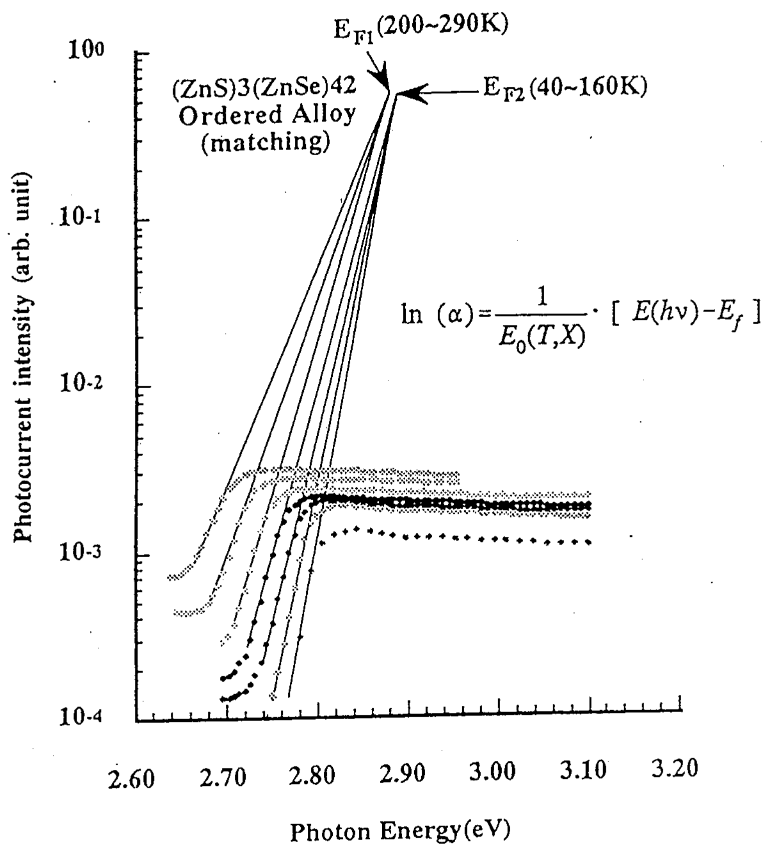

Figure 4-23 The temperature dependence of the PC spectra for $(ZnS)_3(ZnSe)_{42}$ ordered alloy measured from 40 to 290 K. E_F indicates the Urback focus obtained from the slope of the absorption edge.

K), the excitonic absorption disappears due to the exciton thermalization by the increased temperature. Consequently, $E_0(T,X)$ was determined from the Urback parameters where the effect of the exciton is negligible. In $(ZnS)_1(ZnSe)_4$ ordered alloy, on the contrary, only one E_F was observed in the temperature dependence of the PC spectra probably due to the high strain effects.

Figure 4-24 shows the Urback parameter $E_0(T,X)$ of the ordered alloys plotted as a function of the temperature. The theoretical lines calculated from Eqs. (4-12) and (4-13) are also indicated in the figure. In this figure, only the Urback parameters obtained at high temperature are shown. As shown in Fig. 4-24, the Urback parameters of the ordered alloys increase as the sample temperature increases due to the phonon-interaction. The calculated values show good agreements with the observed values, and the

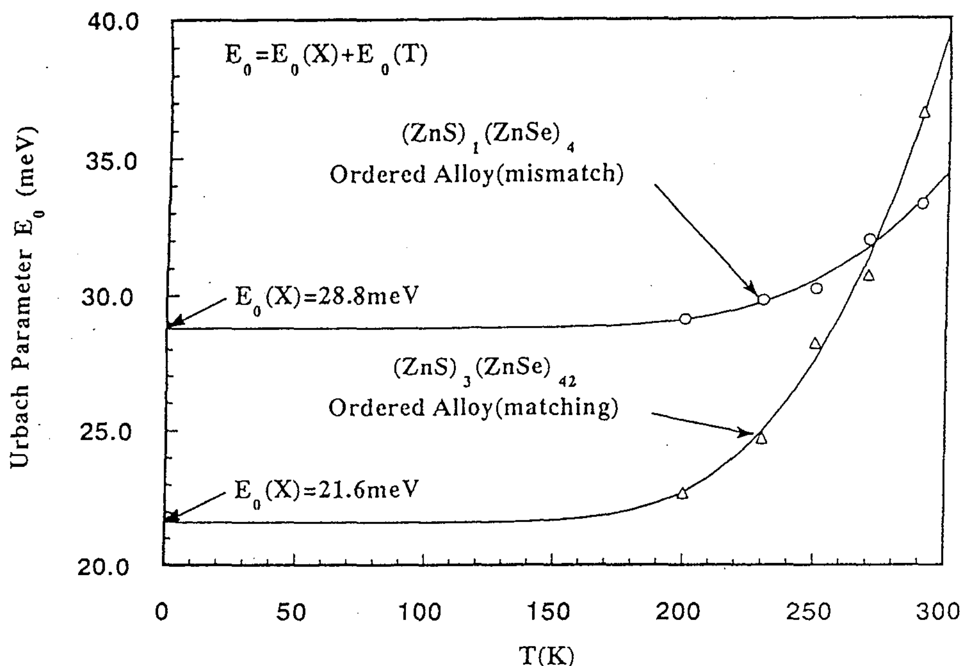

Figure 4-24 The Urback parameter $E_0(T,X)$ of the ordered alloys plotted as a function of the temperature. The calculated theoretical lines are also indicated.

best fitting curves were obtained using parameters of A=15 and θ=274. As a result, the $E_0(X)$ is calculated to be 21.6 meV for $(ZnS)_3(ZnSe)_{42}$ and 28.8 meV for the $(ZnS)_1(ZnSe)_4$ ordered alloys, respectively. Obviously, $(ZnS)_1(ZnSe)_4$ has the higher disorder parameter than $(ZnS)_3(ZnSe)_{42}$ ordered alloy, which is consistent with the result obtained from the XRD or PL spectra. The temperature dependence of the PC measurements, therefore, enables the quantitative analysis of the crystal with regard to the statistical disorder.

4.4 Optical properties of sawtooth superlattice (STS)

In the previous section, we determined the fundamental characteristics and exciton dynamics of $(ZnS)_n(ZnSe)_m$ ordered alloys (n=1~4). In this section, larger scale variations in band-gap are further introduced by the structure of "Sawtooth superlattice" for the purpose of developing a new optical device.

4.4.1 Introduction to Sawtooth superlattice

Recently there has been an intense efforts to use semiconductor quantum well based devices in photonic applications.[45,46] In particular there is the potential to use the quantum-confined Stark effect (QCSE) for electrically controlled absorption and photoluminescence (PL) spectrum.[47,48] To date several QCSE device configurations have been demonstrated.[45-48] Usually, these particular QCSE devices employed III-V compound semiconductors. Other semiconductor materials such as the II-VI semiconductors, ZnS and ZnSe in particular, also have appropriate optical properties for QCSE devices. Since II-VI semiconductors have larger band-gaps, the possibility exist of fabricating devices that function at shorter wavelengths than the corresponding III-V devices. Other advantageous characteristics of this II-VI semiconductor system include a large valence band offset (ΔE_V~0.9eV) and large exciton binding energy of 20meV. Therefore it is reasonable to believe that an exciton trapped in a ZnS-ZnSe quantum well could be exploited for the purpose of short wavelength optical modulation.

Optical absorption can be modulated using several quantum well configurations including: rectangular[45], parabolic[49] and asymmetric triangular quantum wells (ATQW).[47] Among these quantum wells, ATQW is the most attractive structure for QSCE since this structure produces a more pronounced optical effects such as absorption[50] and also demonstrates lower operating voltage ranges as well.[48] Sawtooth superlattices (STS) are special case of ATQW in which the quantum well structure is repeated creating a sawtooth-like band profile. One potential application of such a device is high speed optical modulators for communication applications.

Figure 4-25 (a) shows the schematic structure of the STS investigated in this section. This STS structure consist of ZnS and ZnSe layers where the

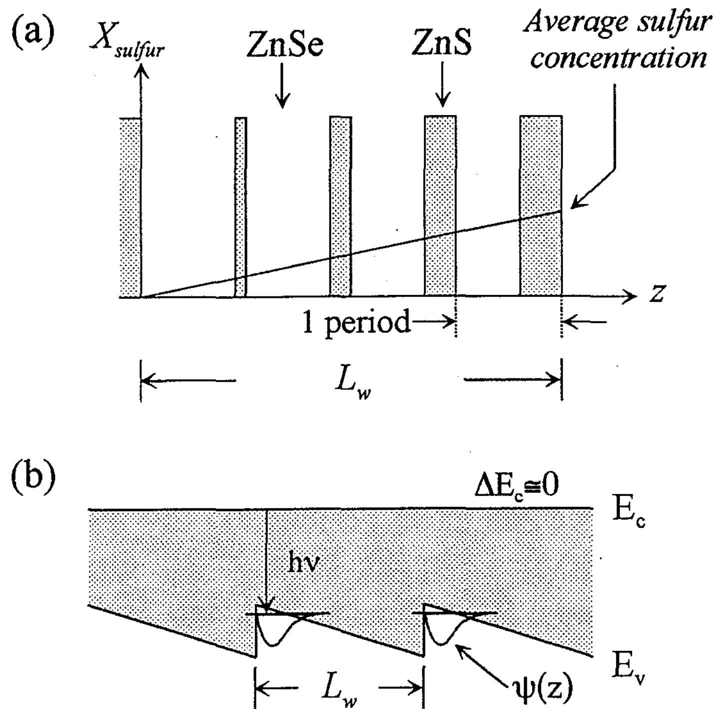

Figure 4-25 The layer-by-layer structures of the ZnS-ZnSe STS with quantum well width of L_W toward the growth direction (a) and the band diagram of STS (b).

ATQW width is L_w. In the STS structure, the ZnS layer thickness relative to that of ZnSe are gradually increased in succeeding regions (z), while holding the thickness of 1 period constant. Consequently, the average sulfur concentration are pseudomorphically described by a solid line in Fig. 4-25 (a), since these fine scale changes are expected to behave as graded sulfur potentials. In this method, the slope of the graded potential are easily controlled by changing each layer thickness ratio. In addition, the formation of defects caused by the lattice mismatch can be suppressed by this layer-by-layer structures using the opposite strain effect of ZnS and ZnSe layers on GaAs (100) substrate, as discussed in section 4-2. The band diagram of ZnS-ZnSe STS are shown in Fig. 4-25 (b). In this STS, the strongest effect is valence band modulation since the conduction band offset between ZnS and ZnSe is small ($\Delta E_c \cong 0$).[11] Accordingly, the localization of the wave function ($\psi(x)$) in this STS occurs at near the valence band minimum.

In this section, the fabrication of Zn(S,Se) STS by ALE are reviewed for the first time. The optical properties of STS at low temperature are investigated to characterize the graded potential structures by conventional

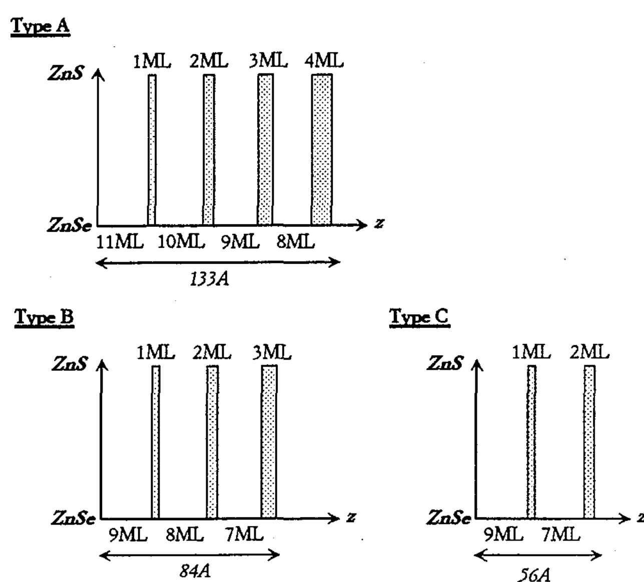

Figure 4-26 The three types of STS structures used in this study (type A, B, and C). The letters "ML" denote the number of monolayers.

PL and time-resolved PL measurements. In addition, the density of states of the graded potential in the STS was further investigated by the photocurrent (PC) spectra. All the STS samples investigated here were grown on GaAs (100): Cr, O substrate by HRCVD at the substrate temperature of 200°C.

Three type of STS structures (Type A, B and C) which have different L_w were grown in this study. These three STS structures had the same total sulfur concentration of 20at%. The maximum thickness of ZnS layer in these STS is about 10Å (4 monolayers) in order to prevent the lattice relaxation of ZnS layers on GaAs substrate. The layered structures of type A, B and C are shown in Fig. 4-26. For the purpose of comparison, the ordered alloy of $(ZnS)_1(ZnSe)_4$ which have the same sulfur composition were grown at the similar growth condition. The total thickness of the entire STS and the ordered alloy crystal were kept constant at 1400Å for this study.

4.4.2 Structure & PL properties of STS

The layer-by-layer structure of the STS samples were determined from XRD spectra. Figure 4-27 shows the XRD spectra of STS samples of type A and B. The total sulfur compositions in STS samples were confirmed to

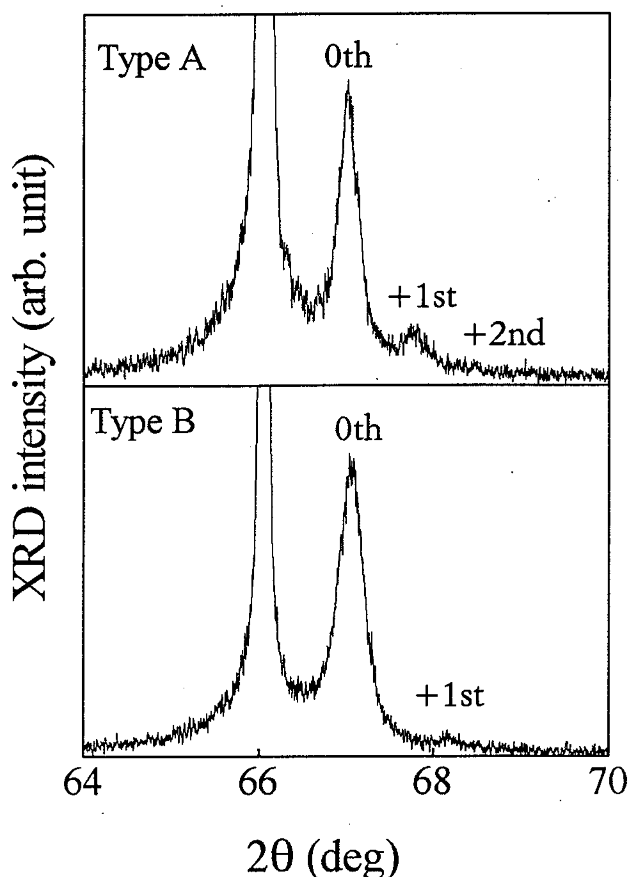

Figure 4-27 The XRD spectra of the STS samples of type A and B.

be 20at% by auger electron spectroscopy. In Fig 4-27, sharp diffraction peaks at 66 deg are the (400) diffraction of GaAs substrate. Rather broad 0-order diffraction peaks of 500 arcsec at full width at half maximum (FWHM) were observed in these sample due to the large composition of sulfur. In these two types of STS, the 0-order peak show the same diffraction angle since these two sample have the same sulfur composition. The satellite peaks which correspond to the periodic quantum well structures were observed in these STS. The calculated thickness of L_w from these satellite peaks are 134Å (type A) and 88Å (type B) and agreed quite well with the intended thickness of 133Å and 84Å, respectively. The type C sample also shows good agreement. These evidences clearly indicate that the grown STS have the periodic structure with designed number of layers.

Figure 4-28 shows the PL spectrum of STS sample of type A measured at 25K. In the PL spectrum of type A, only the strong blue emission with its FWHM of 20meV was observed and other defects-oriented peaks were not

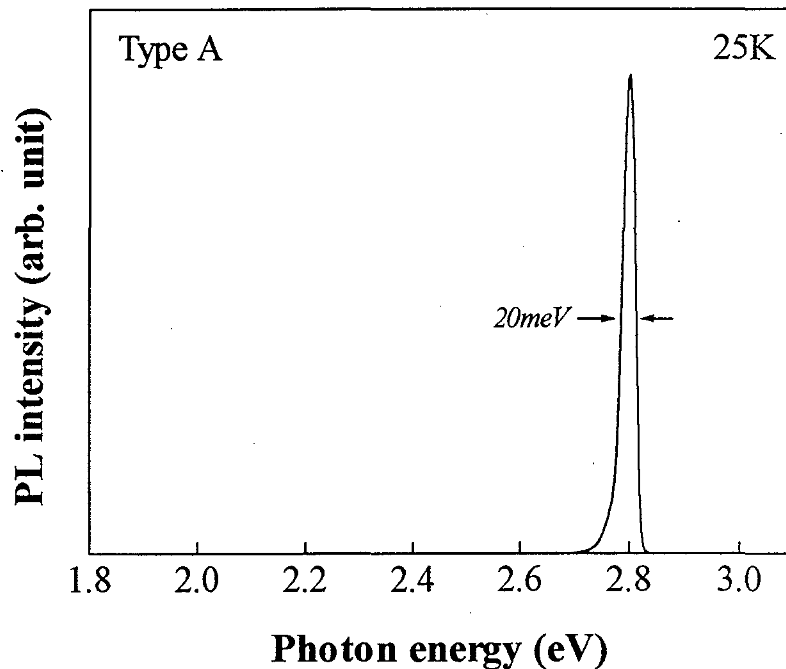

Figure 4-28 The PL spectrum of STS sample (type A) measured at 25 K.

shown. The emission intensity of this sample are about two order of magnitude higher than that of $(ZnS)_1(ZnSe)_4$ which represent the conventional properties of ZnS_xSe_{1-x} with same composition. Moreover, this band-edge emission peak of STS persists up to the room temperature, while the emission of $(ZnS)_1(ZnSe)_4$ is quenched at ~160K. Other STS samples show similar properties as the type A sample. Therefore, the recombination probabilities are increased by the formation of the graded potential well. In addition, it should be noted that the defect formation caused by the lattice mismatch must be negligible even at the sulfur content of 20at%. The PL peak energies of the STS at 25K are shown as a function of L_w in Fig. 4-29 (a). The peak energy of $(ZnS)_1(ZnSe)_4$ is also indicated by the dotted line in the figure. As shown in Fig. 4-29, the peak energies of the STS gradually increased toward the peak energy of the $(ZnS)_1(ZnSe)_4$ with decreasing L_w of these STS. This effect can be explained by the quantum size effects of the ATQW since the average composition of all the STS structure is same. This result suggests that the confinement of exciton occurs by the graded potential formed at the valence band. As a result, it is proved that the graded potential can be prepared by varying short-range

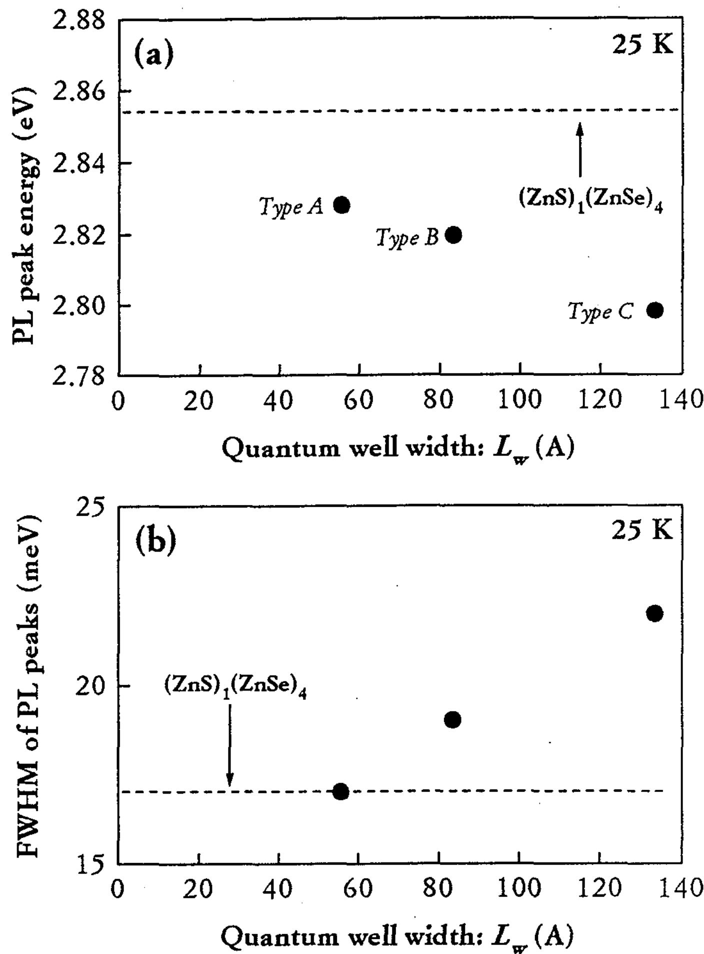

Figure 4-29 The PL peak energies of the STS (a) and the FWHM of the PL peaks plotted as a function of the quantum well width (L_w) of the STS. The dotted lines indicate the value for $(ZnS)_1(ZnSe)_4$ ordered alloy.

thickness ratio of ZnS and ZnSe layers. The FWHM of the PL peaks in these STS, on the other hands, slightly increases from 17 meV (type C) to 22 meV (type A) with increasing L_W of the STS, as shown in Fig. 4-29 (b). This increased potential fluctuations in the graded potential are attributed to the local compositional fluctuation at the heterointerfaces due to the large modulation in the wider quantum well. The strain-induced potential fluctuation may be another reason for this peak broadening since the STS having wider L_w induces the inhomogeneous distribution of the strain in the crystal.

In order to determine the density of states in these STS structure, we

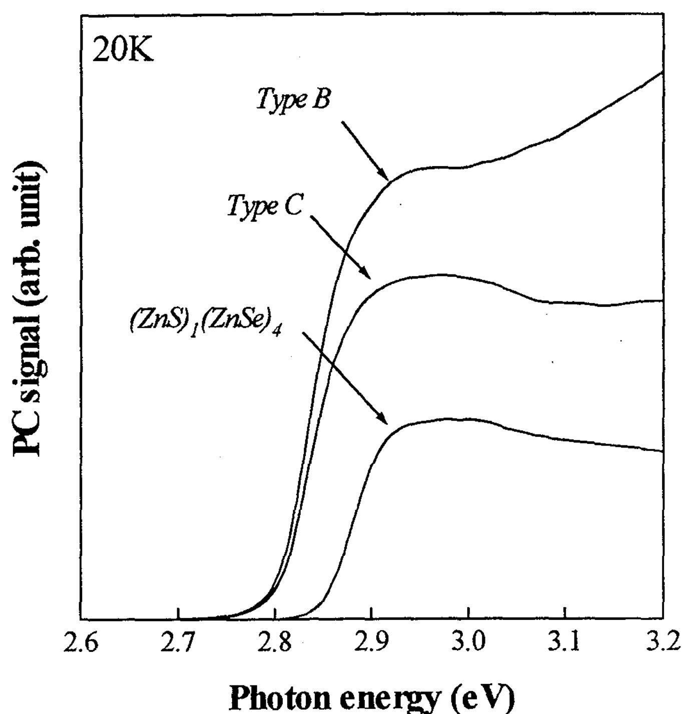

Figure 4-30 The PC spectra of STS (type B and C) and $(ZnS)_1(ZnSe)_4$ ordered alloy measured at 20 K.

measured the PC spectra. Figure 4-30 shows the PC spectra of the STS (type B and C) and $(ZnS)_1(ZnSe)_4$ ordered alloy measured at 20 K. In the PC spectra, the absorption edge monotonously shifts to the higher energy side with decreasing L_w, which is consistent with the result observed in the PL peaks. All the samples show the exciton absorption peaks, and these peaks become clearer as the thickness of L_w increases. This fact also indicates the existence of the confinement states because the confinement of holes (or electron) in quantum well generally provides the sharp absorption edge. Most importantly, the PC signal of the STS also rapidly increases with the changes in the well thickness, indicating the higher absorption coefficient in the STS than in the ordered alloy. In addition, the PC spectra of the STS shows the high PC signals at the high energy region (>3.0 eV), which reflects the sequential density of states arisen from the graded potential. So far, similar absorption profiles were reported in graded-index separate confinement heterostructures (GRINSCH) of AlGaAs crystals.[52] From the results mentioned above, it can be concluded that the graded potential of the STS provides the sharp absorption edge and also high absorption

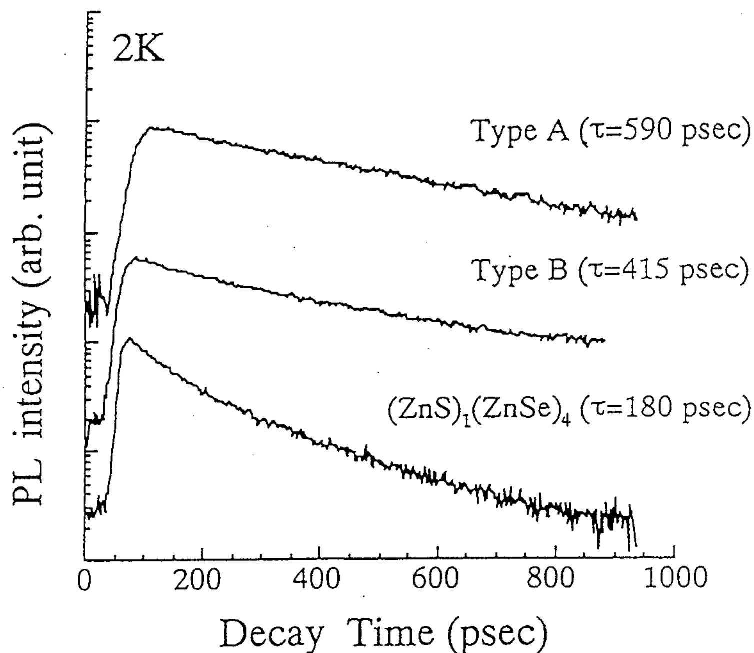

Figure 4-31 The time-resolved PL spectra of the STS (type A and B) and $(ZnS)_1(ZnSe)_4$ at 2K. The obtained life times from Eq.(4-9) are also shown.

coefficient, which is quite useful for various optical device applications.

Figure 4-31 shows the time-resolved PL spectra of the STS (type A and B) and $(ZnS)_1(ZnSe)_4$ at 2K. Emission life time (τ_d) are determined by fitting the PL decay line to the theoretical curve using Eq. (4-9), and the calculated exciton life times are plotted as a function of L_w in Fig. 4-32. In this figure, the exciton life times obtained from the various monitor wavelength are also shown, and the plots labeled "peak" indicate the exciton life time at the PL peak while the plots of ±20 meV shows the life time monitored at 20 meV higher (or lower) position from the PL peaks.

As shown in Fig. 4-31, the emission life time of type A STS at the PL peak is 590 psec, and decreased with decreasing the thickness of L_w. Obviously, this result is caused by the quantum confinement effect since the decreasing well thickness increases the overlap of the wavefunction, which leads to the reduction in the exciton life time, as expressed by Eq. (4-10). In other words, the confinement effect at the quantum level in the STS stabilizes the exciton formation at the valence band. As shown in Fig. 4-32, the exciton life time of the STS changes depending on the monitored wavelength; the

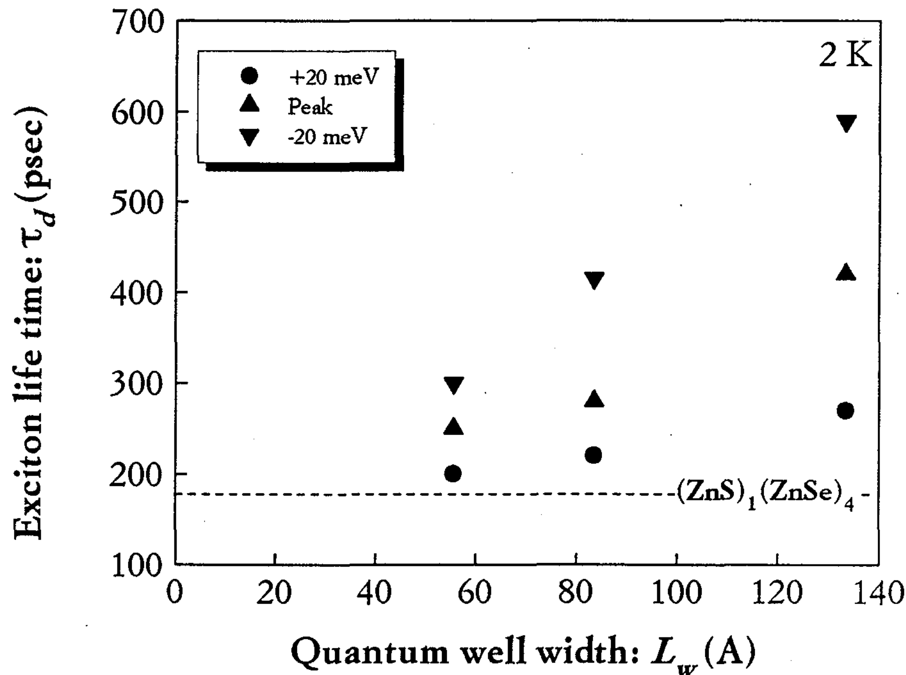

Figure 4-32 The exciton life time of the STS samples plotted as a function of the L_w. The exciton life times obtained from various monitor wavelength are also shown: peak indicates the exciton life time at the PL peak, ±20 meV shows the life time monitored at 20 meV higher (or lower) position from the PL peaks. In addition, the exciton life time of $(ZnS)_1(ZnSe)_4$ is also indicated as the dotted line.

exciton life time is longer at the lower energy side of the PL peaks. In addition, the difference in the exciton life time depending on the monitored wavelength becomes larger as the L_w of the STS increases. In the ordered alloy, on the other hand, the exciton life time is independent of the monitor wavelength. Accordingly, these results indicate that the localized state is formed in the STS due to the thickness fluctuation in the quantum well, and the formation of the localized state is enhanced as the thickness of L_w increases. This effect is also confirmed from the PL peak broadening observed in Fig. 4-29 (b).

From the results mentioned above, it is shown that the STS with low defect density can be prepared by modifying layer-by-layer structures of each layer of ZnS and ZnSe. The fabrication of STS structure was confirmed by the strong blue emission with longer emission life time. These strong blue emissions are consistent with the formation of exciton trapped in the potential well formed by the graded potential.

In summery of this section, three types of sawtooth superlattice (STS) were fabricated by ALE using HRCVD. Satellite peaks which correspond to the thickness of quantum well were observed in all the STS grown. Dominant blue band-edge emissions were shown in their photoluminescence spectra and shifted to the higher energies with decreasing quantum well width. From the time-resolved PL spectra, these emissions were confirmed to originate from the localized state near the band-edge region of the STS. Above results clearly show that the large band-profiling are possible by the STS without forming defects in the crystal.

4.5 Crystal structure stability in Zn(S,Se) ordered alloys

Most recently, defect generation in ZnSe crystals under the high excited-state attracts is attracting wide attention since this effect seriously degrades the device performance of the laser diodes.[53-55] Especially in II-VI crystals which have the localized ionic bonding, strong electron-lattice interaction is expected, which induces the microstructure changes such as defect formation, sublimation or impurity migration. In this section, therefore, the crystal structure stability of the ordered alloys was investigated. The stability of the ordered alloys were determined from both photo- and thermal-induced degradation effect. In addition, these results were further characterized by comparing with that of the lattice relaxed ZnSe crystals in order to determine the defect-formation mechanisms.

4.5.1 Photo-induced degradation effect

In order to determine the photo-degradation effect in the crystal, we used two types of crystal structure; the lattice matched $(ZnS)_3(ZnSe)_{42}$ ordered alloys and the lattice relaxed ZnSe crystal. The thickness of the crystals was 5000A for both case. The photo-degradation of these crystals was carried out using Nd:YAG laser (355 nm: THG) as a light source. Basically, the operating condition of the YAG laser is same with that used in the PL measurement. The laser power, however, was increased to 4 mJ/pulse (power density: 200 kW/cm^2) to accelerate photo-degradation of the crystal.

When the high-intensity pulsed-laser is irradiated to the crystal, the laser light usually causes the temperature rise on the sample surface. The temperature rise on the surface by the laser irradiation can be calculated by solving the thermal-conductive equation as follows:

$$\Delta T = \frac{2(1-R)F}{\sqrt{\pi \lambda C_p P}}\sqrt{t}, \tag{4-14}$$

In Eq. (4-14), R is the reflectivity of ZnSe (R=0.26), and F is the laser power density, λ is thermal conductivity of the crystal (0.045 cal/cm°Csec), C_p is the heat capacity (0.086 cal/°Cg), p is the density of the crystal (5.263 g/cm^3), and t is the FWHM of laser pulse, respectively. Assuming the full

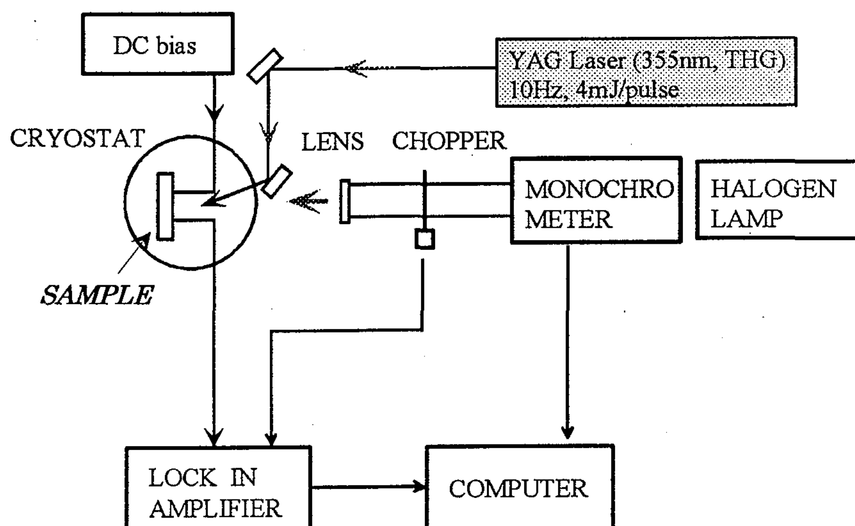

Figure 4-33 The experimental setup for the photo-degradation by YAG laser together with the photocurrent (PC) spectra.

conversion of laser light to the sample heating, the temperature rise on the surface can be estimated to be ΔT=180 °C at most. This temperature is lower than the typical substrate temperature of HRCVD. Accordingly, the sample heating effect by the laser light is negligible in this experiment.

The photo-degradation effects of the crystals were mainly determined from the PC and PL spectra. One of the advantages of the PC measurement include the determination of the depth profile by changing the wavelength of the probe lights which have the different penetration depth. The experimental setup for the photo-degradation and PC measurement is shown in Fig. 4-33. This experimental setup enables the photo-degradation by YAG laser together with the PC measurement without changing the location of the samples, as shown in Fig. 4-33. The photo-degradation was made for two hours (~10^5 laser pulses) at the room temperature, and the changes of the PC and PL spectra were investigated.

Figure 4-34 shows the PC spectra of $(ZnS)_3(ZnSe)_{42}$ ordered alloy and ZnSe crystal for the different number of YAG laser pulses. In this figure, the each PC spectra were normalized by the initial PC spectra since the PC signal gradually decreases with the laser irradiation. In the PC spectra of ZnSe crystal, the reduction in the PC signal intensity can be seen at higher photon energy due to the surface recombination caused by the lattice relaxation. On the other hand, the ordered alloy shows a constant signals after the band-to-band transition occurs at 2.7 eV, indicating the small

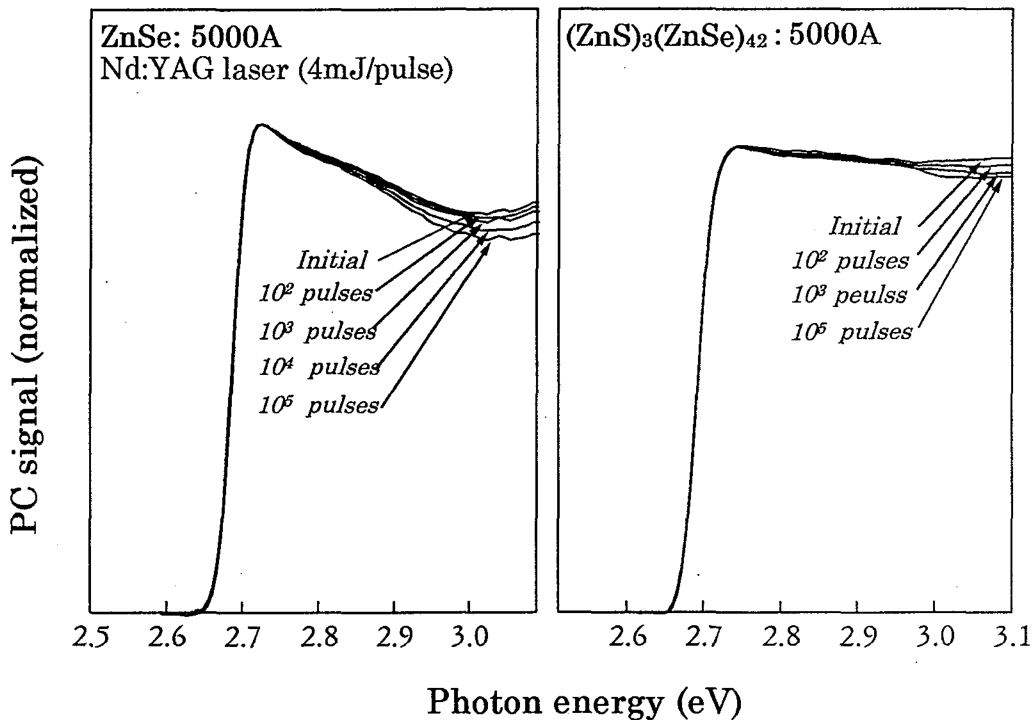

Figure 4-34 The PC spectra of $(ZnS)_3(ZnSe)_{42}$ ordered alloy and ZnSe crystal for the different number of YAG laser pulses.

surface defect densities. As shown in Fig. 4-34, the photo-degradation effects of these crystals can be observed mainly at the higher energy region in both structures. These results indicate that the photo-induced defect formation takes place at the surface region due to the small penetration depth of the YAG laser light (~500Å). It is evident that the ordered alloy shows smaller degradation as compared with the lattice relaxed ZnSe crystal.

Figure 4-35 shows the PC signal intensity ratio of ZnSe and the ordered alloys plotted as a function of the number of YAG laser pulses N. The PC signal intensities are normalized by the initial one, and the signal intensity for different monitor photon energy (2.7 and 3.0 eV) are also shown in this figure. As shown in Fig. 4-35, the PC signal intensities for ZnSe and the ordered alloy rapidly decrease as the number of laser pulses increases. The ordered crystal, however, shows saturation with increasing laser pulses, while the signal for ZnSe crystals continue to decreasing after the saturation of the ordered alloy can be seen. In both cases, the degradation effect is larger at the surface region, which is consistent with the result in Fig. 4-34. From these results, it is shown that the native defects in ZnSe crystals

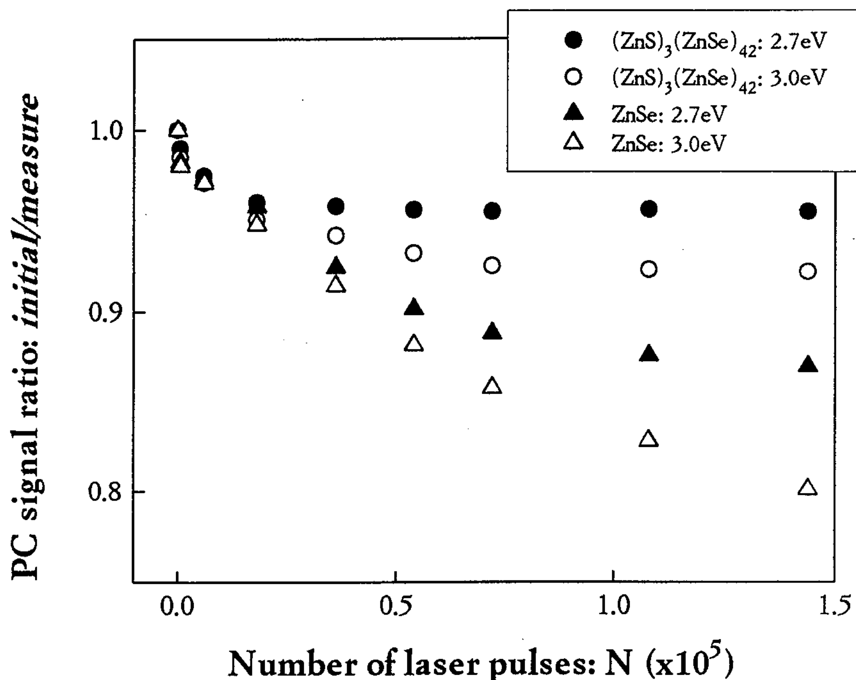

Figure 4-35 The PC signal intensity ratio of ZnSe and $(ZnS)_3(ZnSe)_{42}$ plotted as a function of the number of YAG laser pulses *N*. In this figure, the PC signal intensities are normalized by the initial one

originate from the lattice relaxation enhance the photo-degradation under the high-intensity laser pulses.

Figure 4-36 shows the PL spectra of the ZnSe crystal measured at 25 K for the different number of laser pulses. In the PL spectrum of ZnSe crystal without laser irradiation, the dominant band-edge emission is donor-bound exciton peak and the increased deep level emission intensity was shown due to the lattice relaxation. The PL peaks at 2.75 eV is assigned to the emission due to the formation of Se-vacancy. As shown in Fig. 4-36, this emission peak rapidly increases with increasing laser pulses, indicating the formation of vacancy defects. The deep level emission also increases together with the number of laser pulses. In addition, the reduction in the band-edge emission intensity was indicated, which might be caused by the generation of non-radiative recombination centers. In the ordered alloy, on the other hand, only the reduction in the band-edge emission intensity was observed, and other new defect-oriented PL peak was not indicated.

Consequently, it was shown that various types of defects are formed in ZnSe crystals by the strong light irradiation. These photo-induced defect

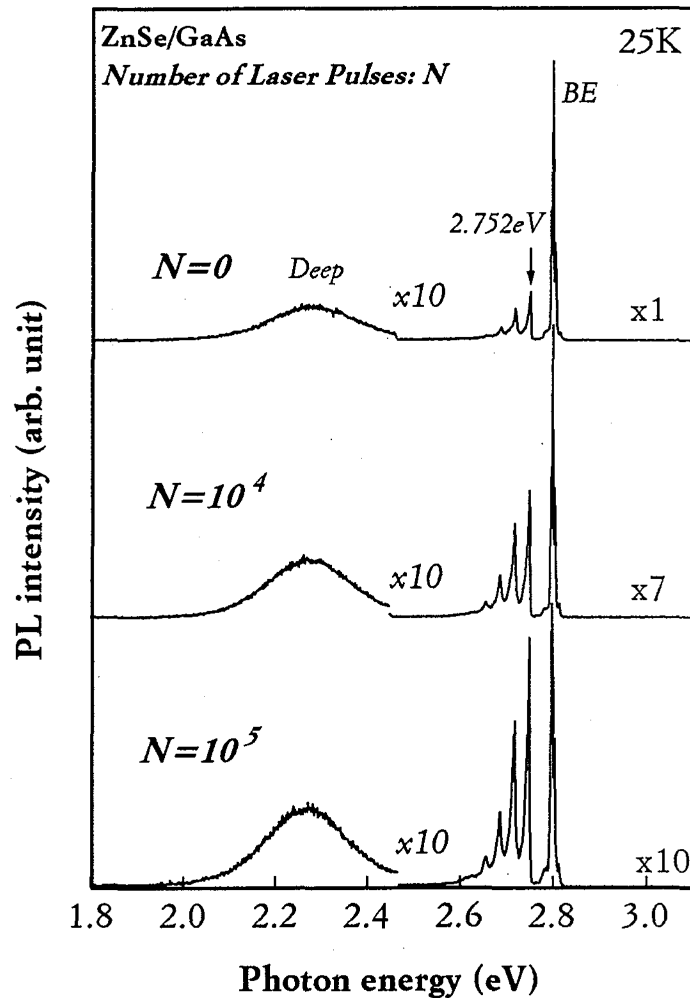

Figure 4-36 The PL spectra of the ZnSe crystal measured at 25 K for the different number of laser pulses.

formation is considered to originate from the dislocation in the ZnSe crystal since the ordered alloy shows much smaller photo-degradation effects. In fact, it has been reported that high-density current injection leads to the generation of dislocation network in the ZnSe-based heterostructures, which act as the non-radiative recombination centers.[53,54)] Most recently, the degradation of (Zn,Cd)Se quantum well structure by the laser pulse was also reported.[55)] From the TEM observation, it was suggested that the stacking faults at the heterointerface are the source for the current- or photo-induced defect formation.[53-55)] These facts agree well with the results observed in this study, and the similar mechanism is expected for photo-induced defect creation. In the ordered alloys, on the contrary, the photo-degradation is

effectively suppressed as shown in Fig. 4-35. This result indicates that the photo-degradation effects can be reduced by the layer-by-layer structure of the ordered alloy. This fact could be explained in terms of the suppression of the stacking fault formation at the interface since the high strain field at the ZnS-ZnSe heterointerface in the ordered alloys is expected to prevents the propagation of the stacking faults (or dislocation), as discussed in section 4.2. Accordingly, it can be concluded that the 2-dimensional structure of the ordered alloys is relatively stable for the photo-degradation, even though this crystal has the microscopic strained layer structures.

4.5.2 Thermal-induced degradation effect

Thermal-induced defect formation was also investigated for the lattice matched $(ZnS)_3(ZnSe)_{42}$ ordered alloy and the lattice relaxed ZnSe crystal in order to clarify the thermal stability of these crystals. The sample thickness of these crystals was maintained to 5000Å. The thermal annealing of the crystals was made in a temperature range from 200 to 470°C for 5 min under the atmosphere of N_2 gas flow, and the resulting crystal degradations were characterized by the PL and XRD spectra.

Figure 4-37 shows the lattice parameters of the ordered alloy and ZnSe crystal plotted as a function of the thermal annealing temperature. A distinctive difference can be seen in the changes of the lattice parameters with the temperature in these two types of the crystals. In the ZnSe crystal, the lattice parameter gradually decreases at the annealing temperature higher than 300°C. The small lattice parameters at the higher temperature region in the ZnSe crystal are caused by the strain effects induced by the difference in the thermal expansion coefficient between ZnSe crystal and GaAs substrate. It should be noted that ZnSe crystal annealed at 200°C also show the small lattice parameter reduction, although this temperature corresponds to the growth temperature of the crystal by HRCVD. This result is another evidence that the lattice parameter of crystal changes during cooling process to room temperature after the crystal growth.

On the other hands, the lattice parameter of the ordered alloy remains unchanged within the whole temperature range measured. This effect can be attributed to the coherent structure of the ordered alloys; during the cooling process the generating thermoelastic strains are elastically absorbed

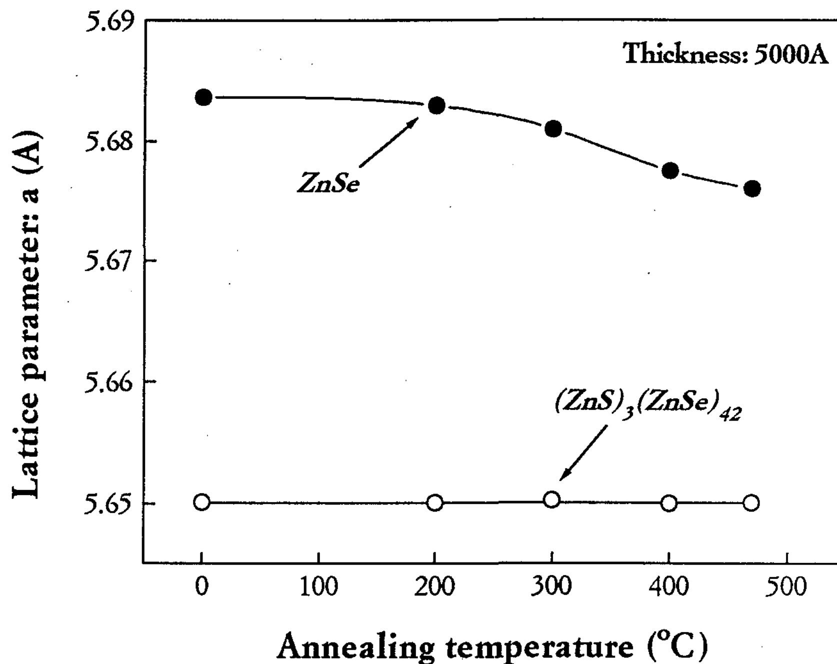

Figure 4-37 The lattice parameters of $(ZnS)_3(ZnSe)_{42}$ ordered alloy and ZnSe crystal plotted as a function of the thermal annealing temperature.

by the layered structure of the ordered alloys. In addition, the satellite peaks in the XRD spectra of these ordered alloys did not show any changes by the thermal annealing. Accordingly, it is evident that the structure of the ordered alloys is highly stable under the thermal annealing up to 500°C.

Figure 4-38 shows the FWHM of the (400) diffraction peaks for the ordered alloy and the ZnSe crystal obtained from the x-ray rocking curves. In this case, the FWHM of the ordered alloy also remains unchanged by the thermal annealing. The sharp diffraction peaks of the ordered alloy (~50 arcsec) imply the high stability of the coherent structures. On the other hands, ZnSe crystals shows the significant broadening effect; the FWHM of the diffraction peak increases linearly with the annealing temperature. This result indicates that the reduction in growth temperature is essential for the fabrication of high quality crystal to suppress the thermoelastic strain effect.

Figure 4-39 shows the PL spectra of ZnSe and the ordered alloy near the band-edge region for the different annealing temperatures measured at 25 K. In the ZnSe crystal, all the band-edge emission peaks shift to the lower energy side, corresponding to the change of the lattice parameters as shown in Fig. 4-37. In addition, the low temperature PL measurement further

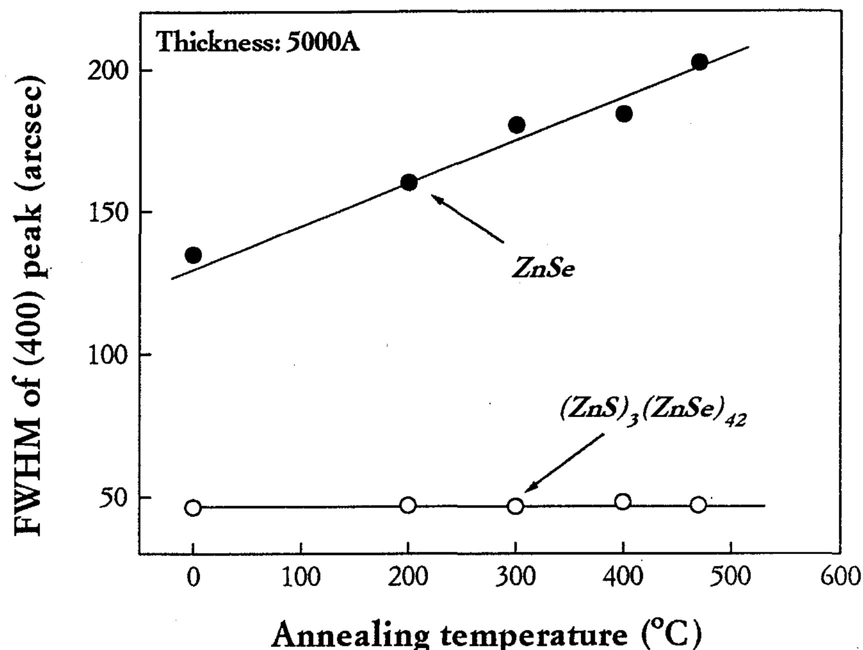

Figure 4-38 The FWHM of the (400) diffraction peaks for $(ZnS)_3(ZnSe)_{42}$ ordered alloy and the ZnSe crystal obtained from the x-ray rocking curves.

induces the thermoelastic strain effects in ZnSe crystal as compared with the XRD spectra measured at room temperature. At annealing temperatures higher than 400°C, a new PL peak can be seen and this PL peak becomes the dominant emission after annealing at a temperature of 470°C. This emission is assigned to I_v emission because of its localization energy (energy difference from the free exciton peak) of 23 meV. This PL emission was reported to originate from the structural defects such as dislocations or stacking faults.[52)] Consequently, it is suggested that the high temperature annealing of ZnSe crystal generates the dislocations due to the thermoelastic strain effect. The rapid reduction in the PL peak intensity at the higher temperature annealing also supports this speculation.

As shown in Fig. 4-39, no remarkable shift of the PL peak was observed in the ordered alloy depending on thermal annealing at temperatures below 470°C, which agrees well with the result confirmed from the XRD measurement. At the annealing temperate of 470°C, however, I_v emission appear in the PL spectrum of the ordered alloy, indicating the generation of the structural defects. It should be mentioned that the I_v emission intensity of the ordered alloy is small compared with that of ZnSe crystals.

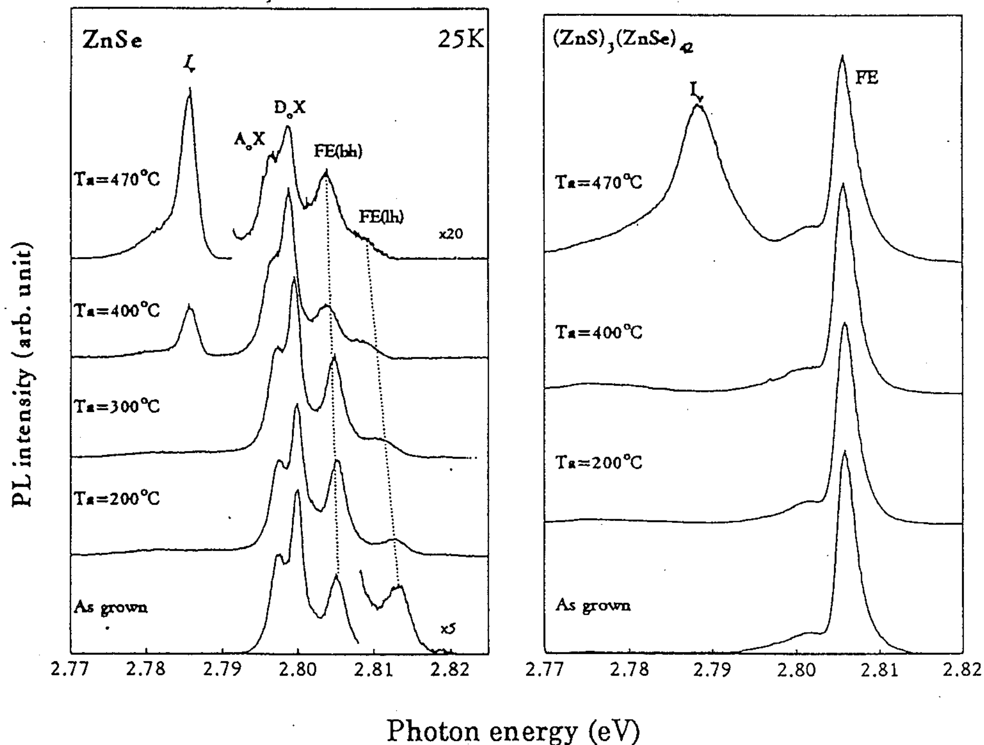

Figure 4-39 The PL spectra of ZnSe and $(ZnS)_3(ZnSe)_{42}$ ordered alloy near band-edge region for the different annealing temperatures measured at 25 K.

Figure 4-40 shows the wide-range PL spectra of the ZnSe and the ordered alloy which correspond to the band-edge PL spectra of Fig. 4-39. As mentioned above, the dominant emission in the ZnSe after annealing at 470°C is Iv emission, and the strong LO-phonon replica can be seen in the same spectra. In addition, a weak deep level emission appears at around 2.0 eV probably due to the defect complex formation. In the ordered alloy, the strong I_v emission with LO-phonon replica was also observed together with the dominant free exciton emission. The deep level emission of the ordered alloy slightly increases with the annealing temperature because of the increased defect formation.

In summary of this section, we determined the photo- and thermal-stability of the lattice matched $(ZnS)_3(ZnSe)_{42}$ ordered alloy and the lattice relaxed ZnSe crystal. The photo-induced defect formation was found for the ordered alloys as well as the ZnSe crystal from the PC spectra.

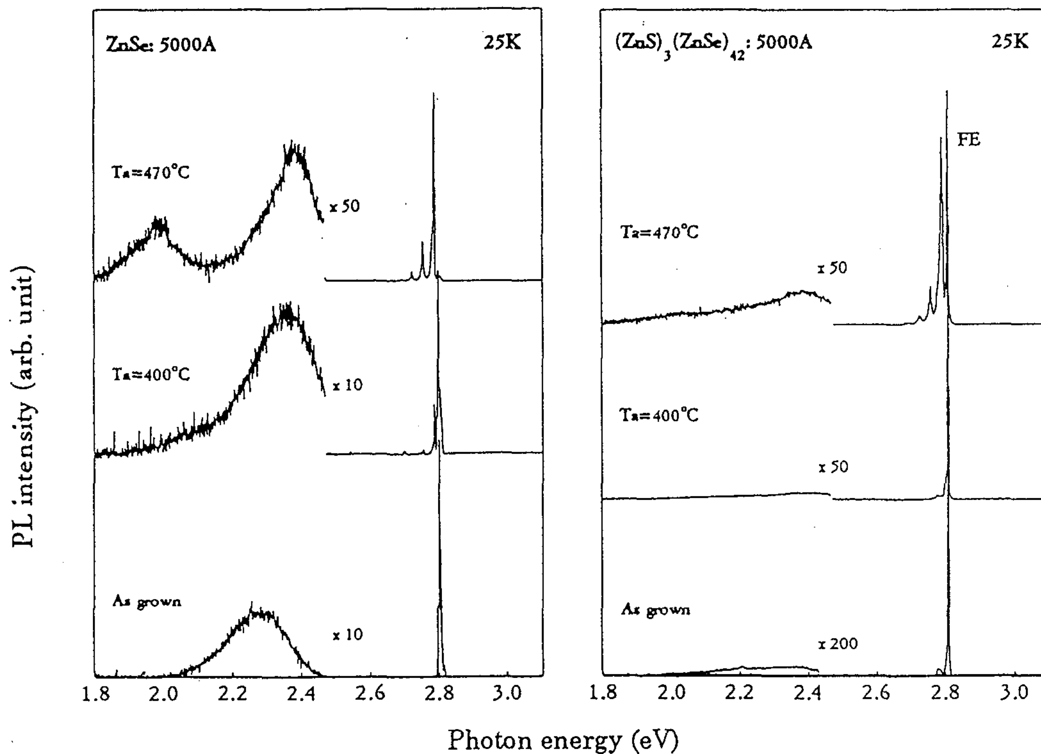

Figure 4-40 The wide-range PL spectra of ZnSe and $(ZnS)_3(ZnSe)_{42}$ ordered alloy which correspond to the band-edge PL spectra of Fig. 4-39.

Nevertheless, the suppression of the photo-degradation effects was indicated in the ordered alloys compared with the ZnSe crystal since the generation of the dislocation can be effectively prevented by the layer-by-layer structure of the ordered alloy. The reduction in the structural defect formation in the ordered alloy caused by the thermal annealing was also confirmed from the XRD and PL spectra. In ZnSe crystal, on the contrary, the thermal annealing leads to the degradation of crystal properties due to the thermoelastic strain effect induced by the difference in the thermal expansion coefficient. Accordingly, it can be concluded that the strained 2-dimensional structure of the ordered alloy provides highly stable crystal for both photo- and thermal-induced degradation.

Chapter 5

Carrier Transport Properties of Zn(S,Se) Ordered Alloys

Carrier transport properties of $(ZnS)_3(ZnSe)_{42}$ ordered and $ZnS_{0.07}Se_{0.93}$ disordered alloys are investigated in this chapter. In the ordered alloys having 2-dimensional ordered structures, a higher electron mobility is expected compared with the disordered alloys due to suppression of the "disorder scattering" induced by local compositional fluctuations. In order to determine the carrier transport properties of these structure, n-type doped samples were prepared using triethylgallium (TEGa) and isobutyliodide (i-BuI). The optoelectronic properties of the resulting n-type crystal films are described in detail. Carrier scattering mechanisms and donor activation processes in the ordered and disordered alloys are further investigated using a temperature dependence of Hall measurement.

5.1 Growth of n-type Zn(S,Se) crystals using TEGa

First Ga doping was attempted using a TEGa since this source molecule has a low vapor pressure and small bond strength of alkyls. Ga-doping of MBE grown ZnSe crystals has been reported.[1,2] In addition, successful fabrication of n-type ZnSe crystals by MBE or MOVPE has also been reported using other column III atoms, such as Al [3-5] and In atoms.[6]

The Ga source was introduced during the Zn source pulse in ALE-mode since Ga substitutes for Zn lattices. The structure of the ordered alloys was set at $(ZnS)_3(ZnSe)_{42}$ (sulfur content: 7 at%) to provide the lattice matching to GaAs substrate. Lattice relaxation effects and the resulting defect formation can be minimized at this sulfur content. All Ga-doped ZnSe and

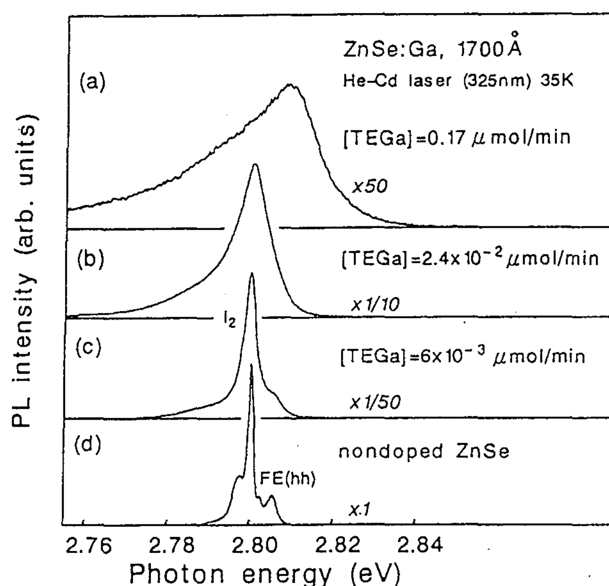

Figure 5-1 PL spectra of Ga-doped ZnSe films near the band-edge region with different doping levels at 35 K

ordered alloys investigated here were grown on semi-insulating GaAs (100) substrates at 200°C. Basically, the growth conditions for ZnSe or the ordered alloys are same as those of chapter 4, except for the introduction of TEGa source gas. The ordered alloys were grown directly on GaAs substrates without buffer layers. The thickness of the ordered alloy studied in this section were 1700Å (PL properties) and 8000Å (electrical characterization).

5.1.1 Growth of n-type ZnSe crystals using TEGa

First, the properties of Ga-doped ZnSe crystals were investigated in order to determine the fundamental doping properties of the crystals. Basic characteristics of n-type ZnSe crystals were determined by the PL properties since electric measurements require thick film thickness (~1μm).

Figure 5-1 shows the PL spectra in the excitonic emission region of the Ga-doped ZnSe films at 35K with different TEGa flow rates. The PL emission intensities are normalized by the non-doped sample in Fig. 5-1 (d). The thickness of all the ZnSe films was 1700Å, and the crystal growth time was roughly 2 hours. Dominant emission lines near the band-edge are assigned to exciton bound to a neutral donor (I_2),[1,7] and this I_2 emission lines become dominant with increasing TEGa flow rates, compared with that of

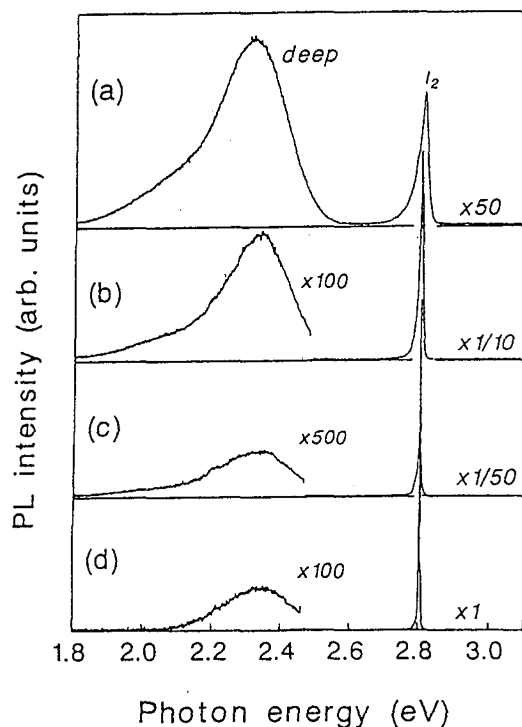

Figure 5-2 PL spectra of Ga-doped ZnSe films with different doping levels, which correspond to their near band-edge PL spectra in Fig. 5-1.

free exciton, as shown in Figs. 5-1 (a) to (d). It was observed that the PL emission peak shifted to higher energies in the case of Fig. 5-1 (a). In the heavily doped samples ($n>10^{18}$ cm^{-3}), it is typically observed that the PL emission lines shift to higher energies due to the Burstein-Moss effect or the phase space filling effect.[8,9] At high doping concentrations, the conduction band becomes significantly filled due to the finite density of states. Due to this band filling, the optical transitions can not occur from the bottom of the conduction band, therefore, the PL shifts to higher energy side. This PL peak shift, therefore, implies a large concentration of donor atoms. These result indicates that the n-type doping of ZnSe crystals can be obtained by HRCVD using TEGa, and the carrier concentrations are also controlled by simply changing flow rate of TEGa. Figure 5-2 shows wide-range PL spectra of the same samples which correspond to their PL spectra in Fig. 5-1. In the doped and non-doped samples (shown in Fig. 5-2 (b) to (d)), the I_2 emission intensity was stronger by two orders of magnitude than that of the deep level emission (2.3 eV). Nevertheless, it was observed in the highly

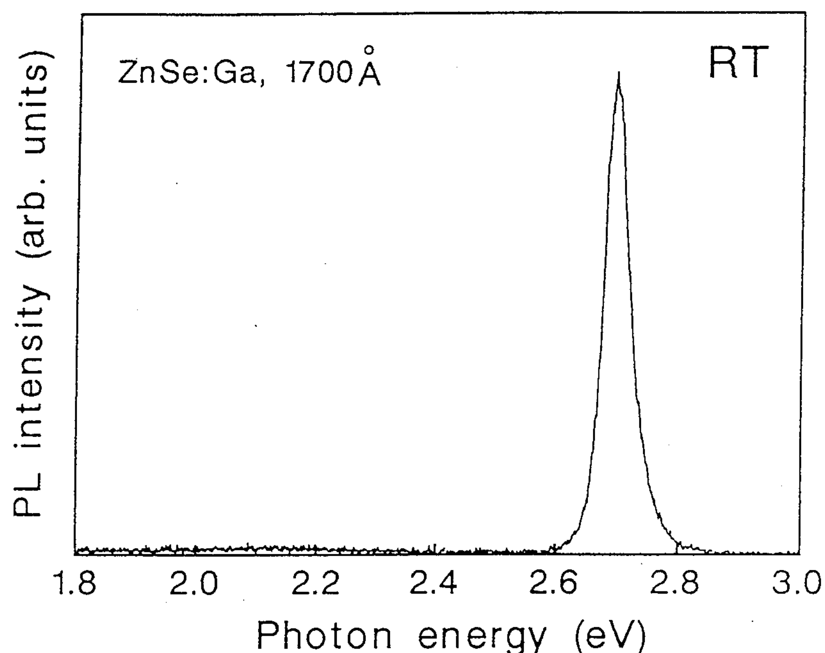

Figure 5-3 Room-temperature PL spectrum of Ga-doped sample which corresponds to the PL spectrum in Fig. 5-1 (b).

doped sample (a) that the deep-level emission intensity is the same as that of the band-edge emission, indicating the defect increase with Ga doping concentration.[1)]

The blue PL emissions can be seen in the Ga-doped ZnSe crystals even at room temperature. Figure 5-3 shows the PL spectrum of the Ga-doped sample of Fig. 5-1 (b) measured at room temperature. A strong blue PL line at 2.67 eV is seen although a small intensity deep level emission is also observed. In contrast to the non-doped sample, the room temperature PL emission was almost non-existent. The blue emission observed in the Ga-doped films is considered to be due to free holes recombining with the Ga bound electrons. This evidence is consistent with Ga atoms on substitutional site which are donor states.

The full width at half-maximum (FWHM) at the (400) diffraction ZnSe peak for the Ga-doped ZnSe films obtained from the X-ray rocking curve is shown in Fig. 5-4. Narrow values (~100 arcs), which are almost the same as those of non-doped ZnSe films, are obtained when the TEGa flow rates are less than $2x10^{-2}$ μmol/min. The heavily doped sample of Fig. 5-1 (a), however, showed a peak broadening in the XRD spectrum, and FWHM of

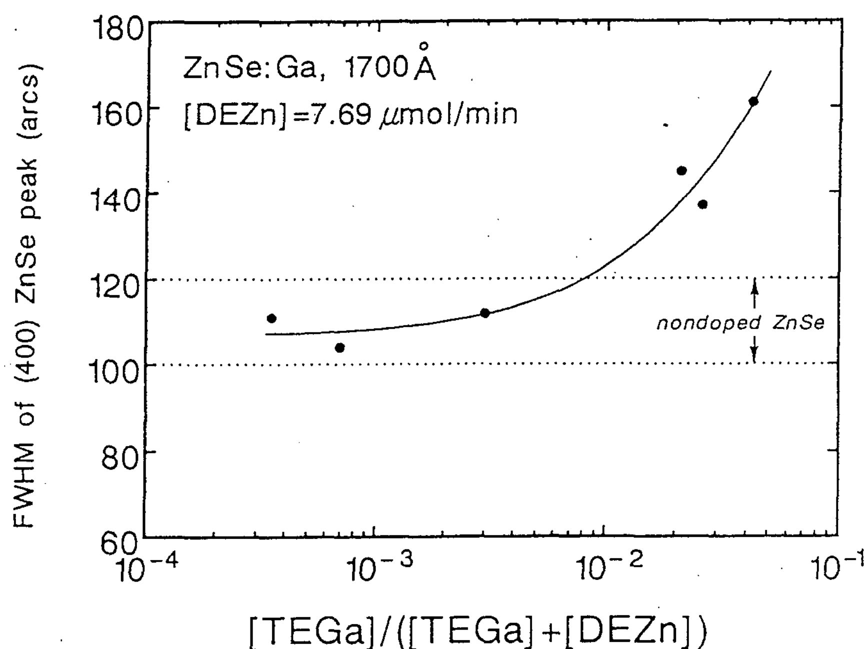

Figure 5-4 FWHM of (400) ZnSe peaks of Ga-doped ZnSe films as a function of TEGa flow rates. FWHM of non-doped samples in also indicated by the dotted line.

this sample was 145 arcsec. Consequently, the growth of n-type ordered alloys can be made at the TEGa flow rates less than $2x10^{-2}$ μmol/min.

5.1.2 Growth of n-type Zn(S,Se) crystals using TEGa

Next we investigated doped Zn(S,Se) ordered alloys. XRD spectra of the doped and non-doped $(ZnS)_3(ZnSe)_{42}$ ordered alloys are shown in Fig. 5-5. The flow rates of TEGa were controlled by changing the vapor pressure of the source while keeping the flow rate of carrier gas in order to maintain the ALE condition same. Satellite peaks corresponding to the layer-by-layer structure of the ordered alloys are seen in all cases. Theoretical satellite peaks, determined based on the assumption that the crystal films grow coherently, are in good agreement with those observed (as shown by the dotted lines of Fig. 5-5). These results indicate that ordered alloys have the expected ordered structure with the intended number of layers. In the Ga-doped ordered alloys, however, the widths of the satellite peaks broaden and

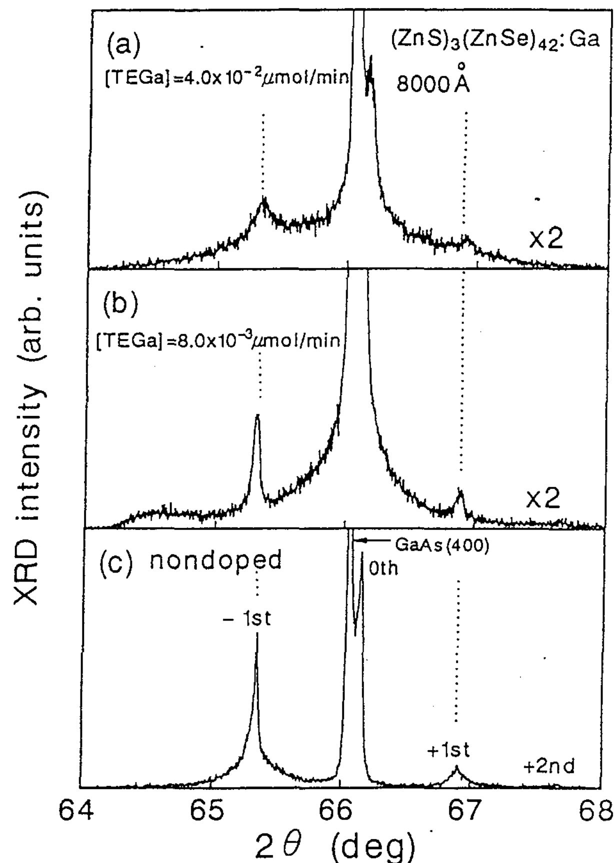

Figure 5-5 XRD spectra of $(ZnS)_3(ZnSe)_{42}$ ordered alloys with different doping levels. Theoretical angles of satellite peaks on the assumption of coherent growth are also indicated by the dotted lines.

their diffraction intensities decrease with increasing TEGa flow rates due to structural fluctuations. These fluctuations may result from the alloying effect at ZnS-ZnSe interfaces due to the degradation of crystallinity caused by Ga doping.

The disordered effect at ZnS-ZnSe heterointerface was also reported in strained-layer superlattices.[10)] In addition to this, it is widely known that Zn dopant atoms induce superlattice disordering in GaAs-AlAs[11)] and GaP-GaAsP.[12)] It has been suggested that the disordered effects in superlattice structure are caused by the interaction between the dopant and the vacancy.[13)]

In superlattice structures, the electron charge are easily accumulated due to its band-offset at heterointerface. Accordingly, the formation of vacancy or the interdiffusion of the constituent atoms can be enhanced at these heterointerfaces, which lead to the disordered effect of the multilayer

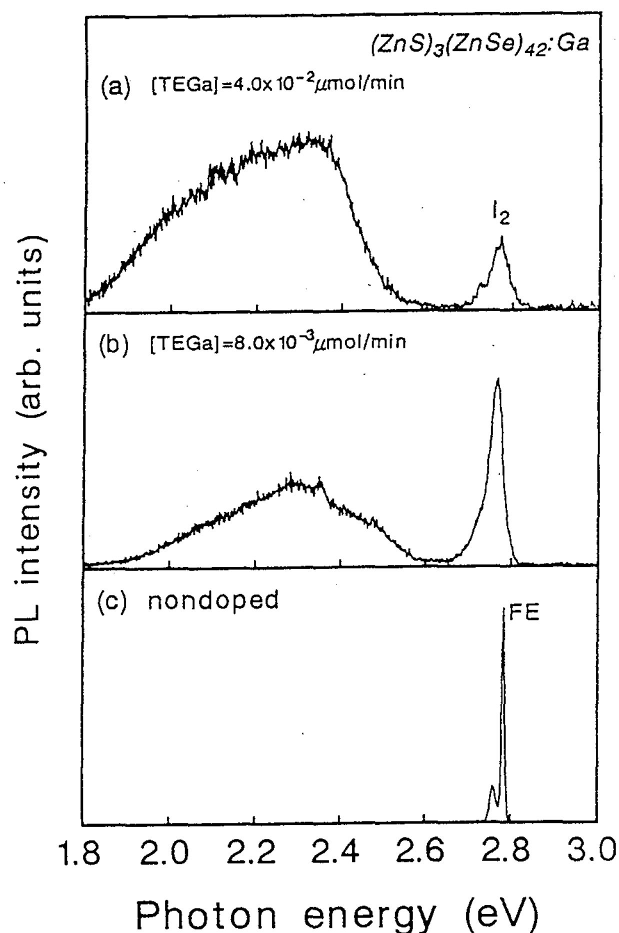

Figure 5-6 PL spectra of Ga-doped $(ZnS)_3(ZnSe)_{42}$ ordered alloys with different doping levels at 35 K.

structures.

Figure 5-6 shows PL spectra of the Ga-doped ordered alloys which correspond to their XRD spectra in Fig. 5. It is obvious that the emission from the deep levels drastically increases with increasing TEGa flow rates, as shown in their PL spectra. The intensity of the deep-level emission was higher than that from the excitons bound with the donors in the Ga-doped crystal, as shown in Fig. 5-6. For the non-doped crystal (c), on the other hand, the emission attributed to deep levels was hardly observed. When the Ga doping is accomplished on ZnSe crystals at this TEGa flow rate, deep level emission is negligible and near band-edge emission is dominant as shown in Figs. 5-2 (b) and (c). These evidences suggest that increasing layer fluctuation caused by Ga doping leads to the formation of defects in the crystals. The Ga-doped ordered alloys generally show high resistivity.

For the sample of Fig. 5-6 (b), however, a Hall mobility of 154 cm^2/Vs at the carrier concentration of $3x10^{16}$ cm^{-3} was obtained from the Hall effect measurement at room temperature. So far, higher electron mobilities up to around 400 cm^2/Vs have been reported in ZnSe crystals using other method. The electron mobility obtained in this study is obvious low compared with the reported values, indicating the increased scattering in the ordered alloys.

In summery of this section, Ga-doped ZnSe and Zn(S,Se) crystals were grown on GaAs by HRCVD using ALE. Strong blue PL emission was observed at room temperature by the optimization of the Ga-doping conditions. In the XRD spectra of $(ZnS)_3(ZnSe)_{42}$, however, the interdiffusion of atoms at ZnS-ZnSe interfaces are shown, which leads to the formation of defects confirmed from the PL spectra. In the Ga-doped ordered alloys, Hall mobility of 154 cm^2/Vs was obtained at carrier concentration of $3x10^{16}$ cm^{-3}.

5.2 Growth of n-type Zn(S,Se) crystals using i-BuI

As shown in the previous section, Ga-doping to Zn(S,Se) crystals gives rise to the defect formation due to layer interdiffusion. To avoid this effect, we chose iodide as a column VII dopant, and iodine-doping to Zn(S,Se) ordered and disordered alloys was investigated. The optoelectric properties of the iodine-doped Zn(S,Se) crystals are presented in this section.

So far, it has been reported that the column VII atoms such as Cl and I are the effective dopant for n-type ZnSe crystals. In MBE system, n-type doping of ZnSe-based crystals has been commonly prepared using $ZnCl_2$.[14,15] Alkyliodides have been also reported to be an superior n-type doping source in MOVPE. Successful fabrications of n-type ZnSe have been shown using methyliodide ($I\text{-}CH_3$)[16] or ethyliodide ($I\text{-}C_2H_5$).[17-21] The high vapor pressure of these molecules, however, makes the control of the carrier concentration difficult.[16,21] Accordingly, we selected iso-buthyliodide (i-BuI) as a n-type dopant source for the first time. Figure 5-7 shows the temperature dependence of the vapor pressure for various iodine sources. Among these alkyliodide, i-BuI has the lowest vapor pressure (1

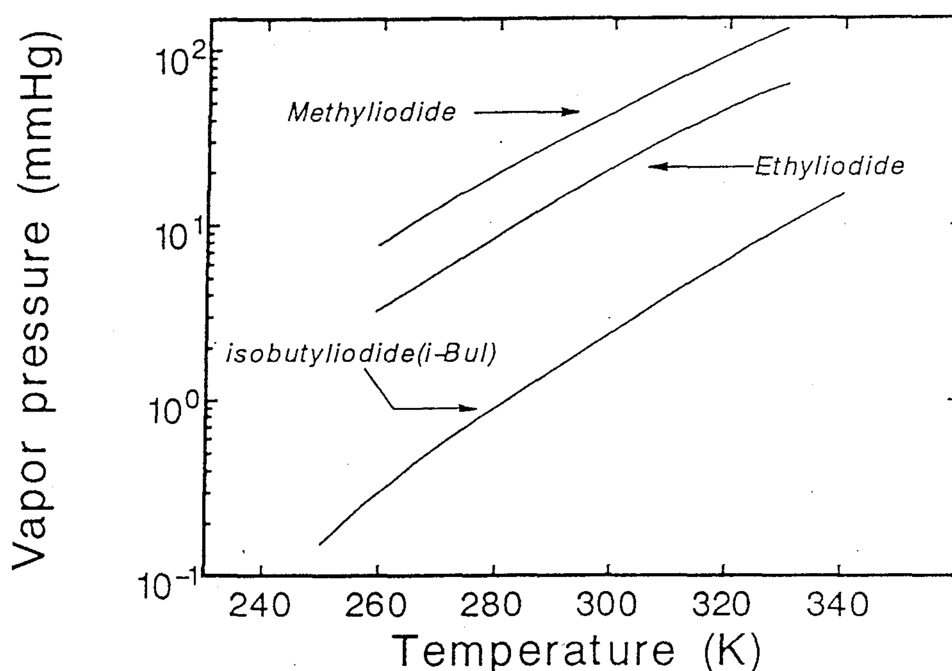

Figure 5-7 Temperature dependence of the vapor pressure for various alkyliodide.

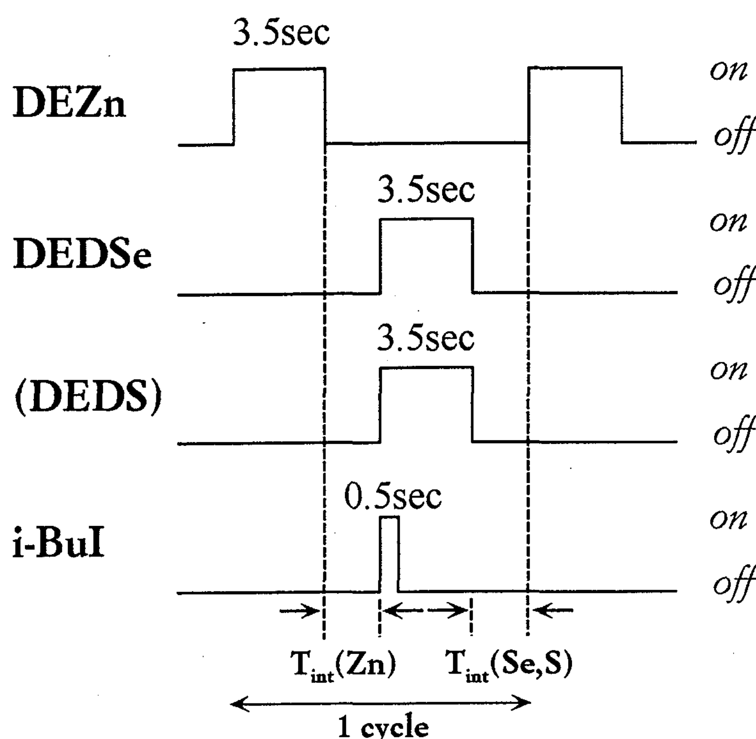

Figure 5-8 The schematic diagram of the gas supply sequence for n-type doping using i-BuI.

mmHg at 10°C), and the flow rates of i-BuI can be accurately controlled. Figure 5-8 shows the time sequences for the n-type doping using i-BuI. The source of group II (DEZn) and group VI (DEDS and DEDSe) were supplied alternately to provide ALE. For the I-doping, i-BuI was supplied with DEDSe periodically for 0.5 sec, as shown in Fig. 5-8. When i-BuI was supplied for 5 sec with DEDSe, the degradation of the crystallinity was observed due to the large iodide concentrations.

The structure of ordered and disordered alloys used here was $(ZnS)_3(ZnSe)_{42}$ and $ZnS_{0.07}Se_{0.93}$, respectively. The sulfur content of these crystals was chosen to be 7 at% to provide good lattice matching to the GaAs substrate. As a result, the carrier transport properties of these crystals can be properly decided since the lattice relaxation effects and the resulting defect formation are minimized at this sulfur content. These films were grown directly on GaAs substrate without any buffer layer, and the thickness of the films were kept constant to 7000Å.

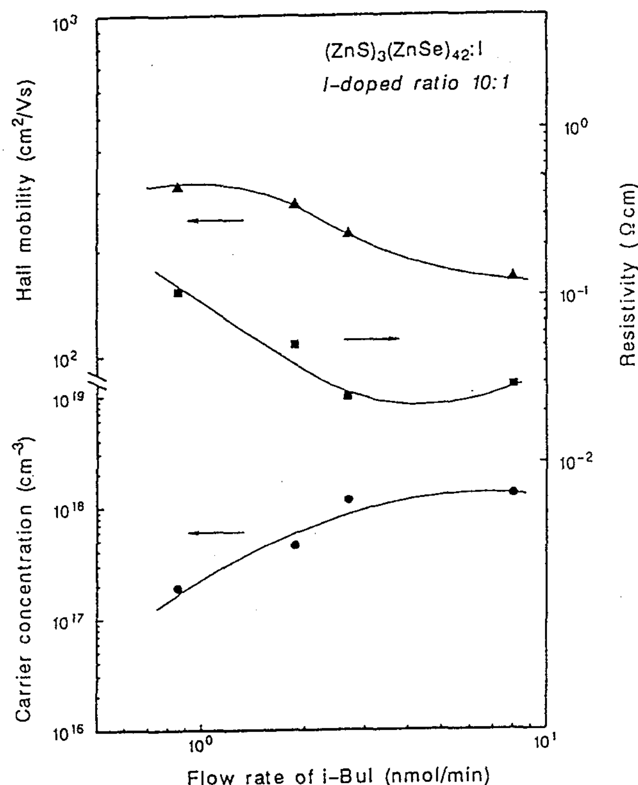

Figure 5-9 The electrical properties of the I-doped $(ZnS)_3(ZnSe)_{42}$ ordered alloys plotted as a function of the i-BuI flow rate.

5.2.1 Growth of iodine-doped Zn(S,Se) crystals

Fugue 5-9 shows the electrical properties of the I-doped $(ZnS)_3(ZnSe)_{42}$ ordered alloys at room temperature plotted as a function of the i-BuI flow rates. All the I-doped ordered alloys show mirrorlike surface morphologies. In order to maintain the same ALE growth condition, the flow rates of DEZn, DEDSe, and DEDS were kept constant and only the low rate of i-BuI was controlled by varying vapor pressure at a constant flow rate of H_2 carrier gas (0.1 sccm). In this I-doping, the i-BuI was supplied into the reactor with DEDSe to make an I-doped ZnSe monolayer in every 10 ZnSe layers. When the I-doping was made homogeneously in all the layers of the ordered alloy, films showed high electric resistivity, except the sample grown by the lowest i-BuI flow rate (0.8 nmol/min). On the other hand, the carrier concentration showed a decrease when the I-doping was made selectively to only the ZnS layers. Consequently, selective doping of ZnSe layers was

adopted in this study. As shown in Fig. 5-9, the carrier concentration of the ordered alloys gradually increases from 10^{17} to 10^{18} cm^{-3} as the flow rate of i-BuI increases. Corresponding to the increase in the carrier concentration, the resistivity of the ordered alloys gradually decreases. The carrier concentration of $1.2x10^{18}$ cm^{-3} corresponding to the resistivity of $2.4x10^{-2}$ Ωcm was obtained as the maximum in this series. This value is about one order of magnitude lower than that of ZnSe fabricated by the conventional n-type doping (~10^{19} cm^{-3}).[14,17,18] The presence of S atoms in this ordered alloys could be the reason of this lower maximum carrier concentration. The carrier concentration obviously decreases again through the maximum (10^{18} cm^{-3}) if the flow rate of i-BuI was further increased. The growth rate was also reduced by supplying i-BuI over 8 nmol/min, which indicates that the chemical reactions on the growth surface may be hindered by large amounts of i-BuI. The Hall mobility of the film with the minimum carrier concentration ($2x10^{17}$ cm^{-3}) was 300 cm^2/Vs at room temperature, and showed a gradual decrease with increasing carrier concentration.

The minimum carrier concentration obtained in this series was $2x10^{17}$ cm^{-3} due to the limit of control over flow rate of i-BuI when the ratio of the I-doped layer to the undoped layer was kept constant (r=1:10). We prepared the sample with lower carrier concentration by varying r. Figure 5-10 shows the carrier concentration of ordered and disordered alloys plotted as a function of r. The flow rate of i-BuI was fixed at 0.8 nmol/min, the lowest flow rate available. In the ordered alloys, a good linear relation was obtained between the carrier concentration n and r down to $n=3x10^{16}$ cm^{-3}, suggesting that the carrier concentration is controlled in a wide range from 10^{16} to 10^{18} cm^{-3}. A minimum carrier concentration of $3.3x10^{16}$ cm^{-3} was obtained in this series when the I-doped ZnSe monolayer was introduced in every 450 layers. Two-dimensional carrier concentrations (n_{2D}) were calculated from $n \times d \times r$, where d is the total thickness of the grown layer. The obtained n_{2D} value from the carrier concentration of $3.3x10^{16}$ cm^{-3} is $4.5x10^{11}$ cm^{-2}. In addition, the corresponding three-dimensional carrier concentration (n_{3D}) calculated from $(n_{2D})^{3/2}$ is $3.1x10^{17}$ cm^{-3}. This n_{3D} indicates the identical carrier concentration when the doping is made homogeneously at the sheet carrier concentration of n_{2D}. This obtained n_{3D} is not dense enough to form doping quantum wells. In a δ-doped n-GaAs, the δ-doped effect, i.e., mobility enhancement by the carrier-impurity

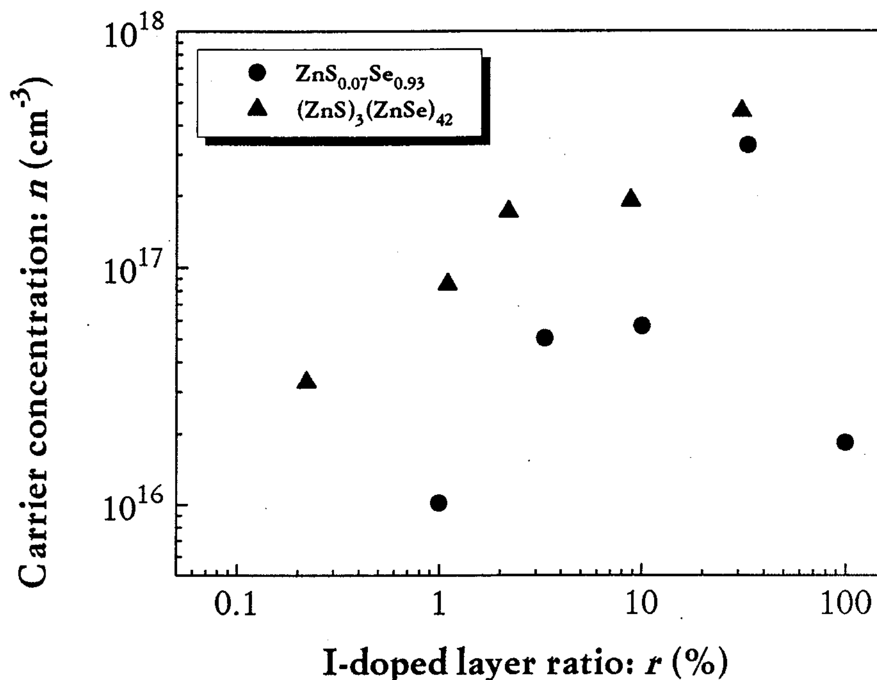

Figure 5-10 The carrier concentration of the ordered and disordered alloys as a function of the ratio of the I-doped layer to undoped layer.

separation, is not typically seen at these low concentrations, as typically concentration of ~10^{19} cm^{-3} are required.[22)] For the reasons mentioned above, we consider that the δ-doped effect is small in our case. In this study, therefore, average carrier concentrations or Hall mobilities will be used.

When the doping was homogeneously made in all ZnSe layers in the ordered alloys, a broad XRD diffraction peak (~400 arcsec) was observed, indicating deterioration of the crystallinity. Together with the degradation of crystallinities, the optoelectric properties such as the PL or doping efficiency were also deteriorated. These degradations are due to a strong chemical affinity of iodide to ZnSe or ZnS layers, resulting in the incorporation of an excessive amount of iodide to these layers. The low growth temperature in ALE-HRCVD, as low as 200°C, may make the desorption of these excessive iodide difficult. In addition, the incorporation of iodide could be enhanced by a favorable atomic hydrogen induced decomposition in HRCVD.

In $ZnS_{0.07}Se_{0.93}$ disordered alloys, a linear relation between n and r can be also seen in Fig. 5-10. Similar carrier concentrations with the ordered

alloys were obtained in the disordered alloys. As a result, the carrier concentration of the disordered alloys are also controlled from $1x10^{16}$ to $5x10^{17}$ cm^{-3} by changing I-doping layer ratio. When the I-doping was homogeneously made to the disordered alloys, the reduction in the carrier concentration was observed along with an increased defect concentration.

From the results mentioned above, it can be concluded that iodine-doped ordered and disordered alloys were successfully prepared by HRCVD using i-BuI. The carrier concentration of these crystals was varied from 10^{16} to 10^{18} cm^{-3} by the i-BuI vapor pressure and/or the I-doped layer ratio.

5.2.2 Structure & optoelectrical properties

In this section, the structures and PL properties of the I-doped disordered and ordered alloys will be investigated using SIMS, XRD and PL spectra. The SIMS measurement was carried out to determine the iodine distribution in the δ-doped $(ZnS)_3(ZnSe)_{42}$ ordered alloys.

Figure 5-11 shows the secondary ion intensities of iodide and sulfur of the ordered alloy as a function of the depth obtained from the SIMS measurement. The schematic layered structure of the ZnS, ZnSe and I-doped layers are also shown in the inset. In the SIMS spectrum, the gaussian-shaped iodine profiles and the oscillation of the secondary ion intensity of sulfur due to the two-dimensional ordered structure were observed. As shown in the inset, I-doped ZnSe monolayer occurred in every 10 periods of ZnS and ZnSe. The result obtained by SIMS measurement shows good agreement with the expected structure. In addition, the maximum I-peak appeared at the point where the S-intensity was minimized. The well-separated I-peaks observed in the SIMS spectrum suggest that the δ-doping occurred in these ordered alloys, since no diffusion was expected as growth temperature was low. It was observed that the secondary ion intensity of sulfur slightly decreased with I-doping. A possible explanation for this effect may be the matrix effect of crystals or the decrease in sulfur content by the heavy I-doping. The FWHM of I-peaks is 13nm, which is simply resolution limit of the SIMS measurement.

Figure 5-12 shows XRD spectra of (ZnS)3(ZnSe)42 ordered alloys with various carrier concentrations. Figure 5-12 (d) represents the simulation of the spectrum assuming of the coherent growth. As shown in Figs. 5-12

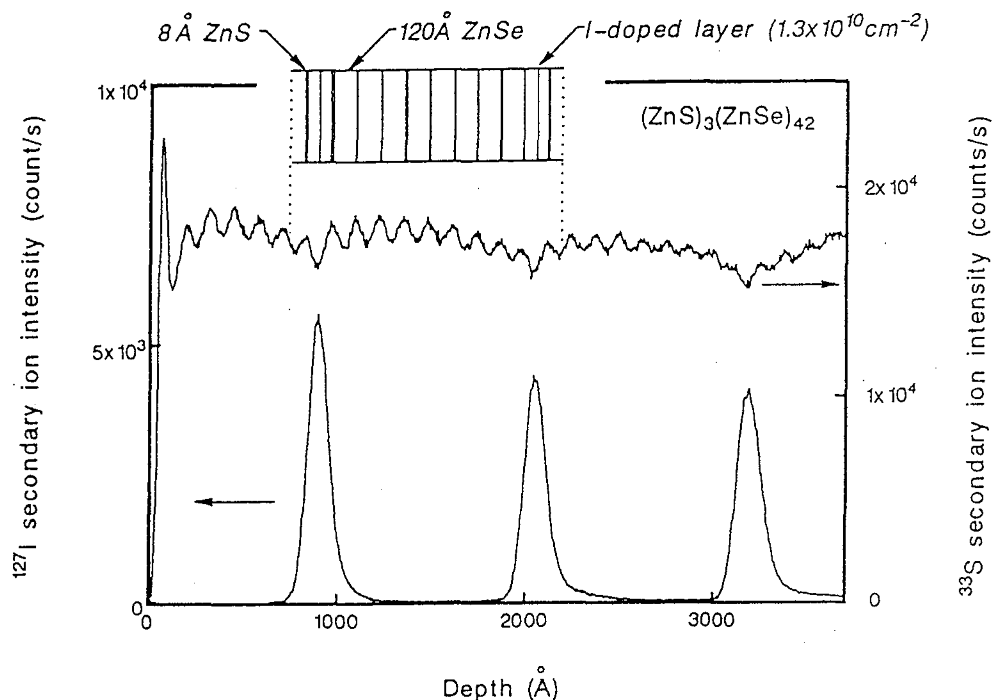

Figure 5-11 The SIMS depth profile of iodide and sulfur for the selectively doped ordered alloys. The structure of this ordered alloy is also indicated in the inset.

from (a) to (c), satellite peaks are present in all the ordered alloys, which is due to the 2-dimensional ordered structure of ZnS and ZnSe. A good agreement is seen between the theoretical and experimental satellite peaks. The lattice parameter perpendicular to the surface obtained from the XRD spectra of (c) is 5.648Å, which agrees well with the value of 5.647Å calculated from the Vegard's law with coherent structure. However, the FWHM of the 0-order and the satellite peaks increase gradually with increasing the carrier concentration. In addition, the rapid decrease in diffraction intensity and the broadening of diffraction peaks are also observed in the heavy doped samples of (a). These evidences show that the structural fluctuations due to I-doping increase gradually with increasing carrier concentration.

In the previous section, n-type doping was made using triethylgallium (TEGa) as the dopant source. The crystallinity of the Ga-doped ordered alloy was inferior compared with the I-doped crystal with the same carrier concentration of around 10^{16} cm^{-3}. Moreover, a broadening effect of the satellite peaks observed in the Ga-doped crystals was not shown when i-BuI

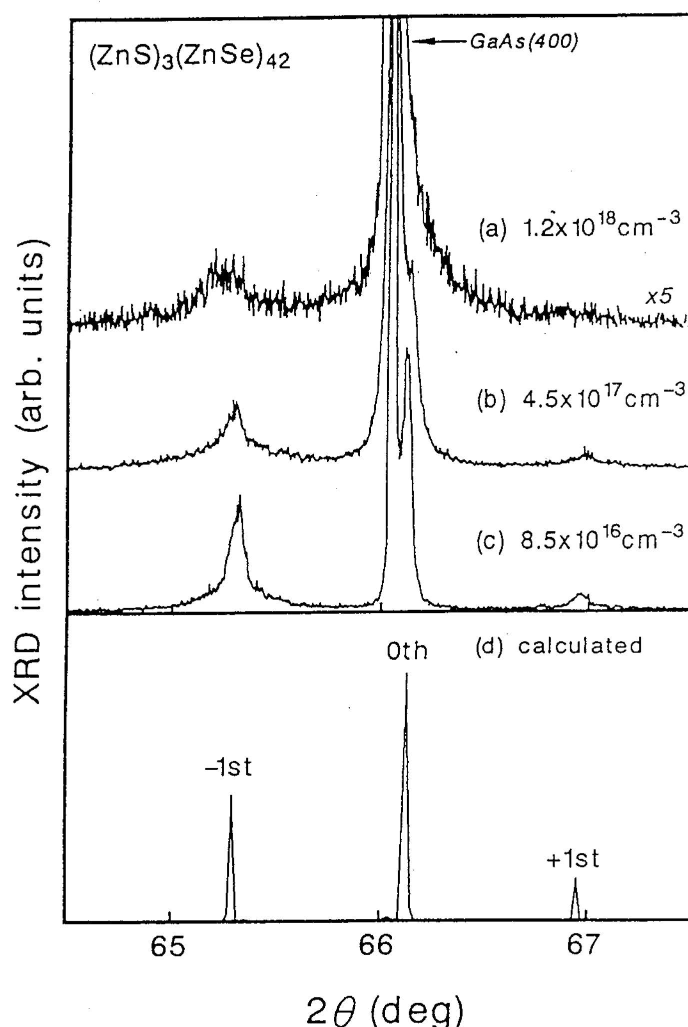

Figure 5-12 The XRD patterns of the $(ZnS)_3(ZnSe)_{42}$ ordered alloys for the different doping levels. The calculated spectrum based on the coherent growth is also shown in (d).

was used. These evidences lead us to a conclusion that i-BuI is an effective n-type dopant for ZnS-ZnSe crystals.

In Fig. 5-13, the FWHM of the (400) peak obtained from XRD spectra are plotted as a function of the carrier concentration for the iodine-doped $(ZnS)_3(ZnSe)_{42}$ and $ZnS_{0.07}Se_{0.93}$. Sharp diffraction peaks as narrow as ~50 arcsec can be seen in both ordered and disordered crystals, indicating the high-quality of the I-doped crystals. The FWHM of these peaks, however, gradually increased as the carrier concentration increase since the incorporation of large amount of donor atoms into the crystal leads to the degradation of the crystal quality. Both ordered and disordered alloys show almost the same behaviors in the FWHM as a function of the carrier

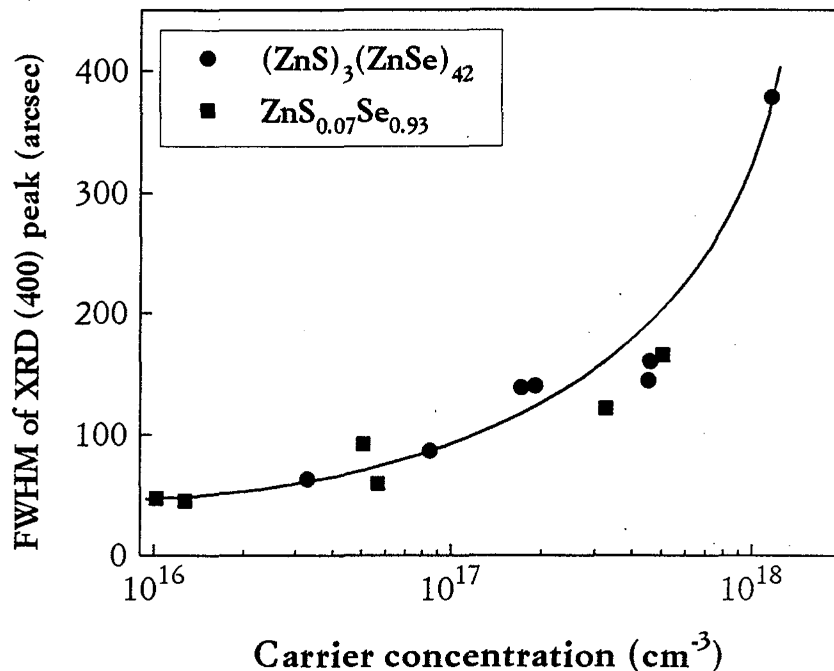

Figure 5-13 The FWHM of the (400) XRD peaks as a function of the carrier concentration of $(ZnS)_3(ZnSe)_{42}$ and $ZnS_{0.07}Se_{0.93}$.

concentration. Consequently, it is evident that these crystals have the similar crystallinity with respect to the lattice distortion.

PL spectra of the I-doped ordered alloys at 35 K with various carrier concentrations are shown in Fig. 5-14. The numbers in the figure indicate the relative intensities for both the band-edge emission and the emission from the deep levels. The band-edge emission intensities are compared with that of the strongest sample (d), whereas the emission intensity of deep level are normalized by the each of the band-edge emission.

It is clearly seen that the band-edge emission is dominant for all samples and the emission from deep levels is efficiently suppressed low by two orders of magnitude or less compared to the band-edge emission. The sharp band-edge emissions with the width of about 4 meV in FWHM are assigned to the exciton bound to neutral donor (I_2). These results indicate that the I-doped ordered alloys are of high-quality. However, the I_2 emission intensity is reduced markedly together with an increase in the deep level emission intensity as the carrier concentration increases. This observation may be related to the fact that the deterioration of crystallinity

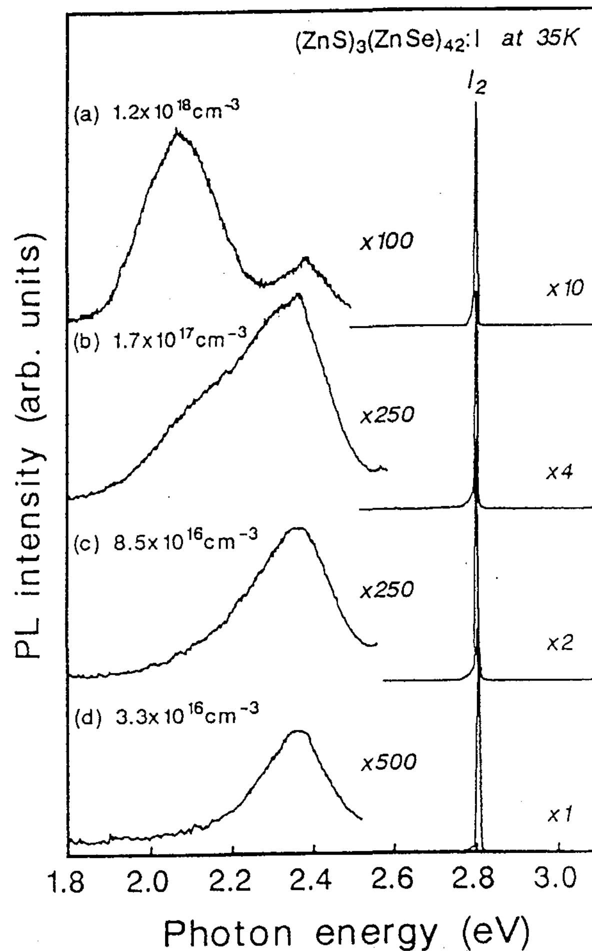

Figure 5-14 The PL spectra of the I-doped $(ZnS)_3(ZnSe)_{42}$ ordered alloys for the different carrier concentration at 35K.

accelerates the non-radiative recombination of exciton in the heavily doped crystals. The emission from the deep levels observed in the heavily doped samples can be divided into two peaks at 2.1eV and 2.3eV, as shown in Fig.5-14 (a). The deep level emission at 2.1eV increases with increasing carrier concentration and finally becomes dominant in the heavily doped sample (a). This deep level emission at 2.1eV could be due to the complex between iodide and Zn-vacancy, as have been shown by other works.[23)]

Figure 5-15 shows room temperature PL spectra of the I-doped ordered alloys corresponding to the PL spectra of Figs.5-14 (a) to (d) at 35 K. The intensities are normalized by the highest one (d). At room temperature, the blue emission at 2.705eV was dominant in all samples, which is the recombination between free holes and electrons bound to iodide.

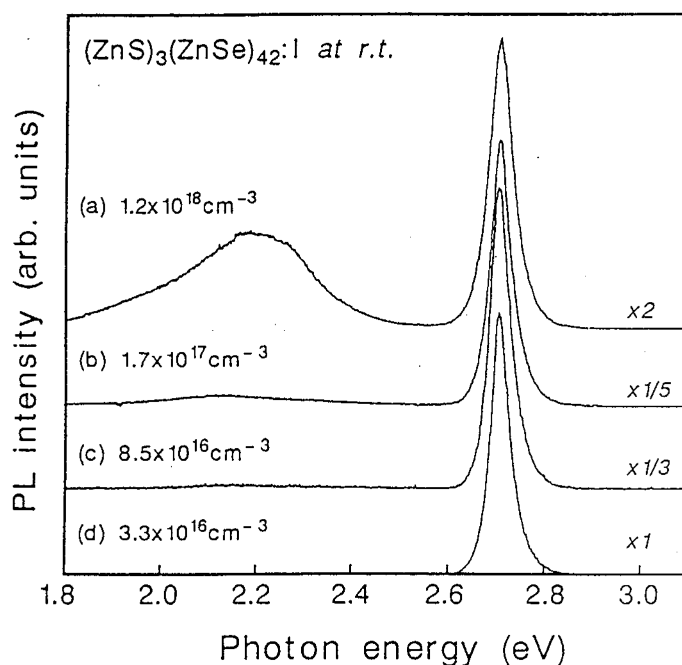

Figure 5-15 The room-temperature PL spectra of the I-doped ordered alloys for the different carrier concentration, which correspond to their PL spectra of Fig. 5-14.

Yellowish emission was seen with the naked eyes at room temperature in the heavily I-doped samples, (a) and (b), whereas pure blue emission was observed in the slightly doped samples, (c) and (d). A rapid increase of the deep level emission was observed for the heavily I-doped samples (carrier concentration $\sim 10^{18}$ cm^{-3}), which is consistent with the results reported previously.[21)]

The PL spectra of non-doped and I-doped $ZnS_{0.07}Se_{0.93}$ with various carrier concentration are shown in Fig. 5-16. As shown in the PL spectra, dominant band-edge emission lines assigned to I_2 are also observed for all the I-doped crystals grown with suppressed deep level emissions. Similar to the ordered alloys, deep level emission at ~2.1 eV can be seen at carrier concentrations of $5x10^{17}$ cm^{-3} due to the defect complex. Other defect-oriented peaks are not observed in PL spectra for these samples. In addition, the strong blue emissions at room temperature are also observed in the I-doped disordered alloys. These PL properties, such as dominant band-edge emission and suppressed deep level emission, are similar to that of the $(ZnS)_3(ZnSe)_{42}$ ordered alloys except for the small shifts in the PL

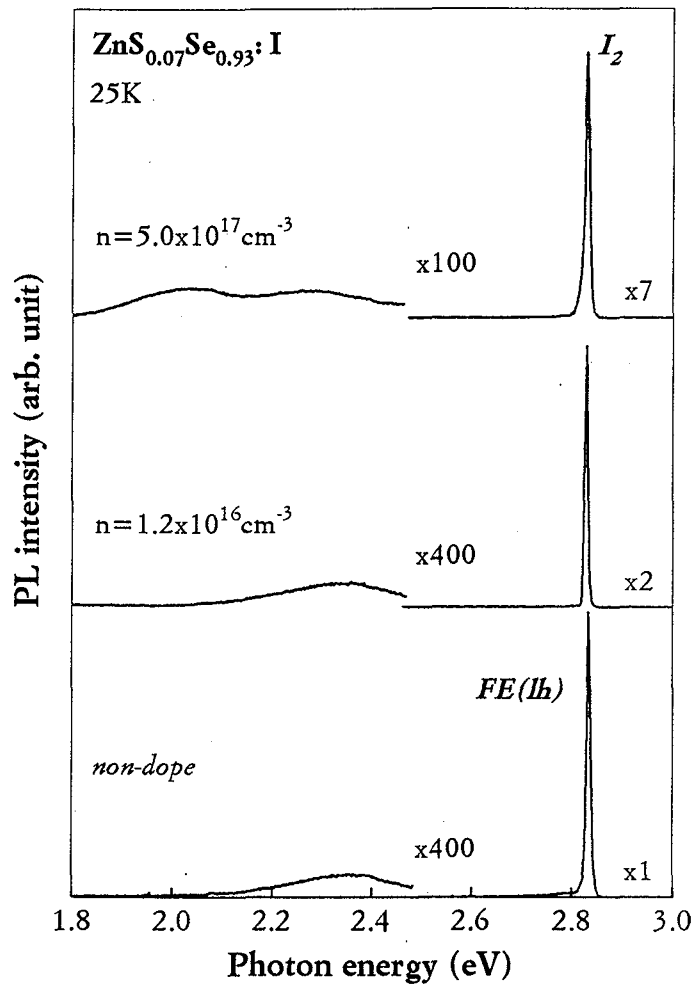

Figure 5-16 The PL spectra of non-doped and I-doped $ZnS_{0.07}Se_{0.93}$ with various carrier concentration.

peaks, as discussed in chapter 4. The low temperature growth at 200°C is considered to assist in the fabrication of high-quality ordered and disordered crystals due to reduced strain and lower defect concentrations.

5.3 Carrier transport properties of Zn(S,Se) crystals

In the previous section, it was confirmed that the high-quality Zn(S,Se) crystals can be prepared by HRCVD using i-BuI as the column VII dopant. For the purpose of revealing the thermal activation of donors and the carrier scattering process of $(ZnS)_3(ZnSe)_{42}$ and $ZnS_{0.07}Se_{0.93}$ crystals, the temperature dependence of Hall measurements were carried out at a wide range of temperatures. In addition, effects of the 2-dimensional ordered structure in the ordered alloys will be further discussed in terms of the structure dependence of $(ZnS)_n(ZnSe)_{14n}$ (n=1~4).

5.3.1 Donor activation process

Figure 5-17 shows the temperature dependence (77-300K) on carrier concentration of several I-doped $(ZnS)_3(ZnSe)_{42}$ ordered alloys. The solid lines in Fig. 5-17 depict the curves calculated from the following equations which relate electron and dopant concentration:[24)]

$$\frac{n(n+N_A)}{N_D-N_A-n}=\left(\frac{N_C}{g}\right)\exp\left(\frac{-E_D}{kT}\right), \tag{5-1}$$

$$N_C=2\left(\frac{2\pi m^* kT}{h^2}\right)^{3/2}, \tag{5-2}$$

where E_D, N_D and N_A are the donor ionization energy and the total densities of donors and compensating acceptors, respectively. N_c, g, m^* and k indicate the density of states of the conduction band, degeneracy, effective mass and Boltzmann constant, respectively. We adopted g=2 for this calculation. The values of N_D, N_A and E_D are determined by fitting the data using Eq.(5-1) and (5-2). The obtained values of E_D and compensation ratio, expressed as N_A/N_D, are also indicated in Fig. 5-17. The slopes of the lines to the reciprocal temperature decrease with increasing carrier concentration due to the degeneration of the donor levels with conduction band. The donor activation energies obtained from these slopes are 28 meV for the sample with the carrier concentration of $3\text{x}10^{16}$ cm^{-3} and nearly 0 eV for the sample

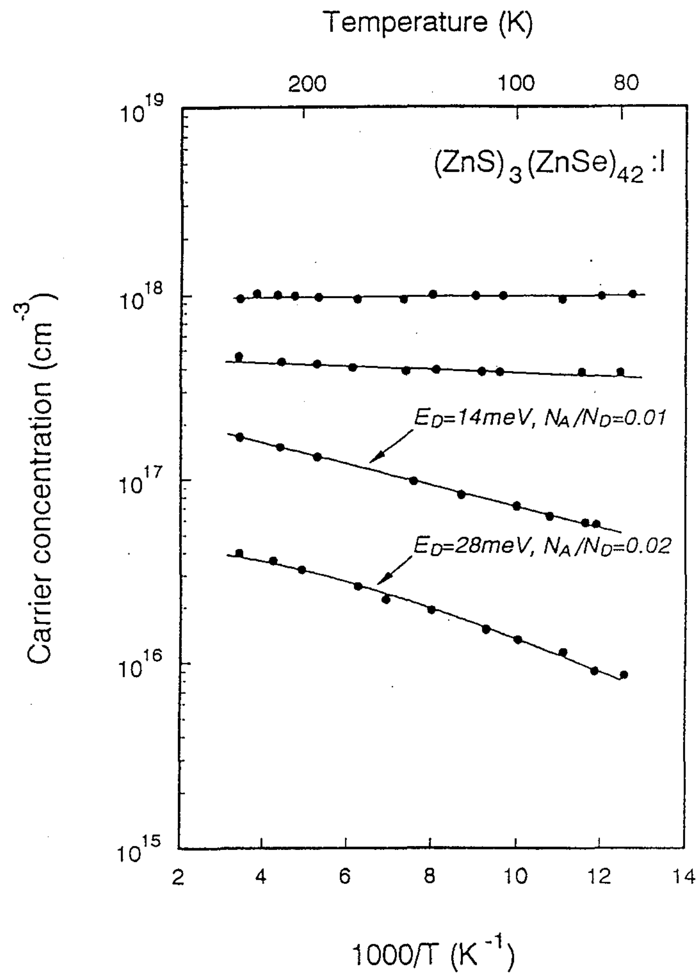

Figure 5-17 The temperature dependence of the carrier concentration for $(ZnS)_3(ZnSe)_{42}$ ordered alloys from 77 to 300 K. The obtained values of ionization energy (E_D) and the compensation ratio (N_A/N_D) are also indicated.

with 4×10^{17} cm^{-3}. The results are consistent with small carrier compensation ratios (1~2%). It should be noted that these compensation ratios are about one order of magnitude less than the reported values (15~40%) in the crystals fabricated by conventional methods.[21,26)] This result clearly shows that acceptors compensation is negligible in this novel technique.

Figure 5-18 also shows the temperature dependence of the carrier concentration for $ZnS_{0.07}Se_{0.93}$ disordered alloys from 77 to 300 K. The calculated curves using Eqs. (5-1) and (5-2) are also indicated together with the donor ionization energies. Similar to that of the ordered alloys, the reduction in E_D of $ZnS_{0.07}Se_{0.93}$ can be seen as the carrier concentration increases due to the degenerate of donor level at the conduction band. The

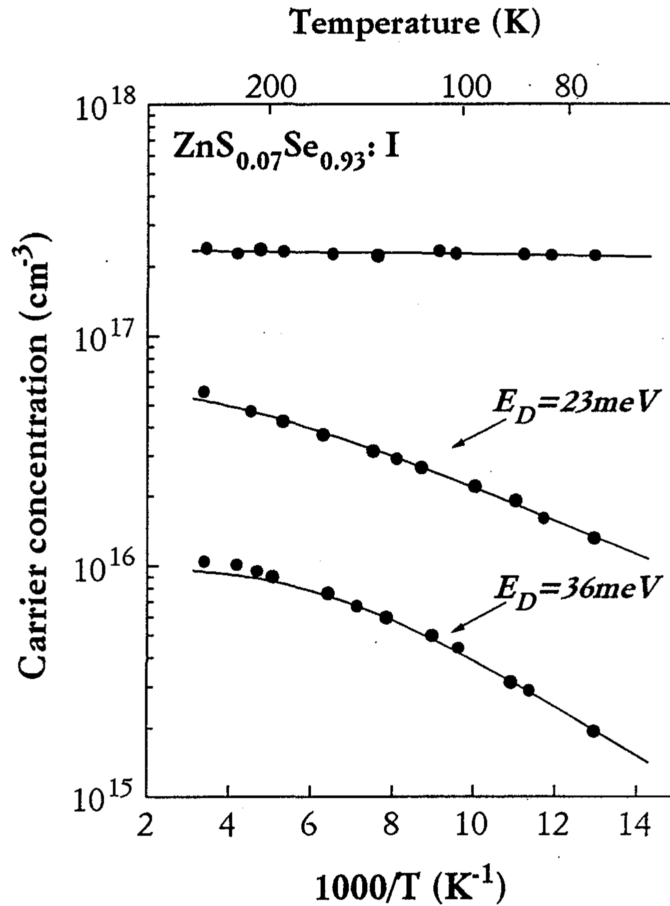

Figure 5-18 The temperature dependence of the carrier concentration for $ZnS_{0.07}Se_{0.93}$ disordered alloys. The E_D are also shown in the figure.

carrier compensation ratio (N_A/N_D) in these crystals is also estimated to be 1~2%, indicating again that compensation is very low in $ZnS_{0.07}Se_{0.93}$.

Figure 5-19 shows the donor activation energy (E_D) of the ordered and disordered alloys plotted as a function of the cubic root of the ionized donor concentration (N_D^+). The donor activation energies are given by the Debye and Conwell equation,[27)]

$$E_D = E_0 - \alpha(N_D^+)^{1/3}, \tag{5-3}$$

where E_0 and α indicate the donor activation energy at infinite dilution and the slope of the line, respectively. The cubic root of N_D^+ indicates the average number of donors in the crystal per cm. In this case, N_D^+ is given by $n+N_A$ from a charge-neutrality condition, and can be obtained from Eq.

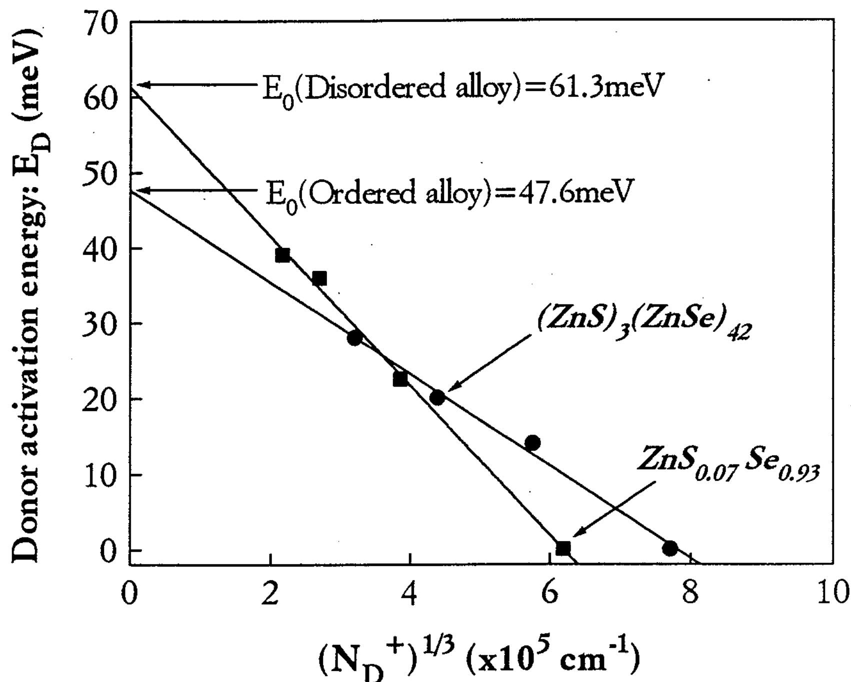

Figure 5-19 The donor ionization energy (E_D) as a function of the cubic root of the number of ionized donor , $(N_D^+)^{1/3}$, for the disordered and ordered alloys. The E_0 indicates the donor ionization energy at infinite dilution.

(5-1) using curve fitting. There is, however, little difference between N_D and N_D^+, because of the small acceptor compensation ratio in $(ZnS)_3(ZnSe)_{42}$ and $ZnS_{0.07}Se_{0.93}$ layer (N_A/N_D=1~2%). From Eq. (5-3), it is evident that the reduction in the donor ionization energy is proportional to the number of donor atoms in the crystal.

Theoretically, this reduction in the impurity ionization energy has been explained by Coulomb potential overlaps. This effect is schematically shown in Fig. 5-20. As shown in Fig. 5-20, the increasing doping concentration enables the overlap of the Coulomb potential. As a result of the overlapping impurity potentials, electrons can transfer more easily from one donor to another donor; thus reducing the activation energy of impurity atoms. Screening of impurity potentials is a second contribution to the reduction in the impurity ionization energy. Impurity potentials are effectively screened at high free carrier concentrations. Screened potentials are less likely to bind electrons. Accordingly, the effective ionization energy decreases due to screening.[27)]

As shown in Fig. 5-19, a good linear relation between E_D and $(N_D^+)^{1/3}$ can

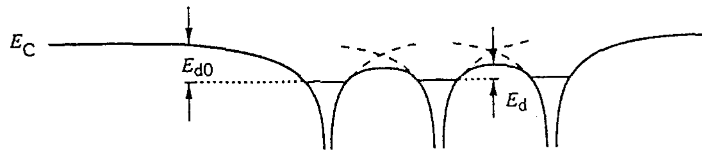

Figure 5-20 Conduction band edge with three donor potentials. For high donor concentrations the Coulomb potentials overlap and the ionization energy E_{d0} is reduced to E_d.

be seen in both the disordered and ordered alloys. The E_0 and α values obtained from the least square fit are E_0=47.6 meV, α=6.1x10^{-5} meV cm for $(ZnS)_3(ZnSe)_{42}$ and E_0=61.3 meV, α=9.9x10^{-5} meV cm for $ZnS_{0.07}Se_{0.93}$, respectively. The value of E_0 for the bulk ZnSe crystal is reported to be about 28.1 meV,[24)] and is considerably smaller than that for the crystal in this work. This discrepancy may be attributed to the presence of sulfur atoms in these alloys. The value of E_D for ZnS single crystal is calculated to be 110 meV from the effective mass theory, and agrees well with the experimental value of ~100 meV.[28,29)] From these facts, it is supposed that the incorporation of sulfur atoms having larger activation energy leads to the formation of deep donor state in these alloys. However, $(ZnS)_3(ZnSe)_{42}$ shows the smaller E_0 compared with $ZnS_{0.07}Se_{0.93}$, since the I-doping was selectively made to ZnSe layers in the ordered alloys. This result implies that the donor activation energy can be changed by the δ-doping. Therefore, this δ-doping technique is a promising approach to p-type doping, where the deep acceptor levels in alloys reduce the hole concentration remarkably.[30)]

In addition, these alloys show the different $(N_D^+)^{1/3}$ values where E_D approach zero. In principle, E_D is zero when the distance between impurities becomes comparable to the Bohr radius of donor atom, as expressed by

$$2a_B^* = N_{crit}^{-1/3}, \qquad (5\text{-}4)$$

where a_B^* is the effective Bohr radius and N_{crit} is the critical impurity concentration at E_D=0 and the effective Bohr radius of impurity atom is given by Eq. (2-14). Taking into account the random distribution of impurity atoms, we obtain the following expression assuming poissonian

distribution,[31)]

$$2a_B^* = \frac{3}{2\pi} N_{crit}^{-1/3} , \qquad (5\text{-}6)$$

Accordingly, the larger $(N_D^+)^{1/3}$ value at E_D=0 implies a smaller Bohr radius of donor atoms. In $ZnS_{0.07}Se_{0.93}$, the value of $(N_D^+)^{1/3}$ at E_D=0 is 6.34x10^5 cm^{-1} and has similar value with that of the bulk ZnSe (6.85x10^5 cm^{-1}),[24)] while the $(ZnS)_3(ZnSe)_{42}$ shows the larger value of 7.80x10^5 cm^{-1}. The calculated $(N_D^+)^{1/3}$ for ZnSe crystal using Eq. (5-6) is 6.94x10^5 cm^{-1} (or n=3.34x10^{17} cm^{-3}) assuming a_B^* to be 34.6Å, and this result agrees well with the observed values of bulk ZnSe or $ZnS_{0.07}Se_{0.93}$. The Bohr radius of the ordered alloys, on the other hand, is calculated to be 30.8Å using Eq. (5-6).

Above these result indicates that the donor atoms in the ordered alloy have the smaller Bohr radius, which may be induced by the layer-by-layer structure. Masselink et al. reported that the Bohr radius of donor atom is reduced when the doping is made selectively to quantum well layers.[32)] In $(ZnS)_3(ZnSe)_{42}$, I-doping was also made selectively to well (ZnSe) layers. Nevertheless, the confinement of donor electrons in the conduction band is unlikely because of the small ΔE_c between ZnSe-ZnS and the extremely thin barrier (ZnS) layers.[33)] Quantitative analysis should be necessary for further discussion.

5.3.2 Carrier scattering mechanism

Figure 5-21 shows the Hall mobility of the I-doped ordered and disordered alloys plotted as a function of the carrier concentration at room temperature. A high mobility of 470 cm^2/Vs was observed for $(ZnS)_3(ZnSe)_{42}$ ordered alloy at n=3x10^{16} cm^{-3}. It should be noted that this mobility is the highest value ever obtained in the ZnS-ZnSe system. In the ordered alloys, the Hall mobility gradually decreases from 470 to 220 cm^2/Vs with increasing carrier concentration. As shown in the XRD spectra of Fig. 5-12, it is confirmed that the FWHM of the ordered alloys gradually increases with increasing carrier concentration. Accordingly, the decrease in the Hall mobility is attributed to the degradation of crystal quality caused by the I-doping. In addition, the ionized impurity (or defect) scattering is also considered to be

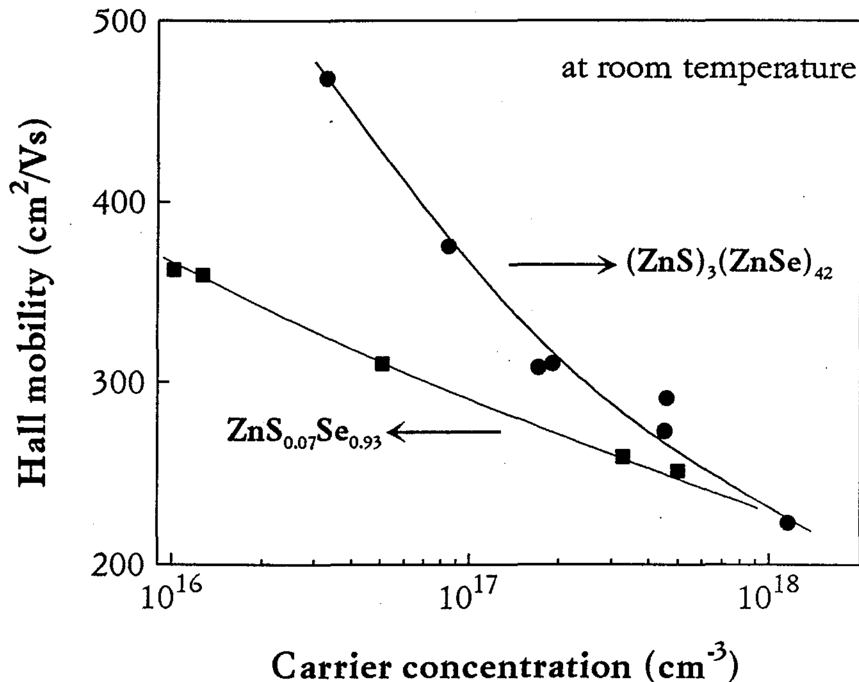

Figure 5-21 The Hall mobilities at room temperature as a function of the carrier concentration of $(ZnS)_3(ZnSe)_{42}$ and $ZnS_{0.07}Se_{0.93}$.

the reason for this effect.

In contrast to $(ZnS)_3(ZnSe)_{42}$ ordered alloys, distinct reductions in the Hall mobilities were found for the disordered alloys, and its differences between the ordered and disordered alloys are more than 100 cm^2/Vs at the low carrier concentrations (~ 10^{16} cm^{-3}). It should be emphasized that these crystals have similar crystallinity (determined by the XRD and PL spectra in section 5.2.2). Consequently, these mobility reduction in $ZnS_{0.07}Se_{0.93}$ disordered alloys can be explained in terms of the scattering by the disordered structures, the so called "*disorder scattering effect*".[34,35] At the high carrier concentrations, however, the difference in mobility became smaller since the mobility is limited by the ionized impurity scattering rather than disorder scattering. It has been reported that ordered crystals often showed rather smaller mobilities, compared with the disordered alloys, perhaps due to interface scattering.[36,37] The ordered alloys made in this study, on the contrary, exhibit higher electron mobilities than that of the disordered alloys, indicating that the scattering at the interfaces between ZnSe and ZnS layers is negligible. So far, a mobility enhancement by the

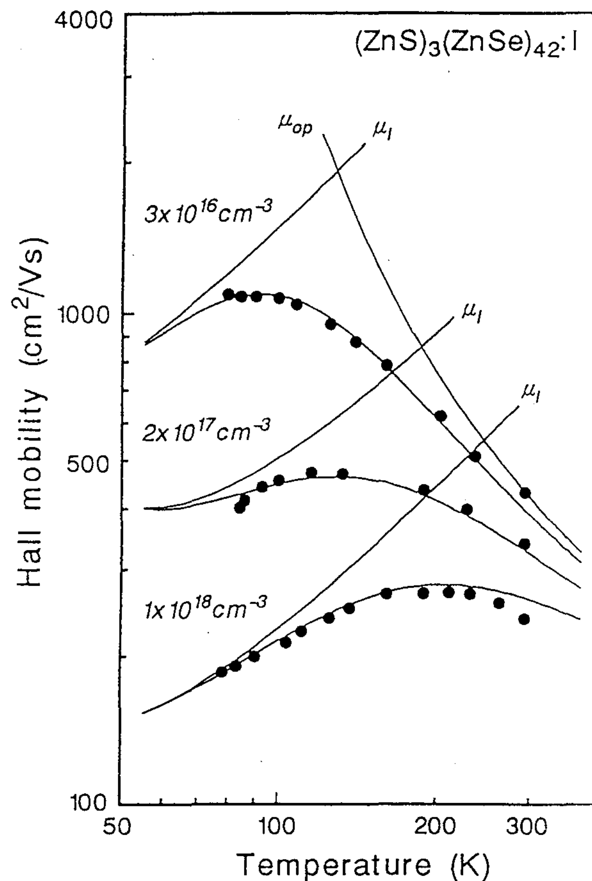

Figure 5-22 The temperature dependence of the Hall mobility for the different doping concentrations of $(ZnS)_3(ZnSe)_{42}$ ordered alloys. The calculated mobilities are also shown in solid line.

two-dimensional structure was also observed in $(InAs)_1(GaAs)_1$ spontaneously ordered crystal, resulting from the suppression of atomic random fluctuations.[38)]

Figure 5-22 shows the temperature dependence on the Hall mobility for $(ZnS)_3(ZnSe)_{42}$ as a function of doping concentrations. A very high mobility of 1000 cm^2/Vs or over was obtained at low temperatures in the slightly I-doped sample with a carrier concentration of $3x10^{16}$ cm^{-3}. The mobility tends to fall linearly with increasing temperature, which is interpreted in terms of the polar optical phonon scattering. In the heavily doped samples, on the other hand, the mobility increases gradually with increasing temperature which is consistent with ionized impurity scattering.

In order to analyze these behavior, we calculated the carrier mobility,

assuming that the ionized impurity scattering and the polar optical phonon scattering are the major scattering process.[39-41] The mobility due to polar optical phonon scattering (μ_{op}) is given by[39,42]

$$\mu_{op} = A\left(\exp\frac{\theta}{T} - 1\right)T^{1/2}, \tag{5-7}$$

where A and θ are the constant and Debye temperature of the crystal, respectively. The best fitting curves were obtained when A=10 and θ=370 K were assumed. In ZnSe bulk crystals, the A=12.9 was found to yield a good fit.[39] The mobility limited by ionized impurity scattering is calculated by the Brooks-Herring formula, which includes the free carriers screening of impurities,[43]

$$\mu_I = \frac{128\sqrt{2\pi}\varepsilon^2(kT)^{3/2}}{N_I e^3\sqrt{m^*}}\left\{\ln(1+\beta^2) - \frac{\beta^2}{1+\beta^2}\right\}^{-1}, \tag{5-8}$$

where N_I is the concentration of ionized impurities ($N_I=n+2N_A$). The parameter β is given by

$$\beta = 2\frac{m^*}{\hbar}\left(\frac{2}{m^*}3kT\right)^{1/2} r_D, \tag{5-9}$$

where $r_D=(\varepsilon kT/e^2n)^{1/2}$ is the Thomas-Fermi screening length. The calculated result using Eqs. (5-8) and (5-9) is expressed as follows:

$$\mu_I = \frac{3.28\times10^{15}T^{3/2}\varepsilon_0^2(m/m^*)^{1/2}}{N_I}\times\left(\frac{\ln 1.29\times10^{14}(m^*/m)\varepsilon_0 T^2}{n}\right)^{-1} \tag{5-10}$$

where N_I and n are the concentration of ionized impurities and the concentration of free carriers, respectively. Hall mobility observed (μ_{Total}) is obtained from the sum of the result of these scattering mechanisms according to Matthiessen's rule,

$$\frac{1}{\mu_{Total}} = \frac{1}{\mu_{op}} + \frac{1}{\mu_I} . \tag{5-11}$$

The solid lines in Fig. 5-22 illustrate the calculated mobility temperature dependence using Eqs. (5-7)~(5-11). It is seen that the calculated mobilities agree quite well with the observed mobilities in the whole temperature range measured. The curves of the mobility limited by μ_I move gradually down with increasing carrier concentration, which supports this analysis. Consequently, it can be concluded that the major scattering process in the ordered alloys is well described by traditional phonon and impurity scattering mechanism (μ_{op} and μ_I).

The carrier compensation ratio (N_A/N_D) can be also calculated from the mobility data, assuming $N_I=n+2N_A$ and $n \cong N_D-N_A$ at room temperature using following expressions:

$$N_A = \frac{(N_I - n)}{2} . \qquad N_D = N_I - N_A \tag{5-12}$$

The compensations ratio are estimated to be around 30~50%. These values are extremely low compared with the other reported compensation ratio (N_A/N_D= over 90%). This fact also indicates the high crystallinity of the ordered alloys grown in this study.

Figure 5-23 shows the temperature dependence on the Hall mobility for $(ZnS)_3(ZnSe)_{42}$ (a) and $ZnS_{0.07}Se_{0.93}$ (b). These samples have the similar carrier concentration of 3.3×10^{16} cm^{-3} (ordered alloy) and 5.7×10^{16} cm^{-3} (disordered alloy), respectively. The calculated mobilities of polar optical phonon scattering (μ_{op}) and ionized impurity scattering (μ_I) by the Brooks-Herring formula are also illustrated in Fig. 5-23, together with the total mobility (μ_{Total}). As described above, in the ordered alloy, the mobility observed coincides remarkably with the calculated μ_{Total}. The best fitting curve with μ_{Total} was obtained when the number of ionized impurities N_I is assumed to be 1.1×10^{17} cm^{-3}.

On the other hands, the significant reduction in mobility is seen in the $ZnS_{0.07}Se_{0.93}$ disordered alloy, and the mobility difference with the ordered alloy became over 400 cm^2/Vs at 77K, as shown in Fig. 5-23 (b). Brooks

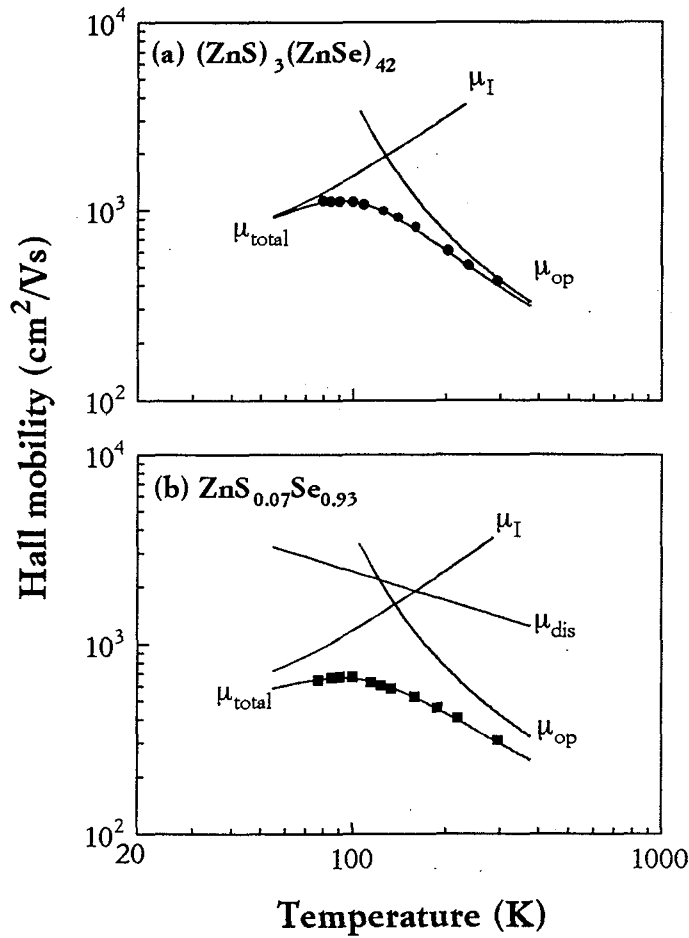

Figure 5-23 The temperature dependence of the Hall mobilities for $(ZnS)_3(ZnSe)_{42}$ (a) and $ZnS_{0.07}Se_{0.93}$ (b). The curves of μ_{op}, μ_I and μ_{dis} represent the calculated mobilities due to polar optical phonon scattering, ionized impurity scattering and disorder scattering. The total mobilities calculated from Eqs. (5-11) and (5-15) are also shown as μ_{Total}.

calculated the disorder scattering mobility assuming that carriers are scattered by the random potential fluctuations corresponding to the conduction (or valence) band offset (ΔE_c or ΔE_v), as follows:[34,35]

$$\mu_{dis} = \frac{(2\pi)^{1/2} e\hbar^4 N_0}{3(m^*)^{5/2}(kT)^{1/2} x(1-x)\Delta E^2}, \qquad (5\text{-}13)$$

where N_0 is the number of atoms per unit volume, x is the fraction of one of the alloy components, respectively. In ZnS-ZnSe crystals, however, this model is not appropriate since ΔE_c of ZnS-ZnSe is almost zero[33]; thus there would be no disorder scattering based on this model. To simplify the

analysis, the mobility limited by the disorder scattering (μ_{dis}) was calculated by the following equation,[35]

$$\mu_{dis} = \alpha T^{-1/2}\ [\mathrm{cm^2/Vs}]\ , \tag{5-14}$$

where T and α are the temperature and the constant. The total mobility of the disordered alloy is then given by the sum of these three mobilities as follows:

$$\frac{1}{\mu_{Total}} = \frac{1}{\mu_{op}} + \frac{1}{\mu_i} + \frac{1}{\mu_{dis}}\ . \tag{5-15}$$

In this calculation, we used the same value of μ_{op} with that of the ordered alloy, assuming that Debye temperature of these crystal is same. The observed mobility in the disordered alloy shows a good agreement with the calculated mobility, when α and N_I are taken as 2.4×10^4 and 1.55×10^{17} cm^{-3}, respectively. It is evident that the disorder scattering causes a reduction in the mobility at room temperature as shown in Fig. 5-21, since this scattering has the temperature dependence of $T^{-1/2}$.

As described above, the sulfur content of only 7 at% seriously affect the carrier transport properties in the disordered alloys. This fact could be explained in terms of the formation of sulfur clusters in ZnS_xSe_{1-x} crystal, because the large lattice mismatch between ZnS and ZnSe crystals induces the cluster formation of sulfur atoms to reduce the strain energy between them, as discussed in chapter 1. In the $(ZnS)_n(ZnSe)_m$, on the contrary, the uniform distribution of sulfur atoms is formed by the layer-by-layer deposition, in which the “disorder scattering” is efficiently avoided. Consequently, we concluded that the layer-by-layer structure of the ordered alloys is quite promising for the compositional modulation technique.

5.3.3 Effect of 2-dimensional ordered structure

In order to determine the effect of the 2-dimensional ordered structures, we fabricated iodine-doped $(ZnS)_n(ZnSe)_{14n}$ (n=1~4) ordered alloys having different periodic structures. These ordered alloys have the average sulfur content of 7 at%, and the ordered alloy of n=3 corresponds to

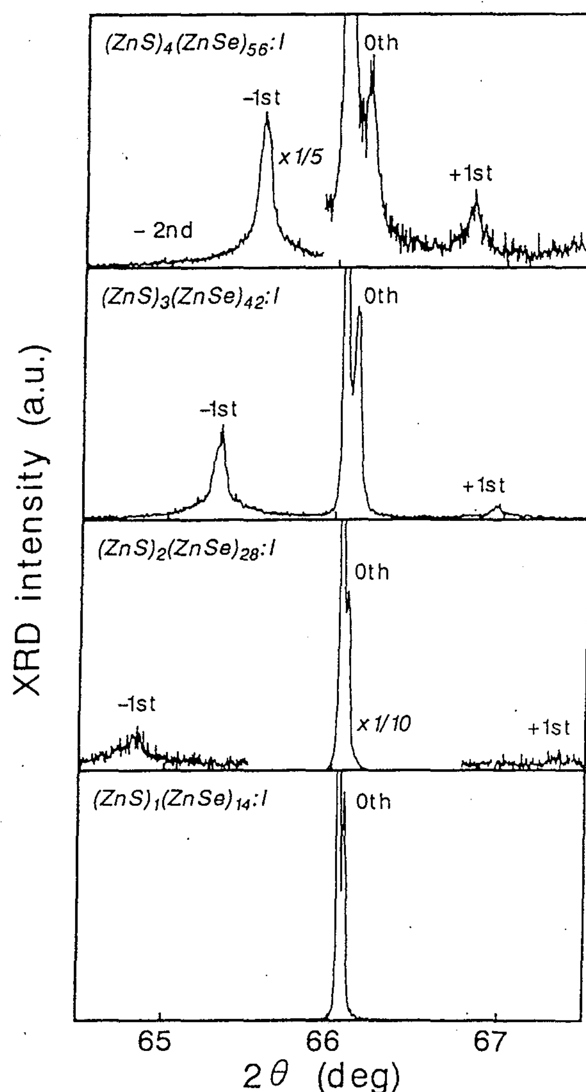

Figure 5-24 The XRD patterns of I-doped $(ZnS)_n(ZnSe)_{14n}$ ordered alloys (n=1~4). The carrier concentrations of the crystals are in a range of $8\sim9\times10^{16}$ cm^{-3}.

$(ZnS)_3(ZnSe)_{42}$, which was discussed in the previous section. In this section, the structure dependence of the carrier transport properties will be discussed from the electrical properties of $(ZnS)_n(ZnSe)_{14n}$.

The growth condition of the I-doped ordered alloys is same with that of $(ZnS)_3(ZnSe)_{42}$ except for the number of ZnS and ZnSe layers. Figure 5-24 shows the XRD spectra of the I-doped $(ZnS)_n(ZnSe)_{14n}$ ordered alloys (n=1~4). In these ordered alloys, the I-doped ratio is 1%; I-doping of ZnSe monolayer was made to every 100 layers. The resulting carrier concentrations in these ordered alloys are in a range of $8\sim9\times10^{16}$ cm^{-3}. In

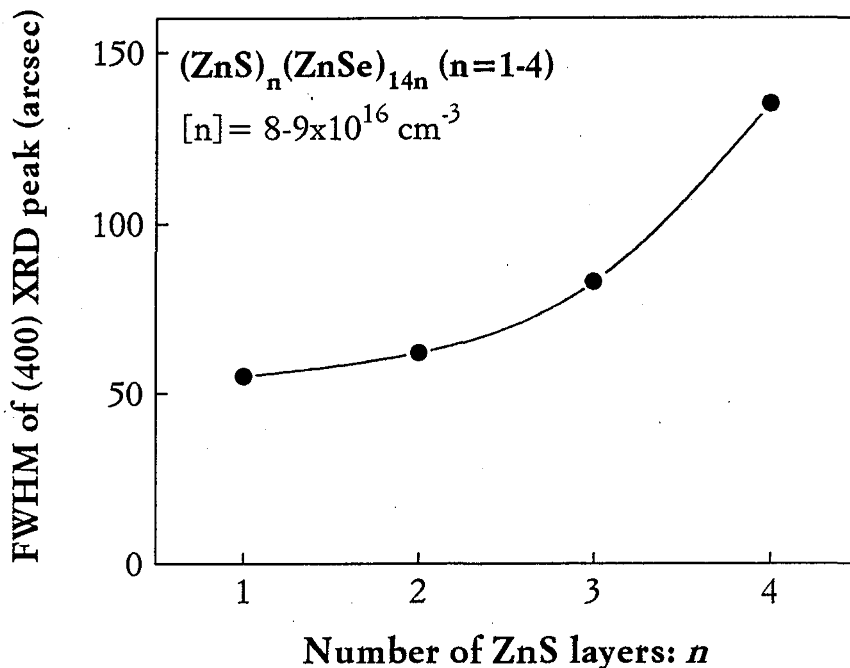

Figure 5-25 The FWHM of (400) diffraction peaks obtained from the X-ray rocking curve plotted as a function of the number of ZnS layers in $(ZnS)_n(ZnSe)_{14n}$ ordered alloys.

these spectra, satellite peaks can be clearly seen (n=2~4), and the layer-by-layer structures of the ordered alloys are confirmed. All the samples grown show the same 0-order diffraction angle, indicating that the average sulfur composition is same in these crystal (sulfur= 7at%). A weak 0-order diffraction peak, however, was observed in the sample (*n*=4), and the lattice relaxation effect is indicated. It should be noted that a strong diffraction peak can be seen in *n*=4 when the I-doping was not made to the ordered alloys. From these results, it is obvious that the additional iodine atoms increase the strain applied to the grown layer, which lead to the lattice relaxation in the crystal.

Figure 5-25 shows the FWHM of (400) diffraction peaks obtained from the X-ray rocking curve plotted as a function of the number of ZnS layers in the ordered alloys. All the grown samples show the sharp diffraction peaks, and the FWHM about 50 arcsec was obtained in *n*=1, indicating the high crystallinity of the grown ordered alloys. The FWHM of the crystals, however, gradually increases with the changes in the periodic crystal structures since the critical thickness of ZnS layers on GaAs substrates are

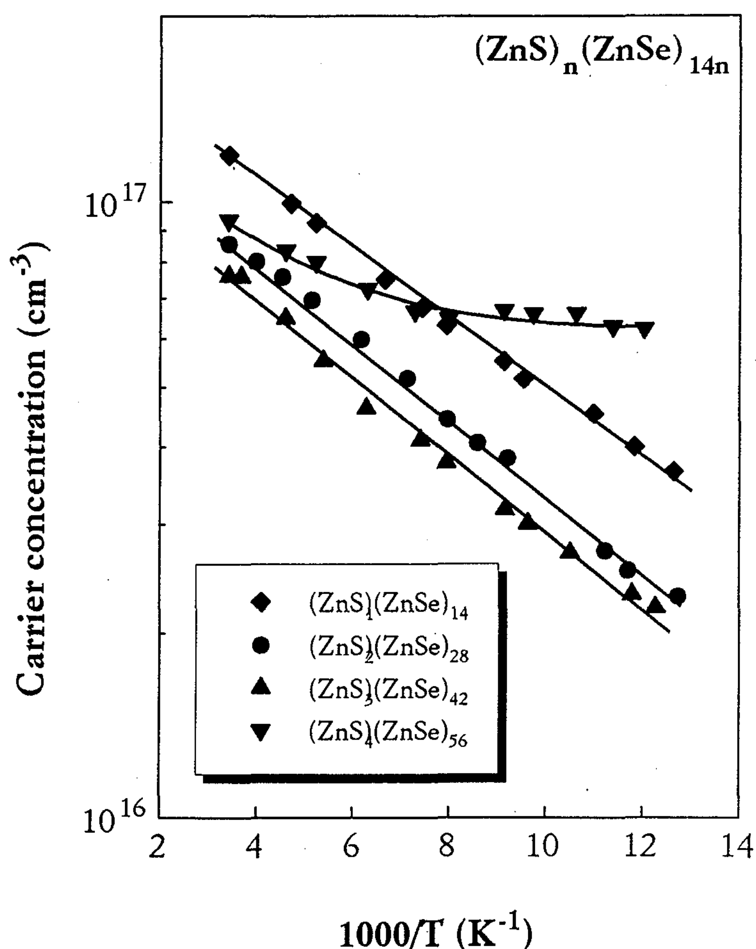

Figure 5-26 The temperature dependence of the carrier concentration for $(ZnS)_n(ZnSe)_{14n}$ ordered alloys (n=1-4) from 77 to 300 K.

only about 4 layers as discussed in chapter 4.

The PL spectra of these I-doped crystals show strong I_2 emission. The emission intensities of deep levels are efficiently suppressed (two orders of magnitude less than the band-edge emission). Nevertheless, a increased deep level emission was observed for the n=4 case due to the strain induced by the incorporation of iodine atoms, which is consistent with the result obtained from the XRD spectra.

The structure differences of the ordered alloys on donor activation process are also measured by the temperature dependence of the Hall measurement. Figure 5-26 shows the temperature dependence of the carrier concentration for $(ZnS)_n(ZnSe)_{14n}$ ordered alloys (n=1-4) from 77 to 300 K. In the ordered alloys (n=1~3), linear dependence of the carrier concentrations on the temperature were indicated. The donor activation energies of these

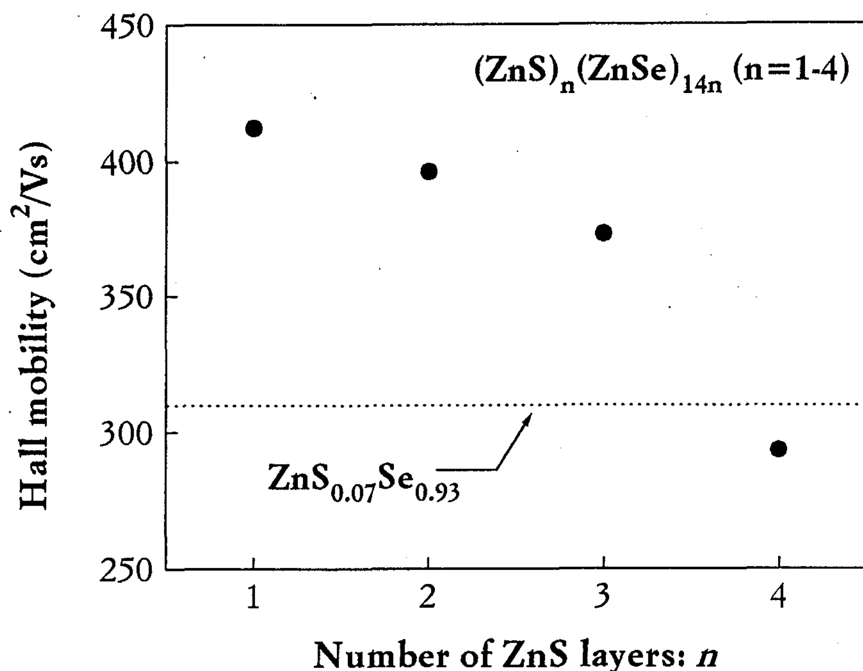

Figure 5-27 Hall mobilities of $(ZnS)_n(ZnSe)_{14n}$ ordered alloys (n=1~4) at room temperature plotted as a function of the number of ZnS layers. The dotted line indicates the Hall mobility of $ZnS_{0.07}Se_{0.93}$.

ordered alloys (n=1~3) are almost same, and calculated activation energies using Eqs. (5-1) and (5-2) are in a range of 14~16 meV. In $(ZnS)_4(ZnSe)_{56}$, a specific behavior of the carrier concentration on the temperature can be seen. The carrier concentration of n=4 indicates a saturation effect at the low temperature region. The saturation of the free carrier concentration at low temperatures (T<135 K) could be attributed to shallow donors which do not freeze out at low tempeatures,[44] and the increasing electron concentration at temperatures higher than 135 K indicate the thermal ionization of the deep donor center. Above these results indicate that the deep donor states could be formed in $(ZnS)_4(ZnSe)_{56}$ as a result of partial lattice relaxation effects by the lattice mismatch strain.

The Hall mobilities of $(ZnS)_n(ZnSe)_{14n}$ ordered alloys (n=1~4) at room temperature are plotted as a function of the number of ZnS layers in Fig. 5-27. The dotted line indicates the Hall mobility of $ZnS_{0.07}Se_{0.93}$ having the same carrier concentration (n=6x$10^{16}$$cm^{-3}$) or sulfur composition with the ordered alloys. Higher electron mobilities are observed in the ordered alloys (n=1~3) compared with $ZnS_{0.07}Se_{0.93}$, and the superior carrier transport

properties in these crystals are confirmed. Obviously, these higher electron mobilities in the ordered alloys result from the suppression of the "disorder scattering" in the disordered alloys, as discussed in the previous section. In the n=4 case, on the other hand, a slightly lower electron mobility is obtained compared with $ZnS_{0.07}Se_{0.93}$ disordered alloy due to the increased scattering caused by the strain effect induced defects. The Hall mobility of the ordered alloys monotonously decreases as the number of ZnS layer increases. This result can be explained in terms of the increasing lattice distortion in the ordered alloys, which is confirmed from the FWHM of the XRD peaks as shown in Fig. 5-25. The interface scattering at ZnS-ZnSe heterointerface could be another reason of this electron mobility reduction since scattering centers are easily created at the heterointerface.

Figure 5-28 shows the temperature dependence of the Hall mobility for the different structure of $(ZnS)_n(ZnSe)_{14n}$ ordered alloys (n=1~4). Very high mobilities of 700 cm^2/Vs or over were obtained at low temperature (~100 K) in the slightly doped ordered alloys (n=1~2), which are limited by both polar optical phonon scattering and ionized impurity scattering. As the number of ZnS layer increase, however, the mobility of the ordered alloys slightly decreases (n=1~3), which is consistent with the result shown in Fig. 5-27. In the ordered alloys (n=1~3), the dominant scattering mechanisms is confirmed to be μ_{op} and μ_I from the theoretical calculations. However, it was found that the compensation ratio (N_A/N_D) increases with increasing ZnS layer thickness. A large reduction in the overall mobility can be seen in the sample n=4. It should be noted that these ordered alloys have the similar carrier concentrations (n=8~9x10^{16} cm^{-3}). Accordingly, the change of the electron mobility in the ordered alloy (n=4) implies the increasing scattering center caused by the defect formation.

The carrier transport mechanisms in Zn(S,Se) crystals with ordered and disordered structures are schematically shown in Figure 5-29 from the results mentioned above. As described above, a distinct reduction in the electron mobility can be seen in $ZnS_{0.07}Se_{0.93}$ disordered alloys compared with $(ZnS)_n(ZnSe)_{14n}$ ordered alloys (n=1~3) due to the "disordered scattering". As a result, it was indicated that sulfur atoms in the disordered alloys even at the sulfur content of 7 at% seriously suppress the electron conduction in the crystals. This fact could be explained by the cluster formation in the disordered alloys, which leads to the potential fluctuations in the crystals

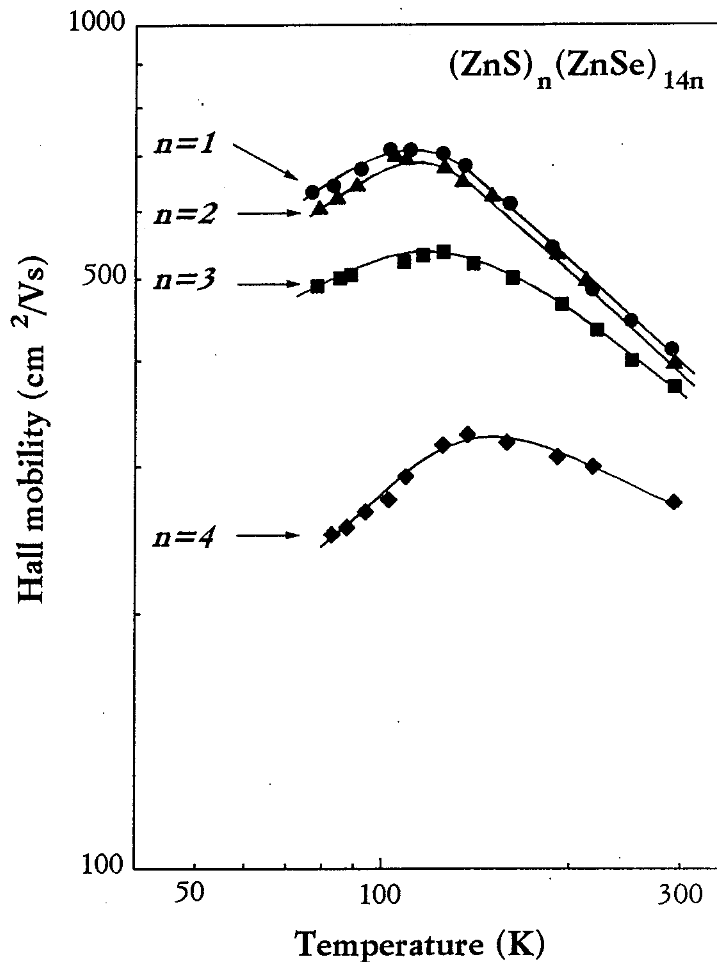

Figure 5-28 The temperature dependence of the Hall mobility for the different structure of $(ZnS)_n(ZnSe)_{14n}$ ordered alloys (n=1~4).

(Fig. 5-29 (a)). Basically, the local compositional fluctuation in the disordered alloys results from the large lattice mismatch between the constituent atoms.[45)] In other word, the growth of lattice mismatch disordered alloys prefers the cluster formation on the surface to reduce the surface chemical potential induced by the strain energy. Consequently, a smaller electron mobility can be observed in the disordered alloys due to the local compositional fluctuation.

In $(ZnS)_n(ZnSe)_{14n}$ ordered alloys (n=1~3) having short period 2-dimensional structures, homogeneous distribution of sulfur atoms is created by the delocalization of the wavefunction. As a result, higher electron mobilities are obtained due to the suppression of the disordered scattering, as shown in Fig. 5-29 (b). In addition, the ordered alloys (n=1~3) show the

1) ZnS_xSe_{1-x} mixed crystal

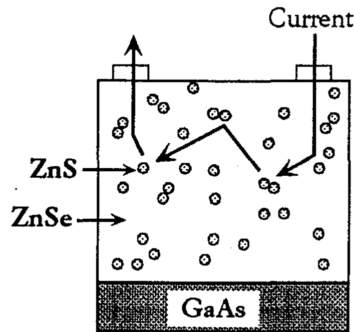

2) Ordered Alloys (n=1-3)

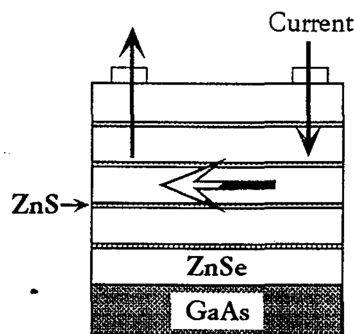

3) Ordered Alloys (n=4)

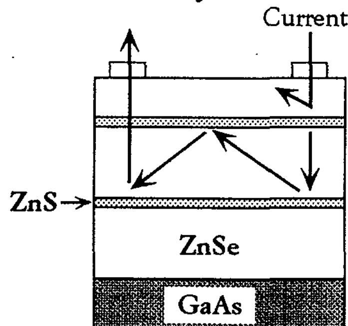

Figure 5-29 Schematic scattering mechanisms in ZnS_xSe_{1-x} disordered alloy (a), $(ZnS)_n(ZnSe)_m$ ordered alloys (n=1~3) (b) and n=4 (c).

weak structure dependence on the carrier transport properties and only the strain effects slightly affect the electron mobility of the ordered structure. In $(ZnS)_4(ZnSe)_{56}$, however, many scattering centers are formed due to the increased ZnS layer thickness having large lattice mismatch with the substrate, as shown in Fig. 5-29 (c).

In conclusion, iodine-doped $(ZnS)_n(ZnSe)_{14n}$ ordered and $ZnS_{0.07}Se_{0.93}$ disordered alloys were grown on the GaAs substrate by HRCVD at the low

temperature of 200°C. $(ZnS)_n(ZnSe)_{14n}$ ordered alloys (n=1~3) showed higher mobilities than that of the disordered alloys, although these crystals have the similar sulfur content and crystallinity, which were confirmed from the XRD and PL spectra. This higher mobility in the ordered alloys is attributed to the suppression of the "disorder scattering" arisen from the random potential fluctuations. The temperature dependence of the Hall mobility in the disordered alloy reveals the existence of the disorder scattering, which reduce the electron mobility remarkably at room temperature. Above evidences lead to a conclusion that crystal structure of the ordered alloys is quite useful for device application requiring high electron mobility.

Chapter 6

Structure and Properties of Zn(Se,Te) Ordered Alloys

For the purpose of realizing p-type conductivity in II-VI group crystals, we developed the layer-by-layer structure to fabricated Zn(Se,Te) ordered alloys. In the Zn(Se,Te) ordered alloys, large p-type doping limit in ZnTe layer is expected to enable the fabrication of the p-type crystal by the selective doping to ZnTe layer, as discussed in chapter 1. In this chapter, we fabricated two types of ordered alloys, $(ZnSe)_n(ZnTe)_{11n}$ and $(ZnSe)_n(ZnTe)_n$ (n=1~4), on InAs and InP substrates, respectively. Especially, specific optical properties of $(ZnSe)_n(ZnTe)_{11n}$ ordered alloys are described in detail. Fundamental characteristics of these multilayer structures are further investigated by comparing properties of $(ZnSe)_n(ZnTe)_{11n}$ with that of $(ZnS)_n(ZnSe)_{12n}$ having the similar compositional modulation ratio. In the last part of this chapter, the results of p-type doping to ZnTe layer using triisopropyl-antimony will be presented.

6.1 Introduction to Zn(Se,Te) crystal

So far, the number of researches have been made concerning the fabrication of ZnTe crystals. Nevertheless, the research efforts for ZnTe crystals have been limited due to its relatively small band-gap (2.3 eV at room temperature) which corresponds to the green light in visible spectra. The growth of ZnTe single epitaxial layers by MBE[1-4] and MOVPE[5-9] has been reported. In MOVPE system, diisoproyltelluride (DIPTe) has been commonly used for the growth of ZnTe crystals at the substrate temperature around 350°C.[5-9] In general, the crystal quality of ZnTe is relatively poor,

compared with the ZnSe crystals, because of the extremely large lattice mismatch of ZnTe layers with the commonly used GaAs substrate (~7%). In addition, thermal expansion coefficient of ZnTe crystal is higher than that of ZnSe (table 2-1), and there are more pronounced thermoelastic strain effects in ZnTe crystals.

The most characteristic feature of ZnTe crystal is a type II band formation with ZnS, ZnSe crystals. In $ZnSe_xTe_{1-x}$ disordered alloys, this band-structure leads to the formation of iso-electric traps in ZnSe crystals.[10-12] In addition, anomalous behavior called "band-gap bowing" can be seen in $ZnSe_xTe_{1-x}$ disordered alloys; the band-gap of $ZnSe_xTe_{1-x}$ crystals does not show the linear dependence of the composition but show the band-gap minimum at the selenium composition of 35 at%.[13,14] In addition, the large lattice mismatch between ZnSe and ZnTe layer (~7%) further causes difficulties in the fabrication of high-quality $ZnSe_xTe_{1-x}$ crystals.

Most recently, the graded structure of Zn(Se,Te) crystals was employed to form ohmic contacts to ZnSe crystal, which attract wide attentions to ZnTe crystals.[15,16] The successful fabrication of p-type ZnTe crystals have been also reported using nitrogen-plasma doping in MBE.[17] As a result, it was confirmed that ZnTe crystal has a larger doping limit than ZnSe crystal.[18,19] In MOVPE, however, the fabrication of p-type ZnTe-ZnSe crystals has not been established, although fabrication of p-type ZnTe crystal was reported.[20]

In the Zn(Se,Te) ordered alloys, the realization of p-type conductivity is expected using selective p-type doping to ZnTe layers. The defect formation caused by the large lattice mismatch can be suppressed by the low temperature growth by HRCVD as well as the asymmetric strain effects in the ordered alloys, as discussed in chapter 4. Moreover, it is also possible to understand the fundamental properties of Zn(Se,Te) crystals from the structural dependence of the ordered alloys.

6.2 Growth of ZnTe crystal

In order to determine fundamental growth conditions of Zn(Se,Te) ordered alloys, we first fabricated ZnTe crystals by HRCVD. Various III-V substrates, such as InAs, InP and GaAs, were employed for the growth of ZnTe single epitaxial layers. Among these substrates, InAs (100) substrate was mainly used for the growth of ZnTe crystal because of the small lattice

mismatch of +0.74%. Diethylditelluride (DEDTe) was chosen as a Te-source for HRCVD since the Te-Te bond of this molecule enables the direct decomposition of the source gas by atomic hydrogen, as discussed in chapter 4. In fact, when diethyltelluride (DETe) was employed as a source molecule for HRCVD, quite low growth rates of ZnTe layers (~ 0.1 ML/cycle) were found probably due to the high metal-ligand bond strength of VI group sources, as shown in Fig. 3-5. In this section, the ZnTe crystals was grown by HRCVD at a low temperature of 200°C. The source molecules were supplied alternately to control atomic structures of ZnTe crystal. Typical growth conditions of ZnTe crystal by HRCVD are listed in Table 6-1.

Table 6-1 Typical growth conditions for ZnTe

Flow rate	
DEZn	6.76 μmol/min
DEDTe	1~10μmol/min
H_2 (sccm)	200
Pulse duration (sec)	4-0-4-0
Susceptor distance (mm)	15
Growth temperature (oC)	150~300

Figure 6-1 shows the growth rate of ZnTe crystals on InAs (100) substrate plotted as a function of the flow rate of DEDTe. The flow rate of DEDTe was sequentially controlled by the vapor pressure of DEDTe while keeping the flow rate of hydrogen carrier gas (30 sccm). As shown in Fig. 6-1, the growth rate increases linearly with the flow rate of DEDTe, indicating the precursor formation by the supply of DEDTe. Nevertheless, the self-limiting growth of ZnTe layers was not shown; the growth rate is larger than 1 ML/cycle at the flow rate over 3 μmol/min. From this result, it is indicated that the growth rate of ZnTe crystal can be simply changed by controlling the vapor pressure of DEDTe.

From XRD spectra of these grown samples, the epitaxial growth of ZnTe crystals on InAs substrate was found. In addition, the ZnTe crystals on InP and GaAs substrates also show the single epitaxial growth at the same growth condition. Figure 6-2 shows full-width at half maximums (FWHM) of the ZnTe (400) diffraction peaks for different substrates plotted as a function of the film thickness. Narrow diffraction peaks of ~200 arcsec can

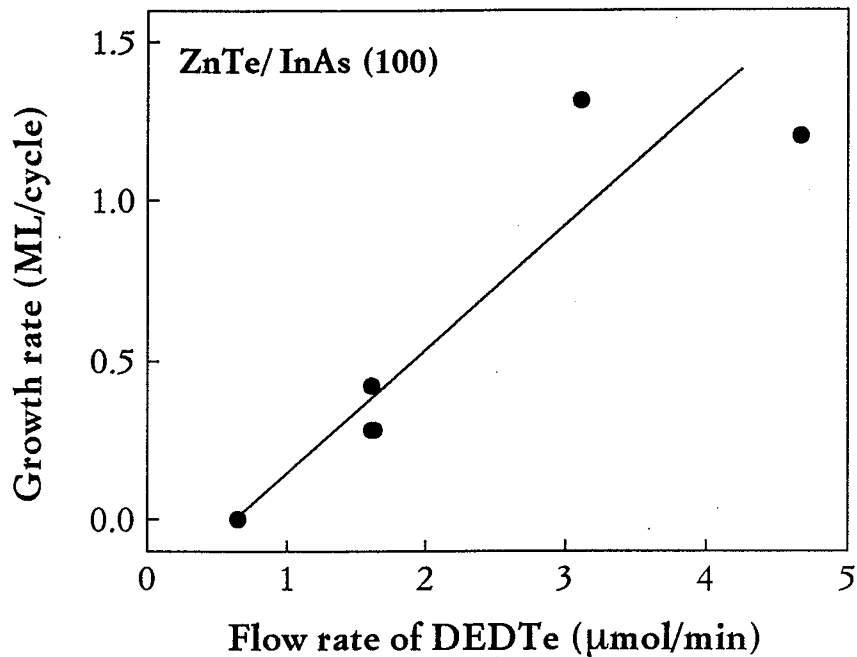

Figure 6-1 The growth rate of ZnTe crystals on InAs (100) substrate plotted as a function of the flow rate of DEDTe.

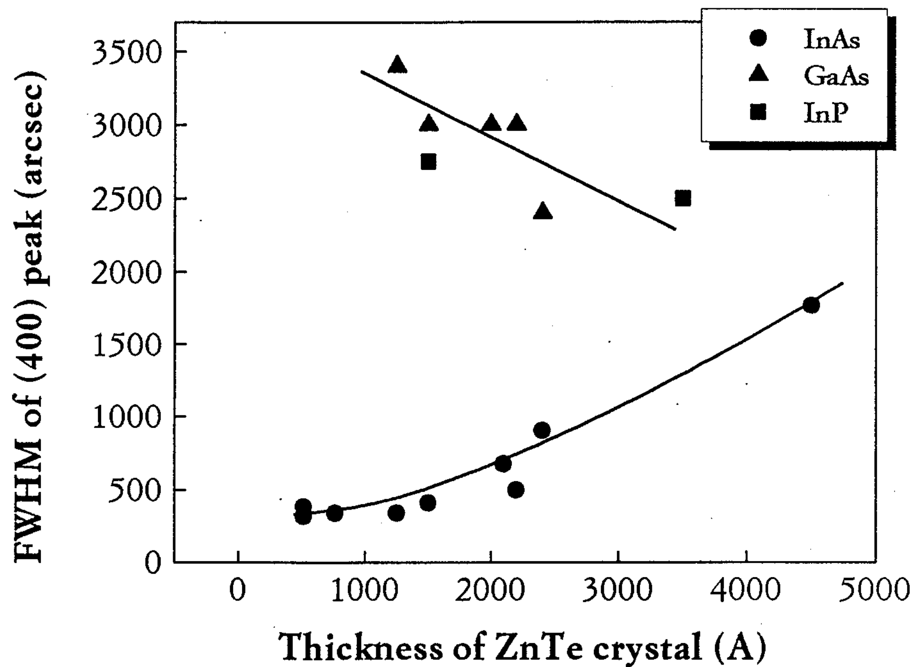

Figure 6-2 The FWHM of the ZnTe (400) diffraction peaks for different substrates plotted as a function of the film thickness.

be seen in the ZnTe crystals grown on InAs substrate at the film thickness less than 1500Å. At this thickness, lattice parameters perpendicular to the surface of ZnSe crystal is around 6.15Å, and agree well with the calculated value using Eq. (3-5) under the assumption of coherent growth (6.155Å). The FWHM of this crystal, however, gradually increase as the film thickness increased due to the lattice relaxation of ZnTe layers on the InAs substrate. When the ZnTe crystals were grown on InP and GaAs substrate, on the other hand, broad XRD peaks of the order of 3000 arcsec were shown because of the dislocation generation results from the larger lattice mismatch of these substrate (InP: 3.5%, GaAs: 7%). It should be mentioned that the FWHM of ZnTe grown on InP and GaAs substrates slowly recovers with the sample thickness since the crystallinity of the lattice relaxed ZnTe gradually improves with increasing sample thickness.[1,6] From these results, the InAs substrate was confirmed to be the most appropriate substrate for the growth of ZnTe crystal at this film thickness.

Figure 6-3 shows the temperature dependence of the growth rate (a) and the FWHM of the diffraction peaks (b). As shown in this figure, the growth rate of ZnTe crystal decrease with the growth temperature, and the monolayer growth was indicated at the substrate temperature of 200 °C. This result is similar to that of the ZnSe crystal (Fig. 3-30), where the adsorption (or desorption) process of the chemical active precursors on the crystal growing surface is the rate determing step for the film growth. Consequently, it was confirmed that DEDTe source molecules can be decomposed by the chemical reaction with atomic hydrogen generated by rf plasma. The FWHM of the ZnTe crystal, on the other hand, shows the minimum value at the substrate temperature of 200°C. As shown in Fig. 6-3 (b), the high temperature growth leads to the significant peak broadening, even though the film thickness is reduced. The thermoelastic strain effects may be responsible for the peak broadening, as mentioned before. At the substrate temperature of 150 °C, a rapid increase in the FWHM was shown probably due to the excess adsorption of the precursors or the formation of the misfit dislocation caused by the increased film thickness. From these results, the optimized growth temperature was determined to be 200°C at this growth condition. As a result, the Zn(Se,Te) crystal can be also grown at this temperature because the growth of ZnSe crystal has been established at the same temperature.

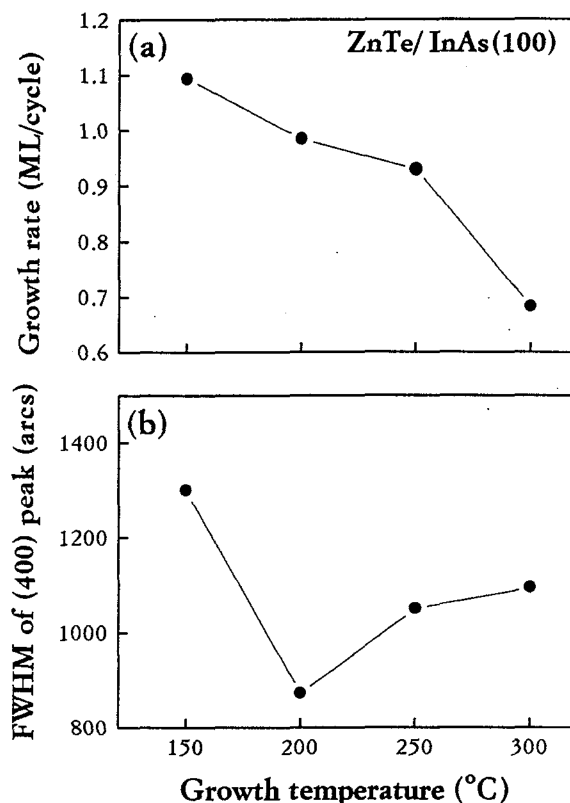

Figure 6-3 The temperature dependence of the growth rate (a) and the FWHM of the diffraction peaks (b).

In the PL spectra of the ZnTe crystals, however, only deep level emissions at 1.9 eV were observed, indicating the large amount of structure defects in the crystals. Obviously, this result is caused by the formation of the lattice mismatch defects since the thickness of these ZnTe crystals (~1500Å) are thicker than the calculated critical thickness of 500Å.[21)] When the film thickness was reduced to 500Å, no PL emissions was observed because of the poor crystallinity at the initial stage of the growth.

In summary of this section, the ZnTe crystals were fabricated by HRCVD using DEDTe as a source molecule. The decomposition of DEDTe source gas was shown from the temperature dependence of the growth rate, where the low temperature growth leads to the increased film thickness. The single epitaxial growth of these crystals were confirmed from the relatively narrow XRD diffraction peaks. Nevertheless, the dominant deep level emissions were observed in their PL spectra due to the defect formations caused by the relatively large lattice mismatch of 0.74% with InAs substrate.

6.3 Growth of $(ZnSe)_n(ZnTe)_{11n}$ (n=1~4) on InAs substrate

In the previous section, it was confirmed that the growth of ZnTe crystal is possible by HRCVD using DEDTe. The lattice relaxation effects was, however, shown in the grown ZnTe crystals due to the lattice mismatch strain with the InAs substrate. In order to prevent this strain effect, $(ZnSe)_n(ZnTe)_{11n}$ ordered alloys were grown by HRCVD. The number of ZnSe layers in this ordered alloy was changed from 1 to 4 (n=1~4) layers to determine to role of ZnSe layers. In this section, fundamental characteristics of these multilayer structures were investigated by comparing properties of $(ZnSe)_n(ZnTe)_{11n}$ with that of $(ZnS)_n(ZnSe)_{12n}$ having the similar compositional modulation ratio.

6.3.1 Optimization of growth conditions

Before the fabrication of this ordered alloys, the optimization of the growth condition was made by $(ZnSe)_1(ZnTe)_{20}$ (average Se content: ~5 at%) grown on the InAs substrate. The number of cycle was maintained to constant (600 cycles, ~1800Å). The crystal was grown by HRCVD at the substrate temperature of 200 °C. Typical growth conditions of this ordered alloy are summarized in Table 6-2.

Figure 6-4 shows the XRD spectra of ZnTe and $(ZnSe)_1(ZnTe)_{20}$ ordered alloys grown on InAs substrates. In the XRD spectra of the ZnTe single epitaxial film, a weak diffraction peak with its FWHM of ~900 arcsec was observed. In addition, this peak shows the tail to the higher diffraction angles due to the lattice relaxation since the lattice parameter of the "bulk state" is smaller than that of the coherent state. A drastic improvement of the

Table 6-2 Typical growth condition of Zn(Se,Te)

Flow rate	
DEZn	3.8 μmol/min
DEDSe	1.2 μmol/min
DEDTe	11.0 μmol/min
Pulse duration (sec)	
ZnTe	4-0-4-3
ZnSe	1.7-0-3.5-0

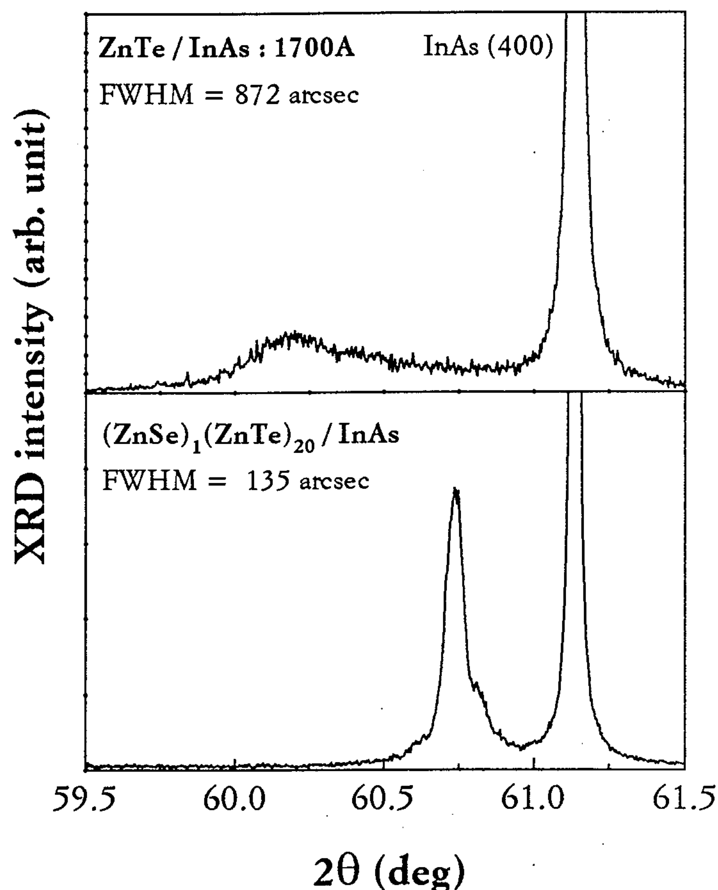

Figure 6-4 The XRD spectra of ZnTe and $(ZnSe)_1(ZnTe)_{20}$ ordered alloy grown on InAs substrates. The FWHM of the diffraction peaks are also indicated.

FWHM as well as the diffraction intensity can be seen in the XRD spectra of the ordered alloys. The FWHM of this crystal is improved up to ~140 arcsec by the introduction of ZnSe layers, suggesting the coherent growth of the ordered alloy. Moreover, the ordered alloy shows the XRD intensity 5 times larger than that of the ZnTe crystals. From these results, it is proved that the high-quality Zn(Se,Te) ordered alloys can be prepared by the 2-dimensional ordered structure even at the large lattice mismatch of 7% in ZnSe layer with InAs substrate.

Figure 6-5 shows the growth rate of ZnTe and ZnSe layer in the $(ZnSe)_1(ZnTe)_{20}$ ordered alloy plotted as a function of the flow rate of

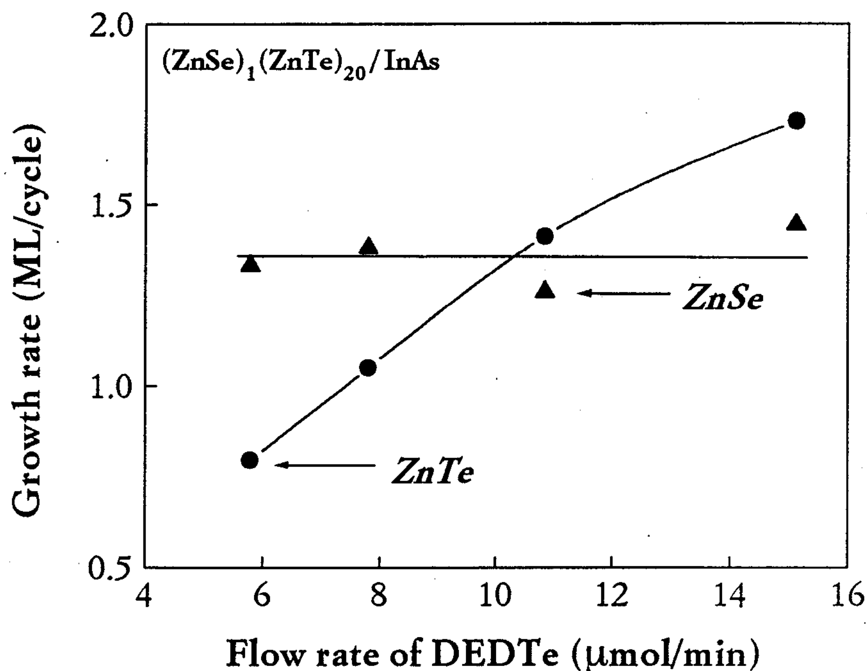

Figure 6-5 The growth rate of ZnTe and ZnSe layers in $(ZnSe)_1(ZnTe)_{20}$ ordered alloy plotted as a function of the flow rate of DEDTe.

DEDTe. As shown in figure, the growth rate of ZnTe layer gradually increases with the flow rate of DEDTe. In addition, it was found that the growth rate of ZnSe layers, roughly estimated from the total thickness and the average Se composition, is independent of the flow rate of DEDTe. The unfavorable mutual interaction between ZnSe and ZnTe layer is, therefore, considered to be small in this study. Nevertheless, the growth rate of ZnSe was constant at 1.3 ML/cycle and we could not reduce the growth rate of the ZnSe layer from this thickness. It should be noteworthy that the ALE growth of Se layers has been observed in ZnSe crystal. It is suggested that the adsorption (or desorption) process of ZnSe may be influenced by the electronic state or the chemical potential of the underlying ZnTe layers. In the PL spectra, on the other hands, the significant reduction in the deep level emission was found at the flow rate of 11 μmol/min. Unfortunately, the ZnTe crystal grown at the condition of 1 ML/cycle (7.5 μmol/min) show the enhanced deep level emission. As a result, the flow rate of 11 μmol/min was adapted for the growth of $(ZnSe)_n(ZnTe)_{11n}$ (n=1~4) ordered alloys.

6.3.2 Structure of $(ZnSe)_n(ZnTe)_{11n}$ (n=1~4)

Figure 6-6 shows the lattice parameter of ZnSe, ZnTe crystals together with their substrates plotted as a function of the band-gap. The structure of the $(ZnSe)_n(ZnTe)_{11n}$ ordered alloys was decided so as to provide lattice matching to the InAs substrate, and the average selenium content of these ordered alloys is 8 at%. In these ordered structures, the ZnSe layers have the large difference in the lattice constant with the InAs substrate, as shown in Fig. 6-6. Consequently, compared with $(ZnS)_n(ZnSe)_{12n}$ ordered alloys, the larger strain effects is expected in $(ZnSe)_n(ZnTe)_{11n}$ ordered alloys. All the samples were grown by HRCVD at the temperature of 200°C with the growth condition listed in Table 6-2. The pulse durations of the source gases were, however, slightly changed depending on the structure because of the incomplete ALE growth in Zn(Se,Te), as mentioned above. The thickness of films were kept at constant (2000Å).

Figure 6-7 shows the XRD spectra of the $(ZnSe)_n(ZnTe)_{11n}$ ordered alloys (n=2~4). Sharp 0-order diffraction peaks of 100 arcs and satellite peaks arisen from the 2-dimensional structure are observed. The calculated angle

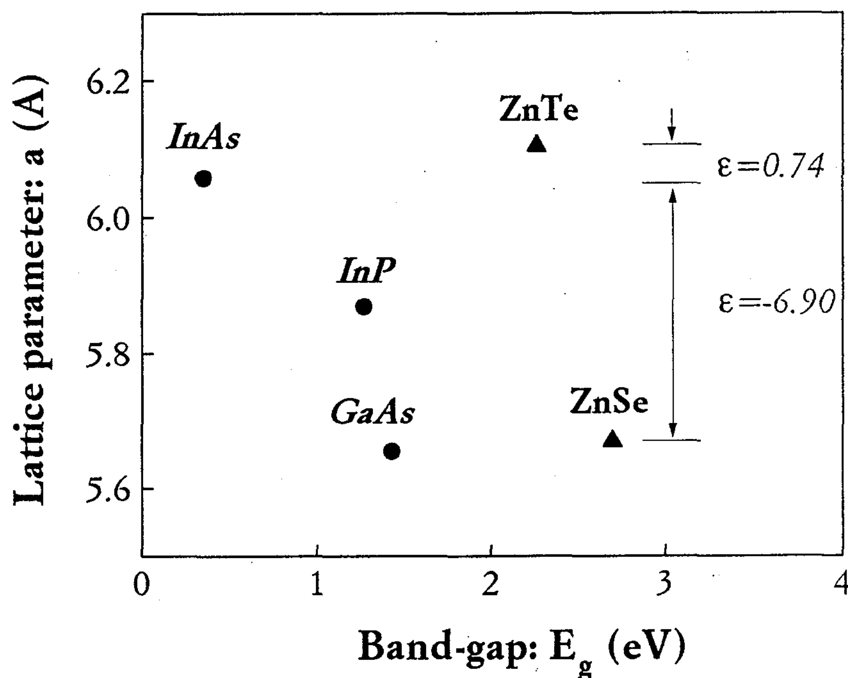

Figure 6-6 The lattice parameter of ZnSe, ZnTe crystals together with their substrates plotted as a function of the band-gap. The lattice mismatches of ZnSe and ZnTe crystals with InAs substrates are also indicated.

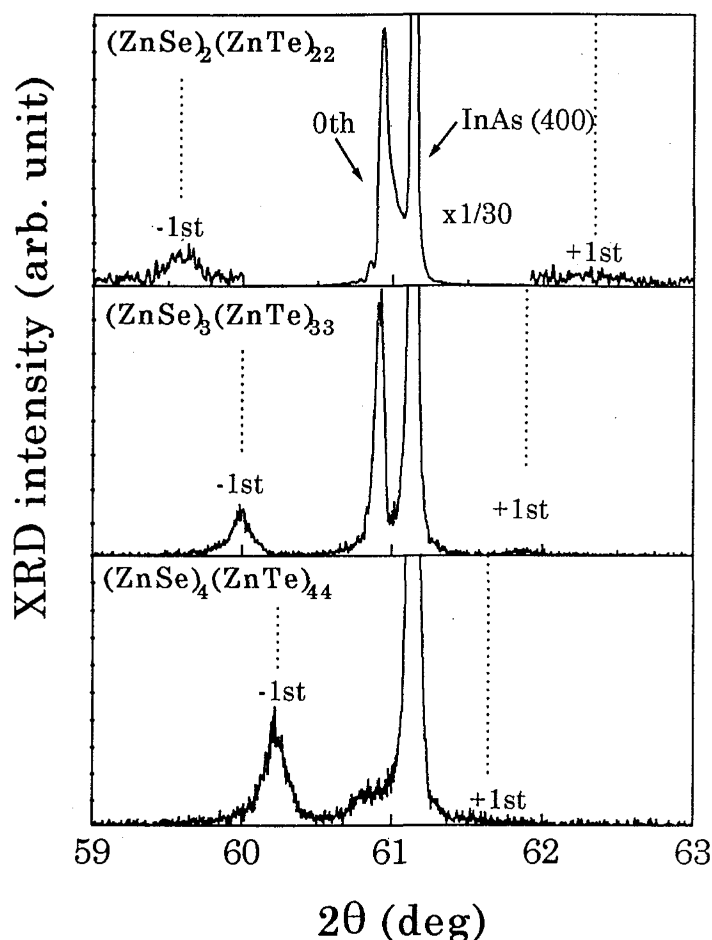

Figure 6-7 The XRD spectra of the $(ZnSe)_n(ZnTe)_{11n}$ ordered alloys (n=2~4). The calculated diffraction angles for the satellite peaks are also indicated as the dotted lines.

assuming the coherent growth (dotted line in Fig. 6-7) agreed well with the observed angles. These evidences lead to a conclusion that these layers were grown coherently on InAs substrate in spite of the large lattice mismatch as large as 7% between the ZnSe layers and the substrate. The satellite peaks was not observed when the ZnSe thickness was reduced to one monolayer (n=1), indicating the imperfect periodic structure at this thickness.

Figure 6-8 shows the FWHM of the (400) diffraction peak of the same samples plotted as a function of the number of ZnSe layers. The sharp XRD diffraction peak of the ordered alloys gradually increases with number

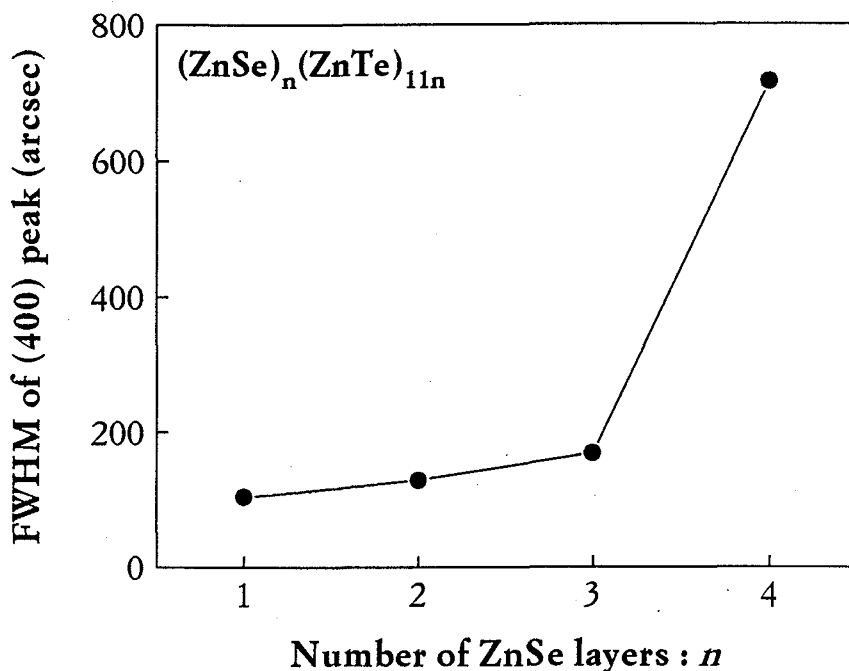

Figure 6-8 The FWHM of the (400) diffraction peak of $(ZnSe)_n(ZnTe)_{11n}$ (n=1~4) plotted as a function of the number of ZnSe layers.

of ZnSe layers (n=1~3). An indication of the lattice relaxation due to large lattice mismatch is given by the very weak 0-order peak observed in the crystal (n=4). From this result, the critical thickness of ZnSe layer on the InAs substrate are determined to be 4 atomic layers. The above results indicate that the ordered alloys grown in this study have the expected ordered structure with little monolayer structural fluctuation.

6.3.3 Optical properties of $(ZnSe)_n(ZnTe)_{11n}$

In this section, optical properties of $(ZnSe)_n(ZnTe)_{11n}$ ordered alloys were investigated by the various PL properties. The specific behaviors of the exciton in $(ZnSe)_n(ZnTe)_{11n}$ ordered alloys were characterized by the PLE and the time-resolved PL spectra. In addition, the band structures of the ordered alloys were further discussed from the comparison between the $(ZnS)_n(ZnSe)_{12n}$ and $(ZnSe)_n(ZnTe)_{11n}$.

Figure 6-9 shows typical PL spectra of ZnTe and $(ZnSe)_1(ZnTe)_{11}$ ordered alloy grown on InAs substrate under the similar condition. The thickness of these sample is 1700Å in both case. A clear difference can be seen in these

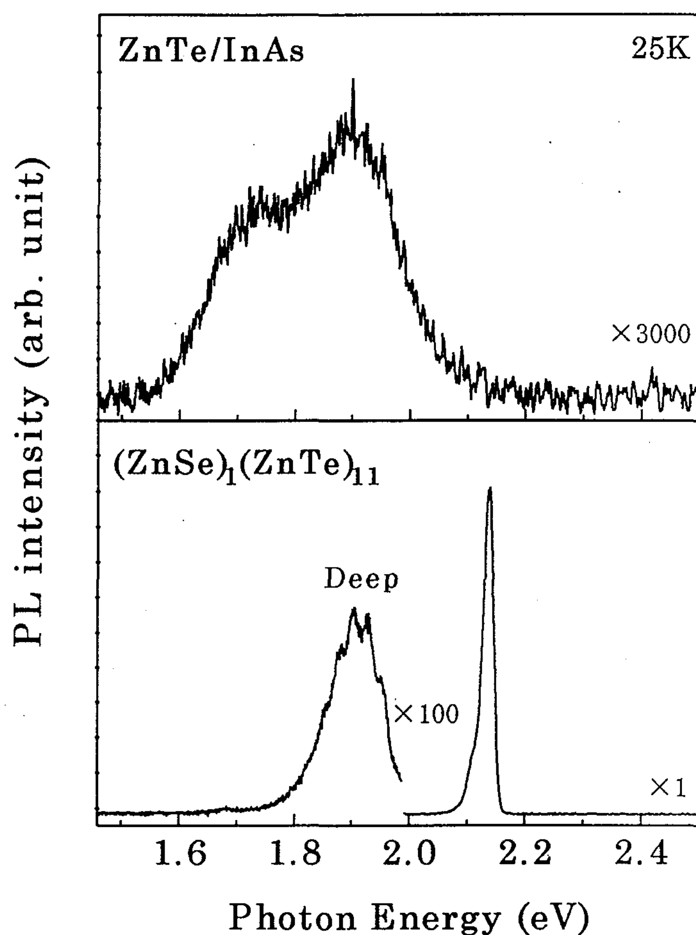

Figure 6-9 Typical PL spectra of ZnTe and $(ZnSe)_1(ZnTe)_{11}$ ordered alloy grown on InAs substrate under the similar condition. The thickness of these sample is 1700Å in both case.

crystals in the PL spectra. In the ordered alloy, the dominant band-edge emission is observed with the suppressed deep-level emission, while only the weak deep level emission is shown in ZnTe crystal. Obviously, this difference originates from the suppression of the defect formation in the ordered alloy by the layer-by-layer structure. Accordingly, it was confirmed that the structure of the ordered alloy is also effective to Zn(Se,Te) crystals.

Figure 6-10 shows the PL spectra of $(ZnSe)_n(ZnTe)_{11n}$ ordered alloys (n=1~3) measured at 25 K. In the ordered alloy (n=4), the PL measurement was not made because of the weak PL emission intensity due to the lattice

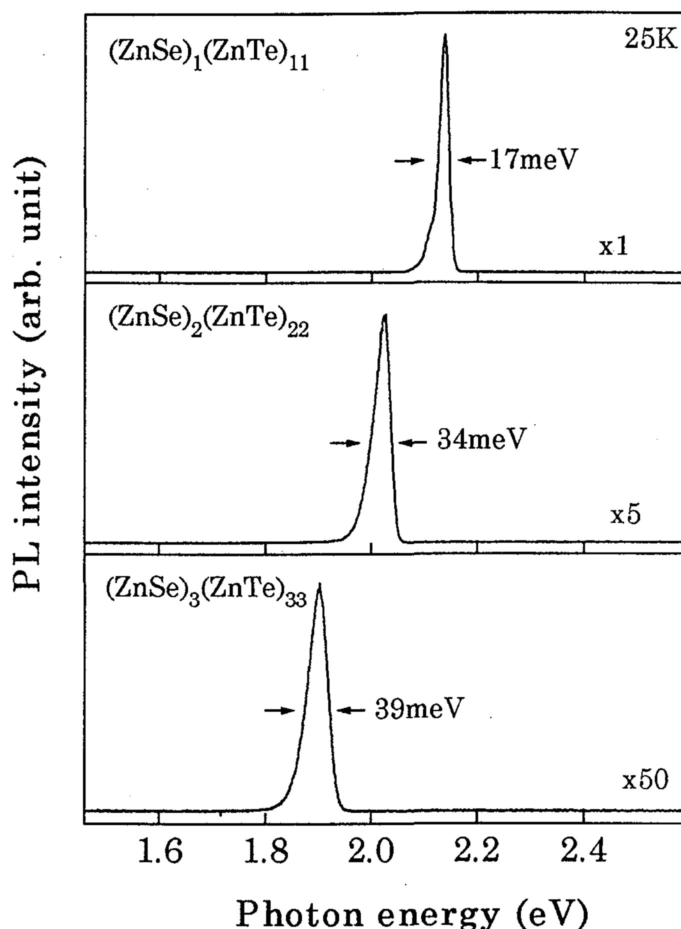

Figure 6-10 The PL spectra of $(ZnSe)_n(ZnTe)_{11n}$ ordered alloys (n=1~3) measured at 25 K.

relaxation. As shown in Fig. 6-10, strong band-edge emissions were observed in these samples, while no remarkable deep level emissions are shown. In the PL spectra, however, broad band-edge emission peaks are observed, and the emission intensity gradually decrease with increasing ZnSe layer thickness. In addition, the peak width of PL peaks in $(ZnSe)_n(ZnTe)_{11n}$ becomes broad from 17 to 39 meV with increasing n (n=1~3).

As mentioned in chapter 4, in $(ZnS)_n(ZnSe)_{12n}$ ordered alloys, the band-edge emission is independent of the ordered structure, and is characterized by the sharp free exciton emission of 4 meV. It is noteworthy that Zn(S,Se) and Zn(Se,Te) ordered alloys have the similar peak width of 0-order diffraction in the XRD spectra. Consequently, marked difference in the

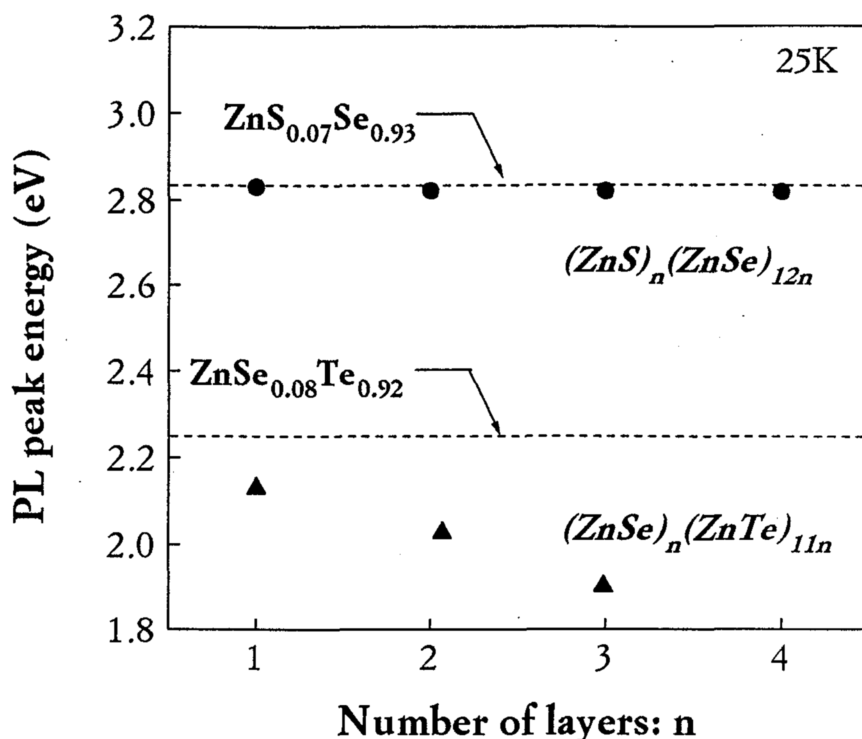

Figure 6-11 The peak energies of PL peaks for $(ZnSe)_n(ZnTe)_{11n}$ and $(ZnS)_n(ZnSe)_{12n}$ measured at 25 K plotted as a function of the number of layers *n*. The dotted lines in the figure indicate the peak positions of $ZnS_{0.07}Se_{0.93}$ and $ZnSe_{0.08}Te_{0.92}$.

band width of PL peaks between these crystals is arisen from the electronic states by the combinations of ZnS-ZnSe and ZnSe-ZnTe, respectively.

Figure 6-11 shows the peak energies of PL peaks for $(ZnSe)_n(ZnTe)_{11n}$ and $(ZnS)_n(ZnSe)_{12n}$ measured at 25 K plotted as a function of the number of layers *n*. The peak energy for $(ZnSe)_n(ZnTe)_{11n}$ corresponds to the PL spectra shown in Fig. 6-10. The dotted lines in the figure indicate the peak positions of $ZnS_{0.07}Se_{0.93}$ and $ZnSe_{0.08}Te_{0.92}$, which have the same chemical composition with their layer-by-layer structures, respectively. In $(ZnS)_n(ZnSe)_{12n}$, the excitonic PL peaks shift slightly to lower energies with increasing *n* by 13 meV (n=1~4), as shown in Fig. 4-10. In addition, the peak energy of the crystal (n=1) is the same as that of $ZnS_{0.07}Se_{0.93}$, suggesting that the band structure of this crystal is similar to that of mixed crystal. In $(ZnSe)_n(ZnTe)_{11n}$, on the other hands, the change of *n* induces a large PL peak shift by 200 meV corresponding to the color change from yellowish green to red, although the macroscopic chemical composition is

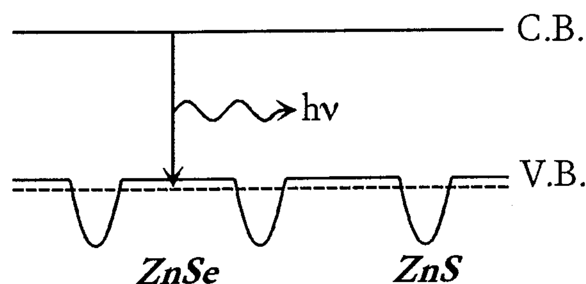

(a) ZnS-ZnSe

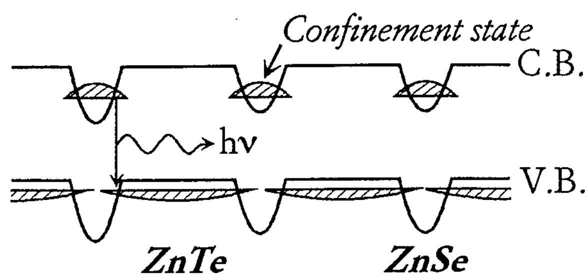

(b) ZnSe-ZnTe

Figure 6-12 The schematic band-diagrams of $(ZnS)_n(ZnSe)_m$ (a) and $(ZnSe)_n(ZnTe)_m$ (b).

unchanged. Obviously, the peak energies of the $(ZnSe)_n(ZnTe)_{11n}$ are lower than that of $ZnSe_{0.08}Te_{0.92}$ and energy difference is about 110 meV even at n=1. It is important to note that the band gap of ZnSe and ZnTe at this temperature is about 2.8 and 2.4 eV, respectively, and the PL peak positions of $(ZnSe)_n(ZnTe)_{11n}$ are much lower compared with each host crystals.

As described above, in the PL properties of crystals with the 2-dimensional ordered structures, distinct differences are observed between $(ZnS)_n(ZnSe)_{12n}$ and $(ZnSe)_n(ZnTe)_{11n}$; namely, the sharp PL peaks of $(ZnS)_n(ZnSe)_{12n}$ shift slightly toward lower energy with increasing n, whereas marked shifts are observed in the broad peaks of $(ZnSe)_n(ZnTe)_{11n}$. These PL shifts observed in the 2-dimensional ordered crystals are explained in term of the band structures formed at the heterointerfaces. Schematic band-diagrams of $(ZnS)_n(ZnSe)_m$ (a) and $(ZnSe)_n(ZnTe)_m$ (b) are shown in Fig. 6-12. The conduction band offset in ZnS-ZnSe is known to be almost zero (ΔE_c=0),[22] as predicted by the common anion rule. Although valence band offset (ΔE_v=0.65 eV) is formed in this structure,

confinement effects of exciton in ZnSe quantum well is weak due to its very thin barrier layer. As the result of the weak confinement effects, the overlap of the wavefunction at the valence band may takes place, as shown in the dotted line in Fig. 6-12 (a). Consequently, the PL spectra are almost same with that of the disordered alloy having same chemical constituent.

The band structure at the heterointerface between ZnSe and ZnTe is not, however, ruled by the common anion rule and the superlattice structure categorized in type II is more likely to be formed.[23,24] The energy offsets at conduction and valence band are calculated to be ΔE_c=1.2 eV and ΔE_v=1 eV, respectively, assuming the coherent growth on InAs substrates.[25] These facts suggest that confinement states are easily formed especially at the conduction band edge in ZnSe-ZnTe heterointerface, as shown in Fig. 6-12 (b). Consequently, the large PL red-shift observed in $(ZnSe)_n(ZnTe)_{11n}$ can be explained by quantum-size effect in ZnSe well layers. The broad PL peaks in $(ZnSe)_n(ZnTe)_{11n}$ indicate formation of the tail states in gaps,[26] since the thickness fluctuation on the atomic scale easily generate the large potential fluctuation in this crystal.

In order to further confirm the specific band structure of $(ZnSe)_n(ZnTe)_{11n}$ ordered alloys, we examined the PL excitation (PLE) spectra. Figure 6-13 shows the PLE of $(ZnS)_n(ZnTe)_{11n}$ (n=1~2) at 2 K. The PL peaks measured at same temperature are also shown in this figure. In these ordered alloys, the PLE spectra clearly shows two absorption peaks labeled *A* and *B*. Figure 6-14 also shows the peak energy of these two peaks plotted as a function of the number of ZnSe layers. The peak position of the PL peaks is also indicated in Fig. 6-14. As shown in Figs 6-13 and 6-14, the PLE peak of *A* shifts largely to the lower energy side together with the corresponding PL peaks, while the PLE peak of *B* only shows the small shift. From these results, the absorption process of *A* can be attributed to the interband transition from the valence band of ZnTe to the ZnSe quantum well at the conduction band. The large absorption peak shifts could be the result of quantum size effects caused by the small dimensions of the well. On the other hand, the transition process of *B* is considered to originates from the direct transition in ZnTe layers since the band-gap of ZnTe at this temperature is calculated to be 2.41 eV, which is close enough with the observed transition energy of *B*. Accordingly, the type II band lineup between ZnSe and ZnTe is proved even though the ZnSe quantum well is

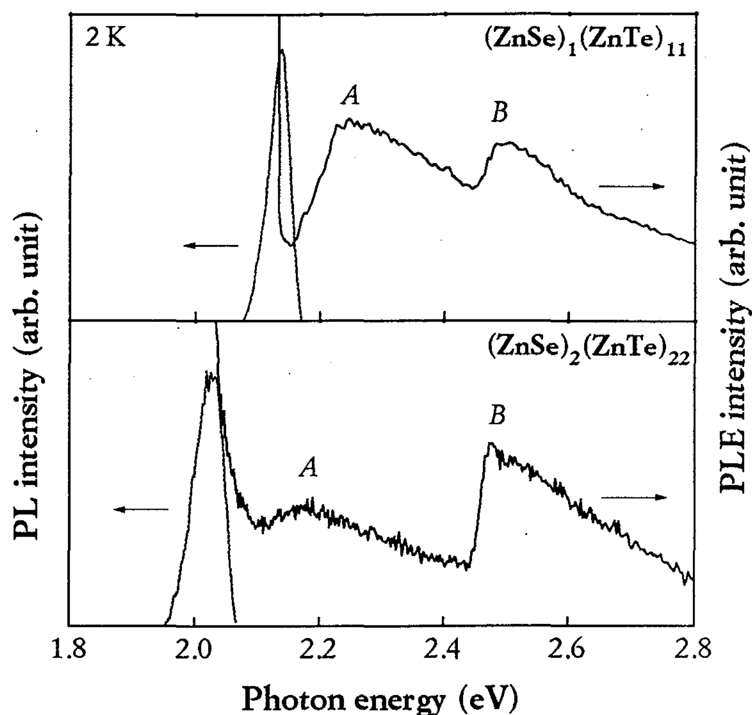

Figure 6-13 The PLE spectra of $(ZnS)_n(ZnTe)_{11n}$ (n=1~2) at 2 K. The PL peaks measured at same temperature are also shown in this figure.

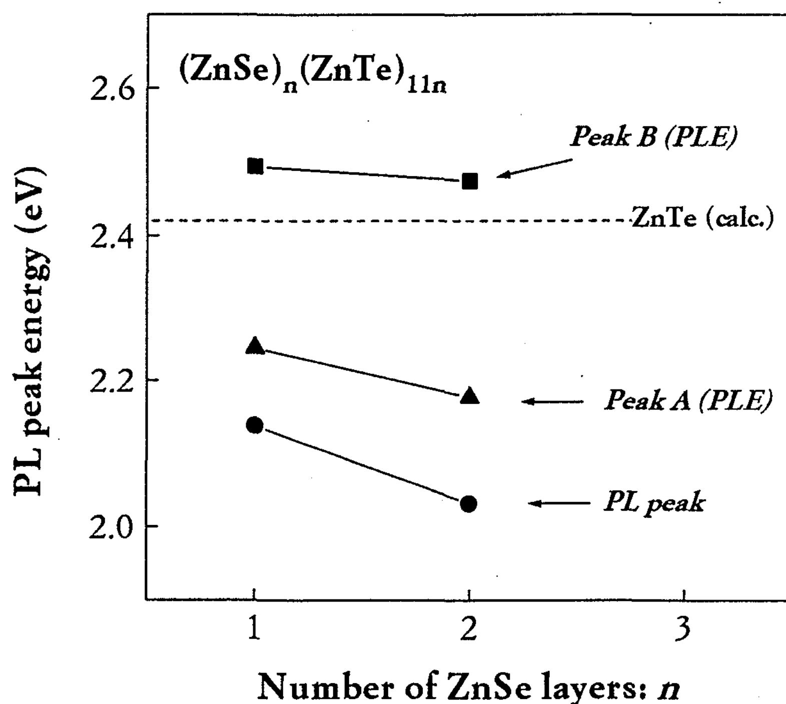

Figure 6-14 The peak energy of A and B in the PLE spectra (Fig. 6-13) plotted as a function of the number of ZnSe layers. The peak positions of the PL peaks are also indicated

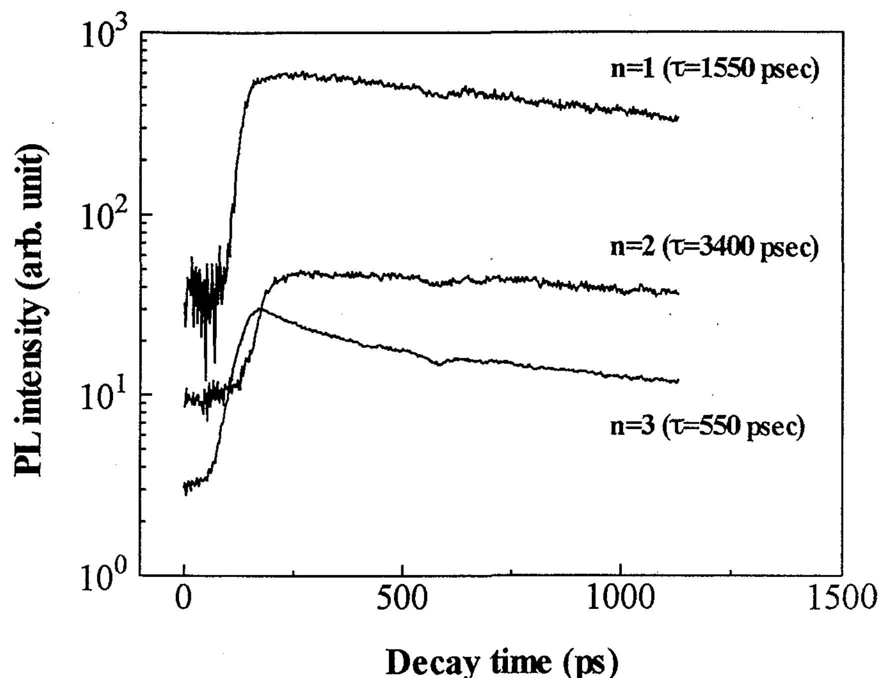

Figure 6-15 The time-resolved PL spectra of $(ZnSe)_n(ZnTe)_{11n}$ ordered alloys (*n*=1~3) at 2 K.

consist of only few monolayers.

This type II band structure at ZnSe-ZnTe heterointerfaces was further characterized by the time-resolved PL spectra. Figure 6-15 shows the time-resolved PL spectra of $(ZnSe)_n(ZnTe)_{11n}$ ordered alloys (*n*=1~3) at 2 K. As shown in Fig. 6-15, very long lifetime of the order of nanosecond was obtained in the ordered alloys (*n*=1~2). A relatively small life time of the ordered alloy (n=3) might be caused by the increased non-radiative recombination centers due to the large strain in ZnSe layers. It should be mentioned that the exciton life time of $(ZnS)_n(ZnSe)_{12n}$ is in a range of 100 psec, as shown in Figs. 4-19 and 4-20. In addition, the emission life time of *n*=2 is more than double than that of *n*=1. These results gives a strong support to the idea that the confinement states are formed at the conduction band edge of ZnSe-ZnTe layers since the type II band-structure significantly reduce the recombination probability by the separate confinement effect. In the case of $ZnSe_xTe_{1-x}$ disordered alloy with the same composition, the similar life time with the ordered alloy of *n*=1 was observed (~1.6 nsec). This evidence suggests that the compositional fluctuation (or potential fluctuation) is easily created in ZnSe-ZnTe crystals.

In summary of this section, high-quality crystals given by $(ZnSe)_n(ZnTe)_{11n}$ (n=1~4) were grown epitaxialy on InAs (100)substrates by HRCVD. Defect formations are efficiently eliminated with the aid of growth at the temperature as low as 200°C. From XRD spectra, it was confirmed that these crystals with ordered structure were grown coherently by adjusting their lattice parameters with that of the substrates. Distinctive differences were found in the electric states between $(ZnSe)_n(ZnTe)_{11n}$ and $(ZnS)_n(ZnSe)_{12n}$ from PL spectra; very sharp emission attributed to the free excitons was dominant in $(ZnS)_n(ZnSe)_{12n}$, whereas broad emissions were obtained in $(ZnSe)_n(ZnTe)_{11n}$. It is suggested that the potential fluctuation due to the large difference in the band structure between ZnSe and ZnTe is responsible for the broadening effect. In these ordered crystals, on the other hands, the emission peaks were systematically shifted toward lower energy with increasing n. These energy shifts are explained in terms of the quantum confinement effects with the periodical modulations. The type II band structure in $(ZnSe)_n(ZnTe)_{11n}$ was confirmed from the PLE spectra. These evidences lead us to a conclusion that HRCVD is a promising growth technique to fabricate high-quality crystals and also to modulate chemical constituents for the aim of "band-engineering".

6.4 Growth of $(ZnSe)_n(ZnTe)_n$ (n=1~4) on InP substrate

In the previous section, it was shown that the coherent growth of the crystals can be made by the layer-by-layer structure of $(ZnSe)_n(ZnTe)_{11n}$ ordered alloy while suppressing the defect formation arisen from the lattice mismatch strains. In order to attain a larger compositional modulation of Zn(Se,Te) ordered alloys, we fabricated $(ZnSe)_n(ZnTe)_n$ ordered alloys (n=1~4) on the InP substrate, in which the average selenium composition is 50 at%. In this section, the effect of the 2-dimensional ordered structure at this maximum compositional modulation ratio are described in detail.

6.4.1 Structure of $(ZnSe)_n(ZnTe)_n$ (n=1~4)

Figure 6-16 shows the lattice parameter of ZnSe and ZnTe crystals together with their substrates plotted as a function of the band-gap at room temperature. The structure of $(ZnSe)_n(ZnTe)_n$ ordered alloys was decided so as to provide lattice matching to the InP substrate; assuming the coherent growth of these crystals, a lattice matching selenium composition of Zn(Se,Te) crystal with InP substrate is calculated to be 53 at%. As a result, the coherent structure of $(ZnSe)_n(ZnTe)_n$ can be prepared using InP at the selenium composition of 50 at%. In $(ZnSe)_n(ZnTe)_{11n}$ ordered alloy discussed in the previous section, the lattice mismatch strain is mainly applied to the ZnSe layers as shown in Fig. 6-6. In contrast to this, the $(ZnS)_n(ZnTe)_n$ ordered alloys provide the similar lattice mismatch stains in each of ZnSe and ZnTe layers ($\varepsilon = \pm$ 3~4%), which corresponds to the strain between ZnS and ZnSe (ε=4.32%). Taking these strains into account, the critical thickness of these ZnSe and ZnTe layers on InP substrate is roughly estimated to be around 3~5 monolayers. All the samples were grown by HRCVD at the temperature of 200°C with the growth condition listed in Table 6-3. Total number of cycle was kept constant to 400 monolayers and the resulting film thickness was typically 1400Å.

Figure 6-17 shows the XRD spectra of $(ZnSe)_2(ZnTe)_2$ ordered alloys grown by the different reactor pressures (P=130~190 mTorr). When the crystal was grown at the typical reactor pressure (130 mTorr), the ordered alloys generally shows the peak splitting of the (400) diffraction peaks. This splitting is considered to be caused by the cluster formation in the

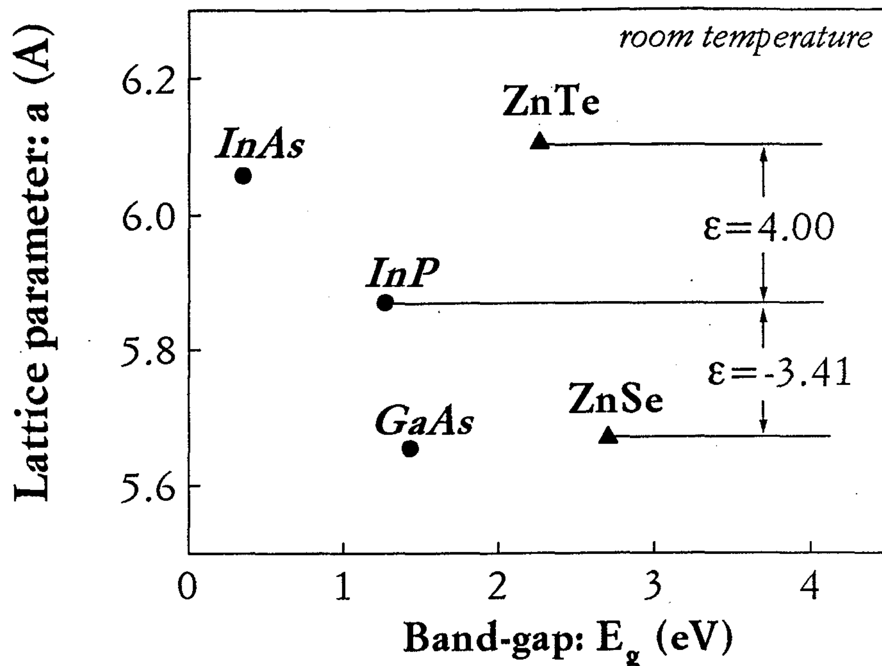

Figure 6-16 The lattice parameter of ZnSe and ZnTe crystals together with their substrates plotted as a function of the band-gap at room temperature.

Table 6-3 Typical growth conditions for $(ZnSe)_n(ZnTe)_n$

Flow rate	
DEZn	3.5 μmol/min
DEDSe	0.9 μmol/min
DEDTe	8.1 μmol/min
Pulse duration (sec)	
ZnTe	5-1-4-3
ZnSe	2.5-0-3.5-0

crystals, which have the difference composition. The existing high strain between the ZnSe and ZnTe layers on the InP substrate might be responsible for this peak splitting effect. In fact, the enhanced 3-dimensional growth was observed in ZnTe crystal grown on GaAs substrate.[27)] Most recently, such crystal "dots" formed by high strain field on crystal surfaces attracts wide attention for device applications in III-V crystals.[28-30)] In addition, it has been reported that the ALE growth enhance the such cluster (or dots) formation.[31)] As a result, it was suggested that the large lattice mismatches of ZnSe and ZnTe layers prefer the cluster formation in order to reduce the

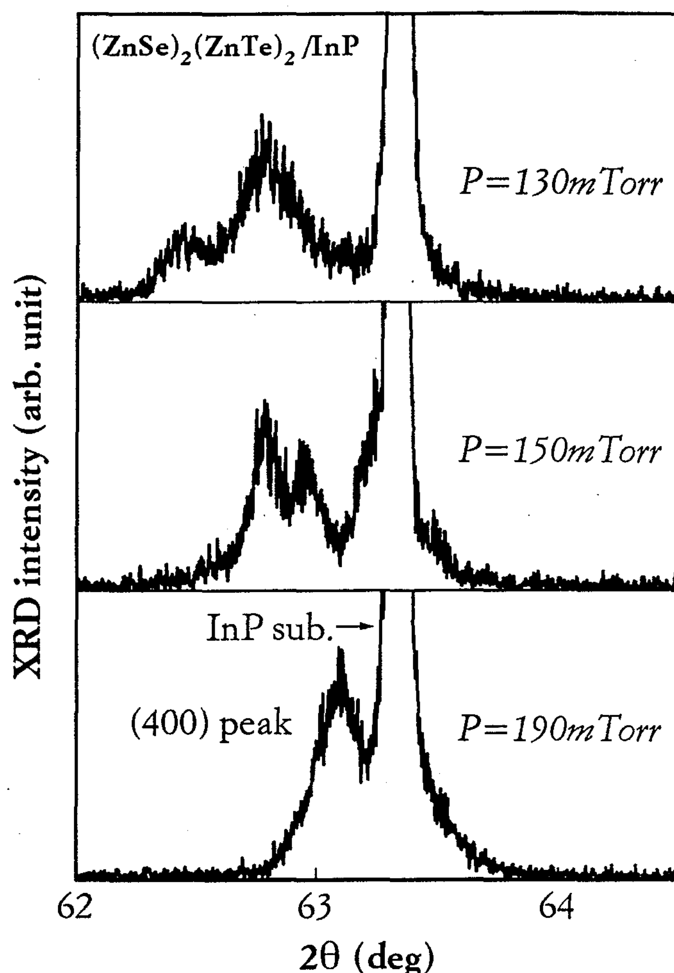

Figure 6-17 The XRD spectra of $(ZnSe)_2(ZnTe)_2$ ordered alloys grown by the different reactor pressures (*P*=130~190 mTorr).

strain energy on the crystal growing surface.

In order to suppress this large compositional fluctuation, the reactor pressure was raised by varying the frequency of a mechanical booster pump since the surface migration of the precursors can be suppressed at the higher reactor pressure. As shown in Fig. 6-17, the single diffraction peak can be seen at the reactor pressure of 190 mTorr, indicating the successful preparation of the crystal by the layer-by-layer growth.

Figure 6-18 (a) shows the XRD spectra of $(ZnSe)_2(ZnTe)_2$ ordered alloys around (200) diffraction. The XRD spectrum of (a) corresponds to the sample grown at *P*=190 mTorr in Fig. 6-17. The inset also shows the XRD

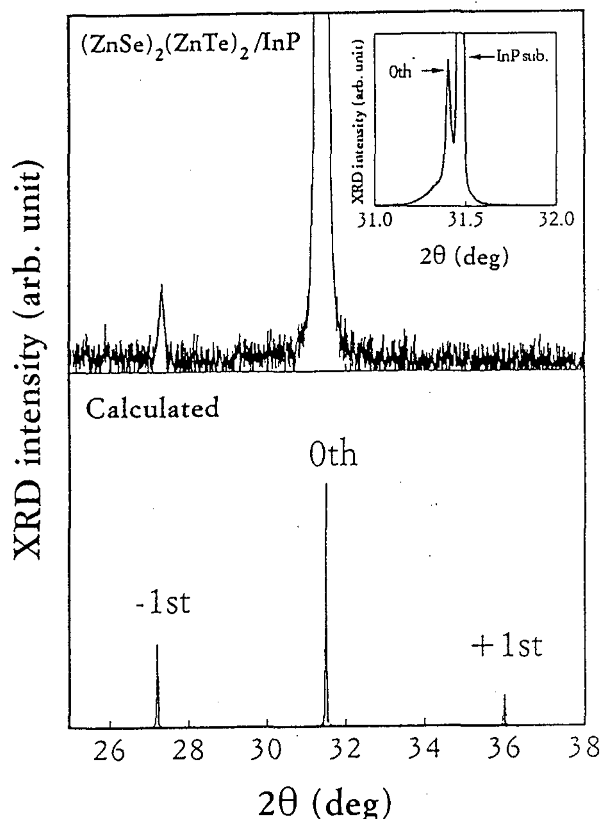

Figure 6-18 The XRD spectra of $(ZnSe)_2(ZnTe)_2$ ordered alloys around (200) diffraction (a) which corresponds to the sample grown at P=190 mTorr in Fig. 6-17. The calculated XRD spectra assuming the coherent growth is also indicated in (b).

spectra at the 0-order diffraction region. The calculated XRD spectra assuming the coherent growth is shown in (b). As shown in Fig. 6-18 (a), -1st-order satellite peak can be seen due to the layer-by-layer structure of the ordered alloy even though each layered structure consists of only two monolayers. In addition, this satellite peak position agrees well with the calculated spectrum. Nevertheless, +1st order satellite peak was not observed due to the weak periodic structure or diffraction intensity as shown in Fig. 6-18 (b). In this observed XRD spectrum, the 0-order diffraction peak also shows a diffraction position which agrees well with the calculated diffraction position by Vegard's law with the coherent structure. Above results indicate that the coherent growth of $(ZnSe)_n(ZnTe)_n$ ordered alloys can be made on InP substrate by HRCVD with the designed number of layers even at the selenium composition of 50 at%.

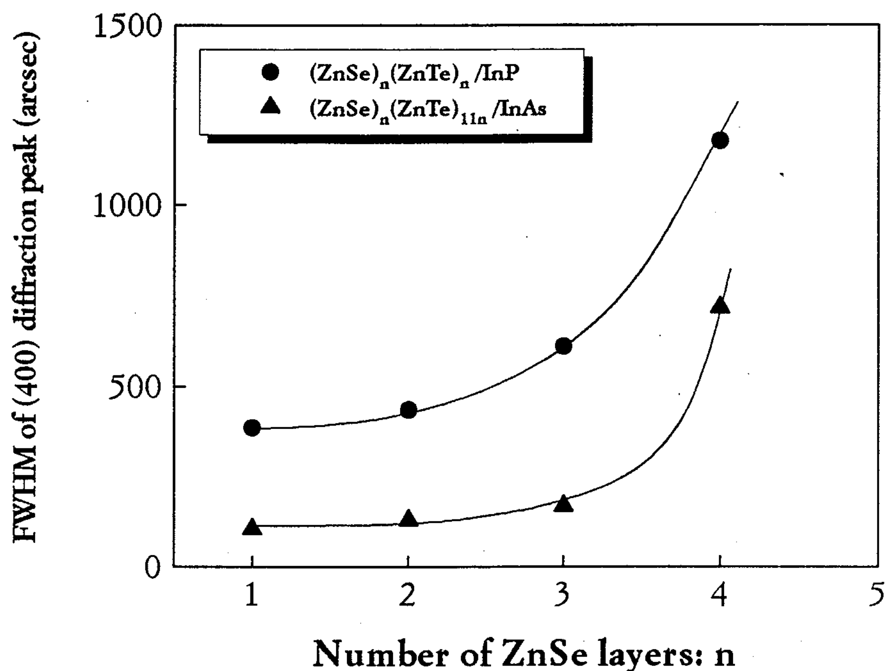

Figure 6-19 The FWHM of the (400) diffraction peaks for $(ZnSe)_n(ZnTe)_n$/InP and $(ZnSe)_n(ZnTe)_{11n}$/InAs plotted as a function of the number of ZnSe layers. The plots of $(ZnSe)_n(ZnTe)_{11n}$/InAs correspond to the data shown in Fig. 6-8.

Figure 6-19 shows the FWHM of the (400) diffraction peaks for $(ZnSe)_n(ZnTe)_n$/InP and $(ZnSe)_n(ZnTe)_{11n}$/InAs plotted as a function of the number of ZnSe layers. In contrast to $(ZnSe)_n(ZnTe)_{11n}$ ordered alloys on InAs substrate, broad diffraction peaks of the order of 500 arcsec are observed in $(ZnSe)_n(ZnTe)_n$ ordered alloys grown on InP substrate. The XRD peak of $(ZnSe)_n(ZnTe)_n$ gradually increases with the number of ZnSe layers (n=1~3), and the rapid broadening of the XRD peak can be seen in the n=4 case probably due to the lattice relaxation effect. From this significant broadening effect in $(ZnSe)_n(ZnTe)_n$, it can be understand that the large compositional modulation enhances the lattice distortion in the grown layers due to the alternating strain layers. In fact, the large lattice distortion in $(ZnSe)_n(ZnTe)_n$ crystals grown by MBE was reported from the TEM.[32)] In order to reduce this effect, the precise ALE growth of these layers should be established.

6.4.2 Optical properties of $(ZnSe)_n(ZnTe)_n$

Figure 6-20 shows the band-edge PL spectra of (ZnSe)n(ZnTe)n ordered alloys (n=1~4) measured at 25 K. No remarkable deep level emissions was observed in these ordered alloys. Nevertheless, the PL emission intensity gradually decreases with increasing number of ZnSe layers n due to the strain effect. Significant broadening of the PL peaks was found in these PL spectra; the FWHMs of the PL peaks are in a range of 50~90 meV and independent of the layered structures. As discussed in the previous section, the type II band-structure at ZnSe-ZnTe heterointerfaces might cause the broadening of the PL peaks. In addition, the large distortion of the ordered alloy confirmed from the XRD spectra could be another reason for this effect.

As shown in Fig. 6-20, the PL peaks of the ordered alloys shift to the lower energy side as the thickness of 1 period increases. The peak energy of the PL peaks is plotted as a function of the number of ZnSe layers in Fig. 6-21. The PL peaks energy of $(ZnSe)_n(ZnTe)_{11n}$ are also shown in this figure. In $(ZnSe)_n(ZnTe)_n$ ordered alloys, similar behavior of the PL peak shift with that of $(ZnSe)_n(ZnTe)_{11n}$ was indicated; the PL peaks shifts largely to the lower energy side with increasing number of ZnSe layers. As discussed in the previous section, this shift can be also explained by the quantum size effect induced by the type II band structure between ZnSe and ZnTe layers. All the PL peaks of $(ZnSe)_n(ZnTe)_n$, however, shows the higher energy than that of $(ZnSe)_n(ZnTe)_{11n}$, as shown in Fig. 6-21. Similar results were also reported in Zn(Se,Te) short-period surperlattices.[33,34] In order to specify this discrepancy, we calculated the band lineup at the heterointerface by taking the strain effect into the account using "Model Solid Theory" developed by Van de Walle.[25] In this model, the position of the conduction and valence band under the coherent growth condition are given by

$$E_c = E_{c,av} + a_c \frac{\Delta\Omega}{\Omega}, \tag{6-1}$$

$$E_v = E_{v,av} + a_v \frac{\Delta\Omega}{\Omega}, \tag{6-2}$$

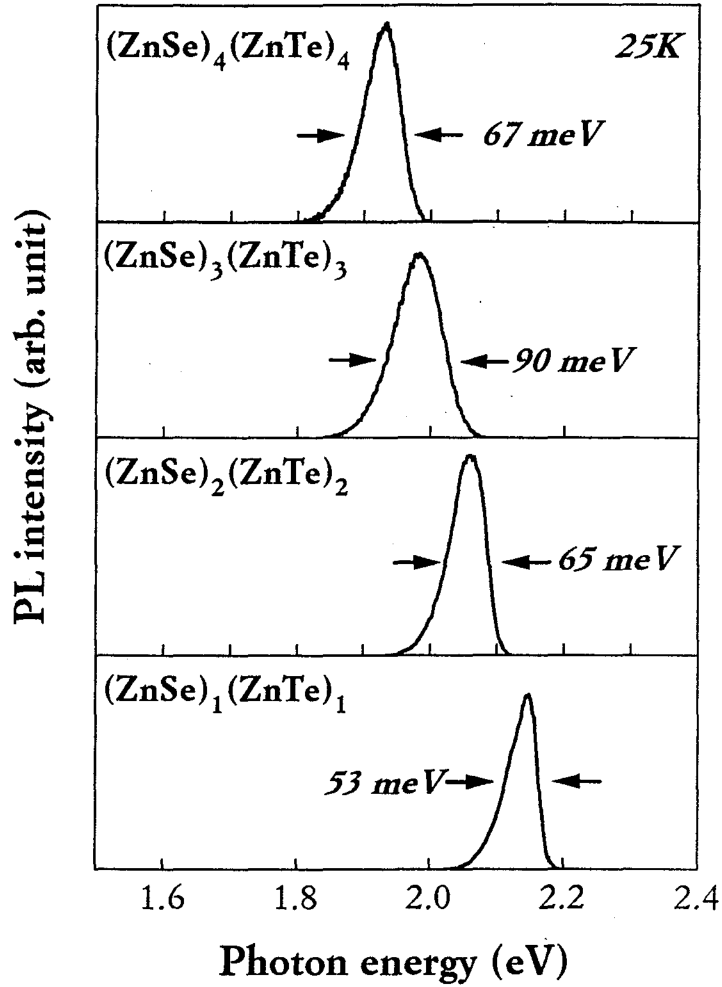

Figure 6-20 The band-edge PL spectra of (ZnSe)n(ZnTe)n ordered alloys (n=1~4) measured at 25 K.

where $E_{c,av}$ ($E_{v,av}$) indicate the average positions of the conduction (valence band) position, and a_c (a_v) are the hydrostatic deformation potentials for the conduction (valence bands). In Eqs. (6-1) and (6-2), $\Delta\Omega/\Omega=(\varepsilon_{xx}+\varepsilon_{yy}+\varepsilon_{zz})$ is the fractional volume change. The conduction band offset can be simply obtained by subtracting the conduction band position between ZnSe and ZnTe. At the valence band, the strain effect further induces the position shift due to the splitting of the degenerate valence band. The position changes of light (E_{v1}) and heavy hole (E_{v2}) bands from $E_{v,av}$ are calculated by

$$\Delta E_{v2} = \frac{1}{3}\Delta - \frac{1}{2}\delta E_{001}, \qquad (6\text{-}3)$$

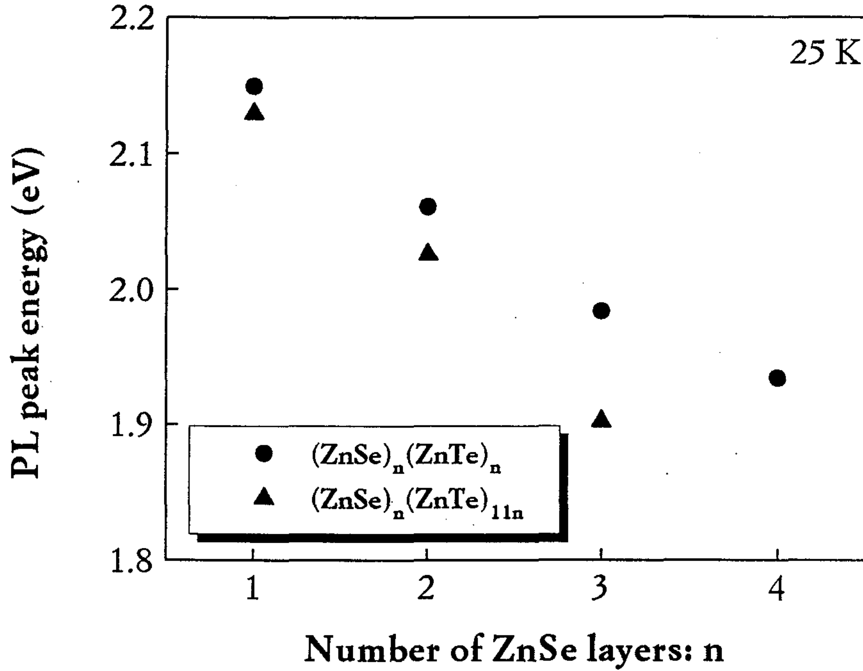

Figure 6-21 The PL peak energy of $(ZnSe)_n(ZnTe)_n$ on InP and $(ZnSe)_n(ZnTe)_{11n}$ on InAs plotted as a function of the number of ZnSe layers.

$$\Delta E_{v1} = -\frac{1}{6}\Delta + \frac{1}{4}\delta E_{001} + \frac{1}{2}\left(\Delta^2 + \Delta\delta E_{001} + \frac{9}{4}\delta E_{001}{}^2\right)^{1/2}, \tag{6-4}$$

where Δ indicates the spin-orbit splitting energy. In these equations δE_{001} is given by

$$\delta E_{100} = 2b(\varepsilon_{zz} - \varepsilon_{xx}), \tag{6-5}$$

where b is the shear deformation potential for a strain. The calculated band offsets for ZnSe-ZnTe grown on InAs as well as InP are shown in Fig. 6-22. From these calculations, it is shown that the interband transition energy of ZnSe-ZnTe on InP (1.27 eV) is larger than that on InAs (1.22 eV). Moreover, the conduction and valence band offset of ZnSe-ZnTe on InP substrate show the higher values compared with that on InAs. As a result, the higher PL peak energy in $(ZnSe)_n(ZnTe)_n$ is considered to originate from the higher interband transition energy as well as conduction and valence band offsets. In fact, similar results were reported from the tight-binding calculations.[24,35]

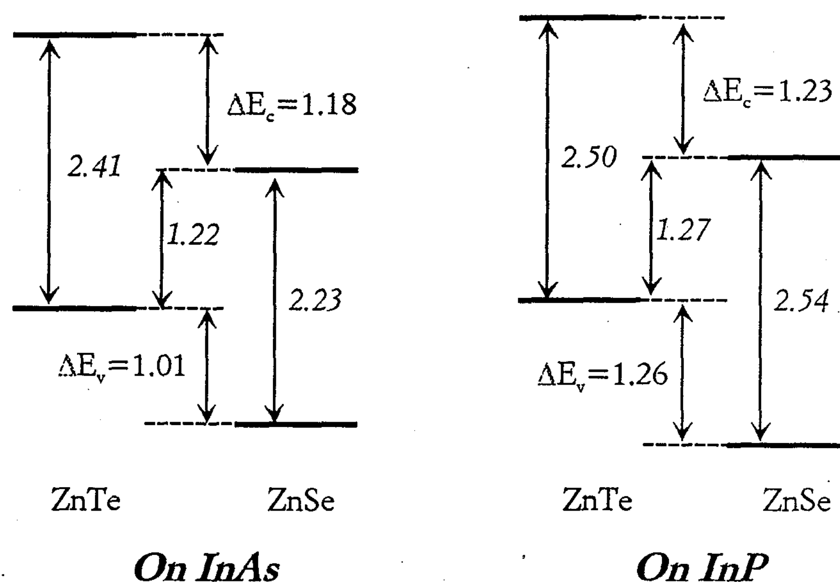

Figure 6-22 The calculated band offsets for ZnSe-ZnTe grown on InAs and InP from model solid theory.

The absorption process in $(ZnSe)_n(ZnTe)_n$ grown on InP substrate was also determined from the PC spectra. Figure 6-23 shows the PC spectra of $(ZnSe)_1(ZnTe)_1$ and $(ZnSe)_3(ZnTe)_3$ ordered alloys. The corresponding PL peaks are also shown in this figure. As a ohmic contact, Au electrodes were used for the PC measurements. As shown in Fig. 6-23, a distinctive difference can be seen in their PL spectra. It was found that the absorption edge shifts to the lower energy side together with the PL peaks as the number of ZnSe increases. In $(ZnSe)_3(ZnTe)_3$, however, the PC spectra shows the broad absorption edge, indicating the tail states induced by the potential fluctuations. On the other hands, these PC spectra shows the same absorption peaks at around 500 nm. At present, the origin of these peaks was not understand well. One possibility is the surface recombination of the photo-generated carriers since this effect significantly reduces the PC signal intensity at the short-wavelength region where the penetration depth is small.

Above results indicate that the $(ZnSe)_n(ZnTe)_n$ ordered alloys grown on InP substrate also shows the quantum size effect on the absorption process in spite of the extremely short periods of the layer-by-layer structures. Accordingly, the large band-profiling can be made using 2-dimensional structure of $(ZnSe)_n(ZnTe)_n$. At the same time, the precise control of the

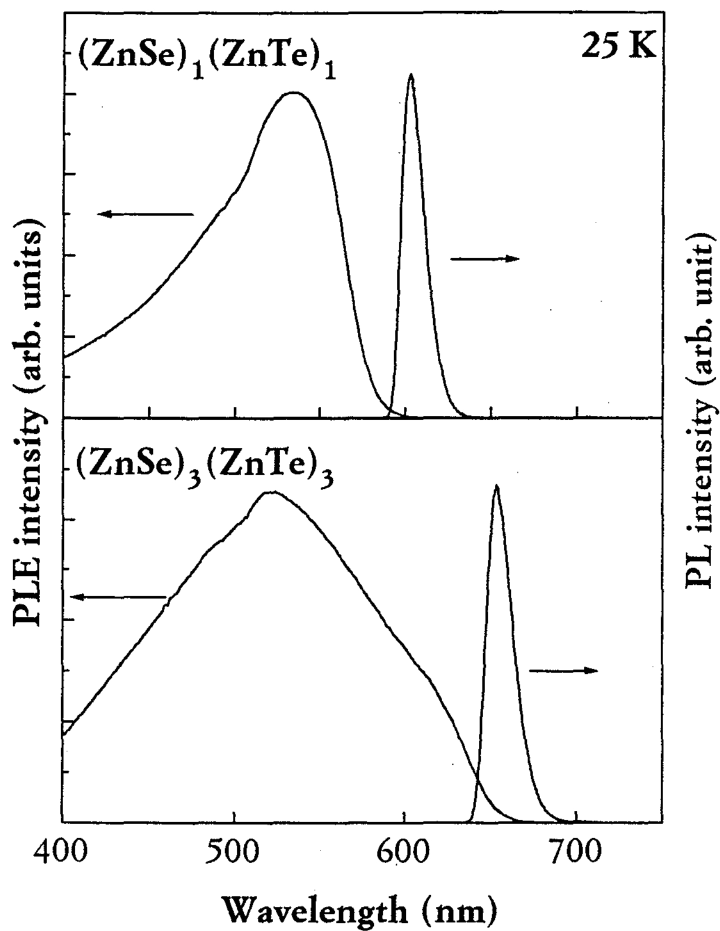

Figure 6-23 The PC spectra of $(ZnSe)_1(ZnTe)_1$ and $(ZnSe)_3(ZnTe)_3$ ordered alloys.

layered structures is required in order to reduce the lattice mismatch strain effect and the formation of tail states.

6.5 Conductivity control of ZnTe crystal

In the previous section, the fundamental characteristics of $(ZnSe)_n(ZnTe)_m$ ordered alloys (n=1~4) were determined, and the possibility of the large band-profiling was suggested from the 2-dimensional ordered structures by taking advantage of the quantum-size effects. In order to create a new optical devices, we tried to obtain the p-type conductivity of crystals. In this section, the p-type doping of ZnTe crystals were made by HRCVD using triisopropyl-antimony (TiPSb) as a dopant molecule, and the result of p-type doping are discussed from the PL measurement.

Before attempting the p-type doping of $(ZnSe)_n(ZnTe)_m$ ordered alloys, we first made the p-type doping to ZnTe single epitaxial layer in order to determine the doping conditions in HRCVD. In this study, Sb was chosen for a p-type dopant atom for ZnTe crystals. So far, the successful p-type doping was reported by MOVPE using tertiary-butylphosphine (TBP) as well as tertiary-butylarsine (TBAs).[6,36] Nevertheless, these dopants are not appropriate in HRCVD since P and As atoms having higher electron negativity are expected to induce the large passivation effect by atomic hydrogen generated by HRCVD. By considering the vapor pressure of the source molecules, TiPSb was finally decided to be the dopant source in this study, and its vapor pressure is 0.1 mmHg at room temperature.

In this section, GaSb substrate was used for the growth of ZnTe crystals because of the small lattice mismatch of 0.1% between ZnTe and GaSb substrates. Accordingly, the lattice relaxation effect of ZnTe layer can be avoided.[2,5,9] The Sb doping was carried out by introducing TiPSb molecules for 0.5 sec between the Zn and Te source gas supply. The growth conditions for p-type doping to ZnTe are summarized in Table 6-4.

Table 6-4 Growth conditions for Sb doping to ZnTe

Flow rate	
DEZn	3.9 μmol/min
DEDTe	4.1 μmol/min
TiPSb	53 nmol/min
PD	0.5 (Sb)-4-0-4-3
Growth temp.	200 °C

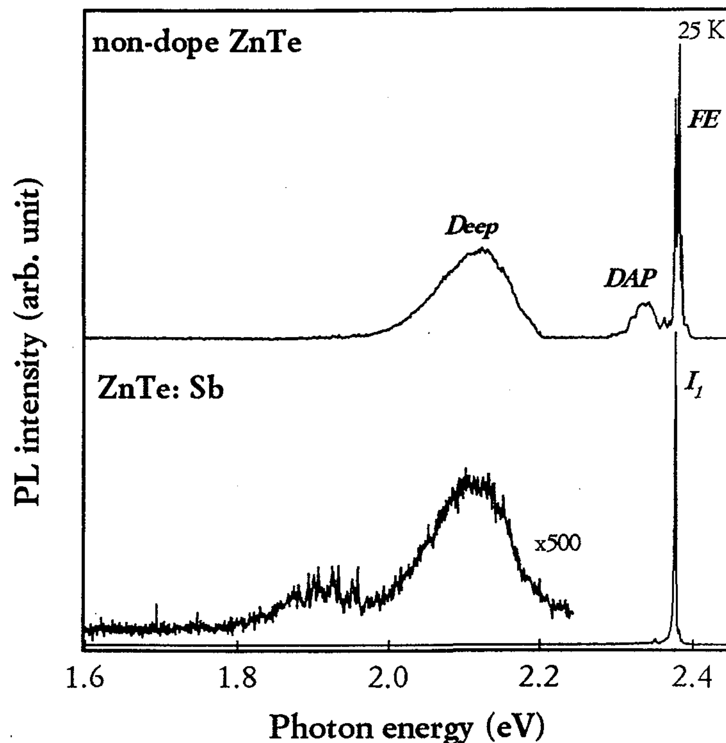

Figure 6-24 The PL spectra of non-dope and Sb-doped ZnTe crystals measured at 25 K.

Figure 6-24 shows the PL spectra of non-dope and Sb-doped ZnTe crystals measured 25 K. A large difference can be seen in these spectra; deep level emission intensity significantly suppressed in Sb-doped ZnTe crystals. In the non-doped sample, the relatively large deep level emission was observed together with the PL peak assigned to donor-to-acceptor pair (DAP) emission at 2.33 eV.[4,6,20] On the contrary, the Sb-doping to ZnTe layer provides the remarkable improvement in the PL properties. Only the weak luminescence of deep level was found in the Sb-doped film. Moreover, the emission intensity of ZnTe:Sb is one order of magnitude larger than that of non-doped ZnTe crystal, indicating the suppressed non-radiative recombination in ZnTe:Sb.

Figure 6-25 shows the PL spectra near the band-edge region which corresponds to the PL spectra in Fig. 6-24. The pair of PL emission peaks at the higher energy side in the non-doped ZnTe crystal are attributed to the free excitonic emissions. This assignment was confirmed from the temperature dependence of the PL measurement, where the emission intensity gradually increase with temperature. Because of the existing small

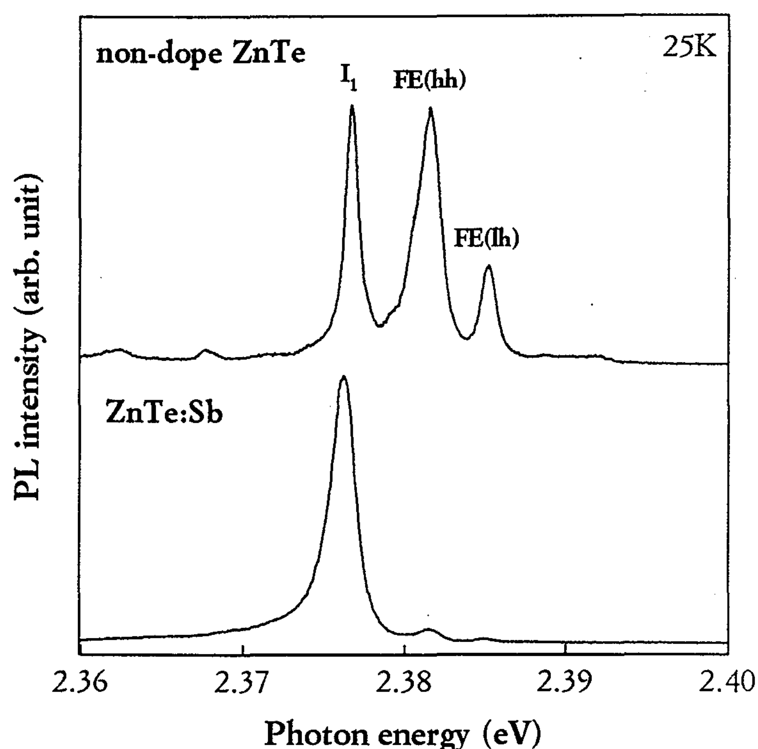

Figure 6-25 The PL spectra of non-dope and Sb-doped ZnTe crystals near the band-edge region which corresponds to the PL spectra in Fig. 6-24.

strain between ZnTe and GaSb substrate, the peak splitting of FE(lh) and FE(hh) was observed. The peak labeled I_1 was assigned to the emission from the acceptor-bound exciton since this peak has the reported localization energy of ~5 meV.[9)] As shown in Fig. 6-25, I_1 emission peak becomes the dominant emission in the Sb-doped ZnTe crystals.

From above these results, it was confirmed that the p-type doping of ZnTe crystals is possible using TiPSb by HRCVD. In the Sb-doped sample, no defect formation was observed by the Sb-doping, as shown in Fig. 6-24. In addition, the XRD diffraction peak of doped sample shows the almost same peak width with the non-doped sample. Consequently, TiPSb is proved to be the appropriate p-type dopant source for ZnTe crystal. It is important to note that the hydrogen passivation effect is negligible in this case, although atomic hydrogen was supplied continuously to the crystal surface. As a result, the realization of the p-type conductivity is expected in Zn(Se,Te) ordered alloys using TiPSb.

Chapter 7

Summary

The results of the compositional modulation of Zn(S,Se,Te) crystals with their optoelectric properties are summarized in this chapter. As described in the previous chapters, we successfully controlled the atomic layer structure of Zn(S,Se,Te) ordered alloys by HRCVD using alternate supply of metalorganic source molecules. As a result, it is proved that the two-dimensional ordered structures of Zn(S,Se,Te) crystals enable a large "band-gap engineering" while suppressing defect formations caused by the large lattice mismatch with substrates or each strain layers. In addition, the conductivity controls for both n- and p-type crystals were also established using HRCVD. These results lead to a conclusion that Zn(S,Se,Te) ordered alloys are the most promising structure for realizing short-wavelength optical devices. The growth of Zn(S,Se,Te) ordered alloys and their specific features are summarized as follows:

Chapter 3 : ALE Growth of ZnSe by HRCVD

The decomposition process of DEZn and DEDSe in HRCVD was investigated from the QMS spectroscopy, and the precursors for the ZnSe growth were determined to be H_5C_2-Zn and H_5C_2-Se radicals, respectively. From the in-situ monitoring of the crystal growth using SPA, the self-limiting growth on the Se-covered surface was confirmed while Zn-covered surface shows the excess adsorption of Zn atoms. The hydrogen passivation on the Se-covered surface was suggested to explain this discrepancy.

Chapter 4 : Structure and Properties of Zn(S,Se) ordered alloys

$(ZnS)_n(ZnSe)_m$ ordered alloys (n=1~4, m=12~72) were grown on GaAs substrate by ALE using HRCVD at the low temperature of 200°C. The layered structure of the ordered alloys were confirmed from the satellite peaks in the XRD spectra. Strong blue PL emissions of the ordered alloys in a wide compositional range (sulfur=4~20 at%) proved the suppression of the defect formation by the layer-by-layer structure. In addition, these ordered alloys showed the higher structure stability over photo- and thermal-degradation effects compared with the lattice relaxed ZnSe crystals. The larger compositional modulations were further made by the graded potential formation in the sawtooth superlattice (STS), in which the higher recombination probability as well as absorption coefficient were confirmed.

Chapter 5 : Carrier Transport Properties of Zn(S,Se)

Carrier transport properties of $(ZnS)_n(ZnSe)_{14n}$ ordered alloys (n=1~4) were investigated using triethylgallium (TEGa) and iso-butyliodide (i-BuI) as dopants. The n-type doping of the ordered alloys using TEGa led to the interface mixing at the ZnS-ZnSe heterostructure. The excellent optical and electrical properties were found in the iodine-doped ordered alloys. As compared with ZnS_xSe_{1-x} disordered alloys having same composition, $(ZnS)_n(ZnSe)_{14n}$ (n=1~3) ordered alloys showed higher electron mobilities more than 100 cm^2/Vs at the low carrier concentration region. This effect was explained in terms of the reduction in the "disorder scattering" in the disordered alloys from the temperature dependence of the Hall measurement.

Chapter 6 : Structure and Properties of Zn(Se,Te) ordered alloys

High-quality $(ZnSe)_n(ZnTe)_m$ ordered alloys (n=1~4, m=1~44) were grown on InAs (100) and InP (100) substrate by HRCVD using DEDTe as a source molecule. In $(ZnSe)_n(ZnTe)_{11n}$, distinctive differences with $(ZnS)_n(ZnSe)_{12n}$ were found in the PL properties; the large peak shift and broadening effect with increasing ZnSe layers. These differences were determined to originate from the type II band structure at ZnSe-ZnTe heterointerface in $(ZnSe)_n(ZnTe)_{11n}$. Larger compositional modulation

effects were further investigated by $(ZnSe)_n(ZnTe)_n$ ordered alloys, and the PL peak broadening and the tail state formation were indicated. In addition, p-type ZnTe crystals were successfully prepared using triisopropyl-antimony as a dopant source.

From above results, it was confirmed that the structures of Zn(S,Se,Te) ordered alloys provides several advantages in the following way:

1) suppression of defects formation caused by the large lattice mismatch with the substrates.
2) electron mobility enhancement and narrower PL peaks by reducing the local compositional fluctuation effect
3) conductivity control for n- and p-type crystals

It should be emphasized that these advantages largely owe to the low temperature growth provided by HRCVD since defect formation easily occurs at the high temperature growth even in the ordered alloys. As a result, it can be concluded that HRCVD is a powerful technique for the growth of various II-VI group crystals.

Acknowlegement

５年間にわたる本研究の遂行に当たり、終始暖かく見守り、さらに部分的な研究だけでなく様々な研究経験をさせていただきました清水勇教授に深く心から感謝いたします。

また御指導、御助言を頂きました半那純一教授、および本研究を進める上で親身に相談してくださった柊元宏教授に感謝いたします。さらに、いろいろな御指導を賜りました山崎陽太郎助教授、小田原修助教授に感謝いたします。

研究をまとめるに当たり、研究及び研究生活全般に渡りめんどうを見ていただきました、安田隆氏（RIKEN フロンティア）、原和彦助手（柊元研）、本田徹助手（伊賀研）、梁嶋克彦氏（ソニー）をはじめとするみなさまに心から感謝いたします。ＰＬ等の光学測定を使用させていただきました柊元、吉野研究室のみなさまに感謝します。また、Ｘ線回折装置を頻繁に使用させていただきました伊賀、小山研究室のみなさまに感謝いたします。

本研究を行うに当たり、在学中は終始厳しく、また卒業後は暖かくいろいろな相談に乗ってくれ、私を育てていただいた後藤順氏（日立製作所）に感謝いたします。 本研究の基礎となった実験を行い、私と激しい議論を交わした鍋田敏之氏（富士フィルム）、朝４時から実験に来てくれた桐生英明氏（松下電器）、体を壊しながらも来てくれた伊井稔博氏（Ｍ２）、研究を手伝ってくれた内田達朗氏（Ｂ４）の４人の私の共同研究者に心から感謝いたします。

I would like to express appreciation to Professor C.M. Fortmann of State University of New York at Stony Brook for helpful discussion as well as English writing. Also, I would like to thank Professor R. W. Collins and Professor C. R. Wronski of the Pennsylvania State University for helpful suggestions. Finally, I would like to appreciate Dr. J. Kocka of Czech Academy of Sciences for the discussion concering photocurrent spectra.

最後に研究生活をより充実なものにしてくれた、清水、半那、柊元研のみなさまに深く感謝いたします。

１９９５年１２月

藤原裕之

Research Report

Publication List I.
(Scientific Journal)

[1] Hiroyuki Fujiwara, Jun Gotoh, Hajime Shirai and Isamu Shimizu, "Low temperature growth of ZnS_xSe_{1-x} alloys fabricated by hydrogen radical enhanced chemical vapor deposition in an atomic layer epitaxy mode", *Journal of Applied Physics*,**74** (1993) 5510~5515.

[2] Hiroyuki Fujiwara, Jun Gotoh and Isamu Shimizu, "Hydrogen Radical enhanced Chemical Vapor Deposition (HRCVD) As a Nobel Technique for the Growth of ZnSe and Related Alloy at Low Temperature Growth Technique", *New Functionally Materials, Volume A*, Optical and Quantum-Structural Properties of Semiconductors, Elsevier Science Publishers B. V. (1993) 163~168.

[3] Hiroyuki Fujiwara, Toshiyuki Nabeta and Isamu Shimizu, "Structure and properties of $(ZnS)_n(ZnSe)_m$ (n=1-4) Ordered Alloys Grown by Atomic Layer Epitaxy", *Japanese Journal of Applied Physics*, **33** (1994) 2474~2478.

[4] Hiroyuki Fujiwara, Toshiyuki Nabeta, Hideaki Kiryu and Isamu Shimizu, "Preparation and Properties of $(ZnS)_3(ZnSe)_{42}$ Ordered Alloys Fabricated by Plasma-enhanced Low-temperature Growth Technique", *Japanese Journal of Applied Physics*, **33** (1994) 4381~4384.

[5] Hiroyuki Fujiwara, Hideaki Kiryu and Isamu Shimizu, "Carrier transport properties of iodine-doped $(ZnS)_3(ZnSe)_{42}$ Ordered Alloys Grown by Atomic Layer Epitaxy", *Journal of Applied Physics*, **77** (1995) 3927~3933.

[6] Hiroyuki Fujiwara, Toshiyuki Nabeta and Isamu Shimizu, "Optical Properties of Zn(S,Se) Sawtooth Superlattices Grown by Atomic Layer Epitaxy", *Applied Physics Letters*: to be published in 1996.

[7] Hiroyuki Fujiwara, Hideaki Kiryu, Toshihiro Ii and Isamu Shimizu, "Growth of iodine-doped $ZnS_{0.07}Se_{0.93}$ Disordered Alloys and Electron Mobility Enhancement by Ordered Structures in $(ZnS)_3(ZnSe)_{42}$", *Journal of Applied Physics*: to be published in early 1996.

[8] Toshihiro Ii, Hiroyuki Fujiwara and Isamu Shimizu, "Optical Properties of $(ZnSe)_n(ZnTe)_{11n}$ Ordered Alloys (n=1~4) and Effects of Ordering", *Journal of Applied Physics*: to be submitted in early 1996.

[9] Jun Gotoh, Hiroyuki Fujiwara and Isamu Shimizu, "Low-temperature Growth of ZnSe-based Pseudomorphic Structures by Hydrogen-radical-enhanced Chemical Vapor Deposition", Journal of Crystal Growth **117** (1992) 85-90.

Publication List II.
(Proceeding of Conference)

[1] Hiroyuki Fujiwara, Toshiyuki Nabeta, Takashi Yasuda and Isamu Shimizu, "Exciton Properties of Zn(S, Se) Ordered Alloys Fabricated by Hydrogen Radical Enhanced Chemical Vapor Deposition", Second International Symposium on Electrochemical Processing of Tailored Materials (1993) 55~70.

[2] Hiroyuki Fujiwara, Toshiyuki Nabeta, Hideaki Kiryu and Isamu Shimizu, "Preparation and Properties of $(ZnS)_n(ZnSe)_m$ (n=1~4) Ordered Alloys Fabricated by Plasma Enhanced Low Temperature Growth Technique", 2nd International Conference on Reactive Plasmas and 11th Symposium

on Plasma Processing (1994) 653~656.

[3] Hiroyuki Fujiwara, Toshihiro Ii and Isamu Shimizu, "Photoluminescence Properties of $(ZnSe)_n(ZnTe)_{11n}$ (n=1~4) Grown by Hydrogen Radical-enhance Chemical Vapor Deposition", 14th Electronic Materials Symposium (1995) 27~28.

[4] Hiroyuki Fujiwara, Toshihiro Ii and Isamu Shimizu, "Compositional Modulation and Its Optoelectric Properties of Zn(S,Se,Te) Crystals Grown by Hydrogen Radical-enhanced CVD", Material Research Society Symposium Proceedings, 417 (1995) in Press.

[5] Jun Gotoh, Hiroyuki Fujiwara and Isamu Shimizu, "ZnS-ZnSe Ordered Alloys on GaAs (100) Fabricated by Hydrogen Radical Enhanced Chemical Vapor Deposition (HR-CVD)", Technical Digest International Workshop on Science and Technology for Surface Reaction Process (1992) 127~128.

Conference

1991

[1] Jun Gotoh, Hiroyuki Fujiwara, Hajime Shirai, Junichi Hanna and Isamu Shimizu, "Low Temperature Growth of ZnS-ZnSe Pseudomorphic Structure by HRCVD", The 52nd Autumn Meeting, *The Japan Society of Applied Physics*, p282 (10p-ZD-7), October. 10, 1991.

1992

[2] Hiroyuki Fujiwara, Jun Gotoh, Hajime Shirai, Junichi Hanna and Isamu Shimizu, "Growth and Properties of ZnS-ZnSe Ordered Alloys by HRCVD", The 39th Spring Meeting, *The Japan Society of Applied Physics*, p234 (29a-Z-10), Nihon University, March 29.

[3] Hiroyuki Fujiwara, Jun Gotoh, Hajime Shirai, Junichi Hanna and Isamu Shimizu, "Growth and Properties of ZnS-ZnSe Ordered Alloys by HRCVD", The 88th Spring Conference, *Japan Society of Printing Science and Technology*, p69-72,Tokyo Institute of Technology,June 18.

[4] Hiroyuki Fujiwara, Toshiyuki Nabeta, Takashi Yasuda, Hajime Shirai and Isamu Shimizu, "Growth and Properties of ZnS-ZnSe Ordered Alloys by HRCVD (2)", The 53rd Autumn Meeting, *The Japan Society of Applied Physics*, p279 (18a-SL-21), Kansai University,Septermper 18.

[5] Jun Gotoh, Hiroyuki Fujiwara and Isamu Shimizu, "ZnS-ZnSe Ordered Alloy on GaAs (100) Fabricated by Hydrogen Radical enhanced Chemical Vapor Deposition", *International Workshop on Science and Technology For Surface Reaction Process*, p127~128, January 28.

1993

[6] Hiroyuki Fujiwara, Toshiyuki Nabeta, Takashi Yasuda and Isamu Shimizu, "Structures and Properties of ZnS-ZnSe Ordered Alloys by HRCVD (3)", The 40th Spring Meeting, *The Japan Society of Applied Physics*, p241 (30a-Zn-3), Aoyama University, March 30.

[7] Hiroyuki Fujiwara, Toshiyuki Nabeta, Takashi Yasuda and Isamu Shimizu, "Exciton Properties of Zn(S,Se) Ordered Alloys Fabricated by Hydrogen Radical Enhanced Chemical Vapor Deposition", *183rd Meeting of Electrochemical Society*, Hilton Hawaiian Village, May 20.

[8] Hiroyuki Fujiwara, Hideaki Kiryu and Isamu Shimizu, "Structure and Properties of $(ZnS)_n(ZnSe)_m$ (n=1~4) Ordered Alloys by ALE", The 54th Autumn Meeting, *The Japan Society of Applied Physics*, p337 (30a-HB-1, Hokkaido University, September 30.

[9] Toshiyuki Nabeta, Hiroyuki Fujiwara, Takashi Yasuda and Isamu Shimizu, "Exciton Dynamics of [(ZnS)n(ZnSe)12n]m (n=1~4) Ordered Alloy", The 40th Spring Meeting, *The Japan Society of Applied Physics*,

p241 (30a-ZN-4), Aoyama University, March 30.

[10]Toshiyuki Nabeta, Hiroyuki Fujiwara, Takashi Yasuda and Isamu Shimizu, "Making and Properties of ZnS-ZnSe STS (Sawtooth Superlattice)", The 54th Autumn Meeting, *The Japan Society of Applied Physics*, p338 (30a-HB-2), Hokkaido University, September 30.

1994

[11]Hiroyuki Fujiwara, Toshiyuki Nabeta, Hideaki Kiryu and Isamu Shimizu, "Preparation and Properties of $(ZnS)_n(ZnSe)_m$ (n=1~4) Ordered Alloys Fabricated by Plasma Enhanced Low Temperature Growth Technique", *2nd International Conference on Reactive Plasmas and 11th Symposium on Plasma Processing*, Pacifico Yokohama, January 27.

[12]Hiroyuki Fujiwara, Hideaki Kiryu and Isamu Shimizu, "n-type doping of $(ZnS)_n(ZnSe)_m$ (n=1~4) Ordered Alloy Using Iso-buthyliodide", The 41st Spring Meeting, *The Japan Society of Applied Physics*, p222 (29p-W-13), Meiji University, March 29.

[13]Hiroyuki Fujiwara, Hideaki Kiryu, Toshihiro Ii and Isamu Shimizu, "Exciton and Carrier Dynamics of Zn(S,Se) Ordered Alloys Fabricated by Hydrogen Radical-enhanced Chemical Vapor Deposition", The Material Research Society of Japan 1994, A06, Kanagawa Science Park, July 12.

[14]Hiroyuki Fujiwara, Toshihiro Ii and Isamu Shimizu, "Carrier Transport Properties of Iodine-doped $(ZnS)_n(ZnSe)_{14n}$ (n=1~4)", The 55th Autumn Meeting, *The Japan Society of Applied Physics*, p212 (20p-MB-5), Nagoya University, September 20.

[15]Hiroyuki Fujiwara, Hideaki Kiryu and Isamu Shimizu, "Excitonic and Electronic Properties of Strained Zn(S,Se) Crystal Grown by Hydrogen Radical-enhanced Chemical Vapor Deposition", *1994 Materials Research Society Fall Meeting*, p153 (D4.10), Boston Marriot Hotel,

November 29.

[16]Toshiyuki Nabeta, Hiroyuki Fujiwara, Takashi Yasuda and Isamu Shimizu, "Optical Properties of ZnS-ZnSe Pseudomorphic by Photocurrent Measurement",The 41st Spring Meeting, *The Japan Society of Applied Physics*, p222 (29p-W-12), Meiji University, March 29.

[17]Hideaki Kiryu, Hiroyuki Fujiwara and Isamu Shimizu, "Reaction Mechanism Analysis of ZnSe Grown by ALE-HRCVD Using Quadrupole Mass Spectrometer", The 41st Spring Meeting, *The Japan Society of Applied Physics*, p178 (28p-W-5),Meiji University, March 28.

[18]Hideaki Kiryu, Hiroyuki Fujiwara and Isamu Shimizu, "Fabrication of Artificial Structure Crystal, Zn(S,Se) Ordered Alloy", The 92nd Spring Conference, *Japanese Society of Printing Science and Technology*, p160~163 (B-11), Tokyo Institute of Technology, June 27.

[19]Hideaki Kiryu, Hiroyuki Fujiwara and Isamu Shimizu, "Study on Surface Reaction of ZnSe Growth by in-situ Observation with SPA", The 55th Autumn Meeting, *The Japan Society of Applied Physics*, p156 (19a-MB-6), Nagoya University, September 19.

1995

[20]Hiroyuki Fujiwara, Toshihiro Ii and Isamu Shimizu, "Photo-degradation Effect of ZnSe Crystal", The 42nd Spring Meeting, *The Japan Society of Applied Physics*, p314 (30p-ZX-12), Toukai university, March 30.

[21]Hiroyuki Fujiwara, Toshihiro Ii and Isamu Shimizu, "Photoluminescence Properties of $(ZnSe)_n(ZnTe)_{11n}$ (n=1~4) Grown by Hydrogen Radical-enhanced Chemical Vapor Deposition, *14th Electronic Materials Symposium*, B7, Hotel Fujimi Haitsu (Izu), July 5.

[22]Hiroyuki Fujiwara, Toshihiro Ii, Tatsuro Uchida and Isamu Shimizu, "Fabrication of $(ZnSe)_n(ZnTe)_n$ (n=1~4) Crystals on InP (100) Substrate by HRCVD Method", The 56th Autumn Meeting, *The Japan Society of Applied Physics*, p301 (29a-W-1), Kanazawa University, August 29.

[23]Hiroyuki Fujiwara, Toshihiro Ii and Isamu Shimizu, "Compositional Modulation and Its Optoelectric properties of Zn(S,Se,Te) Crystals Grown by Hydrogen Radical-enhanced CVD", *1995 Material Research Society Fall Meeting*, p713 (EE7.2), Boston Sheraton Hotel, November 30.

[24]Hideaki Kiryu, Hiroyuki Fujiwara and Isamu Shimizu, "Study on Surface Reaction of ZnSe Growth by SPA in-situ Observation (II)", The 42nd Spring Meeting, *The Japan Society of Applied Physics*, p200 (28p-ZX-5), Toukai University, March 28.

[25]Toshihiro Ii, Hiroyuki Fujiwara, Hideaki Kiryu and Isamu Shimizu, "Fabrication of $(ZnSe)_n(ZnTe)_m$ Ordered Alloys on InAs (100) Substrate by HRCVD", The 42nd Spring Meeting, *The Japan Society of Applied Physics*, p202 (28-ZX-10), Toukai University, March 28.

[26]Toshihiro Ii, Hiroyuki Fujiwara, Hideaki Kiryu and Isamu Shimizu, "Growth Technique of High Quality II-VI Compound Semiconductors - Zn(Se,Te) Alloys - ", The 94th Spring Conference, *Japanese Society of Printing Science and Technology*, B-16, Tokyo Institute of Technology, July 9.

[27]Toshihiro Ii, Hiroyuki Fujiwara, Takashi Yasuda and Isamu Shimizu, "Excitonic Emission of $(ZnSe)_n(ZnTe)_{11n}$ (n=1~4) Pseudomorphic Structure Crystals", The 56th Autumn Meeting, *The Japan Society of Applied Physics*, p33 (29a-W-8).

[28]Toshihiro Ii, Hiroyuki Fujiwara, Takashi Yasuda, Taturo Uchida and Isamu Shimizu, "Low Temperature Growth of Zn(Se,Te) Ordered Alloys and Their Exciton Dynamics", *1995 Material Research Society of Japan*, PA-10M, Kanagawa Science Park, December 7.

1996

[29]Hiroyuki Fujiwara, Toshihiro Ii, Takashi Yasuda and Isamu Shimizu, "Compositional Modulation of Zn(S,Se,Te) Crystals and Their Characteristics", The 43rd Spring Meeting, *The Japan Society of Applied Physics*: to be presented (28p-ZD-1), Touyou University, March 28.

[30]Toshihiro Ii, Hiroyuki Fujiwara, Tatsuro Uchida and Isamu Shimizu, "Fabrication of zinc-telluride on GaSb (100) substrate and p-type doping by HRCVD method", The 43rd Spring Meeting, *The Japan Society of Applied Physics*: to be presented (28a-ZD-1), Touyou University, March 28.

Reference

Chapter 1

1) M. Grynberg, Phys. Rev. B, **9** (1974) 517.
2) S. Adachi and T. Taguchi, Phys. Rev. B, **43** (1991) 9569.
3) W. Stutius, Appl. Phys. Lett., **33** (1978) 656.
4) P. J Wright and B. Cockayne, J. Cryst. Growth, **59** (982) 148.
5) W. Stutius, J. Cryst. Growth, **59** (1982) 1.
6) T. Yodo, H. Oka, T. Koyama and K. Yamashita, Jpn. J. Appl. Phys., **36** (1987) L561.
7) H. Mitsuhashi, I. Mitsuishi and H. Kukimoto, J. Cryst. Growth, **77** (1986) 219.
8) K. P. Giapis, K. F. Jensen, J. E.Potts and S. J. Pachuta, Appl. Phys. Lett., **55** (1989) 463.
9) K. P. Giapis and K. F. Jensen, J. Cryst. Growth, **101** (1990) 111.
10) E. D. Bourret, F. Z. Zach, K. M. Yu and J. M. Walker, J. Cryst. Growth, **147** (1995) 47.
11) M. Heuken, J. Cryst. Growth, **146** (1995) 570.
12) M. A. Haase, J. Qiu, J. M. DePuydt and H. Cheng, Appl. Phys. Lett., **59** (1991) 1272.
13) W. Xie, D. C. Grillo, R. L. Gunshor, M. Kobayashi, G. C. Hua, N. Otsuka, H. Jeon, J. Ding and A. V. Nurmikko, Appl. Phys. Lett., **60** (1992) 463.
14) D. B. Eason, Z. Yu, W. C. Hughes, W. H. Roland, C. Boney, J. W. Cook, J. F. Schetzina, G. Cantwell and W. C. Harsch, Appl. Phys. Lett., **66**

(1995) 115.
15) A. Ishibashi, Y. Mori, J. Cryst. Growth, **138** (1994) 677.
16) Y. Sakuma, M. Ozeki, N. Ohtsuka, Y. Matsumiya, H. Shigematsu, O. Ueda, S. Muto, K. Nakajima, N. Yokoyama, Appl. Surf. Sci., **82/83** (1994) 46.
17) S. Yamaga and A. Yoshikawa, J. Cryst. Growth, **117** (1992) 152.
18) T. Yao and T. Takeda, J. Cryst. Growth, **81** (1987) 43
19) N. Shibata and A. Katsui, J. Cryst. Growth, **101** (1990) 91.
20) A. Yoshikawa, T. Okamoto, H. Yasuda, S. Yamaga and H. Kasai, J. Cryst. Growth, **101** (1990) 86.
21) T. Yao and T. Takeda, Appl. Phys. Lett., **48** (1986) 160.
22) Y. Manabe, S. Hayashi, M. Yoshida, I. Tanahashi and T. Mitsuyu, *Extended abstracts of Inter. Symp. on non-linear photonics materials*, (1994) 281.
23) T. Saiki, K. Takeuchi, M. Kuwata, T. Mitsuyu and K. Ohkawa, Appl. Phys. Lett., **60** (1992) 192.
24) Compound semiconductor, **1** (1995) 34.
25) E. Hanamura, *Extended abstracts of Inter. Symp. on non-linear photonics materials*, (1994) 329.
26) E. Hanamura, Phys. Rev. B, **38** (1988) 1228.
27) S. Schmitt-Rink, D. S. Chemla and D. A. B. Miller, Phys. Rev. B, **32** (1985) 6601.
28) H. Mitsuhashi, I. Mitsuishi, M. Mizuta and H. Kukimoto, Jpn. J. Appl. Phys., **24** (1985) L578.
29) K. Ohkawa, T. Mitsuyu and O. Yamazaki, Phys. Rev. B, **38** (1988) 12465.
30) J. Petruzzello, B. L. Greenberg, D. A. Cammack and R. Dalby, J. Appl. Phys., **63** (1988) 2299.
31) S. Guha, H. Munekata, F. K. LeGoues and L. L. Chang, Appl. Phys. Lett., **60** (1992) 3220.
32) S. Guha, H. Munekata and L. L. Chang, J. Appl. Phys., **73** (1993) 2294.
33) S. Guha, J. M. DePuydt, J. Qiu, G. E. Hofler, M. A. Haase, B. J. Wu and H. Cheng, Appl. Phys. Lett., **63** (1993) 3023.
34) G. C. Hua, N. Otsuka, S. M. Clark, D. C. Grillo, Y. Fan, J. Han, L. He, M. D. Ringle, R. L. Gunshor, M. Hovinen and A. V. Nurmikko, Appl. Phys. Lett., **65** (1994) 142.

35) S. Tomiya, E. Morita, M. Ukita, H. Okuyama, S. Itoh, K. Nakano and A. Ishibashi, Appl. Phys. Lett., **66** (1995) 1208.
36) T. Yokogawa, H. Sato and M. Ogura, Appl. Phys. Lett., **52** (1988) 1678.
37) N. Shibata, A. Ohki, S. Zembutsu and A. Katsui, Jpn. J. Appl. Phys., **27** (1988) L487.
38) *Databook for III-V group compound semiconductor crystals*: Society of Japan Electron Industory Association.
39) T. Soma, Solid State Commun., **34** (1980) 927.
40) S. Permogorov and A. Reznitsky, J. Luminescence, **52** (1992) 201.
41) A. Naumov, S. Permogorov, A. Reznitsky, S. Verbin and A. Klochikhin, J. Cryst. Growth, **101** (1990) 713.
42) M. J. S. P. Brasil, R. E. Nahory, F. S. Turco-Sandroff, H. L. Gilchrist and R. J. Martin, Appl. Phys. Lett., **58** (1991) 2509.
43) A. Naumov, H. Stanzi, K. Wolf, S. Lankes and W. Gebhardt, J. Appl. Phys., **74** (1993) 6178.
44) E. Cohen and M. D. Sturge, Phys. Rev. B, **25** (1982) 3828.
45) L. Makowski and M. Glicksman, J. Phys. Chem. Solids, **34** (1973) 487.
46) M. Glicksman, R. E. Enstrom, S. A. Mittleman and J. R. Appert, Phys. Rev. B, **9** (1974) 1621.
47) W. Leigh and B. W. Wessels, Appl. Phys. Lett., 41 (1982) 165.
48) A. Yoshikawa, H. Nomura, S. Yamaga and H. Kasai, J. Appl. Phys., **65** (1989)1223.
49) D. W. Kisker and A. G. Zawadzki, J. Cryst. Growth, **89** (1988) 378.
50) P. A. Fedders and M. W. Muller, J. Phys. Chem. Sol., **45** (1984) 685.
51) T. Yasuda, I. Mitsuishi and H. Kukimoto, Appl. Phys. Lett., **52** (1988) 57.
52) K. Ohkawa, T. Karasawa and T. Mitsuyu, J. Cryst. Growth, **111** (1991) 797.
53) J. Han, T. S. Stavrinides, M. Kobayashi, R. L. Gunshor, M. M. Hagerott and A. V. Nurmikko, Appl. Phys. Lett., **62** (1993) 840.
54) K. Wolf, H. Stanzl, A. Naumov, H. P. Wagner, W. Kuhn, B. Hahn and W. Gebhardt, J. Cryst. Growth, **138** (1994) 412.
55) E. Tokumitsu, Jpn. J. Appl. Phys., **29** (1990) L698.
56) J. Tersoff, Phys. Rev. B, **30** (1984) 4874.
57) H. Hasegawa, H. Ohno and T. Sawada, Jpn. J. Appl. Phys., **25** (1985) ·L265.

58) D. J. Chadi, Appl. Phys. Lett., **59** (1991) 3589.
59) D. J. Chadi, Phys. Rev. Lett., **72** (1994) 534.
60) D. J. Chadi and K. J. Chang, Appl. Phys. Lett., **55** (1989) 575.
61) A. Kamata, Appl. Phys. Lett., **63** (1993) 3953.
62) K. Yanashima, *Doctoral Thesis.*
63) W. Faschinger, S. Ferreira and H. Sitter, Appl. Phys. Lett., **66** (1995) 2516.
64) W. Faschinger, S. Ferreira, H. Sitter, J. Cryst. Growth, **151** (1995) 267.
65) K. Ohkawa, T. Karasawa and T. Mitsuyu, J. Cryst. Growth, **111** (1991) 797.
66) J. Han, Y. Fan, M. D. Ringle, L. He, D. C. Grillo, R. L. Gunshor, G. C. Hua and N. Otsuka, J. Cryst. Growth, **138** (1994) 464

Chapter 2

1) J. Gotoh, T. Koyabashi, H. Shirai, J. Hanna and I. Shimizu, Jpn. J. Appl. Phys., **29** (1990) L1767.
2) J. Gotoh, H. Shirai, J. Hanna and I. Shimizu, Jpn. J. Appl. Phys., **30** (1991) L1241.
3) T. Adachi, J. Appl. Phys., **69** (1991) 7768.
4) I. Tone, M. Yamada, Y. Ide and Y. Katayama, Jpn. J. Appl. Phys., **31** (1992) L721.
5) O. Murawala, O. Tsuji, S. Fujita and S. Fujita, Jpn. J. Appl. Phys., 30 (1991) 3777.
6) C. Tamargo, J. L. de Miguel, D. M. Hwang and H. H. Farrell, J. Vac. Sci. & Technol. **B6** (1989) 784.
7) Y. Wu, Y. Kawakami, S. Fujita and S. Fujita, J. Cryst. Growth, **111** (1991) 757.
8) Y. Wu, T. Toyoda, Y. Kawakami, S. Fujita and S. Fujita, Jpn. J. Appl. Phys., **29** (1990) L144.
9) M. Besser, C. R. Helms, Appl. Phys. Lett., **52** (1988) 1707.
10) J. Fan, H. Oigawa and Y. Nannichi, Jpln. J. Appl. Phys., **27** (1988) L2125.
11) S. Fujita, N. Yoshimura, Y. Wu and S. Fujita, J. Cryst. Growth, **101** (1990) 78.

12) Y. Nannichi, J. Fan, H. Oigawa and A. Koma, Jpn. J. Appl. Phys., **27** (1988) L2367.
13) H. Oigawa, J. Fan, Y. Nannichi, K. Ando, K. Saiki and A. Koma, Jpn. J. Appl. Phys., **27** (1989) L340.
14) H. Oigawa, J. Fan, Y. Nannichi, H. Sugahara and M. Oshima, Jpn. J. Appl. Phys., **30** (1991) L322.
15) E. Tao, A. Yelon, E. Sacher, Z. H. Lu and M. J. Graham, Appl. Phys. Lett., **60** (1992) 2669.
16) M. Kurihara, Y. Miyamoto and K. Furuya, Jpn. J. Appl. Phys., **32** (1993) L444.
17) M. Fukuda, N. Sanada, M. Kuroda and Y. Suzuki, Appl. Phys. Lett., **61** (1992) 955.
18) J. Petruzzello, B. L. Greenberg, D. A. Cammack and R. Dalby, J. Appl. Phys., **63** (1988) 2299.
19) H. Ohkawa, T. Mitsuyu and O. Yamazaki, Phys. Rev., **B38** (1988) 12465.
20) J. I. Davies, M. J. Parrott and J. O. Williams, J. Cryst. Growth, **79** (1986) 363.
21) Y. Kawakami, T. Toyoda, Y. Wu, S. Fujita and S. Fujita, Jpn. J. Appl. Phys., **29** (1990) 2440.
22) M. Sato and M. Weyers, Jpn. J. Appl. Phys., **30** (1991) L1911.
23) S. Salim, J. P. Lu, K. F. Jensen, J. Cryst. Growth, **124** (1992) 16.
24) K. Fujii, I. Suemune and M. Yamanishi, Appl. Phys. Lett., **62** (1993) 1420.
25) T. Kojima, N. J. Kawai, T. Nakagawa, K. Ohta, T. Sakamoto, M. Kawashima, Appl. Phys. Lett., **47** (1985) 286.
26) L. Samuelson, B. Junno, G. Paulsson, J. Cryst. Growth, **124** (1992) 23.
27) T. Murotani, T. Shimanoe and S. Mitsui, J. Cryst. Growth, 45 (1978) 302.
28) M. Nakamura, K. Iizuka and H. Yano, Jpn. J. Appl. Phys., **28** (1989) 2141.
29) D. W. Kisker, P. H. Fuoss, K. L. Tokuda, G. Renaud, S. Brennan and J. L. Kahn, Appl. Phys. Lett., **56** (1990) 2025.
30) F. J. Lamelas, P. H. Fuoss, P. Imperatori, D. W. Kiskerand G. B. Stephenson and S. Brennan, Appl. Phys. Lett., **60** (1992) 2610.
31) D. E. Aspnes, J. P. Haribson, A. A. Stunda and L. T. Florez, Phys, Rev.

Let., **59** (1987) 1687.
32) D. E. Aspnes, E. Colas, A. A. Stunda, R. Bhat, M. A. Koza and V. G. Keramidas, Phys. Rev. Lett., **61** (1988) 2782.
33) N. Kobayashi and Y. Horikoshi, Jpln. J. Appl. Phys., **28** (1989) L1880.
34) Y. Horikoshi, M. kawashima and N. Kobayashi, **111** (1991) 200.
35) N. Kobayashi and Y. Kobayashi, J. Cryst. Growth, **124** (1992) 525.
36) N. Kobayashi, Y. Kobayashi, Y. Yamauchi and Y. Horikoshi, Appl. Surf. Sci., **60** (1992) 544.
37) N. Kobayashi, T. Makimoto, Appl. Surf. Sci., **82** (1994) 284.
38) J. D. e. McIntyre and D. E. Aspnes, Surface Sci., **24** (1971) 417.
39) K. Shahzad, D. J. Olego and C. G. Van de Walle, Physi Rev., B **38** (1988) 1417.
40) D. T. Marple, J. Appl. Phys., **35** (1964) 1879.
41) Y. X. Liu, Y. Rajakarunanayake and T. C. McGill, J. Cryst. Growth, **117** (1992) 742.
42) E. O. Gobel, J. Kuhl and R. Hoger, J. Luminescence, **30** (1985) 541.
43) J. Cui, H. Wang, F. Gan, X. Huang, Z. Cai, Q. Li and Z. Yu, Appl. Phys. Lett., **61** (1992) 1540.
44) A. Shen, H. Wang and Z. Wang, Appl. Phys. Lett., **60** (1992) 2640.
45) Y. Kawakami, T. Taguchi and A. Hiraki, Appl. Sur. Sci., **33/34** (1988) 1059.
46) Y. Kuroda, I. Suemune, M. Fujimoto, Y. Fujii, N. Otsuka and Y. Nakamura, J. Appl. Phys., **72** (1992) 3029.
47) M. Morita, K. Goto and T. Suzuki, Jpn. J. Appl. Phys., **29** (1990) L-1663.
48) Y. Kuroda, I. Suemune, Y. Fujii and M. Fujimoto, Appl. Phys. Lett., **61** (1992) 1182.
49) J. Feldmann, G. Peter, E. O. Gobel, K. Leo, H. Polland, K. Ploog, K. Fujiwara and T. Nakayama, Appl. Phys. Lett., **51** (1987) 226.
50) R. M. Fleming, D. B. McWhan, A. C. Gossard, W. Wiegmann and R. A. Logan, J. Appl. Phys., **51** (1980) 357.
51) H. Terauchi, S. Sekimoto, K. Kamigaki, H. Sakashita, N. Sano, H. Kato and M. Nakayama, J. Phys. Soc. Jpn., **54** (1985) 4576.
52) H. Mitsuhashi, I. Mitsuishi, M. Mizuta and H. Kukimoto, Jpn. J. Appl. Phys., **24** (1985) L578.
53) T. Yodo, T. Koyama and K. Yamashita, J. Cryst. Growth, **86** (1988)

273.
54) E. D. Bourret, F. X. Zach, K. M. Yu, J. M. Walker, J. Cryst. Growth, **147** (1995) 47.

Chapter 3

1) S. Oda, R. Kawase, T. Sato, I. Shimizu and H. Kokado, Appl. Phys. Lett., **48** (1986) 33.
2) B. Cockayne and P. J. Wright, J. Cryst. Growht, **68** (1984) 223.
3) K. P. Giapis and K. F. Jensen, J. Cryst. Growth, **101** (1990) 111.
4) K. Nishimura, Y. Nagao and K. Sakai, Jpn. J. Appl. Phys., **32** (1993) L428.
5) M. Heuken, J. Cryst. Growth, **146** (1995) 570.
6) J. Gotoh, H. Shirai, J. Hanna and I. Shimizu, Proc. Jpn. Symp. Plasma Chem., vol. 1 (1988) 61.
7) J. Gotoh, T. Kobayashi, H. Shirai, J. Hanna and I. Shimizu, Jpn. J. Appl. Phys., **29** (1990) L1767.
8) J. Gotoh, H. Shirai, J. Hanna and I. Shimizu, Jpn. J. Appl. Phys., **30** (1991) L1241.
9) J. Gotoh, H. Fujiwara, H. Shirai, J. Hanna and I. Shimizu, J. Cryst. Growth, **117** (1992) 85.
10) H. Fujiwara, J. Gotoh and I. Shimizu, New Functionality Materials, Volume **A** (1993) 163.
11) J. B. Mullin, S. J. C. Irvine and D. J. Ashen J. Crst. Growth, **55** (1981) 92.
12) J. I. Davis, M. J. Parrott and J. O. Williams, J. Cryst. Growth, **79** (1986) 363.
13) L. Wei, Y. Cho, C. Dosho, S. Tanigawa, T. Yodo and K. Ymashita, Jpn. J. Appl. Phys., **30** (1991) 2442.
14) S. Akram, H. Ehsani and I. B. Bhat, J. Cryst. Growth, **124** (1992) 628.
15) G. B. Stringfellow: *Organometallic vapor-phase epitaxy*, p21 (1989), Academic press.
16) N. Kobayashi and T. Makimoto, Appl. Surf. Sci., **82/83** (1994) 284.
17) M. Sato and M. Weyers, Jpn. J. Appl. Phys., **30** (1991) L1911.
18) S. Salim, J. P. Lu and K. F. Jensen, **124** (1992) 16.
19) K. P. Giapis, K. F. Jensen, J. E. Potts and S. J. Pachuta, Appl. Phys. Lett.,

55 (1989) 463.
20) H. Sugai and H. Toyada, J. Vac. Sci. Technol., A **10** (1992) 1193.
21) J. I. Davies, M. J. Parrott and J. O. Williams, J. Cryst. Growth, **79** (1986) 363.
22) T. Ozeki and Y. Hiraoka, *Extended Abstracts of Japan Society of Applied Physics*: The 55th Autumn Meeting (1994) 21a-MB-8.
23) H. Mitsuhashi, I. Mitsuishi and H. Kukimoto, J. Cryst. Growth, **77** (1986) 219.
24) N. Kobayashi and Y. Horikoshi, Jpln. J. Appl. Phys., **28** (1989) L1880.
25) Y. Horikoshi, M. kawashima and N. Kobayashi, **111** (1991) 200.
26) N. Kobayashi and Y. Kobayashi, J. Cryst. Growth, **124** (1992) 525.
27) N. Kobayashi, Y. Kobayashi, Y. Yamauchi and Y. Horikoshi, Appl. Surf. Sci., **60** (1992) 544.
28) N. Kobayashi, T. Makimoto, Appl. Surf. Sci., **82** (1994) 284.
29) A. Yoshikawa, M. Kobayashi and S. Tokita, Appl. Surf. Sci., 79/80 (1994) 416.
30) S. Tokita, M. Kobayashi and A. Yoshikawa, J. Cryst. Growth, 136 (1994) 376.
31) T. Fukada, N. Matsumura, Y. Fukushima and J. Saraie, Jpn. J. Appl. Phys., **29** (1990) L1585.
32) N. Matsumura, M. Tsubokura, K. Miyagawa, N. Nakamura, Y. Miyanagi, T. Fukuda and J. Saraie, Jpn. J. Appl. Phys., **29** (1990) L723.
33) A. C. Alton and T. Yodo, J. Cryst. Growth, **130** (1993) 405.
34) S. Adachi and T. Taguchi, Phys. Rev., B **43** (1991) 9569.
35) M. Yoneta, H. Kobashi, M. Arima, C. Hatano, M. Ohishi and H. Saito, *Extended Abstracts of the Japan Society of Applied Physics*: The 55th Autumn Meeting (1994) 20a-MB-5.
36) H. Mitsuhashi, I. Mitsuishi, M. Mizuta and H. Kukimoto, Jpn. J. Appl. Phys., **24** (1985) L578.
37) J. Petruzzello, B. L. Greenberg, D. A. Cammack and R. Dalby, J. Appl. Phys., **63** (1988) 2299.
38) K. Ohkawa, T. Mitsuyu and O. Yamazaki, Phys. Rev. B, **38** (1988) 12465.
39) D. Berlincourt, H. Jaffe and L. R. Shiozawa, Phys. Rev., **129** (1963) 1009.
40) T. Yodo, T. Koyama and K. Yamashita, J. Appl. Phys., **64** (1988) 2403.

41) C. G. Van de Walle, Phys. Rev. B, **39** (1989) 1871.
42) Y. Kawakami, T. Toyoda, Y. Wu, S. Fujita and S. Fujita, J. Cryst. Growth, 107 (1991) 1072.
43) Y. Okada, H. Shimomura and M. Kawabe, Jpn. J. Appl. Phys., **31** (1992) L1121.
44) P. O'Keeffe, C. O'Morain, S. Komura, M. Ishii, T. Meguro, Y. Iimura, S. Den, T. Morikawa and Y. Aoyagi, Jpn. J. Appl. Phys., **31** (1992) 3301.
45) Y. Kawakami, T. Toyoda, Y. Wu, S. Fujita and S. Fujita, Jpn. J. Appl. Phys., **29** (1990) 2440.
46) Y. J. Chun, Y. Okada and M. Kawabe, Jpn. J. Appl. Phys., **32** (1993) L1085.
47) M. J. Matragrano, G. P. Watson and D. G. Ast, Appl. Phys. Lett., **62** (1993) 1417.
48) Y. Okada, S. Ohta, T. Fujita and M. Kawabe, Jpn. J. Appl. Phys., **33** (1994) 759.
49) A. Kamata, Appl. Phys. Lett., **63** (1993) 3953.

Chapter 4

1) S. C. Goyal and R. Prakash, Phys. Stat. Sol. (b), **83** (1977) 509.
2) H. L. Oczkowski, Phys. Stat. Sol. (a), **68** (1981) 199.
3) B. H. Lee, J. Appl. Phys., **41** (1970) 2988.
4) H. Mitsuhashi, I. Mitsuishi and H. Kukimoto, Jpn. J. Appl. Phys., **24** (1985) L864.
5) N. Matsumura, K.Ishikawa, J. Saraie and Y. Yodogawa, J. Cryst. Growth, **72** (1985) 41.
6) S. Fujita, K. Terada, T. Sakamoto and S. Fujita, J. Cryst. Growth, **94** (1989) 102.
7) S. Hirata, S. Fujita, S. Fujita and M. Isemura, J. Cryst. Growth, **104** (1990) 521.
8) S. Asai and K. Oe, J. Appl. Phys., **54** (1983) 2052.
9) N. Matsumura, M. Tsubokura and J. Saraie, J. Crystal Growth, **95** (1989) 525.
10) C. G. Van de Walle, Phys. Rev. B, **39** (1989) 1871.
11) K. Shazad, D. J. Olego, C. G. Van de Walle, Phys. Rev. B, **38** (1988)

1417.
12) K. Ohkawa, T. Mitsuyu and O. Yamazaki, Phys. Rev. B, **17** (1988) 12465.
13) N. Shibata, A. Ohki, S. Zembutsu and A. Katsui, Jpn. J. Appl. Phys., **27** (1988) L487.
14) T. Soma, Solid State Commun., **34** (1980) 927.
15) D. W. Langer and R. N. Euwema, Phys. Rev. B , **2** (1970) 4005.
16) R. People and J. C. Bean, Appl. Phys. Lett., **47** (1985) 322.
17) Y. Yokogawa, H. Sato, and M. Ogura, Appl. Phys. Lett., **52** (1988) 1678.
18) Y. Wu, S. Fujita and S. Fujita, J. Appl. Phys., **67** (1990) 908.
19) J. W. Matthews, S. Mader and T. B. Ligt, J. Appl. Phys., **41** (1970) 3800.
20) N. Shibata, A. Ohki, S. Zembutsu and A. Katsui, Jpn. J. Appl. Phys., **27** (198) L441.
21) E. D. Bourret, F. X. Zach, K. M. Yu, J. M. Walker, J. Cryst. Growth, **147** (1994) 47.
22) T. Nishimura, K. Mizuguchi, N. Hayafuji, and T. Murotani, Jpn. J. Appl. Phys., **26** (1987) L1141.
23) K. Rajan, R. Devine, W. T. Moore and P. Maigne, J. Appl. Phys., **62** (1987) 1713.
24) T. Kawai, H. Yonezu, D. Saito, M. Yokozeki and K. Pak, Jpn. J. Appl. Phys., **33** (1994) 5617.
25) K. Rajan and M. Denhoff, J. Appl. Phys., **62** (1987) 1710.
26) D. C. Houghton, D. D. Perovic, J. M. Baribeau and G. C. Weatherly, J. Appl. Phys., **67** (1990) 1850.
27) J. Petruzzello, B. L. Greenberg, D. A. Cammack and R. Dalby, J. Appl. Phys., **63** (1988) 2299.
28) S. Guha, J. M. DePuydt, J. Qiu, G. E. Hofler, M. A. Haase, B. J. Wu and H. Cheng, Appl. Phys. Lett., **63** (1993) 3023.
29) N. Motta, A. Balzarotti, P. Letardi, A. Kisiel, M. T. Czyzyk and M. Zimnal-stranawska, J. Cryst. Growth, **72** (1985) 205.
30) J. C. Phillips, *Bonds and Bands in Semiconductors*: Academic Press New York, p80 (1973)
31) S. Guha, H. Munekata, F. K. LeGoues and L. L. Chang, Appl. Phys. Lett., **60** (1992) 3220.

32) S. Guha, H. Munekata and L. L. Chang, J. Appl. Phys., **73** (1993) 2294.
33) Q. Fu, D. Lee, A. Mysyrowics, A. V. Nurmikko, R. L. Gunshor and L. A. Kolokziejski, Phys. Rev. B, **15** (1988) 8791.
34) P. R. Newbury, K. Shazad and D. A. Cammack, Appl. Phys. Lett., **58** (1991) 1065.
35) C. Klingshirn, J. Cryst. Growth, **117** (1992) 753.
36) H. Nakata, T. Yodo and K. Yamashita, Jpn. J. Appl. Phys., **29** (1990) L720.
37) H. Okuyama, E. Kato, S. Itoh, N. Nakayama, Y. Ohata and A. Ishibashi, Appl. Phys. Lett., **66** (1995) 656.
38) O. Akimoto and E. Hanamura, Solid State Commun., 10 (1972) 253.
39) P. P. Edwards and M. J. Sienko, Phys. Rev. B, **17** (1978)2575.
40) J. Cui, H. Wang, F. Gan, X. Huang, Z. Cai, Q. Li and Z. Yu, Appl. Phys. Lett., **61** (1992) 1540.
41) J. Massa, G. S. Buller, A. C. Walker, J. Simpson, K. A. Prior and B. C. Cavenett, Appl. Phys. Lett., **64** (1994) 589.
42) E. O. Gobel, J. Kuhl and R. Hoger, J. Lumines., **30** (1985) 541.
43) G. D. Cody, J. Non-cryst. Solid, **141** (1992) 3.
44) T. Tiedje and J. M. Cebulka, Phys. Rev. B, **28** (1983) 7075.
45) D. A. B. Miller, D. S. Chemla, T. C. Damen, A. C. Gossard, W. Wiegmann, T. H. Wood and C. A. Burrus, Phys. Rev. B, **32** (1985) 1043.
46) M. Morita, K. Goto and T. Suzuki, Jpn. J. Appl. Phys., **29** (1990) L1663.
47) R. Droopad, D. S. Gerber, C. Choi and G. N. Maracas, J. Cryst. Growth, **127** (1993) 606.
48) T. Ishikawa and K. Tada, Jpn. J. Appl. Phys., **28** (1989) L1982.
49) S.M.Wang, G.Treideris, W.Q.Chen and T.G.Andersson, Appl. Phys. Lett. **62**, 61 (1993).
50) G.D.Sanders and K.K.Bajaj, J. Appl. Phys. **68**, 5348 (1990).
51) J. Cui, H. Wang, F. Gan, X. Huang, Z. Cai, Q. Li and Z. Yu, Appl. Phys. Lett. **61**, 1540 (1992).
52) J. Feldmann, G. Peter, E. O. Gobel, K. Leo, H. Polland, K. Ploog, K. Fujiwara and T. Nakayama, Appl. Phys. Lett., **51** (1987) 226.
53) M. Hovinen, J. Ding, A. Salokatve, A. V. Nurmikko, G. C. Hua, D. C. Grillo, L. He, J. Han, M. Ringle and R. L. Gunshor, J. Appl. Phys., **77** (1995) 4150.

54) S. Tomiya, E. Morita, M. Ukita, H. Okuyama, S. Itoh, K. Nakano and A. Ishibashi, Appl. Phys. Lett., **66** (1995) 1208.
55) M. Hovinen, J. Ding, A. V. Nurmikko, G. C. Hua, D. C. Grillo, L. He, J. Han and R. L. Gunshor, Appl. Phys. Lett., **66** (1995) 2013.
56) K. Shazad, J. Petruzzello, D. J. Olego, D. A. Cammack, Appl. Phys. Lett., **57** (1990) 2452.

Chapter 5

1) T. Nina, T. Minato and K. Yoneda, Jpn. J. Appl. Phys., **21** (1982) L387.
2) T. Miyajima, H. Okuyama, K. Akimoto, Y. Mori, L. Wei and S. Tanigawa, Appl. Phys. Lett., **59** (1991) 1482.
3) W. Stutius, Appl. Phys. Lett., **38** (1981) 352.
4) S. Yamaga, A. Yoshikawa and H. Kasai, J. Cryst. Growth, **86** (1988) 252.
5) A. Kamata, T. Uemoto, M. Okajima, K. Hirahara, M. Kawachi and T. Beppu, J. Cryst. Growth, **86** (1988) 285.
6) T. Matsumoto, T. Iijima and H. Goto, J. Cryst. Growth, **99** (1990) 427.
7) P. J. Dean, D. C. Herbert, C. J. Werkhoven, B. J. Fitzpatrick and R. N. Bhargava, Phys. Rev. B, **10** (1981) 4888.
8) A. Yoshikawa, H. Nomura, S. Yamaga and H. Kasai, J. Appl. Phys., **65** (1989) 1223.
9) K. Ohkawa, T. Mitsuyu and O. Yamazaki, J. Appl. Phys., **62** (1987) 3216.
10) T. Saitoh, T. Yokogawa and T. Narusawa, Appl. Phys. Lett., **55** (1989) 735.
11) W. D. Laidig, N. Holonyak, Jr., M. D. Camras, K. Hess, J. J. Coleman, P. D. Dapkus and J. Bardeen, Appl. Phys. Lett., **38** (1981) 776.
12) M. D. Camras, N. Holonyak, Jr., K. Hess, M. J. Ludowise, W. T. Dietze and C. R. Lewis, Appl. Phys. Lett., **42** (1983) 185.
13) J. W. Lee and W. D. Laidig, J. Electron. Mater., **13** (1984) 147.
14) K. Ohkawa, T. Mitsuyu and O. Yamazaki, J. Appl. Phys., **62** (1987) 3216.
15) S. O. Ferreira, H. Sitter and W. Faschinger, Appl. Phys. Lett., **66** (1995) 1518.

16) T. Muranoi, S. Onizawa and M. Sasaki, J. Cryst. Growt, **138** (1994) 255.
17) N. Shibata, A. Ohki and A. Katsui, J. Cryst. Growth, **93** (1988) 703.
18) A. Yohsikawa, H. Nomura, S. Yamaga and H. Kasai, Jpn. J. Appl. Phys., **37** (1988) L1948.
19) N. Shibata, A. Ohki and S. Zembutsu, Jpn. J. Appl. Phys., **27** (1988) L251.
20) M. Fujimoto, I. Suemune, H. Osaka and Y. Fujii, Jpn. J. Appl. Phys., **32** (1993) L524.
21) A. Yoshikawa, H. Nomura, S. Yamaga and H. Kasai, J. Appl. Phys., **65** (1989) 1223.
22) E. F. Schubert, J. E. Cunningham and W. T. Tsang, Solid State Commun., **63** (1987) 591.
23) T. Yodo, T. Koyama and K. Yamahsita, J. Appl. Phys., **64** (1988) 2403.
24) H. H. Woodbury and M. Aven, Phys. Rev. B, **9** (1974) 5195.
25) W. T. Tsang and E. F. Schubert, Appl. Phys. Lett., **60** (1992) 115.
26) S. M. Shibli, M. C. Tamargo, J. L. De Miguel, B. J. Skromme, R. E. Nahory and H. H. Farrell, J. Appl. Phys., **66** (1989) 4295.
27) P. P. Debye and E. M. Conwell, Phys. Rev., **93** (1954) 693.
28) R. N. Bhargava, J. Cryst. Growth, **59** (1982) 15.
29) A. Baltz, Appl. Phys. Lett., **7** (1965) 10.
30) J. Han, Y. Fan, M. D. Ringle, L. He, D. C. Grillo, R. L. Gunshor, G. C. Hua and N. Otsuka, J. Cryst. Growth, **138** (1994) 464.
31) E. F. Schubert: *Doping in III-V semiconductors*, Press Syndicate of the University of Cambridge.
32) W. T. Masselink. Y. C. Chang and H. Morkoc, C. W. Litton, K. K. Bajaj and P. W. Yu, Solid State Electron, **29** (1986) 205.
33) K. Shazad, D. J. Olego and C. G. Van de Walle, Phys. Rev. B, **38** (1988) 1417.
34) L. Makowski and M. Glicksman, J. Phys. Chem. Solids, **34** (1973) 487.
35) M. Glicksman, R. E. Enstrom, S. A. Mittleman and J. R. Appert, Phys. Rev. B, **9** (1974) 1621.
36) S. Yamada, T. Fukui and H. Saito, J. Vac. Sci. Technol. B, **5** (1987) 960.
37) M. K. Lee, R. H. Horng and L. C. Haung, Appl. Phys. Lee., **59** (1991) 3261.
38) Y. Nakata, O. Ueda and T. Fujii, Jpn. J. appl. Phys., **30** (1991) L249.
39) W. B. Leigh, P. Besomi and B. W. Wessels, J. Appl. Phys., **53** (1982)

532.
40) T. Yao, M. Ogura, S. Matsuoka and T. Morishita, Appl. Phys. Lett., **43** (1983) 499.
41) H. E. Ruda, J. Appl. Phys., **59** (1986) 1220.
42) H. H. Woodbury, Phys. Rev. B, **9** (1974) 5188.
43) F. J. Blatt, Phys. Rev., 105 (1956) 1203.
44) E. F. Schubert, K. Ploog, Phys. Rev. B, **30** (1984) 7021.
45) D. W. Kisker and A. G. Zawadzki, J. Cryst. Growth, 89 (1988)378.

Chapter 6

1) J. Petruzzello and D. J. Olego, J. Appl. Phys., **63** (1988) 1783.
2) Y. Rajakarunanayake, B. H. Cole, J. O. McCaldin, D. H. Chow, J. R. Soderstrom, T. C. McGill and C. M. Jones, Appl. Phys. Lett., **55** (1989) 1217.
3) R. D. Feldman, R. F. Austin, P. M. Bridenbaugh, A. M. Johnson, W. M. Simpson, B. A. Wilson and ?C. E. Bonner, J. Appl. Phys., **64** (1988) 1191.
4) F. Iida, K. Imai and K. Kumazaki, J. Cryst. Growth, **127** (1993) 356.
5) H. P. Wagner, W. Kuhn and W. Gebhardt, J. Cryst. Growth, **101** (1990) 199.
6) K. Wolf, A. Naumov, T. Reisinger, M. Kastner, H. Stanzl, W. Kuhn and W. Gebhardt, J. Cryst. Growth, **135** (1994) 113.
7) T. Cloitre, N. Briot, O. Briot, B. Gil and R. L. Aulombard, J. Cryst. Growth, **133** (1993) 101.
8) N. Lovergine, D. Manno, A. M. Mancini and L. Vasanelli, J. Cryst. Growth, **128** (1993) 633.
9) A. Naumov, K. Wolf, T. Reisinger, H. Stanzl and W. Gebhardt, J. Appl. Phys., **73** (1993) 2581.
10) T. Yao, M. Kato, J.J. Davies and H. Tanino, J. Cryst. Growth, **86** (1988) 552.
11) D. Lee, A. Mysyrowics, A. V. Nurmikko and B. J. Fitzpatrick, Phys. Rev. Lett., **58** (1987) 1475.
12) K. Dhese, J. E. Micholls, J. Goodwin, W. E. Hagston, J.J. Davies, M. P. Halsall, B. Cockayne and P. J. Wright, J. Cryst. Growth, **117** (1992) 91.

13) M. J. S. P. Brasil, R. E. Nahory, F. S. Turco-Sandroff, H. L. Gilchrist and R. J. Martin, Appl. Phys. Lett., **58** (1991) 2509.
14) A. Naumov, H. Stranzi, K. Wolf, S. Lankes and W. Gebhardt, J. Appl. Phys., **74** (1993) 6178.
15) Y. Fan, J. Han, L. He, J. Saraje, R. L. Gunshor, M. Hagerott, H. Jeon, A. V. Nurmikko, G. C. Hua and N. Otsuka, Appl. Phys. Lett., **61** (1992) 3160.
16) A. Ishibashi, Y. Mori, J. Cryst. Growth, **138** (1994) 677.
17) J. Han, T. S. Stavrinides, M. Kobayashi, R. L. Gunshor, M. M. Hagerott and A. V. Nurmikko, Appl. Phys. Lett., **62** (1993) 840.
18) W. Faschinger, S. Ferreria and H. Sitter, Appl. Phys. Lett., **64** (1994) 2682.
19) W. Faschinger, S. Ferreira, H. Sitter, J. Cryst. Growth, **151** (1994) 267.
20) K. Wolf, H. Stanzl, A. Naumov, H. P. Wagner, W. Kuhn, B. Hahn, W. Gebhardt, J. Cryst. Growth, **138** (1994) 412.
21) R. People and J. C. Bean, Appl. Phys. Lett., **47** (1985) 322.
22) K. Shazad and D. J. Olego, Phys. Rev. B, **38** (1988) 1417.
23) M. Konagai, M. Kobayashi, R. Kumura and K. Takahashi, J. Crst. Growth, **86** (1988) 290.
24) Y. Rajakarunanayake, R. H. Miles, G. Y. Wu and T. C. McGill, Phys. Rev. B, **37** (1988) 10212.
25) C. G. Van de Walle, Phys. Rev. B, **39** (1989) 1871.
26) S. Permogorov and A. Reznitsky, J. Lumin., **52** (1992) 201.
27) S. Tatarenko, J. Cibert, K. saminadayar, P. H. Jouneau, V. H. Etgens, M. Sauvage-Simkin and R. Pinchaux, J. Cryst. Growth, **127** (1993) 339.
28) K. Y. Chang, K. C. Hisieh, and J. N. Baillargeon, Appl. Phys. Lett., **60** (1992) 2892.
29) R. Notzel, J. Temmyo, A. Kozen, T. Tamamura, T. Fukui, and H. Hasegawa, Appl. Phys. Lett., **66** (1995) 2525.
30) R. Notzel, J. Temmyo and T. Takamura, Nature, **369** (1994) 131.
31) M. Kitamura, and Y. Arakawa, Appl. Phys. Lett., **66** (1995) 3663.
32) Y. Takemura, H. Nakanishi, M. Konagai, K. Takahashi, J. Crystl. Growth, **111** (1991) 802.
33) M. Konagai, M. Kobayashi, R. Kimura and K. Takahashi, J. Cryst. Growth, **86** (1988) 290.
34) Y. Takemura, S. Dosho, M. Konagai and K. Takahashi, J. Cryst. Growth,

101 (1990) 81.
35) Y. Wu, S. Fujita and S. Fujita, J. Appl. Phys., **67** (1990) 908.
36) K. Wolf, M. Worz, H. P. Wagner, W. Kuhn, A. Naumov and W. Gebhardt, J. Cryst. Growth, **126** (1993) 643.

博士論文公聴会

研究論文

Zn(S,Se,Te) 結晶の組成変調とその電気光学的性質

－Compositional Modulation of Zn(S,Se,Te) crystals and Their optoelectric properties－

東京工業大学総合理工学研究科電子化学専攻　博士課程

藤原裕之氏

日時：平成８年１月９日（火）15:00～16:30

会場：東京工業大学総合理工学研究科（長津田）

　　　ＧＩ棟 820 号室　電子化学専攻会議室

司会教官：清水　勇　教授　（内線５４２４）

藤原裕之氏博士論文公聴会出席者名簿 平成8年1月9日 15:00-16:30

氏名	所属	氏名	所属
伊井稔博	東工大・総理工	半那純一	東工大・像情報
内田達朗	東工大・総理工	鈴木康生	同和鉱業(株)
大嶋治一郎	同和鉱業	成田長仁	同和鉱業(株)
亀田善秋	〃	内藤武志	同和鉱業(株)
藤原貞夫	藤田観光(父)	萩野公人	東工大・総理工
〃 トキ	(母)	清水勇	東工大 総理工
北沢信章	東工大 総理工	徳丸克己	東工大・像情報
和才容子	〃	深海隆	日本電気(株)
山本泰幸	〃	小田啓治	東工大・電子化学
二子渉	〃	原和彦	東工大・像情報
宮本祐介	〃	大竹秀人	資源研
広瀬伸吾	東工大 総理工	鍋田敏之	富士フイルム
桐生英明	松下電産	賀徳行	東工大 総理工
Paul M Reimer		石田信之	東工大・電電工・電子
石原俊一	キヤノン	水野祐	三菱化学・横総研
吉田彰宏	東工大・総理工	上野啓	東工大 電気電子工
白石健一	〃	高橋國林	東工大・物情
井上浩介	〃	白井隆	埼玉大工
山崎陽一郎	東工大 電子化学	本田徹	東工大・精研
後藤順	日立中研	飯島光太	東工大 総理工
金子啓敬	東工大 電物	森田義和	東工大・総理工 山崎研
鈴木誠一	東工大 電電	舟橋正浩	東工大 像情報
阿部久也	〃		